Single-Photon Events in the DELPHI Experiment

Elisabeth Falk Harris

DEPARTMENT OF PHYSICS, LUND UNIVERSITY
LUND 1998

ISBN 91-628-3174-7
LUNFD6/(NFFL-7159) 1998

Single-Photon Events in the DELPHI Experiment

Thesis submitted for the degree of
Doctor of Philosophy in Physics

by

Elisabeth Falk Harris

Department of Physics
Lund University
Professorsgatan 1
Box 118
S-221 00 LUND
Sweden

This thesis is based on the following articles:

I *The Small Angle Tile Calorimeter in the DELPHI Experiment,*
CERN-EP/98-132; submitted to Nuclear Instruments and Methods.

II *Analysis of the single photon channel at LEP 2,*
DELPHI 98-76 CONF 144; contribution to the International Conference on High Energy Physics (ICHEP '98), Vancouver, July 1998.

III *Photon Analysis with STIC,*
DELPHI 98-147 PHYS 791.

IV *Simulation of Off-Energy Electron Background in DELPHI,*
CERN SL/94-04 (EA); also available as DELPHI 97-12 LEDI 8.

V *Performance of the STIC Silicon Detectors at LEP2,*
DELPHI 98-43 CAL 140.

VI *Algorithms for Reduction of Coherent Noise in the Silicon Shower Maximum Detector of STIC,*
INFN/TC-97/33; also available as DELPHI 97-60 CAL 137.

VII *The Fast Wire Scanner of the CERN PS,*
CERN PS/95-06 (BD/OP).

In addition, the following article appears as an appendix:

A *Precision Electroweak Tests at LEP,*
CERN-OPEN-98-024; to appear in *Proceedings of the XII International Workshop on High Energy Physics and Quantum Field Theory,* ed. B.B. Levtchenko, Moscow State University Publishing House.

Abstract

A series of studies pertaining to the STIC calorimeter at the DELPHI experiment at LEP is presented, and a new generation of fast wire scanners for emittance measurements at PS is described.

The STIC studies are centered around a single-photon analysis, in which the reaction $e^+e^- \rightarrow \gamma +$ invisible particles was studied at center-of-mass energies of 161, 172 and 183 GeV. The cross section thus obtained was used to measure the number of neutrino families, and also to set limits on physics reactions occuring outside the framework of the Standard Model. The single-photon analysis is rendered difficult by an abundance of off-energy electron background. This type of background was examined in a separate series of Monte Carlo simulations, which are also reported. The STIC calorimeter modules have been equipped with a tracking device in the form of silicon-strip detectors, in order to improve the rejection of off-energy electrons in single-photon analyses. Results from a study of the performance of these detectors are presented. A method to reduce coherent noise in the silicon-strip detectors is also described.

A new generation of fast wire scanners was installed at PS in 1994. The wire scanners are an important tool for measuring transverse beam profiles, from which transverse emittances are derived. An upgrade of a previous set of wire scanners was essential in order to obtain a reliable instrument that provides highly accurate emittance measurements, in particular in view of the future use of the PS accelerator complex as part of the injector chain for LHC. A presentation is given of the new instrument.

Contents

Preface

This dissertation summarizes my participation in projects and studies at the DELPHI experiment and in the PS Division at CERN. It is based on seven reports, enclosed as Articles I to VII. Chapters 3 to 5 and Articles I to VI are related to my participation in the STIC team of the DELPHI collaboration from 1994 to 1998. Chapter 6 and Article VII concern my work in the Beam Diagnostics group of the PS Division from 1992 to 1994. All of the reports describe the results of team efforts. In order to clarify to the reader which were my contributions to the different projects, I wish to make the following remarks:

Article I describes the electromagnetic calorimeter STIC in the DELPHI experiment. My contributions to the development of this calorimeter are mainly related to the silicon-strip detectors with which the calorimeter is equipped.

Article II describes a single-photon analysis carried out at DELPHI. My involvement in this analysis exclusively concerns the STIC calorimeter, with some emphasis on the background studies. The details of the STIC analysis are described in Article III.

Article IV concerns a study of off-energy background in DELPHI. G. von Holtey has carried out several simulation studies of different types of machine background in the LEP experiments in the past. I carried out all of the simulations reported here, but the tools for the study were all kindly provided by him, as were many of the ideas. The comparison of the simulation with DELPHI data is mainly the work of V. Hedberg.

A study of the performance of the silicon-strip detectors of STIC is reported in Article V. All of the performance studies were carried out by me, although many of the ideas behind the study were those of V. Hedberg. The reconstruction of showers described in the article is almost entirely the work of others. I have, however, made contributions to certain parts of the readout and data-processing software for these detectors.

Three algorithms for the suppression of coherent noise in the silicon-strip detectors are presented in Article VI. The algorithm that was finally chosen for an on-line implementation was developed by V. Hedberg and myself; the other two algorithms are the works of G. Della Ricca and I. Gouz. I carried out the study comparing the algorithms, again with ideas supplied by V. Hedberg.

My contributions to the development of a new fast wire scanner, reported in Arti-

cle VII, extend to practically all of the software. Although I did not contribute to any of the specifications for the instrument, I designed, implemented and tested the control system, as well as the data-acquisition and the data-analysis routines. I carried out a large part of the integration of the software for the wire scanner into the PS control system, but the transfer of data to the central system and the final user interface are not products of my work.

At the XII International Workshop on High Energy Physics and Quantum Field Theory (QFTHEP '97), which took place in Samara, Russia, 4-9 September 1997, I was invited to give a presentation on behalf of all of the LEP collaborations. My talk was entitled "Precision Electroweak Tests at LEP". The contribution to the proceedings of this workshop appears as Appendix A.

CERN, September 1998
Elisabeth Falk Harris

ISBN 91-628-3174-7
LUNFD6/(NFFL-7159) 1998

Elisabeth Falk Harris

Single-Photon Events in the DELPHI Experiment

ERRATA

Page	*Line*	*Reads*	*Should read*
iv	10	94-04	97-04
2	13	framework	framework of the
12	2	σ_E/E	$\sigma_E/E(\%)$
32	27	possiblities	possibilities
43	11	Syncrotron	Synchrotron

Chapter 1

Introduction

Experimental particle physics during the past 25 years has revolved around the Standard Model, which provides an elegant quantum-field-theoretical description of the elementary particles and their interactions as we know them today. The theory of the unification of the electromagnetic and the weak forces was developed by Glashow, Salam and Weinberg in the 1960s. Quantum chromodynamics (QCD), which describes the strong interaction, was later added to this theory, and the Standard Model was born.

Strong experimental support for the theory of the electroweak interaction came with the discovery of neutral currents in neutrino and polarized-electron scattering experiments in the 1970s, and with the direct observation of the Z^0 and the $W^{\pm}$ bosons at the Sp$\bar{\text{p}}$S proton-antiproton collider at CERN in 1981 [1]. A range of large and small experiments have since confirmed almost every aspect of the Standard Model, and, to date, there are no convincing experimental indications for failures of this theory.

In the 1980s, a new accelerator was built at CERN in order to allow mass production of, first, Z^0s and, later, $W^{\pm}$ pairs. LEP, the Large Electron Positron Collider, was inaugurated in 1989, and four experiments (ALEPH, DELPHI, OPAL, and L3) have collected data from electron-positron annihilations since then. The wealth of data collected has allowed unique precision tests of various parameters of the electroweak theory of the Standard Model, and the results obtained have been in excellent agreement with the model.

Yet, the Standard Model does not provide the ultimate description of the smallest constituents of matter. The model has certain drawbacks, which make it an unsatisfactory and incomplete description of nature. One of the most serious weaknesses is related to the manner in which the Z^0 and $W^{\pm}$ bosons acquire mass. They do so through the so-called Higgs mechanism, which breaks the symmetry of the electroweak theory. A consequence of the Higgs mechanism is the existence of a Higgs boson, which has yet to be observed. The problem (often called the hierarchy problem) arises in giving the Higgs boson a mass that is smaller than the upper end of the range within which the theory remains valid [1, 2].

Several different models have been developed that address the problems of the

Standard Model. Supersymmetry (SUSY) models are commonly believed to overcome its weaknesses [2]. These models transform bosons to fermions and vice versa. As a consequence thereof, they predict the existence of several new elementary particles, all of which remain to be discovered. Supersymmetry cannot be an exact symmetry in nature, because if SUSY particles exist, they must have masses different from those of their Standard Model partners.

Observation of a Higgs boson, as well as of any SUSY particles or of processes pertaining to some other model beyond the Standard Model, requires experiments to be performed at high center-of-mass energies. Since 1995, LEP has been upgraded and rebuilt in several steps in order to increase the energy available for creation of new particles. During the remainder of the LEP program, which is planned to end in the year 2000, the main effort will go into searching for evidence of a Higgs boson and/or of physics outside the framework Standard Model.

The next step, after LEP, will be the Large Hadron Collider (LHC), which is foreseen to begin operation in 2005. This proton-proton collider, with center-of-mass energies two orders of magnitude higher than those of LEP, will provide a powerful probe into the structure of matter, thus addressing some of the fundamental questions that remain unanswered. If the Standard Model is correct and the Higgs boson is not discovered at LEP, it should be visible in the LHC experiments. Many of the particles predicted by, e.g., the supersymmetry models are likely to have masses that would allow them to be produced at LHC.

Most of the projects presented in this dissertation are closely related to the DELPHI experiment, in particular to the calorimeter STIC, and to the LEP accelerator. One project is related to the Proton Synchrotron (PS) accelerator, which is part of the injector chain for LEP. A brief description of these machines, with a certain emphasis on the features relevant to this thesis, is given in Chapter 2. STIC is described in detail in Article I.

Several parallel analyses at the four LEP experiments look for signs of processes outside the framework of the Standard Model. One of them uses data collected with the DELPHI detector to search for reactions in which the only detectable particle after the collision of the electron and the positron is a photon. Constraints on several different models, including a couple of SUSY models, are deduced from the results of this so-called single-photon analysis. This analysis is reported in Article II. The most important detector components of DELPHI in the single-photon analysis are three electromagnetic calorimeters. The details of the part of the analysis concerning the STIC calorimeter are reported in Article III. A brief discussion of the analysis, and of the models that were tested with its results, is given in Chapter 3.

The single-photon analysis with STIC is rendered difficult by a particular type of background, the so-called off-energy electron background. A separate study of this background was carried out in order to investigate whether its rate might be reduced by

improvement of any of the data-taking conditions. The study of off-energy electrons is discussed in Chapter 4 and in Article IV.

The STIC calorimeter modules were equipped with a special tracking device in the form of silicon-strip detectors in order to improve the rejection of off-energy electrons in analyses of the type mentioned above. A study of the performance of the detectors, as well as the development of a noise-reduction scheme, are reported in Chapter 5 and in Articles V and VI.

The LHC project requires that several of the existing accelerators at CERN be rebuilt to serve as components of the injector chain for LHC. One of the accelerators that are presently undergoing significant development for this purpose is the Proton Synchrotron. Not only does the machine itself need modifications; several of the systems for beam diagnostics must also be renewed in order to allow adequate monitoring of the intricacies of the LHC acceleration scheme. The work to upgrade PS has been going on since the early 1990s. One of the many steps in this upgrading was the renewal of the so-called fast wire scanners, which measure transverse emittances in PS. This project is reported in Chapter 6 and in Article VII.

Chapter 2

Apparatus

2.1 The CERN Accelerator Complex

CERN is the largest laboratory for high-energy physics in the world. At present, the laboratory runs a complex of ten accelerators to supply experiments in high-energy and nuclear physics with particle beams. The biggest of these accelerators are LEP (the Large Electron Positron Collider), SPS (the Super Proton Synchrotron), and PS (the Proton Synchrotron). LEP currently (1998) operates at an energy of 94.5 GeV per beam and has allowed its experiments to perform a series of precision tests of the electroweak theory of the Standard Model. SPS serves as a pre-accelerator for LEP and also supplies various fixed-target experiments with proton and heavy-ion beams. During one stage of its life, in the late 1970s and the early 1980s, it was operated as a $p\bar{p}$ collider (Sp$\bar{\text{p}}$S). The experiments running there at that time made the discoveries of the Z^0 and $W^{\pm}$ bosons. PS is the most powerful machine in what is often called the PS complex, which refers to the eight smallest accelerators. Many of the accelerators in the PS complex form injector chains for SPS and LEP. They also provide a number of experiments and test set-ups with low-energy proton beams. The accelerator complex at CERN is shown in Figure 2.1.

2.2 PS — the Proton Synchrotron

The Proton Synchrotron is the heart of the accelerator complex at CERN, because most of the beams serving physics experiments at CERN pass through this accelerator. Inaugurated in 1959 and improved at several occasions since then to suit the changing needs of the physics experiments, it is today a versatile machine capable of producing beams of different particle types in a wide range of energies and intensities. It serves as an injector for the larger accelerators and also delivers beams to several fixed-target areas at CERN.

As the name suggests, PS is a synchrotron and was originally designed to accelerate protons. Today, it accelerates electrons, positrons, and heavy ions in addition to protons.

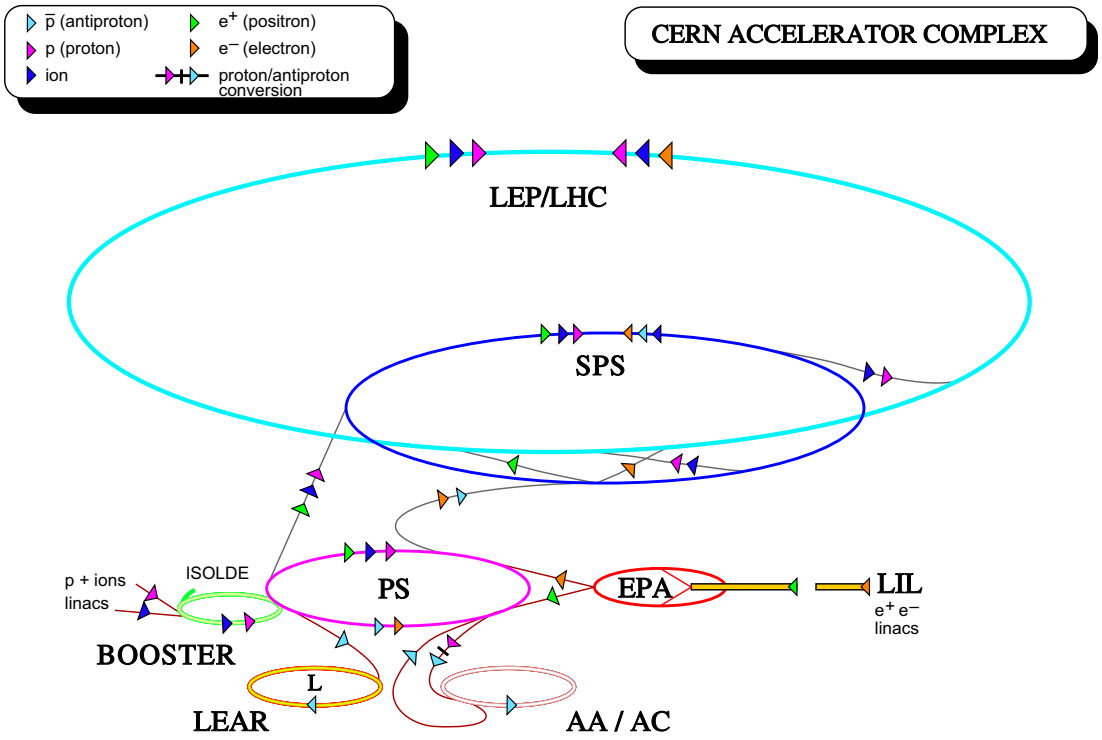

Figure 2.1: The CERN accelerator complex.

Until recently, antiprotons were also accelerated in PS. The accelerator measures 200 m in diameter, and hence 628 m in circumference. Its magnets can reach a field strength of 1.4 T. They are of the so-called combined-function type, which means that the bending and the focusing functions are combined in the same magnet, the field of which contains a dipole as well as a quadrupole component [3].

Beams accelerated in PS are either sent to SPS for further acceleration or are extracted at one of the fixed-target stations in the so-called East Area. Lepton beams are always passed on to SPS, whereas proton beams can either be extracted at the East Area or be sent to SPS. After further acceleration, SPS sends leptons to LEP and protons to the fixed-target stations in the West Area or the North Area. In 1994, a program for lead ions was started at PS [4]. These ions are sent via SPS to the West Area. Until 1996, there was also a program for antiprotons. Antiprotons were produced from a target by proton beams from PS. They were injected in the Antiproton Accumulator (AA), where they were cooled and passed on to the Antiproton Collector (AC). The cooled antiproton beams were sent back into PS, accelerated, and transferred to the Low Energy Antiproton Ring, LEAR. The LEAR program is being replaced by a smaller-scale antiproton program scheduled to begin in 1999, for which the AA/AC complex is being modified to become an Antiproton Decelerator (AD). LEAR itself is undergoing modification to become a Low Energy Ion Ring (LEIR), which will be used as an ion storage ring for LHC.

Particles are injected into PS either from the PS Booster or from EPA, the Electron Positron Accumulator. PS beams are divided into packets, or so-called bunches; there are normally eight of these, circulating with a period of down to 2.1 μs at the highest energies.

The beams of PS vary in energy from 1 to 25 GeV and in intensity from 10^9 to $2.7 \cdot 10^{13}$ particles per pulse. Protons can be accelerated to an energy of 25 GeV, whereas leptons are normally accelerated to 3.5 GeV. Lead ions are accelerated to an energy of 4.2 GeV/u.

PS serves its clients according to a schedule composed of so-called cycles and supercycles. A cycle usually lasts for 1.2 or 2.4 seconds. This is the time needed to inject, accelerate, and eject one beam of particles for a specific destination. The cycle that follows is often used for a different type of beam. After a time on the order of 15 seconds, which normally encompasses some ten cycles, the scheme repeats itself in the next supercycle.

Over a period of several years, which began in 1993, PS is undergoing gradual changes in order to meet a new challenge: Together with its pre-accelerators and SPS it will serve as an injector chain for the next big accelerator at CERN, LHC, the Large Hadron Collider, which will be installed in the tunnel that LEP occupies at present and which is scheduled to start operating in the year 2005. Beams of protons, ions, and electrons will be delivered to LHC to be used both in colliding mode and for fixed-target experiments [5].

2.3 LEP — the Large Electron Positron Collider

LEP, the Large Electron Positron Collider, is at present the largest accelerator at CERN. It measures 27 km in circumference and was inaugurated in 1989. It serves four competing experiments, located at the four points where collisions between the electron and the positron beams take place. Until 1995, it operated at an energy of 45.6 GeV per beam, producing Z^0 bosons with a rest mass of 91.2 GeV/c^2. The purpose of the mass production of Z^0 bosons that took place during this period (often called LEP1) was to allow tests of various aspects of the theory of unified weak and electromagnetic interactions of the Standard Model.

Beginning in December 1995, the energy of LEP was increased in several steps to the present 94.5 GeV per beam (1998). A further increase of a few GeV is foreseen for 1999. (This stage of the LEP program is usually called LEP2.) These higher energies permit the production of pairs of $W^{\pm}$ bosons, which have a rest mass of 80.2 GeV/c^2. They also open windows for searches for a Higgs particle as well as for particles beyond the Standard Model, notably the lightest supersymmetric particles.

The LEP program will come to an end, and the accelerator will close down, in the year 2000, in order to allow for the installation of LHC apparatus to begin.

2.4 The DELPHI Detector

DELPHI (DEtector with Lepton, Photon and Hadron Identification) is one of the four experiments at LEP. It is a general-purpose detector built of several subdetectors, with particular emphasis on particle identification. A layout of DELPHI with its subdetectors is shown in Figure 2.2. The ensemble of subdetectors forms one cylindrical part, the so-called "barrel", and two endcaps covering the "forward" regions.

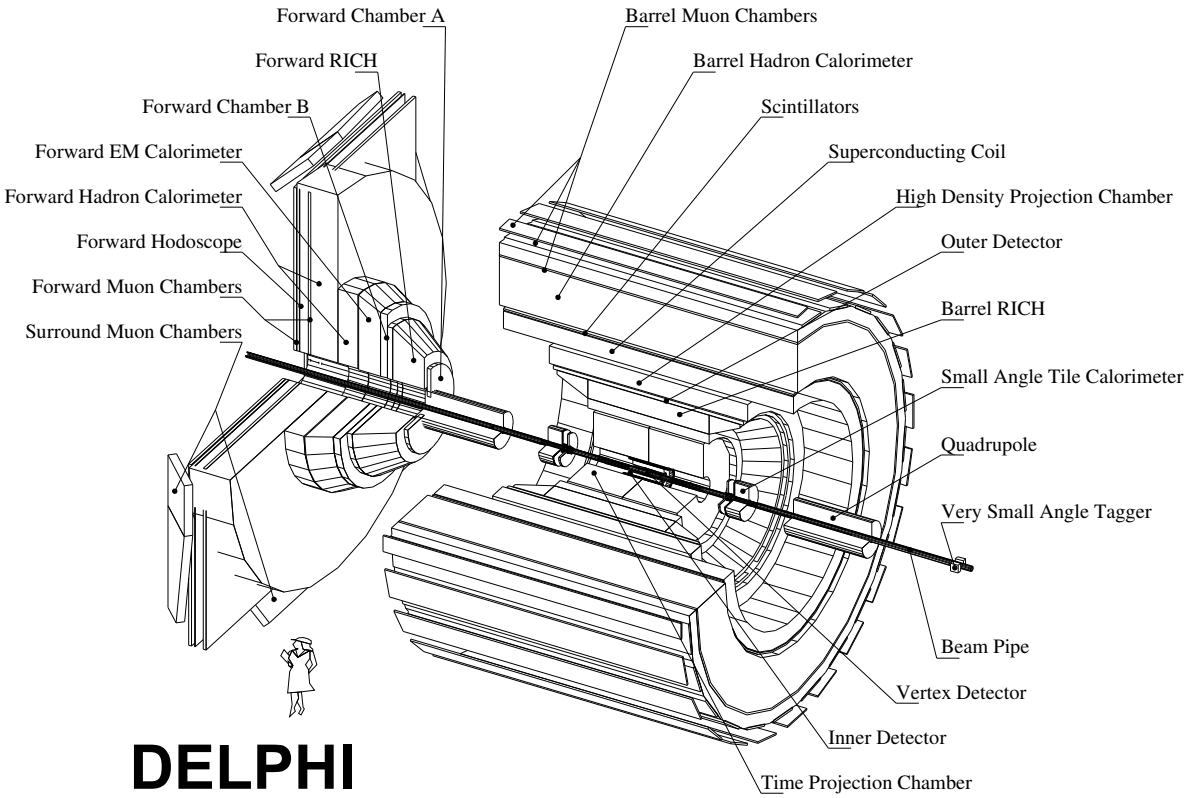

Figure 2.2: The DELPHI detector.

A set of tracking detectors covers the volume closest to the interaction point. The most important of these are the Vertex Detector (VD), with its extension the Very Forward Tracker (VFT) (not shown in the figure), and the Time Projection Chamber (TPC). The Ring Imaging Cherenkov detector (RICH) makes use of Cherenkov light in order to identify hadrons. Outside the tracking detectors are a set of electromagnetic calorimeters: the High Density Projection Chamber (HPC) in the barrel region and the Forward Electromagnetic Calorimeter (FEMC), the Small Angle Tile Calorimeter (STIC) and the Very Small Angle Tagger (VSAT) in the forward region. Located immediately outside HPC is the coil of a superconducting solenoid that provides a magnetic field for the identification of particle charge. It reaches a field strength of 1.2 T and was the largest superconducting magnet ever constructed when it was installed in DELPHI. Interleaved in the return yoke of the magnet is the Hadron Calorimeter (HAC). On

the outside of DELPHI are the Barrel, Forward and Surrounding Muon Chambers (MUB, MUF and SMC) for identification of muons. Not shown in the figure are the so-called 40°-taggers, which are scintillators that were added to improve the hermeticity of DELPHI by providing detection of electrons and photons in the regions between the barrel and the endcaps.

The standard coordinate system used in DELPHI, which will also be used here, is oriented so that the z axis is parallel to the beam line and points in the direction of the electron beam, the x axis points towards the center of LEP, and the y axis points upwards. φ denotes the azimuthal angle around z, $r = \sqrt{x^2 + y^2}$ is the radial coordinate, and θ is the polar coordinate with respect to z.

A large part of the work related to this thesis concerns the STIC detector, which is described separately in Section 2.5. The characteristics of the main tracking devices are summarized in Section 2.4.1, due to the importance of these detectors to DELPHI as a whole. The physics analysis described in Chapter 3 makes use mainly of the electromagnetic calorimeters, which are described briefly in Section 2.4.2. For a more detailed description of DELPHI and its subdetectors, the reader is referred to [6] and the references therein.

2.4.1 Tracking

The Vertex Detector and the Very Forward Tracker [7] together form the Silicon Tracker. The VD consists of silicon-strip detectors in three coaxial cylindrical layers surrounding the beam pipe. The innermost and the outermost layers, as well as the external parts of the central layer, have silicon strips on both sides. The strips are arranged orthogonally to each other on the two sides, thus permitting measurements of track coordinates in z as well as in r and φ. The three layers are located at average radial distances of 63, 90 and 109 mm from the beam line. They cover the polar-angular region $25° \leq \theta \leq 155°$. The VFT consists of two sets of four conical layers of silicon detectors: two layers of pixel detectors and two layers of strip detectors. One set is located on either side of the VD. The four layers together cover the region $10° \leq \theta \leq 25°$.

The Time Projection Chamber [8] is the principal tracking device of DELPHI. It consists of two large drift volumes, separated by a central drift anode, and two ring-shaped endcaps. The structure has an inner radius of 32 cm and an outer radius of 116 cm. Each of the endcaps is divided into six sectors. Each sector is equipped with a multi-wire proportional chamber with 192 sense wires and 16 pad rows shaped as segments of 16 concentric circles. The detector provides 16 space points per particle trajectory at polar angles $39° \leq \theta \leq 141°$. At least three rows of pads are crossed by particles entering at polar angles $20° \leq \theta \leq 160°$. The drift volumes contain a gas mixture of methane and argon.

2.4.2 Electromagnetic Calorimetry

The High Density Projection Chamber is a gas sampling calorimeter covering the barrel region of DELPHI ($43° \leq \theta \leq 137°$). Layers of lead converter are interleaved with slots of a gas mixture of argon and methane, and the detector measures the position and the energy of a shower in the same way as a time-projection chamber. It consists of 144 modules arranged in six rings inside the magnetic field. The rings have an inner radius of 208 cm and an outer radius of 260 cm, corresponding to a thickness in radiation lengths (X_0) of $18X_0/\sin\theta$. A shower is sampled nine times radially. The readout granularity is $\sim 0.1°$ in θ and $\sim 1°$ in φ. The calorimeter has an energy resolution given by $\sigma_E/E = 0.043 \oplus 0.32/\sqrt{E}$, where the energy E is in GeV.

The Forward Electromagnetic Calorimeter consists of two circular discs of lead-glass blocks, placed one on either side of the interaction point at a distance of 284 cm. The discs have a diameter of 5 m and a depth of 40 cm, corresponding to 20 radiation lengths. Each disc contains 4532 glass blocks, which have the shape of truncated pyramids pointing to the interaction region. The Cherenkov light produced in the glass by the charged particles in a shower is read out by phototriodes. Each FEMC module has a polar-angular coverage of 8°–35° and a readout granularity of about 1° in φ as well as in θ. The energy resolution has been parametrized as $\sigma_E/E = 0.03 \oplus (0.12/\sqrt{E}) \oplus (0.11/E)$, where E is in GeV.

The Small Angle Tile Calorimeter completes the calorimetric coverage in the forward region of DELPHI. It consists of two calorimeter modules located immediately outside the beam pipe. The calorimeters are equipped with a veto system providing electron-photon separation, and with planes of silicon-strip detectors that provide a simple tracking facility. STIC is described in greater detail in the following section.

2.5 STIC — The Small Angle Tile Calorimeter

The STIC calorimeters were installed in DELPHI in 1994. Their main purpose was to measure the luminosity with a systematic uncertainty of the order of 0.1% when LEP was running at the Z^0 peak. Luminosity is determined at LEP through high-precision measurements of the so-called Bhabha scattering process, i.e., the elastic scattering of an electron-positron pair (see Figure 2.3). The Bhabha cross section is proportional to $1/\theta^3$, where θ is the scattering angle, which makes it necessary to choose a region with small polar angles and a well-defined acceptance.

Another reason to build STIC was the need to improve the hermeticity of DELPHI in the forward region by closing a gap between the old luminosity monitor SAT (Small Angle Tagger) and the FEMC calorimeter. Good hermeticity in the forward region is essential in the current phase of the LEP research program, at center-of-mass energies above the Z^0 resonance, where the main goal of the data analyses is to search for particles beyond the Standard Model.

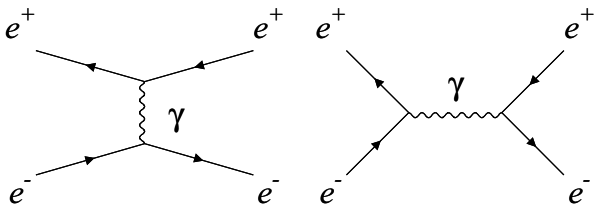

Figure 2.3: First-order diagrams for the Bhabha scattering process.

STIC consists of two electromagnetic calorimeters surrounding the beam pipe and located at a distance of 2.2 m on either side of the interaction point. The calorimeters are described in Section 2.5.1. In front of each calorimeter is a veto system consisting of a set of scintillators. This veto system is part of a neutral trigger providing separation between photons and electrons/positrons. The veto system and the triggers are discussed in Section 2.5.2. Inserted in the sampling structure of each calorimeter are two planes of silicon-strip detectors. These provide a tracking facility with which the direction of a shower can be measured. The silicon-strip detectors are presented in Section 2.5.3. An outline of a STIC calorimeter is shown in Figure 2.4. For complete descriptions of STIC and its components, see Article I and references [9, 10, 11].

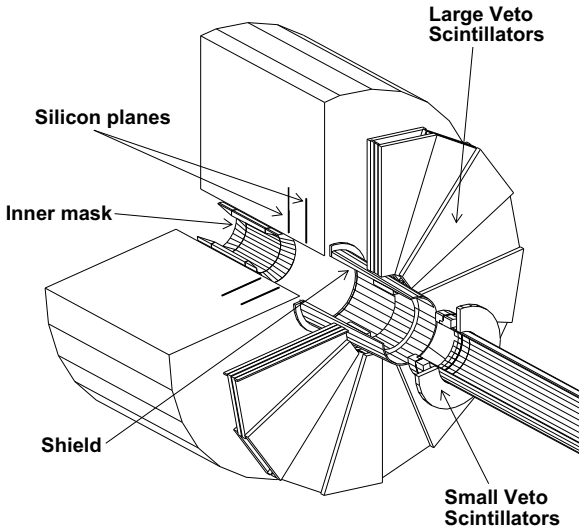

Figure 2.4: Outline of a STIC calorimeter. The planes of silicon-strip detectors inserted into the calorimeter are shown in the drawing. Placed in front of the calorimeter are the scintillators of the veto-counter system. The inner, or synchrotron, mask and the shield are tungsten rings that protect the TPC from synchrotron radiation.

2.5.1 The Calorimeters

Each of the two calorimeter modules consists of 47 sandwich layers of lead and scintillator, read out by wavelength-shifting fibers. The total depth is 37 cm, corresponding to about 26 radiation lengths. The scintillator layers are cut into segments of 10 rings and 16 sectors in such a manner that they form 160 towers that point to the interaction region. The structure of one such layer is shown in Figure 2.5. The towers are twisted by approximately 3° in the azimuthal direction in order to avoid cracks pointing to the interaction region. The calorimeters are usually referred to as arm A and arm C, according to the DELPHI convention of calling the side of incoming electrons side A and that of positrons side C.

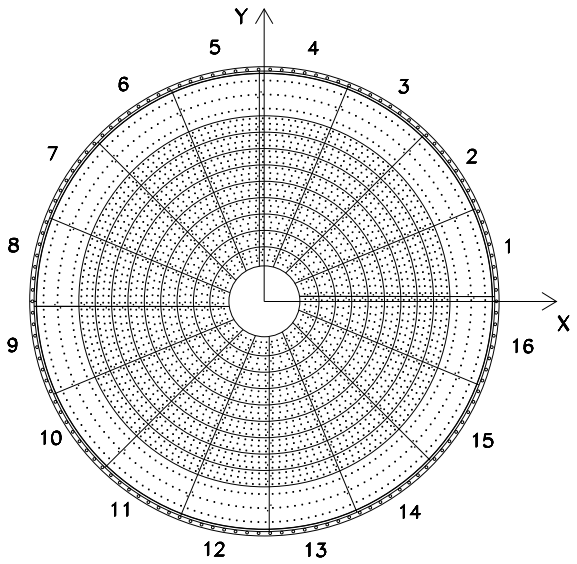

Figure 2.5: The first scintillator layer of STIC. The structure with 10 rings and 16 sectors is shown. The holes for the fibers are also indicated.

The wavelength-shifting fibers run perpendicularly through the lead-scintillator layers in such a way that they look like a set of skewers, which has earned this type of calorimeter the epithet "shashlik" calorimeter after the Russian word for skewer. The fibers have a density of approximately one per cm^2. They are read out at the back of the calorimeter by phototetrodes, one per tower.

The calorimeters extend radially from 65 mm to 417.5 mm, measured from the beam line. This corresponds to a polar-angular acceptance of 29 to 188 mrad (1.7°–10.8°). In reality, however, the inner acceptance is determined by a system of tungsten masks and shields mounted in front of STIC. Some of these were used to define the acceptance in the luminosity measurements at LEP1; others protect the TPC from synchrotron radiation. The configuration of these masks and shields has varied from year to year [11]. Currently (1998) the inner acceptance is at a radius of 84 mm (2.2°).

The energy resolution σ_E/E of the calorimeters has been parametrized as

$$\sigma_E/E = (0.68 \pm 0.09) \oplus (14.1 \pm 0.4)/\sqrt{E}.$$

The experimental error on the luminosity during data taking at the Z^0 peak is less than 0.1%.

2.5.2 The Veto Counters and the STIC Triggers

A set of scintillators constituting a charged-particle veto system is mounted in front of each arm of STIC. The veto system is part of a neutral trigger that provides electron-photon separation. Photons are identified by the absence of signals in the scintillators in front of the point where a showering particle entered STIC. The neutral trigger is used to select candidate events for the single-photon analysis discussed in Chapter 3.

The scintillator counters are composed of two parts: the main detector, called the large veto counters, and an extension to cover small polar angles, the so-called small veto counters (see Figure 2.4). The large veto counters consist of two layers of scintillator mounted in front of each arm of STIC and covering all but the innermost of its rings. The scintillator planes are divided into 16 sectors that match the segmentation of the calorimeters. The small veto counters consist of one layer of scintillator divided into two half-rings that are mounted directly on the beam pipe, in front of the large veto counters. They cover the two innermost calorimeter rings.

STIC provides a so-called single-arm trigger. This requires an electromagnetic shower in one of the arms of STIC, with an energy deposit $E \geq 0.16E_{\text{beam}}$, where E_{beam} is the beam energy, and with the showering particle entering at a radius $r > 10$ cm. This trigger is used to select and monitor so-called off-energy electrons, i.e., bremsstrahlung particles that are created anywhere in the beam line, which constitute a large background in the single-photon analysis. The neutral trigger requires the same conditions to be fulfilled as the single-arm trigger, but in addition to this, there is a requirement for the absence of any signal in at least one of the scintillator planes in the region in front of the point where the showering particle entered the calorimeter. In the large veto counters, this region is confined to the sector in which the particle entered STIC and the two adjacent sectors. In the region of the small veto counters there is no matching between the scintillator half-rings and the calorimeter sectors, and in order to fulfill the requirements for the neutral trigger, neither half may register a signal.

2.5.3 The Silicon-Strip Detectors

The design of the STIC calorimeters, with the projective geometry and the "shashlik" arrangement of the optical fibers, prevents any directional determination of showers. Instead, each calorimeter is equipped with two planes of silicon-strip detectors with

which the direction of a shower can be measured. The purpose of this tracking device is to improve rejection of off-energy electron background.

The silicon detectors consist of planes of circular strips replacing one lead-scintillator layer at a depth of 4.0 radiation lengths and another at 7.4 radiation lengths in each of the two arms of STIC, thus giving a total of four silicon planes (see Figure 2.4). The silicon planes cover 32–77 mrad in polar angle (71.5–174.2 mm and 73.2–178.4 mm in radius respectively).

Each silicon strip covers 22.5° in azimuthal angle, thus conforming to the sector geometry of the calorimeter. The strips have a radial pitch of 1.172 mm in the first plane and 1.754 mm in the second plane. They are mounted on wafers that make up two concentric rings in each of the four detector planes. Each 45° sector of a silicon plane consists of three wafers, with one inner wafer covering two calorimeter sectors and holding 2×24 strips, and two outer wafers covering one calorimeter sector and holding 36 strips each. Half of the inner ring of a silicon plane is shown in Figure 2.6.

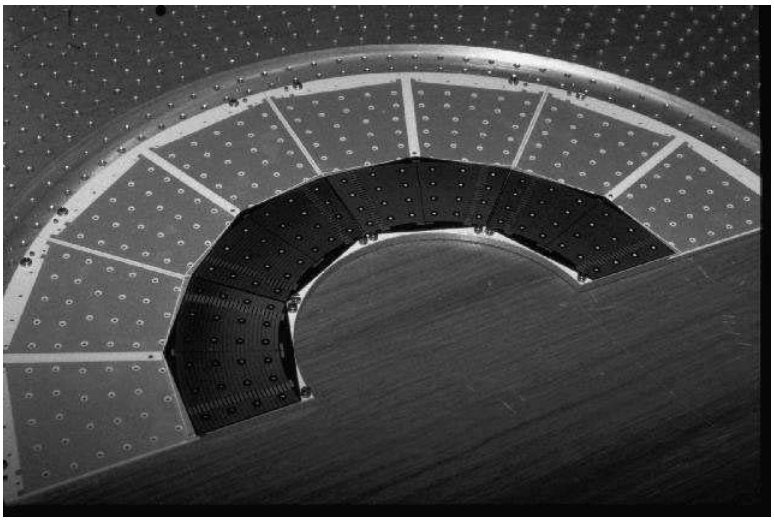

Figure 2.6: Half of the inner ring of a plane of the silicon-strip detectors mounted on its aluminum support. The inner ring is made up of eight 45° wafers (four per half-plane), each holding the strips of two sectors. The places for the 22.5° wafers of the outer plane are clearly visible. Note the holes for the wavelength-shifting fibers in the wafers as well as in the aluminum plate.

Each 45° sector of a silicon plane is connected to one Microplex MX4 amplifier chip [12] having an input capacity of 128 channels. The strips are connected to the MX4 by flat cables consisting of thin copper tracks deposited on a substrate of Kapton[1] (see Figure 2.7). These cables are matched to the input of the MX4 by a hybrid fan-in card

[1]Registered trademark of DuPont.

mounted on the cylindrical surface of STIC. The output signals from the MX4 chips are multiplexed and clocked into two Sirocco IV Fastbus modules [13], where the data are digitized by flash ADCs.

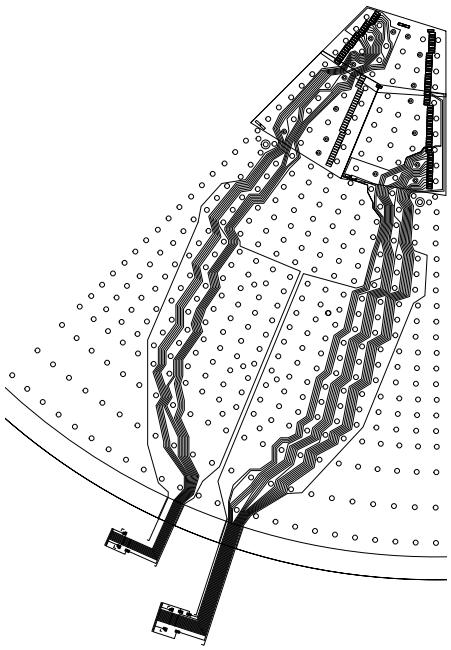

Figure 2.7: A 45° wedge (corresponding to two 22.5° calorimeter sectors) of the silicon-strip detector, with two of its eight Kapton cables shown. The strip structure within the sectors is not drawn; only the connections to the strips are indicated.

The performance of the silicon-strip detectors, as well as a scheme for the reduction of coherent noise, in which the Kapton cables play an important role, are discussed in Chapter 5.

Chapter 3

Analysis of Single Photons with STIC

In a recent analysis of so-called single-photon events recorded by DELPHI, STIC was one of three electromagnetic calorimeters used to identify and study events in which the only detectable particle is a photon. In other words, the analysis studied events corresponding to the process

$$e^+e^- \rightarrow \gamma + \text{invisible particles.}$$

The other two calorimeters were the Forward Electromagnetic Calorimeter, FEMC, and the High-Density Projection Chamber, HPC. This was the first time that STIC had been used to analyze events with a photon in the very forward region of DELPHI. The results of the analysis were used to measure the number of neutrino generations and to set limits on physics reactions occuring outside the framework of the Standard Model.

According to the Standard Model, the only invisible particles that may be produced in the process $e^+e^- \rightarrow \gamma +$ invisible particles are neutrinos. Neutrinos are produced either through s-channel annihilation of the electron and the positron to a Z^0 boson, which then decays to a neutrino-antineutrino pair, or through t-channel exchange of a $W^{\pm}$ boson between the electron and the positron. If a photon is radiated from the electron or the positron, or, in the case of W exchange, from the W, such an event becomes detectable. The Standard Model description of single-photon events makes it possible to use these events to count the number of neutrino generations, N_ν. Although the cross section for radiative neutrino production is rather small, it is very sensitive to N_ν. This method of measuring the number of neutrino families provides a complement to the so-called lineshape method, which was used to determine the number of neutrino generations from data taken at LEP1; it is free from many of the assumptions about the validity of the Standard Model on which the lineshape method is based. Beyond the Standard Model, there is also a possibility of contributions to the single-photon final state coming from some other neutral weakly interacting particle or from a new particle decaying into a photon. Therefore, the final state $\gamma +$ invisible particles provides an important tool to explore the possible existence of such hitherto unknown particles.

Some of the main features of the single-photon analysis with STIC are briefly

described in Section 3.1. Section 3.2 gives a short explanation of how the number of neutrino generations is determined. It also contains brief descriptions of the models that were used to set limits on physics beyond the Standard Model.

3.1 Experimental Aspects of the Analysis

Performing the single-photon analysis with STIC served a dual purpose: to explore the possibilities of using STIC to identify photons, and to investigate what means are available to maintain control over difficult background situations in this type of analysis. It was, so to speak, a "pilot analysis". The STIC analysis was carried out on data taken during 1996 and 1997 at center-of-mass energies $\sqrt{s}$ of 161, 172 and 183 GeV. Only the results of the analysis at 183 GeV were combined with those of the FEMC and HPC single-photon analyses. The combined analysis is reported in Article II, whereas a more detailed description of the STIC analysis is presented in Article III. Single-photon analyses using HPC data at lower center-of-mass energies (between the Z^0 peak and 172 GeV) have been performed and reported in the past [14].

3.1.1 Background

The analysis of single-photon data recorded at small polar angles, i.e., with STIC, is subject to particular difficulties, because the data contain large amounts of background. A considerable contribution to this background comes from off-energy electrons that are misidentified as photons in the analysis. The off-energy electrons are produced in interactions between beam particles and residual gas molecules in the beam pipe and are swept into the STIC acceptance region by the quadrupole magnets located near DELPHI. Another important source of background is the QED process $e^+e^- \to e^+e^-\gamma$, where the photon is detected but the electrons either escape in the beam pipe or enter DELPHI undetected. The principal challenge of the single-photon analysis with STIC was therefore to explore different methods to reduce the large background to a level where a meaningful identification of single-photon events became possible. Two subdetectors of STIC were specifically used as tools to reject background: The veto counters were used to distinguish photons from electrons, and the silicon-strip detectors were tested as a means of rejecting off-energy electrons.

Two different methods to eliminate the background contamination of the data sample were developed and studied. One method giving a satisfactory result made use of a set of cuts on the polar-angular acceptance and on the fraction of the beam energy carried by the photon. The other method allowed the inclusion of a somewhat larger region of phase space by making use of two additional cuts, one on the vertex reconstructed by the silicon detectors, and one eliminating a region within the acceptance of the calorimeter where the off-energy electron background is particularly abundant. Careful comparisons showed that the two methods yielded equal results in terms of number of events detected.

Including the cut on the vertex and the cut on the acceptance of course had the advantage of allowing a larger region of phase space to be taken into account in the analyis. The efficiency of the region gained, however, was found to be low, and including it would not have improved the significance of the analysis. As a consequence, this region was not taken into account in the final calculation of the cross sections and the derived results.

3.1.2 Results

The number of neutrino families was calculated for each of the measured cross sections at 161, 172 and 183 GeV. The three results were combined, yielding

$$N_\nu = 3.2 \pm 0.5 \pm 0.4,$$

where the first uncertainty quoted is statistical and the second is systematic. Comparisons were made with the results from the single-photon analyses carried out with the FEMC and HPC calorimeters. The comparisons showed that the results obtained with STIC are competitive with those of FEMC and HPC, despite the very difficult background conditions in the STIC analysis. The results from the three different measurements at $\sqrt{s} = 183$ GeV could thus be combined. The number of neutrino families obtained from these three measurements is

$$N_\nu = 2.92 \pm 0.25\,(\text{stat.}) \pm 0.14\,(\text{syst.}).$$

The various limits derived from the combination of the measured cross sections are presented along with the model descriptions in Section 3.2. The analysis showed that measurements with STIC should provide a valuable addition to those carried out with HPC and FEMC in future single-photon analyses.

3.2 Theoretical Aspects

As discussed above, the single-photon analysis studies the reaction

$$e^+e^- \to \gamma + \text{invisible particles},$$

where a single photon is the only detectable particle amongst the final-state products. Such events can be used to count the number of neutrino generations, because the Standard Model requires the invisible particles to be neutrino-antineutrino pairs. The only condition is that the neutrinos must be "light", i.e., have a mass $m_\nu \leq \frac{1}{2}M_Z$, where M_Z is the mass of the Z^0 boson [15]. Since the process $e^+e^- \to \nu\bar{\nu}\gamma$ is well understood theoretically, deviations from Standard Model predictions could indicate the presence of physics processes taking place beyond the Standard Model. Thus, studies of single-photon topologies also permit searches for particles of various proposed extensions to the Standard Model, for example supersymmetric (SUSY) particles; many such models would have particle interactions where the only detectable particle is a photon. If no new

particles are found, the analysis instead provides upper limits on such new phenomena. In addition to counting the number of neutrino generations, the DELPHI single-photon analysis at $\sqrt{s} = 183$ GeV was used to put limits on the neutralino mass; on the gravitino mass; on a compositeness model; and on other, unknown but model-independent, neutral states. The results from the STIC analysis were included in the calculations of the limits on the gravitino mass and on unknown neutral states. For the sake of completeness, outlines of all of the models are given below.

3.2.1 The Number of Light Neutrino Types

Counting the number of light neutrino types N_ν provides an important test of the Standard Model, because this number also yields the number of generations of fermions. There are several different ways to do this, at LEP as well as through other experiments. The most widely known method used by the LEP experiments at LEP1 energies is the lineshape method, which indirectly measures the invisible decay width $\Gamma_{\text{inv}} = N_\nu \Gamma_{\nu\nu}$ of the Z^0 boson, where $\Gamma_{\nu\nu}$ is the partial width for decay into a neutrino-antineutrino pair. An alternative technique, henceforth called the radiative method, relies on the analysis of single-photon events. The number of neutrino families is then calculated directly from the cross section of the process $e^+e^- \to \nu\bar{\nu}\gamma$. This method is rather delicate at LEP1 energies, due to the low energy of the radiated photon, but it is well suited for LEP2 energies. Since the lineshape method is restricted to energies at the Z^0 pole, the radiative method is the only method to count the number of neutrino types at higher energies. Short descriptions of both methods are given below.

The Lineshape Method

The lineshape method provided the first spectacular result of the LEP experiments when they started collecting data in 1990; it was rapidly confirmed that the number of light neutrinos is three. Relying on a wealth of statistics—20 million Z^0 bosons were recorded during the LEP1 era, which lasted until 1995—and combining their individual results, the LEP experiments have determined, through the lineshape method, the number of light neutrinos to be (see Appendix A)

$$N_\nu = 2.993 \pm 0.011.$$

In determining the number of neutrinos, one uses the fact that the total decay width Γ_Z of the Z^0 boson is

$$\Gamma_Z = \sum \Gamma_{ff} = \Gamma_h + 3\Gamma_{ll} + \Gamma_{\text{inv}}, \tag{3.1}$$

where Γ_{ff} and Γ_h are the partial widths for decay into fermions and hadrons respectively. Γ_{ll} denotes the partial width for decay into a charged lepton-antilepton pair under the assumption of lepton universality, i.e., $\Gamma_{ll} = \Gamma_{ee} = \Gamma_{\mu\mu} = \Gamma_{\tau\tau}$, where Γ_{ee} is the partial

width for decay into an electron-positron pair, and analogously for the μ and τ leptons. The total width of the Z^0, as well as its mass and the peak cross sections σ^0_{ff} for the decay of the Z^0 into different fermion-antifermion pairs, are obtained from the shape of the Z^0 resonance (i.e., the cross section as a function of the center-of-mass energy). The visible decay widths are determined from the peak cross sections, which are defined as

$$\sigma^0_{ff} \equiv \frac{12\pi\Gamma_{ee}\Gamma_{ff}}{M_Z^2\Gamma_Z^2}. \tag{3.2}$$

The number of neutrinos is then determined from the invisible decay width through

$$N_\nu = \frac{\Gamma_{ll}}{\Gamma_{\nu\nu}}\frac{\Gamma_{\rm inv}}{\Gamma_{ll}} = \frac{\Gamma_{ll}}{\Gamma_{\nu\nu}}\left(\sqrt{\frac{12\pi R_{ll}}{M_Z^2\sigma^0_h}} - R_{ll} - 3\right),$$

where Equations 3.1 and 3.2 have been used to determine the expression for N_ν. σ^0_h is the peak cross section for decay into hadrons, and R_{ll} is defined as $R_{ll} \equiv \Gamma_h/\Gamma_{ll}$. The ratio $\Gamma_{ll}/\Gamma_{\nu\nu}$ is taken from the Standard Model (see Appendix A).

The Radiative Method

The cross section for the process $e^+e^- \to \nu\bar{\nu}\gamma$ is proportional to the number of light neutrino species. The radiative method measures directly the cross section for this process, and the experimentally measured value is then compared with the theoretical prediction for the cross section as a function of N_ν. The cross section, although rather small, is very sensitive to N_ν, much more so than the total decay width of the Z^0 boson: An additional neutrino type contributes an increase to the cross section for radiative neutrino production of about 30%, whereas it contributes only about 6% to the total Z^0 width [15, 16].

Within the Standard Model, radiative neutrino production takes place either through annihilation of an electron and a positron to a Z^0, where the photon is produced through initial-state radiation by the electron or the positron (so-called radiative return to the Z^0 resonance), or through $W^\pm$ exchange, where the photon either is produced through inital-state radiation or is radiated from the W boson. The Feynman diagrams of the contributing processes, in the lowest order, are shown in Figures 3.1 and 3.2. The W-exchange processes only contribute to the production of electron neutrinos, ν_e, and so are independent of N_ν. Their overall effect on the cross section is small (a few percent) at the Z^0 resonance, but they become relatively important at higher energies (about 20% in total at $\sqrt{s} = 150$ GeV) [15, 16, 17]. Due to the radiative return to the Z^0 resonance, the radiated photons are visible as a peak in the energy spectrum of the single photons at $E_\gamma = (1 - M_Z^2/s)\,(\sqrt{s}/2)$, where E_γ is the energy of the photon, M_Z is the mass of the Z^0 and $\sqrt{s}$ is the center-of-mass energy. The contribution from W exchange to the energy spectrum is negligible in the vicinity of the radiative-return peak.

The theoretical cross section for $e^+e^- \to \nu\bar{\nu}\gamma$, from which the number of neutrino generations is derived, is calculated through integration of the doubly differential cross

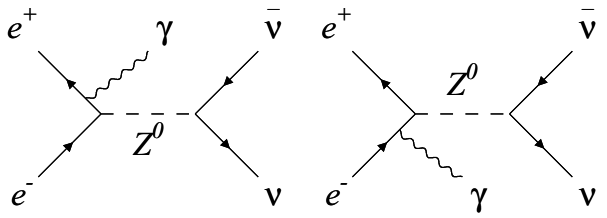

Figure 3.1: First-order processes involving annihilation to a Z^0 and contributing to the radiative production of neutrino pairs.

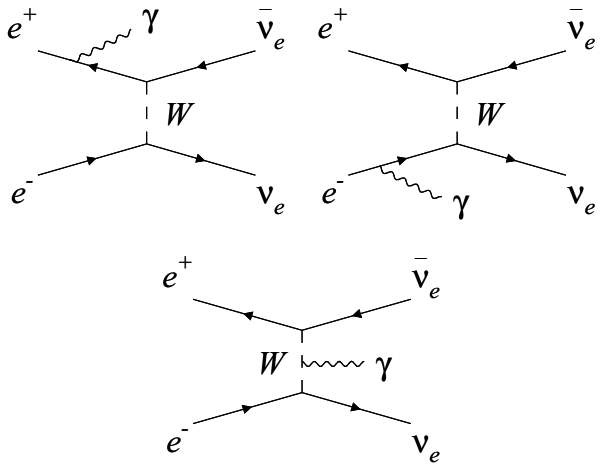

Figure 3.2: First-order processes involving W exchange and contributing to the radiative production of neutrino pairs.

section over the appropriate acceptance and kinematic region. The doubly differential cross section is [18]

$$\frac{d^2\sigma}{dx\,dy} = \frac{G_F^2 \alpha s\,(1-x)\left[(1-x/2)^2 + x^2y^2/4\right]}{6\pi^2 x\,(1-y^2)} \times \left(2 + \frac{N_\nu\,(g_V^2+g_A^2) + 2\,(g_V+g_A)\,[1-s\,(1-x)\,/M_Z^2]}{[1-s\,(1-x)\,/M_Z^2]^2 + \Gamma_Z^2/M_Z^2}\right),$$

where x is the fraction of the beam energy carried by the photon, and $y = \cos\theta_\gamma$ is the cosine of the polar angle of the photon with respect to the direction of the incident beam. G_F is the Fermi constant and α is the fine-structure constant; other variables follow definitions made previously.

The radiative method cannot compete with the lineshape method in the precision with which the number of neutrino species is determined, because the statistics available for the radiative method are limited in comparison with the data available for the lineshape measurement. Nevertheless, it is an interesting complement to the latter, because the two methods rely on different theoretical inputs from the Standard Model

and so in many respects are independent of each other [15]. As mentioned previously, the radiative method is the only technique available to count neutrinos — and to detect the production of other stable neutral particles — at energies beyond those of LEP1 [17].

3.2.2 Unknown Neutral States

Without making any assumptions about a specific model describing physics beyond the Standard Model, one can use the experimental results to set an upper limit on the probability of the existence of a new particle, X, which would be produced in association with a photon in the reaction $e^+e^- \to \gamma X$. The particle X would either be stable or would decay into invisible products. The limit is calculated from the distribution of the mass of the system recoiling against the photon, with the expected Standard Model background from $e^+e^- \to \nu\bar{\nu}\gamma$ having been taken into account.

The information from the three DELPHI calorimeters HPC, FEMC and STIC was used to determine a limit, at the 95% confidence level, for the cross section $\sigma(e^+e^- \to \gamma X)$. This varies between 0.35 and 1.1 pb for recoiling masses between 60 and 160 GeV/c^2 in the acceptance $3.8° \leq \theta_\gamma \leq 176.2°$, where θ_γ is the polar angle of the photon trajectory with respect to the beam line. A limit at the 95% confidence level, calculated with STIC data only ($\sqrt{s} = 183$ GeV), is shown in Figure 3.3.

3.2.3 Searches for SUSY Particles

Neutralino Production

Supersymmetric extensions to the Standard Model predict the existence of a fermionic superpartner to each Standard Model boson and a bosonic superpartner to each Standard Model fermion. Several different supersymmetric models exist. According to the Minimal Supersymmetric Standard Model (MSSM) [19], the four fermionic partners of the neutral Standard Model gauge and Higgs bosons are the photino, $\tilde{\gamma}$, the zino, $\tilde{Z}$, and two higgsinos, $\tilde{H}_1^0$ and $\tilde{H}_2^0$. These fermions are interaction eigenstates that mix to form four physical particles, the neutralinos. The neutralinos are believed to be amongst the lightest of the supersymmetric particles, and hence should be some of the first particles possible to discover experimentally. In particular, the lightest neutralino, $\tilde{\chi}_1^0$, is usually assumed to be the lightest SUSY particle (LSP). A possible channel for discovery of SUSY in the single-photon analysis would then be the production of a neutralino pair, $e^+e^- \to \tilde{\chi}_1^0\tilde{\chi}_2^0$, where $\tilde{\chi}_2^0$ is the second-lightest neutralino, followed by the subsequent radiative decay $\tilde{\chi}_2^0 \to \tilde{\chi}_1^0\gamma$ (see [20]). Unfortunately, however, this channel has a large cross section only in a very small region of parameter space, and the predicted cross section for the DELPHI analysis at $\sqrt{s} = 183$ GeV is too small to be of any interest.

However, other SUSY models exist that suggest instead that the gravitino $\tilde{G}$ would be the LSP. In such models, the lightest neutralino would always decay radiatively into

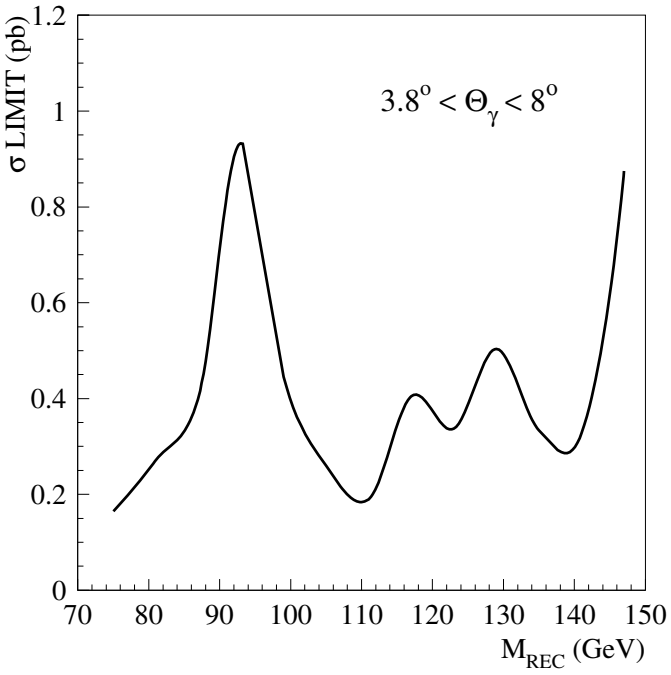

Figure 3.3: Limit at 95% confidence level for the production of an unknown, stable, neutral object. The limit was calculated from STIC data at $\sqrt{s} = 183$ GeV. It is poorer around 92 GeV/c^2 than elsewhere due to the background of radiative-return events.

a gravitino and a photon. If this is the case, the expected discovery channel in the single-photon analysis would be

$$e^+e^- \to \tilde{G}\tilde{\chi}_1^0 \to \tilde{G}\tilde{G}\gamma, \tag{3.3}$$

where the gravitinos would escape undetected. This process would take place at LEP2 only for very light gravitinos, because the cross section scales as the inverse of the gravitino mass squared [21]. This is the channel that the DELPHI analysis has investigated. Only the results from HPC were taken into account; simulation studies showed that the acceptances of STIC and FEMC would yield cross sections that are too small. The analysis determined an upper limit, at a confidence level of 95%, for the cross section for the reaction (3.3) as a function of the neutralino mass. The upper limit on the cross section is about 0.8 pb for a neutralino mass of 50 GeV/c^2 and about 0.5 pb for a neutralino mass of 150 GeV/c^2.

Gravitino Production and Mass

Supersymmetry is broken through the mass splitting between the Standard Model particles and their superpartners. From a phenomenological viewpoint, this mass splitting is arbitrary. This opens up the possibility that the gravitino may be "superlight", with a mass $m_{3/2}$ several orders of magnitude below the eV scale. Recently, it was suggested

that this may be the case, while the other supersymmetric particles are too heavy to be produced on-shell at present experiments [22]. If so, then one of the most important processes to look for in the search for a superlight gravitino would be the radiative production of a gravitino pair,

$$e^+e^- \to \tilde{G}\tilde{G}\gamma. \tag{3.4}$$

The doubly differential cross section for the process (3.4) is [22]

$$\frac{d^2\sigma}{dx_\gamma\, d\cos\theta_\gamma} = \frac{\alpha s^3}{320\pi^2|F|^4} \cdot f\left(x_\gamma,\, \cos\theta_\gamma\right),$$

where

$$f\left(x_\gamma,\, \cos\theta_\gamma\right) \simeq \frac{2\left(1-x_\gamma\right)^3\left(2-2x_\gamma+x_\gamma^2\right)}{x_\gamma \sin^2\theta_\gamma}.$$

Here, x_γ is the fraction of the beam energy carried by the photon, and θ_γ is the scattering angle of the photon with respect to the incident beam. $|F|^{1/2}$ denotes the supersymmetry-breaking scale. The function f is independent of the center-of-mass energy $\sqrt{s}$ and of $|F|^{1/2}$, but it carries all of the dependence on the photon fractional energy and on the photon angle. The integrated cross section becomes

$$\sigma = \frac{\alpha s^3}{320\pi^2|F|^4} \cdot I\left(x_{\gamma,\min},\, x_{\gamma,\max},\, |\cos\theta_\gamma|_{\min},\, |\cos\theta_\gamma|_{\max}\right),$$

where the integral

$$\begin{aligned} I &= \int_{x_{\gamma,\min}}^{x_{\gamma,\max}} dx_\gamma \int_{|\cos\theta_\gamma|_{\min}}^{|\cos\theta_\gamma|_{\max}} d\cos\theta_\gamma\; 2f\left(x_\gamma,\, \cos\theta_\gamma\right) \\ &\simeq \int_{x_{\gamma,\min}}^{x_{\gamma,\max}} dx_\gamma \int_{|\cos\theta_\gamma|_{\min}}^{|\cos\theta_\gamma|_{\max}} d\cos\theta_\gamma\; \frac{4\left(1-x_\gamma\right)^3\left(2-2x_\gamma+x_\gamma^2\right)}{x_\gamma \sin^2\theta_\gamma}. \end{aligned}$$

The integral I can be evaluated analytically over the chosen acceptance and kinematical region. The largest sensitivity is obtained with photons of low energy and/or small polar angle. If the measured cross section is used to set an upper bound σ_0, the experimental limit translates into a limit on the gravitino mass [22]:

$$m_{3/2} > 3.8 \cdot 10^{-6}\ \text{eV}\ \left[\frac{\sqrt{s}\ (\text{GeV})}{200}\right]^{\frac{3}{2}} \left[\frac{I}{\sigma_0\ (\text{pb})}\right]^{\frac{1}{4}}. \tag{3.5}$$

This limit is highly sensitive to the center-of-mass energy $\sqrt{s}$. The data taken at $\sqrt{s} = 183$ GeV therefore provide the best sample with which to search for the reaction $e^+e^- \to \tilde{G}\tilde{G}\gamma$.

The three DELPHI calorimeters HPC, FEMC and STIC were used in this part of the single-photon analysis. No anomalous production of single-photon events was observed

in the analysis, so the results were used to set an upper limit on the cross section for the process (3.4). The limit on the cross section, computed from the results of the individual calorimeters, is

$$\sigma_0 < 0.50 \text{ pb at } 95\% \text{ C.L.}$$

This yields a lower limit on the gravitino mass, according to Equation (3.5), of

$$m_{3/2} > 6.6 \cdot 10^{-6} \text{ eV}/c^2 \text{ at } 95\% \text{ C.L.},$$

corresponding to a supersymmetry-breaking scale $\sqrt{F} > 166$ GeV.

3.2.4 Compositeness

Several alternatives to supersymmetric models address the weaknesses of the Standard Model. Some of these suggest that particles regarded as fundamental by the Standard Model may in fact be composed of smaller objects. The model that was investigated in the DELPHI single-photon analysis is a so-called preon model [23]. This considers quarks, leptons and weak bosons as composite particles. It introduces preons with charge $e/2$ as well as a preonic charge, which is identified with the magnetic charge. Preons are composed of subpreons, which are fully specified by conserved charges. According to this model the preon dynamics, rather than the Higgs mechanism, is responsible for generating the masses of bound states.

The model predicts many new particles, amongst which are $U^{\pm}$ and U^0, vector bosons that form a weak-isospin doublet ($U^{\pm}$, U^0). Furthermore, it predicts the existence of a neutral iso-singlet vector boson D_1, which can mix with the photon. The process $e^+e^- \to U^0\bar{U}^0$ takes place through s-channel exhange of a Z^0 or a D_1, and the U^0 bosons decay invisibly. Under certain conditions, the cross section for this process would be relatively large. The radiative production of a U^0 pair would therefore also be sizeable, and such events would have the experimental signature $e^+e^- \to \gamma +$ invisible particles.

Other particles predicted by this preon model are the fermions l_s and q', which are connected with the neutrinos and the down-type quarks. l_s, which is neutral and decays invisibly, can also contribute to the single-photon signal through the radiative production $e^+e^- \to l_s\bar{l}_s\gamma$. This can take place through two channels: s-channel exchange of a D_1 and t-channel exchange of a $U^{\pm}$. The s-channel exchange takes place for all three types of l_s (l_s^i, $i = e, \mu, \tau$), whereas the t-channel exchange takes place only for the electron-type l_s^e, in close analogy with the production of neutrino pairs through Z^0 and $W^{\pm}$ exchange. The s-channel production is expected to be negligible at LEP2, but the cross section of the t-channel process may be sizeable and may thus give a visible signal at LEP2 energies.

The single-photon analysis was used to put an experimental lower limit on the mass of the U boson, M_U, under the hypothesis that a D_1 boson exists and has a mass M_D in the range $5M_{Z^0} \leq M_D \leq 7M_{Z^0}$. The contributions from direct production of U^0 pairs and from $U^{\pm}$ exchange were summed. The limit was determined from the measured cross

section $\sigma(e^+e^- \to \gamma + \text{invisible particles})$ obtained from the HPC and FEMC data, after subtraction of the expected contribution to radiative neutrino production according to the Standard Model. The obtained limit is

$$M_U > 68\text{–}78 \text{ GeV at } 95\% \text{ C.L.}$$

for a variation of M_D in the above range.

Chapter 4

Off-Energy Electron Background in DELPHI

The circulating beams of a collider give rise to various interactions other than those of the collisions between the beam particles themselves. Some of the particles created in these unwanted interactions reach the experimental detectors and may cause large amounts of background.

The two main types of beam-induced background at LEP are off-energy electrons and synchrotron-radiation photons [24]. The synchrotron radiation takes place in the bending dipole magnets and in the focusing quadrupole magnets. The photons that reach the experiments can cause radiation damage to the silicon-strip vertex detectors and may also disturb the data taking of the TPC. The rate of this type of background increases rapidly with beam energy. It is kept at a tolerable level by means of collimators in the beam line, as well as by various synchrotron masks and shields made of tungsten and placed in the vicinity of the experiments. Off-energy electrons are created in bremsstrahlung interactions between beam particles and residual gas molecules in the beam pipe. The residual gas is a mixture of CO, CO_2, H_2 and CH_4; the bremsstrahlung process takes place mostly with the CO molecules. The cross section of this process is, to first order, independent of the beam energy. The rate of the background is proportional to the vacuum pressure and to the beam current. The off-energy electrons are responsible for a high trigger rate in the luminosity monitors, and in some cases they also degrade the precision of the luminosity analysis. The off-energy electrons are difficult to remove with collimators, because they stay close to the beam until they reach the last strong quadrupoles, which bend them into the region of acceptance of the experiments. Both types of background have been examined in several different studies [24, 25, 26].

4.1 Motivation for the Study

A study of off-energy electron background in STIC is described in Article IV. Its purpose was to gain a better understanding of phenomena seen in data taken during the third

running period (P3) of 1995.

During the P3 period, which took place in November 1995, LEP was operated at 68 GeV in so-called bunch-train mode. Earlier that year, the bunching scheme of LEP had been altered from eight to four bunches per beam, with each bunch then consisting of up to four mini-bunches, or bunch wagons. Electrostatic separators had been installed near the interaction points in order to create vertical bumps in the beam orbits, and thus to prevent the bunch wagons of the counter-rotating beams from colliding outside the interaction points.

The P3 running period was the first in which the DELPHI experiment operated the neutral trigger described in Chapter 2 and used in the single-photon analysis discussed in Chapter 3. It immediately became apparent that this trigger was very sensitive to off-energy electron background.

The OPAL experiment reported an increase in off-energy electron background in their luminosity analysis when LEP began operating in bunch-train mode at 45 GeV [26]. A simulation of off-energy electrons showed that an increase in background in the vertical plane was due to the electrostatic separators that create the vertical separation bumps for the bunch trains. In DELPHI, this background is not seen in the luminosity measurement. The inner acceptance for Bhabha electrons is at a larger radius in DELPHI than in OPAL, and the radial distribution of the off-energy electron background is very steep; therefore, DELPHI has a lower acceptance for off-energy electrons than OPAL does. In the single-photon analysis, however, DELPHI typically triggers on several thousand off-energy electrons for every true single-photon event. For this reason, a study of this background in DELPHI together with a simulation of off-energy electrons was carried out in order to investigate what the optimal running conditions of LEP might be, and also to determine whether the neutral trigger might be improved. Knowledge gained from this study was also used in the single-photon analysis discussed in Chapter 3.

4.2 The Simulation Program and the Conditions Simulated

The study was carried out with a modified version of the CERN library program Decay Turtle [27], which simulates the motion of charged particles through beam transport systems. A length of approximately 650 m of the LEP beam line was modeled, beginning 640 m upstream of the DELPHI interaction point. The program does not make allowance for energy loss in material; therefore, any interaction with material resulted in full interception in this study.

The 27 km long LEP ring has an eight-fold symmetry, with each octant consisting of an approximately 500 m long straight section, centered around the interaction point, and $\sim$ 1.4 km long bending arcs on either side [24]. The length of the beam line modeled

in the simulation covers the straight section on one side of the interaction point at DELPHI, and about 400 m of the bending arc upstream thereof, as well as a few meters of the straight section downstream of the interaction point. This part of LEP contains 25 quadrupole magnets upstream and three downstream of the interaction point, and 12 dipole magnets in the arc. Several of the collimators that shield the experiments from some of the beam-induced background are located in the modeled part of the beam line. Each collimator consists of one or two tungsten jaws with adjustable openings. The electrostatic separators that create the vertical separation bumps are also located in this part of the beam line.

The simulation program assumes constant vacuum pressure (10^{-9} torr) along the beam line. In reality, the vacuum pressure is known to differ between different sections of LEP and also within sections over time. It is difficult, however, to obtain retroactively accurate records of the actual vacuum pressures during a certain running period. Therefore, the effects of varying vacuum pressures were not taken into account in the study.

The simulations were carried out at a beam energy of 68 GeV, with varying amplitudes of the vertical separation bump (including zero amplitude). The simulated conditions correspond to the LEP operating modes of part of the third running period (P3) of November 1995. Data taken under those conditions were used for comparisons with the simulations. Simulations were also made with a beam energy of 80.5 GeV and conditions resembling those of the first period (P1) of July–August 1996.

4.3 Results

4.3.1 Background Components and Their Origins

The simulation study showed that the off-energy electron background appears in distinct groups. The behavior of the groups depends on the amplitude of the vertical bunch-train bump created by the electrostatic separators. Without a vertical bump, the vast majority of the background is located in the horizontal plane. When the electrostatic separators are switched on, a large part of the background is shifted from the horizontal plane into the vertical plane. Three different main groups were defined, and two of these were each divided into two subgroups:

- One group enters STIC in the horizontal plane; one subgroup is of higher energy (peaked around 45 GeV at a beam energy of 68 GeV) and one of lower energy (10–25 GeV).
- A vertical group is deflected in the direction parallel to that of the bunch-train bump; it enters STIC in the upper part of side A and in the lower part of side C, and it is peaked in energy around 35 GeV.

- Another vertical group is antiparallel to the bump; it is composed of one subgroup of higher energy (peaked at 35 GeV) and one of lower energy (peaked at 15 GeV).

The definition of these groups is illustrated in Figure 4.1.

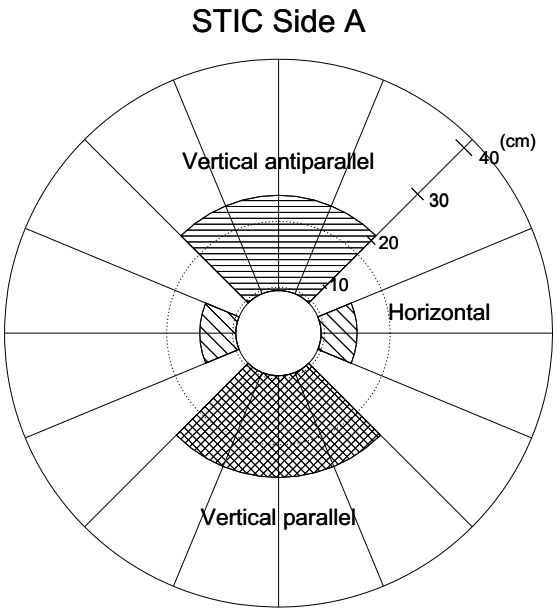

Figure 4.1: Definition of the different off-energy electron groups. The vertical antiparallel group enters side A of STIC in one of the four upper sectors (and side C in one of the four lower sectors); the vertical parallel group enters side A in one of the four lower sectors (and side C in one of the four upper sectors); and the horizontal group enters STIC in one of the four horizontal sectors. The shaded areas show the approximate radial extension of the different groups. The dotted circles mark the boundaries of the area covered by the silicon-strip detectors.

Each of the background groups described above originates from a specific part of the beam line upstream of the interaction point. Figure 4.2 shows the distances from the interaction point at which the backgrounds are created. The accelerator components of the straight section on one side of DELPHI are shown in Figure 4.3. The particles of the high-energy horizontal group are created beyond a distance of 106 m, or upstream of the quadrupole magnet QS6. The high-energy vertical antiparallel group also originates from this part of the beam line, mainly immediately upstream of QS6. The low-energy horizontal group is created in the section between the interaction point and the electrostatic separator ES.QS2, located 24 m upstream of the interaction point. The low-energy antiparallel group originates from the region between ES.QS2 and the quadrupole pair QS3 and QS4, located 58 m and 64 m respectively upstream of the interaction point. Finally, the vertical parallel group is created in the section between QS3/QS4 and QS6.

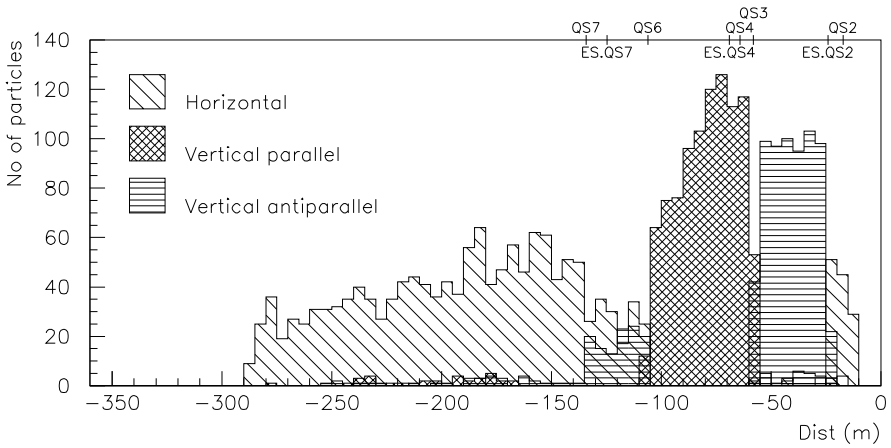

Figure 4.2: Distances, measured from the interaction point, at which the electrons of the different background groups are created. The locations of the electrostatic separators (ES.QS2, ES.QS4 and ES.QS7) and nearby quadrupoles (QSn) are marked. The low-energy components of the horizontal and the vertical antiparallel groups are created in the regions near the interaction point, whereas the high-energy components originate from the regions far upstream.

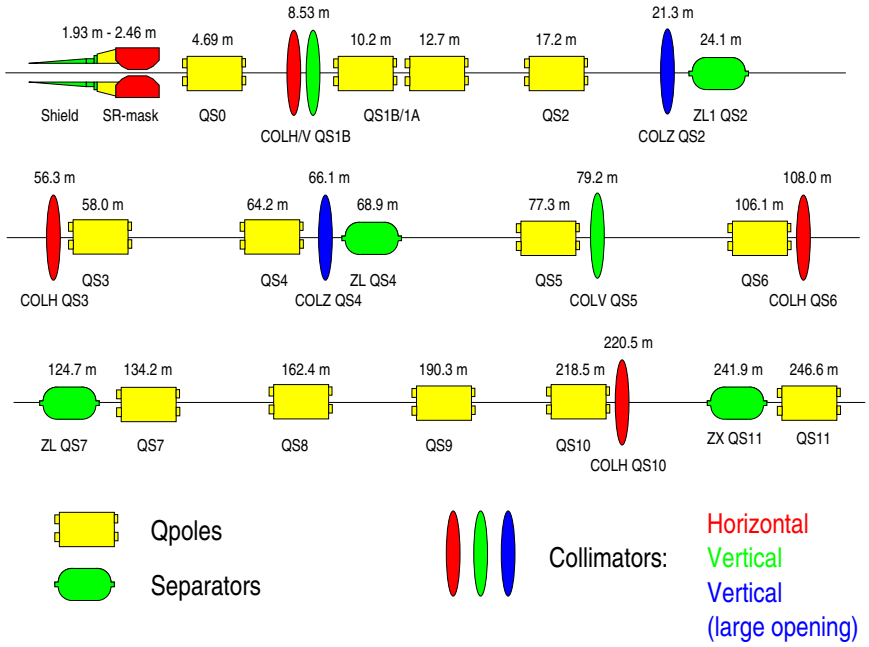

Figure 4.3: One half of the straight section surrounding the DELPHI interaction point. The layout shows the elements in their locations during 1996. The horizontal collimator COLH.QS3 was not present in 1995. The electrostatic separators, which have labels beginning with ZL or ZX in the drawing, also have names of the form ES.QSn. All distances are measured from the interaction point.

4.3.2 Comparison Between Data and Monte Carlo

The simulated background was compared to data taken during the 1995 P3 run at $\sqrt{s} = 136$ GeV. This comparison showed good qualitative agreement between the Monte Carlo and the data. All three major background components described above were seen in the data (see Figure 4.4). The low-energy and the high-energy parts of the horizontal and the vertical antiparallel components were also clearly distinguishable. For each group, the Monte Carlo and the data samples showed similar distributions in energy and in radius. However, the simulations did not agree with the data on the relative population of the different groups. The most likely explanation for these discrepancies is the fact that the vacuum pressures differ between different parts of the beam line, which was not accounted for in the simulation.

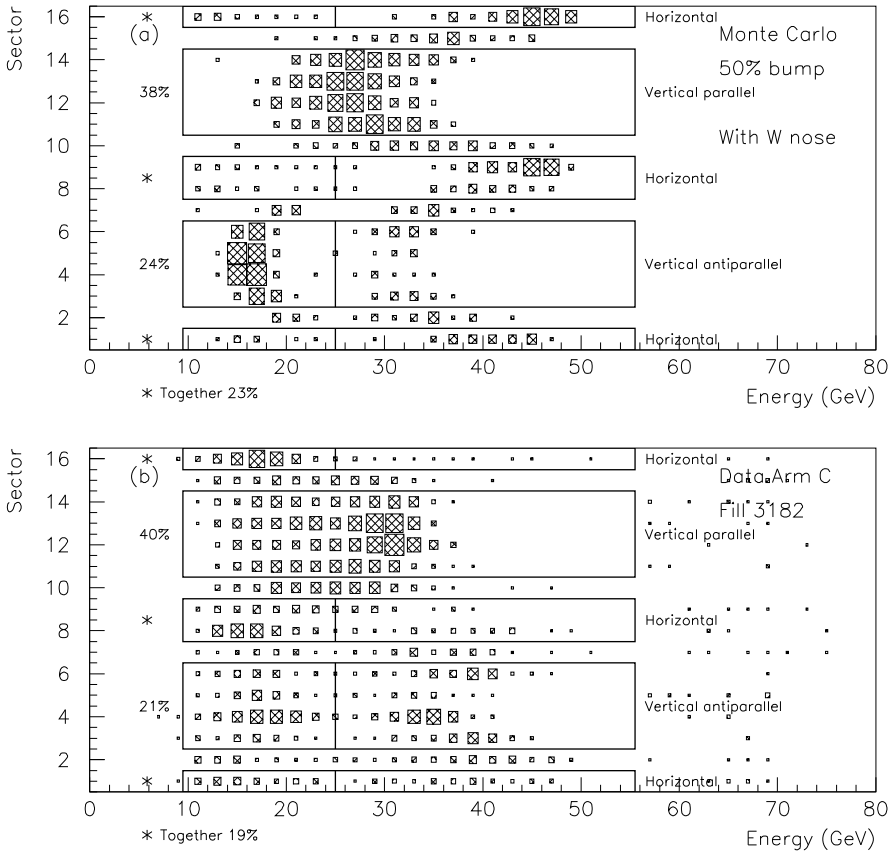

Figure 4.4: Comparison of calorimeter sector *vs.* energy between (a) Monte Carlo and (b) data for arm C at 68 GeV beam energy and 50% bump amplitude. The vertical lines mark the division between low-energy and high-energy groups. The histograms have been normalized to have the same number of entries. Side C was covered by a tungsten nose extending to a radius of 97 mm; this was taken into account in the simulation.

4.3.3 Off-Energy Electrons Entering STIC Elsewhere than through the Front

The possibility of off-energy electrons entering STIC either from behind (upstream of the interaction point) or from below was also investigated in the simulation study. It was found that a significant portion — some 25% — of the off-energy electrons that hit STIC enter the detector in one of these ways. Most of this background enters from the back, and a large fraction thereof comes from the high-energy horizontal group. Since these particles do not follow the projective geometry of STIC, their energy is not necessarily correctly reconstructed in the off-line data processing. This could account for some of the relative abundance of low-energy horizontal background seen in the data but not in the Monte Carlo (see Figure 4.4).

4.3.4 Off-Energy Electron Background at LEP2 Energies

Between 1995 and 1996, LEP underwent major upgrades, and the beam optics were modified. The beam energy was increased from 68 GeV at the end of 1995 to 80.5 GeV during the first running period of 1996. The effects of these machine modifications on the background situation were investigated through simulations of the new beam optics with a beam energy of 80.5 GeV. The only significant effect observed was an increase of the background energy, which scales linearly with the beam energy for each of the different background groups. The qualitative behavior of these groups, and in particular of their radial distributions, remains practically unaltered.

The beam energy was further increased to 86 GeV later in 1996, and to 90.5 GeV in 1997. The simulations were not repeated for these beam energies, but the off-energy electron background studied in the single-photon analysis (see Chapter 3) had energy distributions that followed the predicted scaling with beam energy.

4.3.5 Possibilities to Reduce the Off-Energy Electron Background

The simulation study investigated the possiblities of reducing the exposure of STIC to off-energy electrons, either by closing the nearest beam collimators, the vertical collimator named COLV.QS1 and the horizontal COLH.QS1, or by changing the amplitude of the vertical separation bump. It was seen that it would be possible to reduce the rate of vertical high-energy background by closing the vertical collimator COLV.QS1. In 1997, this collimator was moved to a new location further upstream; the study showed that one might be able to reduce this background by 50% by closing it to 13 mm in its new location. On the other hand, closing the horizontal collimator COLH.QS1 enough to reduce the rate of horizontal background would not be possible. Nor would reducing the bunch-train bump amplitude be an efficient solution. It was concluded that the most important factor concerning operation of LEP is the quality of the vacuum in the region

of the electrostatic separators.

The study showed that an effective method to reduce the background is to apply a radial cut rejecting events of small radii. The STIC neutral trigger was improved during 1996 by the addition of the small veto counters and by the inclusion of a radius requirement in the trigger decision. Furthermore, a lead ring was installed at the back of the calorimeter in order to shield the TPC from backscattered synchrotron photons; this ring also prevents some of the off-energy electrons from entering STIC from behind. These improvements decreased the rate of the neutral trigger significantly, but the off-energy electron background remained the most difficult problem in the single-photon analysis.

Chapter 5

The Silicon-Strip Detectors and Their Performance

The silicon-strip detectors described in Chapter 2 were installed as part of STIC in 1994, in order to make it possible to measure the direction of calorimeter showers, and hence to improve rejection of off-energy electrons. These silicon-strip detectors became fully operational in 1996. The reconstruction of shower parameters from the silicon-strip data, which is carried out off-line, was fully implemented in 1997. The performance of the silicon-strip detectors was evaluated in a study carried out in 1997 and reported in Article V. Some of the main points of this study are presented in Section 5.1.

One of several important steps in the treatment of the data read out from the silicon-strip detectors is the reduction of coherent noise. Article VI presents the algorithm that is currently used to carry out the coherent-noise subtraction, together with two other algorithms that were also evaluated for this purpose. A short presentation of the algorithm currently in use is given in Section 5.2.

5.1 Performance of the Silicon-Strip Detectors

The silicon-strip detectors were designed with the goal of obtaining a resolution of $\sim$ 10 mrad on the direction of a shower axis [28]. The study presented in Article V confirmed that the silicon-strip detectors meet these design criteria. The study examined different aspects of the performance of these detectors at the different energies at which LEP was operated in 1996 and 1997. The issues examined include the determination of the coordinates of the showering particles, and the angular resolution obtained in determining the direction of the shower. The reconstruction of the vertices of the showering particles was also studied. The vertex of a shower is defined to be the distance between the interaction point and the point where a straight line through the reconstructed radii in the silicon planes intercepts the beam line. The efficiencies of the vertex reconstruction and of the rejection of off-energy electrons were likewise investigated.

The angular resolution of the shower direction depends on the energy of the showering particle. It was found to be approximately 9 mrad for electrons at 91.5 GeV and about 14 mrad at 45 GeV. The resolution is poorer, however, in the regions of the holes for the wavelength-shifting fibers. The efficiency of the vertex reconstruction is about 90% at energies above 25 GeV. A cut at ± 0.5 m on successfully reconstructed vertices was found to keep 61% of events originating from the interaction point and to reject 89% of the off-energy electrons.

The study also showed that the resolution of the radius reconstruction in STIC in the region covered by the silicon-strip detectors can be improved if one calculates a weighted average of the radii from the two silicon planes and from the calorimeter. One can thus obtain a radius determination with a resolution of 150 to 300 μm, compared to 200 μm to 1 mm if one uses the calorimeter only.

5.1.1 Data Treatment

The treatment of the data from the silicon-strip detectors is divided into three logical parts. First, a certain amount of basic processing of the raw data takes place. This first treatment includes pedestal subtraction and correction for coherent noise. These steps are described in Section 5.2 and in Article VI. The pulse height of each signal is also converted to an energy, and strips with pulse heights below a certain threshold are discarded. Second, there is a search for showers in the silicon-strip data, and the geometrical parameters (radius as well as polar and azimuthal angles) are calculated for each of the showers that are found. Finally, there is a matching of the showers that are found in the two silicon-strip planes to those that were found previously in the STIC calorimeter.

5.1.2 Vertex Reconstruction

A shower's radial coordinates in the two silicon planes are used to calculate the vertex of the showering particle. This is carried out by simple extrapolation of the straight line through the two reconstructed radii to the beam line. The reconstructed vertices of samples of Bhabha events were compared to those of samples of single-arm events (i.e., events with a shower detected in only one of the two STIC arms). A comparison of the vertex distributions of the two types of event sample is shown in Figure 5.1. The vertices of the Bhabha events are peaked in a narrow distribution around the interaction point; this agrees with expectations, since the Bhabha events are created at the interaction point. The single-arm events are dominated by off-energy electrons, which are created at random locations within the beam line; the vertex distribution of these events is therefore much broader than that of the Bhabha events.

The "holes" in the distributions of Figure 5.1, at about 2.5 m from the interaction point, are located at the position of the silicon detectors. They are caused by the geometrical acceptance of the two silicon planes, which makes it impossible to reconstruct

tracks that intercept the beam line below the silicon detectors.

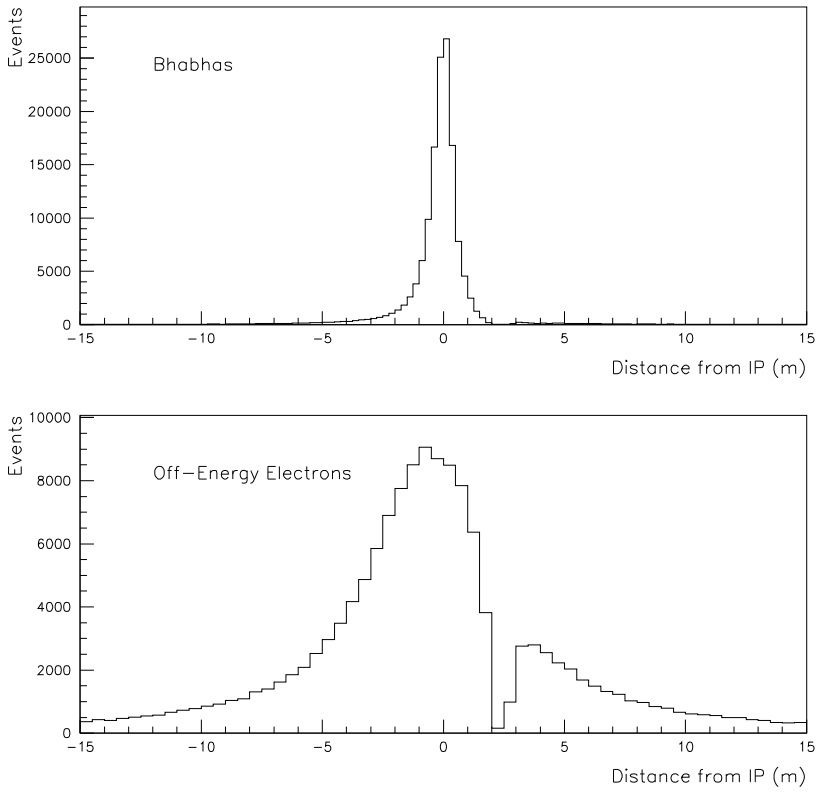

Figure 5.1: Distribution of reconstructed vertices of Bhabha events and of single-arm events (i.e., events with a shower detected in only one of the two STIC arms) respectively ($\sqrt{s} = 161$ GeV). The sample of single-arm events nearly exclusively consists of off-energy electrons, which originate mainly elsewhere than from the interaction point; therefore, this distribution is much broader than that of the Bhabha events.

5.1.3 Efficiencies

The reconstruction of a vertex requires one reconstructed shower in each silicon plane to be associated with a shower in the calorimeter. The efficiency of the vertex reconstruction for the silicon detectors is defined to be the number of calorimeter showers having associated with them one reconstructed shower in each silicon plane divided by the total number of calorimeter showers passing through the silicon region. Figure 5.2 shows the energy distributions of calorimeter showers before and after the requirement of two associated silicon showers was imposed, together with the corresponding efficiency plot. Bhabha events show up as a clear, isolated peak just above 90 GeV, whereas the single-arm events appear in the region below 50 GeV. The efficiency of the vertex reconstruction is nearly constant at a level of approximately 95% down to energies of about 30 GeV, where it begins to decrease. It decreases rapidly below 20 GeV, and it

reaches a level of 30% at 10 GeV.

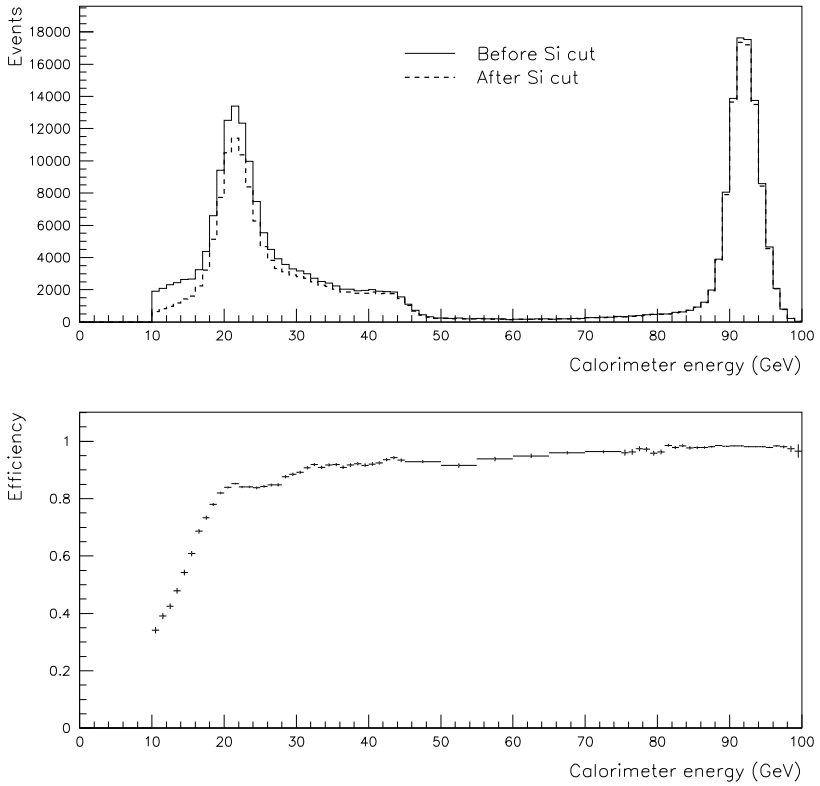

Figure 5.2: Energy distributions of STIC calorimeter showers ($\sqrt{s}$ = 183 GeV) before and after the requirement that each calorimeter shower has associated with it one reconstructed shower per silicon plane. The corresponding efficiency plot is also shown.

Since the aim of the silicon-strip detectors is to allow the rejection of off-energy electrons, the fraction of off-energy electrons surviving a cut on the reconstructed vertex was studied and compared with the fraction of Bhabha events surviving the same cut. The result is shown in Figure 5.3. Each point in the figure represents an increase by 10 cm of the cut on the vertex, starting with a cut at $\pm$10 cm. Only calorimeter showers having silicon showers in both planes associated with them were used. A cut at $\pm$0.5 m keeps 61% of events originating from the interaction point and rejects 89% of the off-energy electrons, whereas a cut at $\pm$1.0 m keeps 80% of the events from the interaction point and rejects 79% of the off-energy electrons.

5.2 Reduction of Coherent Noise

Data taken with the silicon-strip detectors show the presence of a coherent-noise source that produces a common shift, on an event-by-event basis, of the pulse heights for large

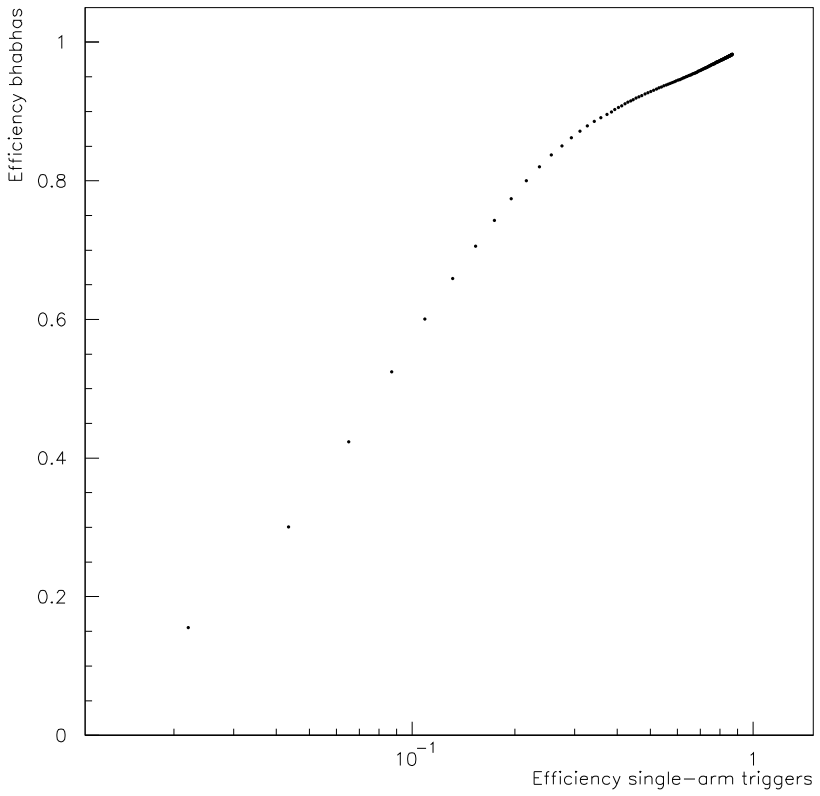

Figure 5.3: Fraction of Bhabha events surviving a cut on the reconstructed vertex *vs.* fraction of single-arm events surviving the same cut. Each point represents an increase by 10 cm of the cut on the vertex, beginning with a cut at ± 10 cm near the lower left corner. Only calorimeter showers with one reconstructed shower per silicon plane were used before the vertex cut was imposed.

groups of the silicon-strip channels. The origin of this coherent noise is not entirely understood. One possible source is electromagnetic pick-up from other devices in the surroundings of the detectors. Another possibility is noise being generated internally by the front-end electronics (preamplifiers etc.) of the silicon-strip detectors. It is essential, however, to reduce the presence of such noise in the data read out from the silicon-strip detectors in order to ensure accurate reconstruction of the energy and the position of the shower.

It is also important to have a tool to reduce the amount of information that must be read out from the silicon detectors. They consist of approximately 4000 strips, and thus require considerable amounts of data storage space if all channels are read out for every event triggered by STIC. An algorithm for reduction of coherent noise that would be possible to implement for on-line use in the readout chain was therefore sought for these detectors. Such an implementation would permit localization of showers after the coherent-noise subtraction, whereupon readout and storage could be reserved for a small selection of silicon-strip channels in the vicinity of the showers.

In view of the benefits of an on-line implementation, a simple method to reduce coherent noise from the silicon detectors was developed and tested. The method was designed with the aim of carrying out the coherent-noise subtraction in the Sirocco IV Fastbus modules, where the signals from the silicon strips are digitized, and which are equipped with digital signal processors (DSPs). The available memory of the DSPs is limited, imposing restrictions on the size of the coded implementation and thus on the complexity of the method. Further constraints are imposed by the fact that little time is allowed for the execution of any on-line noise-subtraction scheme. The method developed was found in the tests to be accurate in its subtraction of noise. Being simple and fast enough, it was later implemented in the Sirocco IV modules. It has been in successful operation in the STIC readout chain since August 1997. It has also been used in the off-line processing of some of the data taken prior to its on-line implementation.

5.2.1 Principles

The method for coherent-noise reduction used for the STIC silicon-strip detectors processes raw data event by event in only two steps. The first step subtracts pedestals, and the second step calculates and subtracts coherent noise. The Kapton cables, which connect the silicon strips to the Microplex MX4 amplifier chips via the fan-in cards, play an important role in this method. The strips of two sectors of each detector plane are connected to one fan-in card (and one MX4 chip) by eight Kapton cables. Each cable has a capacity of either 12 or 20 channels.

Pedestals

Pedestals can be calculated on-line with good accuracy on the basis of only a small subsample of events and without the use of any external trigger or calorimeter information. Due to sampling conditions that are altered at the beginning of each DELPHI data-taking run, the pedestals must be calculated for each new run; this may be done with data taken with any DELPHI trigger.

Coherent Noise

It has been observed that there is correlation in the noise between different channels within the same Kapton cable. There is also noise correlation between channels of adjacent Kapton cables, i.e., cables that belong to the same fan-in card and that emerge from the detector along the same path and are placed on top of one another. Other patterns of coherence are also present, but they are less important. It is necessary to make use of the correlation between channels that are located some distance apart in order to find coherent pulse-height shifts over strip areas larger than a shower, which is typically wider than 20 strips; otherwise, one would not be able to determine the

amplitude of the coherent noise at the location of the shower.

The present method makes use of the correlation between Kapton cables. The same pattern of correlation applies to most, but not all, fan-in cards; therefore, look-up tables are used to store the correlations. There is one such table for each fan-in card, and the table contains 8×8 entries, one for each pair of Kapton cables of the fan-in card in question. For simplicity, each entry is either 1 or 0, depending upon whether or not there is strong correlation with a slope near unity. At present, correlations other than those with a slope near 1 are not included, although such exist and some of them can be relatively strong. The tables have been produced manually after a study of plots of the correlation of the average pulse height for each pair of Kapton cables within a fan-in card and over a large number of events. Examples of such correlation plots are shown in Figure 5.4. For reasons not fully understood, the correlations sometimes vary slightly from year to year. (1% of the correlations between Kapton cables changed between 1996 and 1997; there were no changes between 1997 and 1998.) Therefore, the correlation tables are checked and, if necessary, updated once per year.

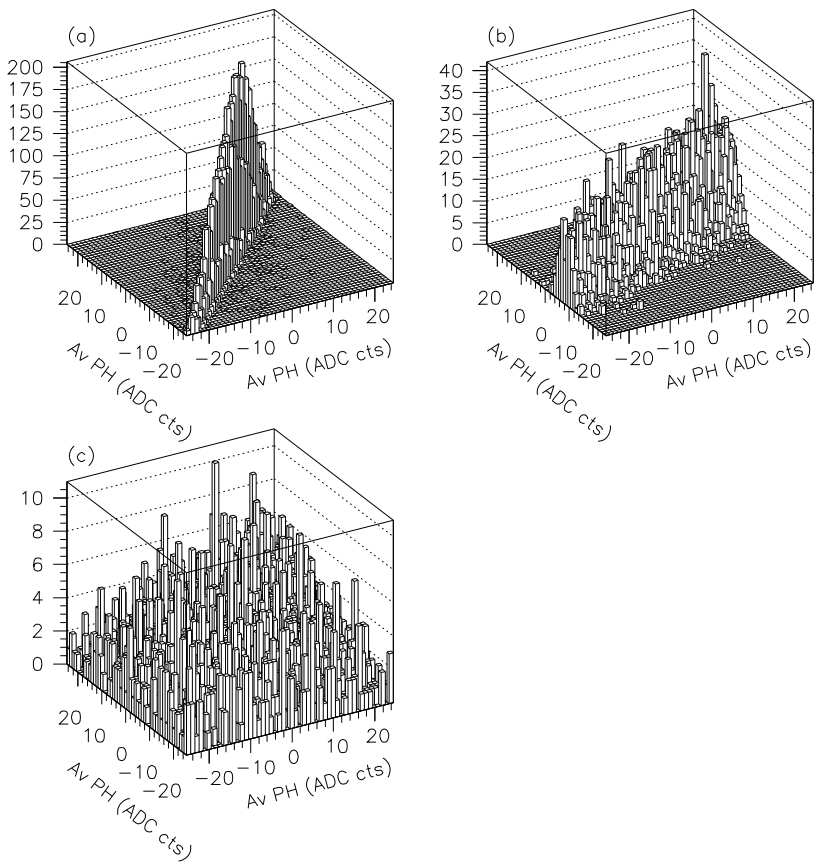

Figure 5.4: Examples of (a) "strong" correlation, (b) "weak" correlation, and (c) "no" correlation between the average pulse heights of pairs of Kapton cables.

5.2.2 Algorithm

The algorithm consists of two separate parts: one performed at the beginning of each new physics run in order to establish pedestal values for each silicon strip, and one that carries out pedestal and coherent-noise subtraction for the rest of the run.

Calculation of Pedestals On-line

The first 100 DELPHI triggers at the beginning of a physics run are used to calculate pedestals in two steps: *i)* The signal of each of the first 50 events is added for each individual strip, and then one calculates the mean p_i' and rms r_i' for each strip i. *ii)* The operation is repeated for the following 50 events, but for each strip one now includes only those events for which the signal a_i passes the cut $a_i \leq p_i' + 2r_i'$, where p_i' and r_i' are those obtained from the first 50 events. This selection is made in order to minimize the influence of showers. The mean p_i and rms r_i obtained after the second calculation are those that will be used as pedestal values for the remainder of the run.

Optionally, this procedure can be repeated on every set of 100 events and the pedestal values used only for the following 100 events instead of for the remainder of the run. This would take care of any sudden jumps in the pedestals during a run. (This phenomenon occurred a few times during the data taking of 1995 and has not been explained.) This option has been used in the on-line implementation since the start in 1997.

Correction for Pedestals and Coherent Noise

After the first 100 triggers of a run, each event is treated as follows: The pedestal mean value obtained at the beginning of the run (or, optionally, at the latest pedestal calculation) is subtracted from the raw value a_i of each strip, i.e.,

$$a_i' = a_i - p_i.$$

Thereafter, one calculates, for each Kapton cable k, the average pulse height $\langle a \rangle_k$ of all the Kapton cables that are correlated to k (according to the look-up table discussed above). In this calculation only those strips are included that fulfill the condition

$$a_i' \leq br_i,$$

where b is a constant that typically has a value of 2–3. The purpose of this cut is once again to exclude showers. The value obtained is the estimate of the coherent noise for the group of strips belonging to the Kapton cable in question. This is subtracted from each channel of the Kapton cable, so that one obtains a corrected pulse height for each strip, a_i'':

$$a_i'' = a_i' - \langle a \rangle_k.$$

After having applied the above correction to all Kapton cables, one reads out only those strips for which the pulse height passes a suitably chosen threshold.

5.2.3 Evaluation

The two parts of the coherent-noise subtraction method, i.e., the coherent-noise subtraction itself and the calculation of pedestals, were evaluated in several different ways; this evaluation is discussed in Article VI. As an example, Figure 5.5 offers a visual comparison of the pulse heights of the strips of a fan-in card before and after correction for coherent noise. The corrected data show a much narrower distribution around zero ADC counts than the data that are only pedestal-corrected. Moreover, after coherent-noise subtraction, hardly any events populate the region below the band where the bulk of the events are concentrated, which indicates that the tables of correlations between Kapton cables are correct.

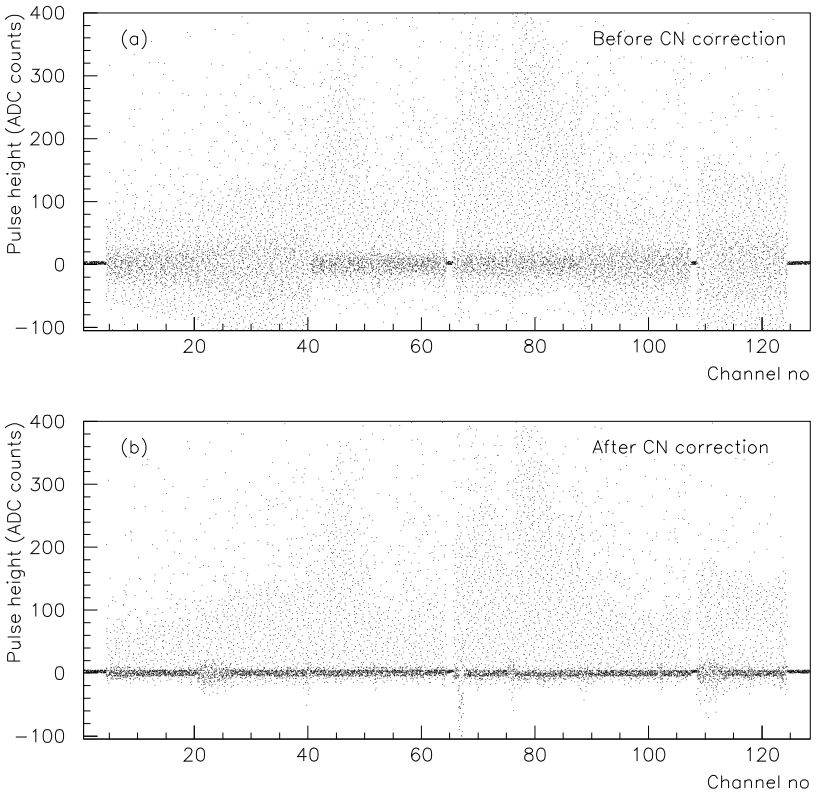

Figure 5.5: Pulse heights of the strips of a fan-in card reading out side A, (a) before and (b) after coherent-noise subtraction.

An estimate of the number of strips remaining to be read out after coherent-noise subtraction showed that, in most cases, there are fewer than 70 channels remaining in events with one shower in the calorimeter and fewer than 30 in events with no calorimeter shower.

Chapter 6

Emittance and a Fast Wire Scanner

Beam emittance is an important concept in accelerator physics. It characterizes the beam in phase space, and it is closely related to the beam profile in real space. Accelerators are often linked in chains in order to obtain colliding beams of high energy and high luminosity at the last accelerator stage. It is essential that the beam fits within the dynamic aperture of the beam pipe as it is transferred from one stage to the next in the accelerator complex. This is where emittance becomes a concern.

The fast wire scanner is an important instrument for measuring transverse beam profiles. A profile is obtained through a scan of the beam by a thin wire. The Proton Syncrotron has been equipped with wire scanners since 1985 [29]. The first system consisted of two wire-scanner units, one for measuring horizontal beam profiles and one for vertical profiles. In 1994, this system was completely renovated and extended to four units, two for each transverse direction. The upgrade was essential in order to obtain a reliable instrument that provides emittance measurements of high accuracy, and that is also easy to use, especially in view of the future use of the PS accelerator complex as part of the injector chain for LHC.

Section 6.1 presents a short summary of concepts relevant to the definition of emittance. A complete treatment of the topic can be found in many places in literature [30]. The discussion in Section 6.1 is relevant only to circular accelerators and to emittance related to transverse particle motion. Section 6.2 gives a brief presentation of the new fast wire scanners at PS. A complete description of the wire scanners is given in Article VII.

6.1 Emittance and Dispersion

6.1.1 Particle Trajectories in Phase Space

In every accelerator, there is exactly one orbit that, ideally, all particles should follow. This trajectory is referred to as the design orbit. Beam particles that are slightly displaced from the design orbit will be forced by the fields of focusing magnets to oscillate about it — the particles will perform so-called betatron oscillations. Differences in

momentum will also cause particles to follow different trajectories in the machine, and thus to deviate slightly from the design orbit.

If there is no coupling between the particle motions in the longitudinal and the two transverse directions, the equations of motion of the beam particles can be treated separately for each of the three degrees of freedom. The beam emittance may then also be defined separately for the horizontal, the vertical, and the longitudinal phase-space planes. The motion of the beam particles is conveniently described in a local Cartesian coordinate system travelling with the design orbit. In the following, x will be used to denote the horizontal coordinate, y the vertical coordinate, and s the path length with respect to some reference point. For an accelerator containing only dipole and quadrupole magnetic fields, the equations describing transverse particle motions are then

$$\frac{\partial^2 x}{\partial s^2} + k_x(s)x = \frac{\delta}{\rho(s)} \tag{6.1}$$

and

$$\frac{\partial^2 y}{\partial s^2} + k_y(s)y = 0, \tag{6.2}$$

where

$$k_x(s) = \frac{1}{\rho^2} - \frac{qg}{p_0}$$

and

$$k_y(s) = \frac{qg}{p_0}.$$

Here p_0 is the design momentum, $\delta = \Delta p/p_0$ is the ratio of momentum deviation to design momentum, ρ is the local radius of curvature, q is the charge of the beam particles, and g is the x or y component of the local magnetic field gradient. In a dipole field, $g = 0$, and in a quadrupole field, $g = -\partial B_y/\partial x = -\partial B_x/\partial y$. The homogeneous solutions to these equations describe the betatron oscillations in the horizontal and the vertical planes. The particular solution for the horizontal coordinate is related to the spread in particle momentum.

Since the orbit of a circular accelerator is a closed curve, the equations of motion are periodic with some period L, which may be the entire circumference of the accelerator or a part thereof. If z is used to denote either the x or the y coordinate, the homogeneous solutions to Equations 6.1 and 6.2, which have a quasi-harmonic form, may be written as

$$z(s) = A\sqrt{\beta(s)}\cos\left(\Phi(s) + \Phi_0\right). \tag{6.3}$$

A and Φ_0 are constants. The amplitude function $\sqrt{\beta(s)}$ is periodic with the period L, and $\Phi(s)$ is a non-periodic phase of the oscillations, related to β by $d\Phi/ds = 1/\beta$. The solution represents an ellipse in the plane $(z, z' = dz/ds)$, which are the preferred coordinates in which to describe transverse phase space.

The shape and the orientation of a given phase-space ellipse of the form (6.3) change along the beam path s, but the ellipse is transformed back to the same shape and orientation after each period L. However, the area $a = \pi A^2$ of the ellipse remains constant around the orbit. Particles with the same amplitude A but different phase constants Φ_0 lie on the circumference of the same ellipse for any given s. Particles with an amplitude B smaller than A trace out a correspondingly smaller phase-space ellipse with the same center and orientation. Any particle moving along a trajectory inside a given ellipse thus remains inside this ellipse when the particles move around the accelerator. As a consequence thereof, the phase-space density in the vicinity of any trajectory in phase space constant; this is the application of Liouville's theorem to accelerator physics. The function $\beta(s)$ is called the betatron function or the beta function. In addition to describing the betatron oscillations of individual particles in the accelerator, it characterizes the envelope of the orbiting particle beam.

6.1.2 Definition of Emittance and Normalized Emittance

Beam phase-space ellipses form the basis for the definition of emittance. Ideally, the behavior of the collective of beam particles at a given location in the accelerator would be described by an ellipse in which all particles are enclosed. In reality, however, the particle distribution in phase space is rarely well described by an ellipse enclosing the entire beam. Therefore, the choice is generally to use an ellipse containing a certain fraction of the beam. The emittance ε of the beam is usually defined as the area a of this ellipse divided by π, i.e.,

$$a = \pi\varepsilon.$$

Sometimes, however, ε is defined as the area itself. In order to avoid confusion, the factor π is often written explicitly when emittances are quoted.

In practice, the particle distribution in phase space is often approximately two-dimensionally Gaussian. Therefore, it is suitable to define $\pi\varepsilon$ as the area of the ellipse for which the maximum deviation $z_{\max}$ from the design orbit is equal to σ or 2σ of the particle distribution along the transverse coordinate axis (see Figure 6.1). With

$$z_{\max} = \sqrt{\varepsilon\beta},$$

the emittances ε for these two cases are

$$\varepsilon = \frac{\sigma^2}{\beta}$$

and

$$\varepsilon = \frac{4\sigma^2}{\beta}$$

respectively. The convention is to use the 2σ definition for proton beams and the σ definition for electron beams. At PS, however, 2σ is used for all beams irrespective of

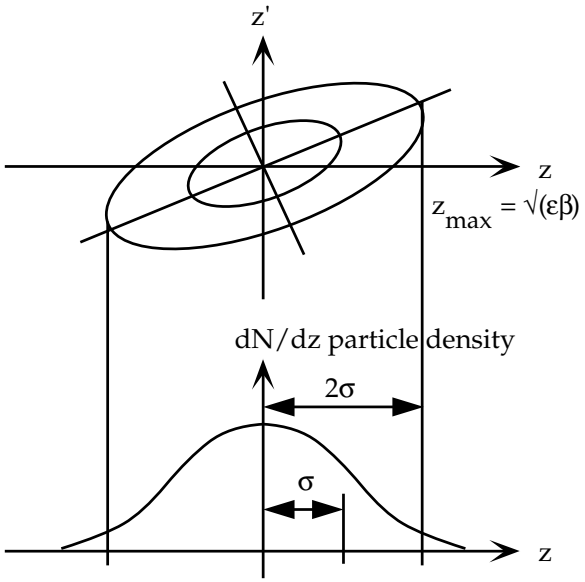

Figure 6.1: Definition of the emittance ε from the transverse particle distribution in real space. $\pi\varepsilon$ is usually defined as the area of the ellipse for which the maximum deviation $z_{\max}$ from the design orbit is equal to σ or 2σ of the particle distribution along the transverse coordinate axis.

particle type.

The emittance remains constant as the beam moves around the accelerator; this is an effect of Liouville's theorem. An important exception is the case when beam particles undergo acceleration. When particles are accelerated, the longitudinal component of the momentum vector increases, whereas the transverse component does not change. Hence, the divergence and the emittance shrink. This motivates the use of an additional quantity, the so-called *normalized* emittance ε^*, which is defined as

$$\varepsilon^* = \beta\gamma\varepsilon,$$

where β and γ are the relativistic parameters. This quantity is invariant under acceleration.

6.1.3 Momentum Deviation and Dispersion

The complete expression for horizontal particle trajectories contains, in addition to the homogeneous solution, a particular solution to the inhomogeneous equation, describing the effects of deviations Δp in momentum from the design momentum p_0. The particular solution $x_D(s)$ is of the form

$$x_D(s) = D(s)\frac{\Delta p}{p_0}.$$

$D(s)$ is a periodic function; $D(s+L) = D(s)$. The solution describes the deviation of the closed orbit for off-momentum particles from the reference orbit. $D(s)$ is called the "periodic dispersion" and is often denoted $\eta(s)$. The departures from the ideal orbit of the particle trajectories are thus composed of one part due to betatron oscillations and another part due to dispersion, with the consequence that the horizontal beam size depends on both of these factors. Statistically, the total beam size may be obtained from the beam-size components added in quadrature:

$$\sigma_{\mathrm{tot}}^2 = \sigma_\beta^2 + \left(\eta \frac{\sigma_p}{p_0}\right)^2 ,$$

where σ_{tot} is the total beam size, σ_β is the component due to betatron oscillations, η is the dispersion function, σ_p is the rms momentum spread, and p_0 is the design momentum.

Only the betatron component of the beam size is relevant to the emittance. The quantity that is measured in an accelerator, however, is the total beam size, and the dispersion component must be subtracted from the beam size before the emittance can be calculated.

6.2 The Fast Wire Scanners of the PS

The fast wire scanner sweeps a thin wire at high velocity through a particle beam. Interactions between the beam particles and the nuclei of the wire create secondary particles, some of which are caught by a monitor placed downstream of the point where the wire traverses the beam. Signals corresponding to the output of the monitor and the transverse position of the wire are acquired simultaneously. In this way, a transverse profile of the beam is obtained. When the values of the β function, the dispersion and the momentum spread at the interaction point are known, the emittance and the normalized emittance can be calculated from the beam profile. An important feature of the fast wire scanner is that it is a nearly non-destructive device, i.e., it causes very little interference with the beam and therefore a reasonably small blow-up of the emittance.

6.2.1 Improvements to the Wire Scanners at PS

Between 1992 and 1994, the fast wire scanners of PS underwent substantial improvement. Two entirely new units were built and installed. Increased accuracy was obtained with a new method to measure the transverse position of the wire and with the use of new electronics and control software. New photomultipliers in the secondary-emission detectors enhanced their linearity and dynamic range. The use of a new wire material extended the lifetime of the wire. The new software facilitated the use of the instrument and allowed it to become part of the integrated PS accelerator-control system. After successful testing of these units, the two units of the old wire-scanner system, which had been in use at PS since 1985, were upgraded to the same standard. Thus, the new system consists of four units, two for measuring horizontal beam profiles and two for vertical profiles.

6.2.2 The New Fast Wire Scanners

The mechanical arrangement of the PS wire scanners is such that a wire is stretched between the two tines of a metal fork and is thereby held perpendicular to the beam. An electric motor with a crankshaft drives a push-pull device, which turns the two arms of the fork in a circular movement, thus sweeping the wire through the beam. The mechanical assembly is shown in Figure 6.2. A schematic view of its movement with respect to the beam is shown in Figure 7 of Article VII. The monitors detecting the secondary emission produced when the wire traverses the beam consist of a scintillator mounted outside the beam pipe and connected to a photomultiplier via a light guide. The purpose of this arrangement is to avoid direct radiation on the photomultipliers. A carousel holding optical filters is inserted between the light guide and the photomultiplier, in order to allow a wide dynamic range for the profile measurements. Each wire scanner is accompanied by two monitors, placed one on either side of the device itself. This permits measurements on beams of negatively as well as positively charged particles, which circulate in opposite directions in the accelerator. The set-up is shown in Figure 1 of Article VII.

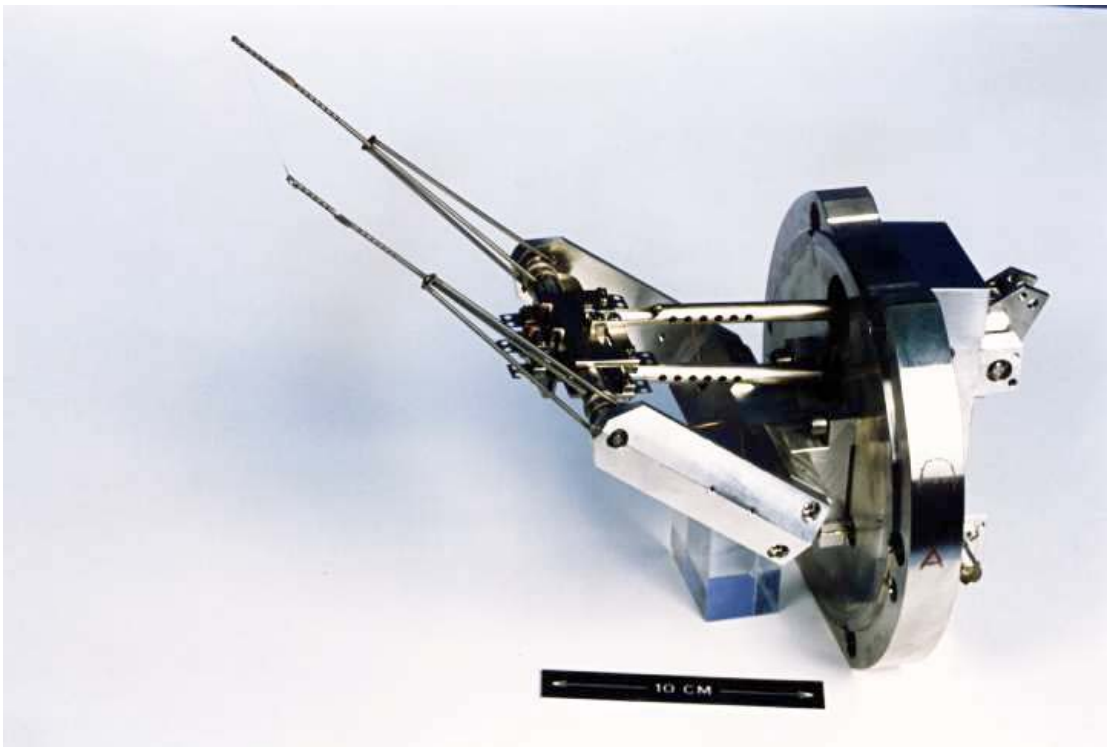

Figure 6.2: The mechanical assembly of a wire-scanner module. The wire, which is barely visible in the photograph, is strung between the two tines of the fork. It has a thickness of ~ 30 μm.

The four wire scanners are controlled and read out by a VMEbus microcomputer

system connected via Ethernet to the workstations of the PS control network. A DAC module housed in the VME system delivers a command voltage to the velocity servo loop of a controller unit for the electric motor. The position of the wire is measured by a resolver, connected to the shaft of the motor, and two ADC modules that are part of the VME system. The resolver delivers two analog signals, the amplitudes of which are proportional to the cosine and sine of the angle of the motor shaft with respect to some reference position. These two signals are sampled by both ADC modules; one is used for real-time control of the movement of the motor, and the other, a transient digitizer equipped with a large memory, is used for data taking. A third ADC module in the VME system is dedicated to sampling the photomultiplier signal. It is read out together with the transient digitizer after a scan of the beam. The resolver signals are converted to transverse positions of the wire. They are then combined with the photomultiplier signal to form a beam profile, from which the emittance is derived.

The new fast wire scanner system was designed to carry out measurements under virtually any of the conditions present in the PS accelerator: It measures profiles of beams of protons, antiprotons (until 1996), electrons, and positrons ranging in energy from 1 to 25 GeV (protons) and in intensity from 10^9 to $2 \cdot 10^{13}$ particles per pulse. Profiles can be obtained at any time during the acceleration cycle from approximately 220 ms after injection until the beam is ejected from the machine. This covers most of the existing conditions in PS as well as those foreseen for PS as a future pre-accelerator of LHC. One exception is lead-ion beams; the wire removes electrons from the ions, and the beam is lost without providing a measurement result [31]. A measurement can be carried out at one of three different velocities of the wire as it traverses the beam, namely 10, 15, and 20 m/s. Normally, one wishes to execute the measurement at the largest possible velocity in order to cause the least interference with the circulating beam, but at high energies a lower velocity is accepted in order to reduce strain on the mechanical assembly. The wire may be swept through the beam in both directions during the same acceleration cycle, which makes it possible to obtain beam profiles from two different stages of the acceleration. Moreover, two units can scan the beam at the same time, which permits simultaneous measurements of horizontal and vertical profiles.

6.2.3 Performance

The first two units of the new fast wire scanner were used extensively under difficult conditions at the LHC machine-development session in December 1993. The acceleration scheme foreseen for PS as a preinjector of LHC was tested during a 12-day period [32]. This session provided the first test on a grand scale of the new instrument. The wire scanners contributed to the success of the test, and they performed more than 1300 profile measurements without failure during this period. Comparisons were made with other profile-measurement devices, mainly the beam scope in the PS Booster, the SEM grids in the PS injection line, and the SEM grids in the PS transfer line TT2. Checks were also made against the old wire scanner. The measurements, which are reported in [32, 33], showed good agreement between the different instruments. At the beginning of

1994, the two units of the old fast wire scanner were upgraded to the same standard and incorporated into the new system. The system as a whole was integrated with the PS control system and became fully operational during 1994. The instrument is now a key component of the PS beam-diagnostics system.

The main factor limiting the accuracy of the measured emittance is the precision of the dynamic position measurement. It seems to be somewhat lower than expected due to irreproducible flexing of the fork holding the wire. Other important sources of uncertainty are the values of the β function and the dispersion used for the emittance calculation. They are provided by the software tool MAD [34], which simulates the accelerator optics. The quality with which the PS accelerator is modeled by this program is difficult to evaluate precisely. With the above limitations having been taken into consideration, the new fast wire scanner is estimated to be accurate to within $\pm 5\%$ in emittance for small beams [31].

Acknowledgements

My sincere gratitude must go to my supervisor in DELPHI, Vincent Hedberg, who has skillfully guided me through the past four years of my studies. His generosity with advice and support has been invaluable throughout this time. With great patience he has helped me to work out solutions to the various problems I have encountered along the way, providing me at the right moments with both encouragement and insight. Working with him has been a true privilege.

I am indebted to Göran Jarlskog for providing me with the opportunity to pursue a Ph.D. in particle physics, and for encouraging me in many ways during my studies. The financial support that I have received from CERN and from Lund University is most gratefully acknowledged.

My work related to STIC owes a great deal to the various efforts of my many DELPHI colleagues, and in particular, of my colleagues in the STIC team, to whom I extend my gratitude and appreciation. I would especially like to thank Clara Matteuzzi for valuable help and interesting discussions concerning the physics behind the single-photon analysis, and Tiziano Camporesi for the many useful ideas and suggestions that he has contributed to several different aspects of my work. I would also like to thank Georg von Holtey of the SL Division for the pleasant collaboration on the study of off-energy electron background.

Many people in the PS Division contributed in important ways to the development of the new fast wire scanners. I would like to thank in particular Heribert Koziol, group leader of the Beam Diagnostics group; Charles Steinbach, project leader; and my colleagues on the wire-scanner team Jan Olsfors, Frans Hoekemeijer, Vassilis Agoritsas, Ulrich Raich, and Gérard Martini for much support and rewarding collaboration. My thanks must also go to Magnus Hansen and Thomas Pettersson, whose encouragement and clever ideas at crucial moments have been invaluable to me.

Not all of the support and encouragement that has helped me through the past few years was limited to the purely professional. The members of our CERN "lunch crowd", in its various constellations, have shared many memorable moments with me. The same is true of the Lund graduate students and engineers, both former and present. I very

much appreciated the pleasant company of Barbro Åsman and Maria Gunther Axelsson during their visits to CERN.

Finally, my deepest gratitude is directed to my husband Philip and to my parents Margaretha and Christer, who were always there when I needed them, and who always kept their faith in me. This work would have been far more difficult without them.

Bibliography

[1] P.S. Drell, hep-ex/9701001.

[2] G.F. Giudice, hep-ph/9605390.

[3] *Le synchrotron à protons de 25 GeV,* CERN PIO/75-4.

[4] F. Blas *et al.* in *Proceedings of the 1995 Particle Accelerator Conference and International Conference on High-Energy Accelerators,* IEEE, Piscataway NJ 1996;
G. Arduini *et al.* in S. Myers *et al.*, eds., *Proceedings of the 5th European Particle Accelerator Conference – EPAC '96,* IOP Publishing, Bristol 1996.

[5] *The Next Step,* information brochure from the Communication and Public Education Group, CERN 1993.

[6] DELPHI Collaboration, P. Aarnio *et al.*, Nucl. Inst. and Meth. A303 (1991) 233;
DELPHI Collaboration, P. Abreu *et al.*, Nucl. Inst. and Meth. A378 (1996) 57.

[7] A. Andreazza *et al.*, Nucl. Inst. and Meth. A367 (1995) 198;
A. Andreazza, DELPHI 98-64 MVX 24.

[8] C. Brand *et al.*, Nucl. Inst. and Meth. A283 (1989) 567;
O. Bärring, thesis, Lund Univ., LUNFD6/(NNFL-7071) 1992.

[9] S.J. Alvsvaag *et al.*, Nucl. Phys. B, Proc. Suppl. 44 (1995) 116; also available as DELPHI 95-12 CAL 119;
S.J. Alvsvaag *et al.*, IEEE Trans. Nucl. Sci. 42 (4) (1995) 478; also available as DELPHI 94-157 CAL 120;
S.J. Alvsvaag *et al.* in H.A. Gordon and D. Rueger, eds., *Proceedings of the 5th International Conference on Calorimetry,* World Scientific Publishing Co., Singapore 1995; also available as DELPHI 94-148 CAL 118;
S.J. Alvsvaag *et al.* in H.S. Chen, ed., *Proceedings of the Beijing Calorimetry Symposium,* IHEP, Beijing 1995; also available as DELPHI 95-14 CAL 123.

[10] S.J. Alvsvaag *et al.*, Nucl. Inst. and Meth. A360 (1995) 219; also available as DELPHI 94-126 CAL 117;
S.J. Alvsvaag *et al.*, IEEE Trans. Nucl. Sci. 42 (4) (1995) 469; also available as DELPHI 94-158 CAL 121;

S.J. Alvsvaag *et al.*, DELPHI 95-13 CAL 122; contribution to the 4th International Conference on Advanced Technology and Particle Physics, Como, Italy, October 1994.

[11] P. Ferrari and V. Hedberg, DELPHI 98-49 CAL 141.

[12] P.P. Allport *et al.*, Nucl. Inst. and Meth. A279 (1989) 189;
J. Santon and N. Kurtz, RAL-89-028.

[13] M. Burns *et al.*, Nucl. Inst. and Meth. A277 (1989) 154.

[14] DELPHI Collaboration, P. Abreu *et al.*, Eur. Phys. J. C1 (1998) 1;
DELPHI Collaboration, P. Abreu *et al.*, Phys. Lett. B380 (1996) 471;
DELPHI Collaboration, P. Abreu *et al.*, Z. Phys. C74 (1997) 577.

[15] G. Barbiellini *et al.* in G. Altarelli, R. Kleiss and C. Verzegnassi, eds., CERN Yellow Report 89-08 vol. 1, p. 129.

[16] F.A. Berends *et al.*, Nucl. Phys. B301 (1988) 583.

[17] E. Accomando *et al.* in G. Altarelli, T. Sjöstrand and F. Zwirner, eds., CERN Yellow Report 96-01 vol. 1, p. 207.

[18] G. Barbiellini, B. Richter and J.L. Siegriest, Phys. Lett. 106B (1981) 414.

[19] See, e.g., S. Dawson in T. Ferbel, ed., *Techniques and Concepts of High Energy Physics IX,* Plenum Press, New York 1997.

[20] S. Ambrosanio and B. Mele, Phys. Rev. D55 (1997) 1399;
Erratum *ibid.* D56 (1997) 3157;
S. Ambrosanio *et al.*, Nucl. Phys. B478 (1996) 46;
S. Ambrosanio and B. Mele, Phys. Rev. D53 (1996) 2541;
S. Ambrosanio and B. Mele, Phys. Rev. D52 (1995) 3900.

[21] ALEPH Collaboration, R. Barate *et al.*, Phys. Lett. B420 (1998) 127;
L3 Collaboration, M. Acciarri *et al.*, Phys. Lett. B411 (1997) 373;
OPAL Collaboration, K. Ackerstaff *et al.*, Eur. Phys. J. C2 (1998) 607.

[22] A. Brignole, F. Feruglio and F. Zwirner, Nucl. Phys. B516 (1998) 13.

[23] H. Senju, Prog. Theor. Phys. 95 (1996) 455;
H. Senju, Prog. Theor. Phys. 92 (1994) 611;
H. Senju, Prog. Theor. Phys. 89 (1993) 709;
Erratum *ibid.* 89 (1993) 1121.

[24] G. von Holtey *et al.*, Nucl. Inst. and Meth. A403 (1998) 205.

[25] A.H. Ball, H. Burkhardt and G. von Holtey, EPAC 96:430;
G. von Holtey, CERN SL/95-29 (EA).

[26] G. von Holtey, CERN SL/95-86 (EA).

[27] K.L. Brown and Ch. Iselin, CERN 74-2.

[28] DELPHI Collaboration, CERN-LEPC/92-6.

[29] S. Hancock *et al.*, Tsukuba ABI Workshop 1991:126; also available as CERN PS/91-12 (OP).

[30] See, e.g., M. Conte and W.W. MacKay, *An Introduction to the Physics of Particle Accelerators,* World Scentific Publishing Co., Singapore 1991;
H. Wiedemann, *Particle Accelerator Physics,* Springer-Verlag, Berlin and Heidelberg 1993;
K. Potter in CERN Yellow Report 85-19 vol. 1, p. 301;
J. Rossbach and P. Schmüser in CERN Yellow Report 94-01 vol. 1, p. 17;
J. Buon in CERN Yellow Report 94-01 vol. 1, p. 89;
E. Wilson in CERN Yellow Report 94-01 vol. 1, p. 131.

[31] Ch. Steinbach, Tsukuba Accelerators 1994:285; also available as CERN PS/95-04 (OP).

[32] R. Cappi *et al.*, CERN PS/94-11 (DI); also available as LHC Note 266.

[33] E. Falk *et al.*, CERN PS/OP Note 94-11 (MD).

[34] H. Grote and F.C. Iselin, CERN SL/90-13 (AP).

Article I

The Small Angle Tile Calorimeter in the DELPHI Experiment

EUROPEAN ORGANIZATION FOR NUCLEAR RESEARCH

CERN–EP/98–132
September 2nd, 1998

The Small Angle Tile Calorimeter in the DELPHI Experiment

S.J. Alvsvaag[1)], M. Bari[12)], G. Barreira[5)], A.C. Benvenuti[2)], M. Bigi[11)], M. Bonesini[7)], M. Bozzo[4)], T. Camporesi[3)], H. Carling[6)], V. Cassio[11)], L. Castellani[9)], R. Cereseto[4)], F. Chignoli[7)], G. Della Ricca[12)], D.R. Dharmasiri[8)], M.C. Espirito Santo[5)], E. Falk[6)], A. Fenyuk[10)], P. Ferrari[7)], D. Gamba[11)], V. Giordano[2)], Yu. Gouz[10)], M. Guerzoni[2)], S. Gumenyuk[7)], V. Hedberg[6)], G. Jarlskog[6)], A. Karyukhin[10)], A. Klovning[1)], A. Konoplyannikov[10)], I. Kronkvist[6)], L. Lanceri[12)], R. Leoni[7)], O.A. Maeland[1)], A. Maio[5)], R. Mazza[7)], E. Migliore[11)], F.L. Navarria[2)], P. Negri[7)], B. Nossum[8)], V. Obraztsov[10)], A. Onofre[5)], M. Paganoni[7)], M. Pegoraro[9)], L. Peralta[5)], L. Petrovykh[7)], M. Pimenta[5)], P. Poropat[12)], M. Prest[12)], A.L. Read[8)], A. Romero[11)], N. Shalanda[10)], L. Simonetti[11)], T.B. Skaali[8)], B. Stugu[1)], F. Terranova[7)], B. Tome[5)], E. Torassa[11)], P.P. Trapani[11)], M.G. Verardi[2)], E. Vallazza[12)], E. Vlasov[10)], A. Zaitsev[10)]

Abstract

The **S**mall angle **TI**le **C**alorimeter (**STIC**) provides calorimetric coverage in the very forward region of the DELPHI experiment at the CERN LEP collider. The structure of the calorimeters, built with a so-called "shashlik" technique, gives a perfectly hermetic calorimeter and still allows for the insertion of tracking detectors within the sampling structure to measure the direction of the showering particle. A charged-particle veto system, composed of two scintillator layers, makes it possible to trigger on single photon events and provides e-γ separation. Results are presented from the extensive studies of these detectors in the CERN testbeams prior to installation and of the detector performance at LEP.

(*To be submitted to Nuclear Instruments and Methods A*)

[1)] Department of Physics, University of Bergen, Bergen, Norway
[2)] Dipartimento di Fisica, Università di Bologna and INFN, Bologna, Italy
[3)] CERN, European Organization for Nuclear Research, Geneva, Switzerland
[4)] Dipartimento di Fisica, Università di Genova and INFN, Genoa, Italy
[5)] LIP, IST, FCUL, UCP, Lisbon and Coimbra, Portugal
[6)] Department of Physics, University of Lund, Lund, Sweden
[7)] Dipartimento di Fisica, Università di Milano and INFN, Milan, Italy
[8)] Department of Physics, University of Oslo, Oslo, Norway
[9)] Dipartimento di Fisica, Università di Padova and INFN, Padua, Italy
[10)] Institute for High Energy Physics, Serpukov, Russia
[11)] Dipartimento di Fisica, Università di Torino and INFN, Turin, Italy
[12)] Dipartimento di Fisica, Università di Trieste and INFN, Trieste, Italy

The Small Angle Tile Calorimeter in the DELPHI Experiment

The **S**mall angle **TI**le **C**alorimeter (**STIC**) provides calorimetric coverage in the very forward region of the DELPHI experiment at the CERN LEP collider. The structure of the calorimeters, built with a so-called "shashlik" technique, gives a perfectly hermetic calorimeter and still allows for the insertion of tracking detectors within the sampling structure to measure the direction of the showering particle. A charged-particle veto system, composed of two scintillator layers, makes it possible to trigger on single photon events and provides e-γ separation. Results are presented from the extensive studies of these detectors in the CERN testbeams prior to installation and of the detector performance at LEP.

1. INTRODUCTION

At e^+e^- colliders the luminosity is monitored by measuring with high accuracy a well-known process, i.e., Bhabha scattering. The continuing progress in theoretical calculations and in Monte Carlo simulations of this process has reached an accuracy of <1‰ which has stimulated the construction of better luminosity monitors for high precision Z^0 physics at LEP. The difficulty in this task is given by the steep angular dependence of the Bhabha cross section ($d\sigma/d\theta \propto 1/\theta^3$) which makes it necessary to extend the measurement to as small angles as possible with a very well defined acceptance. In the DELPHI experiment [1,2] an uncertainty of 1‰ in the luminosity measurement requires a control of the biases in the shower position at the inner edge of the acceptance at a level of 50 μm.

In the present phase of the LEP research program, at center-of-mass energies above the W^+W^- production threshold, one of the main goals is the search for the Higgs boson through the reaction $e^+e^- \to H^0\ Z^0$ with the H^0 decaying into two jets and the Z^0 into $\nu\bar{\nu}$. This process is the most sensitive to a massive H^0 near the kinematic limit, but it requires a very hermetic detector in the forward region to eliminate background processes such as $e^+e^- \to Z^0\ \gamma$ and $e^+e^- \to W^+W^- \to q\bar{q}e\bar{\nu}$ with the photon or the electron escaping detection.

In 1992, the DELPHI Collaboration decided to meet these challenges by replacing the existing luminometer [2,3] by a new calorimeter, the **S**mall angle **TI**le **C**alorimeter (**STIC**) [4]. This detector has completed the calorimetric coverage in the forward region and provided a monitoring of the luminosity with an uncertainty of 0.9‰ when taking data on the Z^0 peak.

The addition of a charged-particle veto system to the detector allows DELPHI to take advantage of the rather large cross-section for $e^+e^- \to Z^0\ \gamma$ in order to measure the invisible decay width of the Z^0. This measurement requires a trigger on single photons and thus relies on an efficient and fast photon identification system. Two layers of scintillators, read out with 10 m long optical fibers, provide such a system.

Off-energy electrons created in bremsstrahlung interactions between beam particles and residual gas molecules in the beampipe constitute the largest source of background to a single photon study. The insertion of two layers of silicon strip shower maximum detectors within the sampling structure makes it possible to measure the shower direction and thereby significantly reduce the off-energy electron background.

In the following the most salient features of the construction of the STIC, the veto system and the silicon strip shower maximum detectors will be described. This is followed by a presentation of the testbeam studies of these devices. Finally, the performance of the detectors at LEP will be discussed.

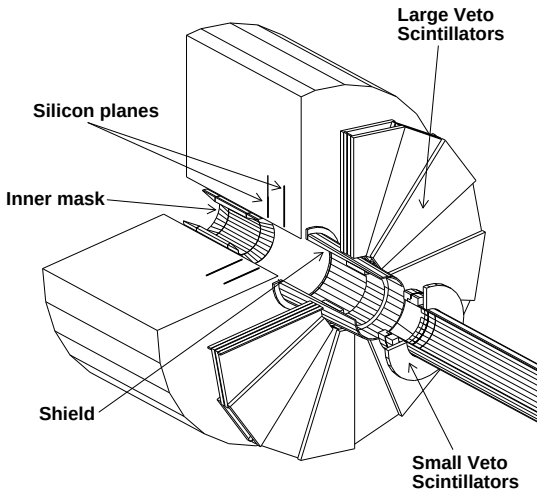

Figure 1. Drawing of one of the two calorimeters showing the silicon shower maximum detector and the veto scintillator counters. The "shield" and the "inner mask" are tungsten rings used to protect the central tracking chambers in DELPHI against low-energy photon background.

2. THE CALORIMETER

The STIC is a sampling lead-scintillator calorimeter where the blue light produced in the scintillator by an electromagnetic shower is carried to the photodetectors at the back of the calorimeter by means of plastic optical fibers[1] doped with green wave length shifter (WLS). The novel feature of the calorimeter is given by a projective tower structure with continuous converter plates providing full hermeticity and eliminating non-uniformities in the energy response typical of calorimeters built with separate towers.

[1] This type of calorimeter has been nicknamed shashlik calorimeter from the Russian word for skewer since the fibers traversing the calorimeter layers look like skewers.

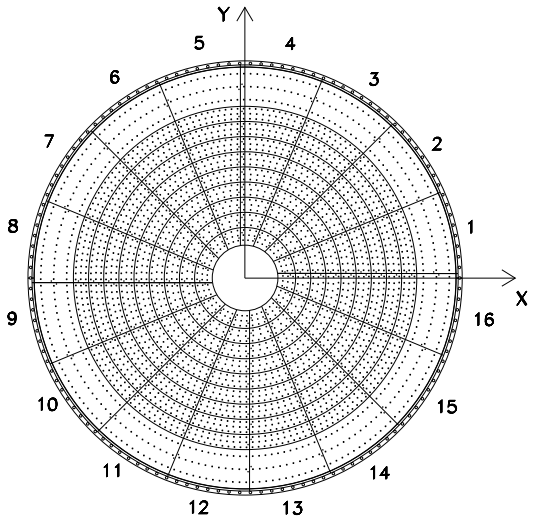

Figure 2. The first scintillator plane with the tower structure consisting of 16 sectors and 10 rings for a total of 160 towers for each calorimeter. The holes for the fibers are also shown.

The detector [5] consists of two cylindrical calorimeters placed on either side of the DELPHI interaction region at a distance of 2200 mm, covering the angular region $29 - 185$ mrad ($65 - 420$ mm in radius)[2]. Each calorimeter is made up of two half-cylinder modules mounted around the beampipe (Figure 1) and supported by the LEP low-beta quadrupole-girder. A STIC module consists of 47 layers of 3 mm thick lead plates and 3 mm thick scintillator tiles. Two layers of silicon strip detectors were inserted into the sampling structure after 7 and 13 sampling layers. The total depth of the calorimeter is 367.5 mm corresponding to 26 radiation lengths.

The fibers run perpendicularly to the lead (scintillator) layers through precision punched (drilled) holes and collect the light over the whole depth of the calorimeter. They are uniformly distributed over the calorimeter cross section (with about 0.79 fiber/cm^2), and the large fiber density, pioneered by Russian groups [6], reduces to a large extent the non-uniformities in light collection that are normally present with wavelength shifting techniques [7].

The scintillators have been cut into segments (tiles) in order to produce a tower structure with 10 rings and 16 sectors as shown in Figure 2. The radial width of the scintillator rings in the first layer is 35 mm for the inner ring 1, 30 mm for rings 2 to 9 and 78 mm for the outer ring 10. In order to prevent particles from tunneling through the fiber holes, the tower structure was made such that while all towers point to the interaction point in the radial direction, they are twisted by three degrees in azimuth. To obtain this, the border of the sectors were displaced by 375 μm from one plane to the next, resulting in a total shift of 18 mm from the first to the last layer.

[2]In the DELPHI coordinate system, the x axis points towards the center of LEP, the y axis points upwards and the z axis is in the direction of the electron beam. θ is the polar angle w.r.t. the z axis and ϕ is the azimuthal angle around the z axis. The radius (R) from the beamline in STIC is given by $R(\mathrm{mm}) = 2200{\cdot}\tan(\theta)$.

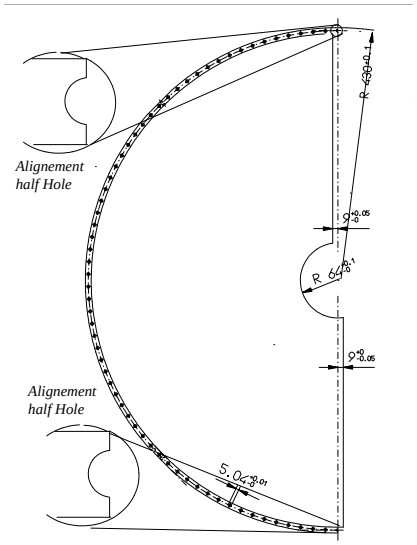

Figure 3. A drawing of one of the lead converter plates showing the aluminum ring around the edge.

2.1. Mechanical construction

The converter plates were made of lead plates strengthened by two steel foils (100 μm thick) glued to both sides of the lead using a resin pre-impregnated fiberglass cloth (resulting in a total thickness of 3.4 mm). A schematic drawing of a converter plane is shown in Figure 3. Around the outer edge is an aluminum ring (7.5 mm wide) which acts as the support structure for one converter/scintillator layer. Aluminum was chosen as support material because its thermal expansion coefficient is very close to that of the lead-steel plates and this reduces the geometrical distorsions that could be caused by thermal stress. The radial thickness of the ring is minimal in order to reduce the inactive part of the calorimeter. A stack of 49 layers are held together by 62 steel rods (⊘5 mm) going through the holes in the ring. A half-hole (shown enlarged in Figure 3) at each end of the aluminum ring was used for positioning of the layer during the stacking and for guidance of the two half-cylinder modules when they were mounted around the beampipe.

The requirement of a very high mechanical accuracy motivated the following production technique:

- The scintillators were made of injection molded polystyrene doped with 1.5% paraterphenyl and 0.05% POPOP. A total of 470 different shapes of scintillator tiles were needed to complete the tower

structure. The scintillator tiles were attached to the converter plates by means of precision pins ($\oslash$1 mm) located in reference holes drilled in the scintillator and converter layers. The tiles were machined from a slab of scintillator in one operation (edges, fiber holes and positioning pin holes). The positions of the pin holes with respect to the edges were measured on an optical bench and the differences to the expected values were less than 30 μm after sampling 10% of the tile production;

- The converter plates were then machined to the final shape and positioned on a numerically controlled punching machine which made all the fiber holes;

- The aluminum ring was glued to the edge of the converter plate. The plate was then positioned on a numerically controlled milling machine located in a room maintained at 23.5$\pm$0.5 °C, and the two reference half-holes on the aluminum ring and the holes for the alignment of the scintillator tiles were made. The distances between the centers of the two reference half-holes were the same to within 20 μm for all layers (verified with an optical bench in a controlled temperature environment). The thicknesses of the aluminum rings were measured to be within 2 μm of their nominal values. This translates into a difference in thickness between the various STIC modules of less than 100 μm;

- White 120 μm thick Tyvek® paper[3] was inserted between the absorber and the scintillator plane in order to increase the light collection, and also between tiles for optical separation. This paper was cut and the fiber and pin holes were made with a numerically controlled laser mill;

- The mounting of the scintillator tiles and the Tyvek® paper on the converter plate was made manually by using the two precision positioning pins in each tile.

The overall accuracy of the assembly was determined by measuring, on a high-precision X-Y table equipped with optical measuring devices, the center and the radius of the circumferences defined by the edges of the first three tile rings (for all the calorimeter layers). The resulting distribution showed that the centers and the radii were less than 50 μm from the specification in all layers.

2.2. Optical fibers

Two types of WLS fibers have been used in STIC: Kuraray Y7 with single cladding made of fluorinated plexiglass until 1995 and Kuraray Y11 with double cladding from 1996 onwards. The WLS fibers absorb light at ~420 nm and have an emission peak at ~500 nm. The Y7 fibers had a length varying between 500 and 517 mm, while the Y11 are 20 mm longer. The fibers were polished at both ends using an air-cushion diamond mill[4]. One end was aluminized by sputtering[5] to increase the light collection.

The light yield and the attenuation length of all the fibers in the calorimeters were measured before assembly. For this purpose, an automatic test-bench based on a computer-controlled scanning table, with a precision of 20 μm, was used. In the test-bench a thin scintillator excited by a radioactive ^{90}Sr source was moved along the fiber, and the light output from the fibers was measured with a photomultiplier.

In order to avoid local light yield non-uniformities in the calorimeters, the measured light yield and the attenuation length were used to group the fibers. During the assembly, fibers from the same group were used for each individual tower. Approximately 10% of the 10,000 fibers studied were discarded, either because visual inspection revealed damage or because the measured attenuation length was less than 130 cm or because there were defects in the individual light attenuation pattern.

Photocathode type	Bialkali
Useful photocathode diameter	22 mm
No. of dynodes	2
Anode dark current	~ 0.1 nA
Quantum eff. at 500 nm	~ 10%
Typical gain (HV= -900V, B= 0 T)	~ 30

Table 1. Characteristics of the Hamamatsu R2149-03 tetrode.

2.3. Phototetrodes and front-end electronics

The light from the fibers coming from one tower was viewed through a 5 mm air gap by a 1" Hamamatsu R2149-03 phototetrode. The main characteristics of this device are given in Table 1. The tetrode amplification chain consists of a bialkali photocathode, a fine-mesh dynode, a fine-mesh anode and a plate dynode. Secondary electrons from the fine-mesh dynode are collected by the anode, in part directly after emission and in part after multiplication on the plate dynode. The tetrodes were tested in a laboratory set-up with the operating voltages set to -900 V, -500 V and -180 V for the cathode, the fine-mesh dynode and the plate dynode respectively [8]. The total gain was then about 30 due to a multiplication factor three between the cathode and the fine-mesh dynode and a multiplication factor ten between the fine-mesh dynode and the anode.

Inside the 1.2 T magnetic field of DELPHI, the tetrodes gain is reduced. The field affects the acceler-

[3]Tyvek® is a registered trademark of Du Pont.

[4]GEBEX, Uster, Switzerland.

[5]Precitrame, Tramelan, Switzerland.

ated electrons inside the tetrode, producing a significant dependence of the relative gain on the orientation angle. The upper plot in Figure 4 shows the dependence of the gain on the angle, at a field of 1.2 T, for five different tetrodes, while the bottom plot shows the average profile for a sample of 25 tetrodes. An increase in gain of 20% is obtained by tilting the tetrodes by 15^o, and the tetrodes were therefore mounted with this angle in STIC. Figure 5 shows the ratio of the gain at 1.2 T to 0 T for a sample of 280 tetrodes when these were mounted at an angle of 15° w.r.t. the magnetic field direction.

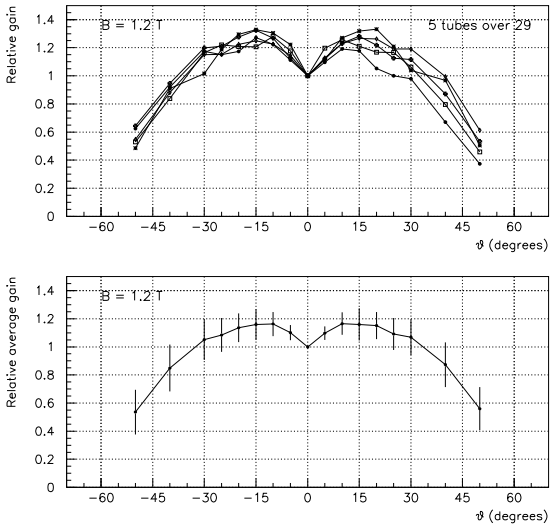

Figure 4. Distribution of gains as a function of the orientation angle with respect to the magnetic field direction for a sample of 25 R2149-03 Hamamatsu tetrodes in a 1.2 T field. The upper plot shows the distribution for individual tubes, while the bottom plot shows an average profile. The error bars give the rms spread.

Each tetrode was placed inside an aluminum housing, containing a charge sensitive JFET preamplifier and a high voltage divider. The preamplifier incorporates a high-pass filter to eliminate the microphonics noise induced by mechanical vibrations of the dynode structure. The photodetector contribution to electronic noise comes from the anode capacitance ($\leq$10 pF) and from the dark current ($\sim$0.1 nA). The equivalent noise charge, using a Gaussian shaping time of 500 ns, was 250 electrons. The preamplifier gain was adjusted by means of a resistor to 0.24 μV/electron with a maximum output signal of 1.5 V. The average rise time was 15 ns, followed by an exponential fall ($\tau \sim 10\ \mu s$) to match the shaper input characteristics. The differential output signals are fed via 40 m long cables to the counting room where they are digitized. For testing purposes, a set of programmable pulse generators allows injection of a precise charge signal at the input of each preamplifier.

2.4. The LED monitoring system

A luminosity measurement with 1‰ systematic uncertainty requires a monitoring of all detector channels

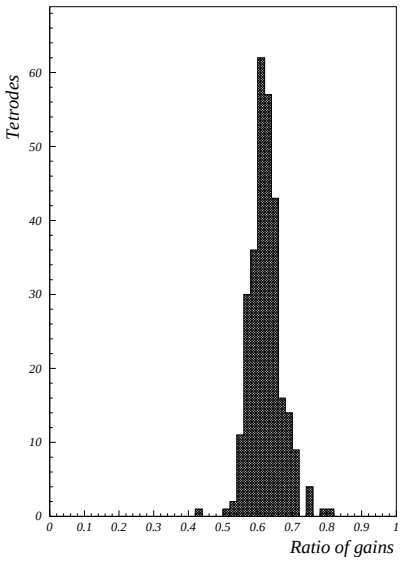

Figure 5. Distribution of the ratio of gains at 1.2 T to 0 T for a sample of 280 R2149-03 Hamamatsu tetrodes.

and of the trigger system. A LED-based monitoring system was built for this purpose [9].

Four driver boards were mounted on the front face of each of the two calorimeters. Each board generates the electrical pulses for flashing up to 40 light emitting diodes. The LEDs[6] are inserted into plexiglass tiles which are arranged in a layer in front of the first converter plane of the calorimeter in a way similar to that of the regular STIC scintillator planes. The blue light from the LED propagates inside the tile and is absorbed by the fibers which continue out of the calorimeter into holes in the tiles. The re-emitted green light propagates inside the fibers to the photocathode of the tetrode. This design allows monitoring of the stability of the whole light collection chain.

The driver board can deliver pulses with independently selected amplitudes to any combination of up to 40 LEDs and the selection is made via an 8 bit control bus. The temperature stability of the system is better than 0.3‰ per degree and the rms variation of the charge injected into a LED is <1‰ for the maximum signal. The stability of the LED signals was studied during a seven hour time period, i.e., a typical LEP fill lifetime. The variations of the signals, measured with the calorimeter readout chain, was within $\pm$1.5‰ .

The number of photoelectrons produced in the tetrodes was measured with the LED system as a function of the high voltage and the amplitude of the LED signal. The effective number of photoelectrons (N_{pe}^{eff}) can be calculated from $\sigma_{pe}/E = 1/\sqrt{E \cdot N_{pe}^{eff}}$ where σ_{pe}/E is the energy resolution measured by the LED system. N_{pe}^{eff} was found to be independent of the amplitude but showed a dependence on the high voltage with a maximum around 200-250 V and a decrease at higher voltages (Figure 6). At LEP, the detector was

[6] 102CR-ND, manufactured by CREE.

operated at 550 V, which gave $N_{pe}^{eff} = 306$ per GeV averaged over all the phototetrodes (rms= 64) in a magnetic field of 1.2 T. Without magnetic field this number was 30% higher.

The number of photoelectrons produced at the photocathode (N_{pe}) can be calculated from N_{pe}^{eff} if the dynode amplification is taken into account since $N_{pe} = (1/\delta_1 + 1/(\delta_1 \cdot \delta_2)) \cdot N_{pe}^{eff}$ where δ_i is the amplification of dynode i [10]. In the laboratory set-up at -900V, N_{pe} was estimated to be a factor 1.64 (1.37) larger than N_{pe}^{eff} at 1.2 T (0 T).

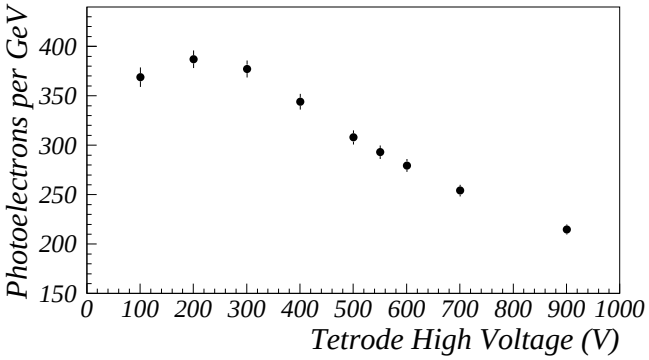

Figure 6. The effective number of photoelectrons per GeV as a function of tetrode high voltage. N_{pe}^{eff} was measured as an average over all phototetrodes in the calorimeter, and the measurement was done with a magnetic field of 1.2 T.

3. CHARGED-PARTICLE VETO SYSTEM

Photons are identified and triggered on by requiring that there is no signal in two sets of scintillators called the large and the small veto counter. An unusual feature of these counters is that the light produced in the scintillators is transported out of the DELPHI magnetic field to the photomultipliers by WLS fibers and clear fiber optical cables.

3.1. The large veto counters

The STIC large veto counters [11] consist of 64 trapezoidal scintillators assembled into two matching planes on each side of DELPHI, at a distance of between 2010 and 2050 mm from the interaction point (Figure 1). The center of the inner edge of the scintillators is at a radius of 86 mm and the outer edge is at a radius of 379 mm.

The counters are made of 10 mm thick Bicron BC-408 plastic scintillator. The light is collected from each scintillator by 2×8 55 cm long Kuraray Y7 WLS fibers glued with optical cement[7] in two 8.35 mm wide and 1.2 mm deep grooves, machined along each of the two longest edges of the scintillator. The inner and outer edges of the counter are coated with a reflector paint made of titanium dioxide in a water soluble binder[8]. The scintillator is wrapped with Tyvek® paper to improve light collection and it is made light-tight with black plastic material.

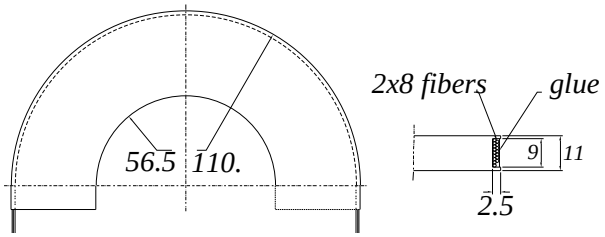

Figure 7. A drawing of one of the four small veto scintillators and the groove along the outer edge which contains the WLS fibers. All distancies are in mm.

The light is read out by a 10 stage Hamamatsu H3165 photomultiplier located outside the DELPHI magnetic field. The photomultiplier is coupled to the WLS fibers via a 10 m long fiber optic cable made of 16 clear Kuraray polystyrene fibers (⌀1 mm). The photomultiplier side of the cable was terminated by gluing the 16 fibers to the inside of a plexiglass cylinder and polishing the surface with a diamond mill. At the counter side, the fiber optic cable was split into two bundles of eight fibers, and these bundles were glued into optical connectors. The WLS fibers from the scintillator were terminated with matching connectors. The light transmission across the connector was found to vary between 85 and 90%.

The counters were tested with cosmic rays using a 1.2 m long clear fiber cable and one H3165 photomultiplier. The average response of the counters was found to be 32 photoelectrons per minimum ionizing particle (MIP). The clear fiber cables, tested with a green light emitting diode coupled to each of the connectors, gave a distribution of the light transmission with an rms spread of 9%.

3.2. The small veto counters

During data taking at the Z^0 peak, the inner edge of the STIC acceptance was defined by a tungsten ring (see Section 8). However, at higher energies this ring was removed. This increased the coverage of DELPHI, but at the same time it created a gap in the STIC veto coverage in the critical region close to the beampipe.

In order to close this gap, scintillator counters were installed directly on the DELPHI beampipe, using a flange for support (Figure 1). These two so-called small veto counters are located on either side of the interaction point at a distance of 1800 mm and each counter consists of two scintillators. These are 10 mm thick and have a half-ring shape with an inner radius of 56.5 mm, an outer radius of 110 mm and a 15 mm straight section at each end (Figure 7). The size of the inner radius is dictated by the size of the beampipe, 55 mm in radius, while the outer radius was chosen to match approximately the transition region between the STIC tower rings 2 and 3.

[7]Bicron BC-600.
[8]Bicron BC-620.

The light is collected by 16 WLS fibers, 1 mm in diameter and 110 mm long, with one end polished and the other aluminized by sputtering. The fibers are divided into two bundles which, except for the length, are identical to those used in the large veto system. The bundles are glued with optical cement in two layers to the inside of a 9 mm wide and 1.5 mm deep groove machined on the outer perimeter of the counters, as shown in Figure 7. The first layer contains nine fibers, and the seven remaining fibers form a second layer in such a way as to optimize the light collection. The bundle with the fibers glued directly to the scintillator collects ~60% of the light.

The counters were tested with cosmic rays before installation and gave a response of ~12 photoelectrons per MIP at the end of a 10 m long fiber optic cable.

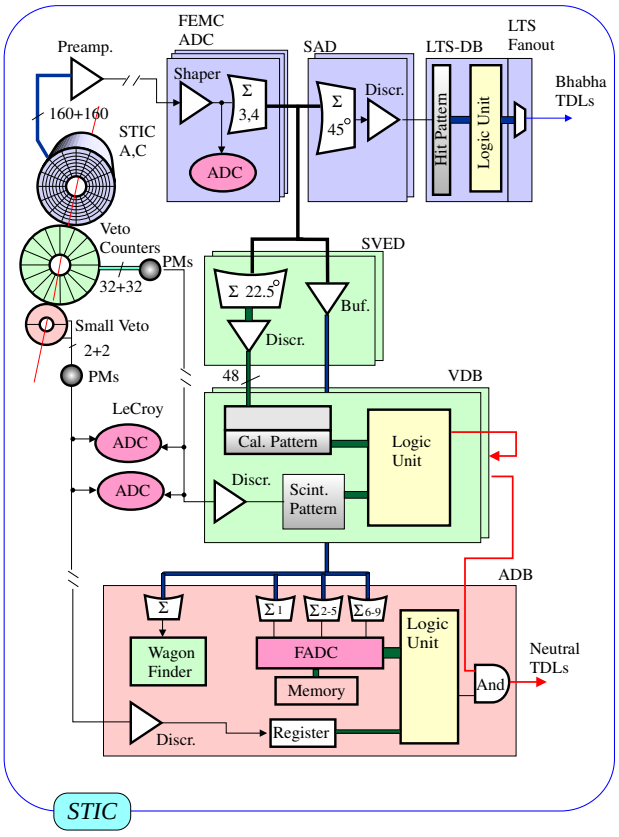

Figure 8. Block diagram of the trigger and the readout system.

4. TRIGGER SYSTEM AND READOUT

The trigger and the readout chain of the calorimeter and veto system are shown in Figure 8. The 320 signals from the preamplifiers of the calorimeters are sent to Fastbus shaper & ADC boards developed originally for the forward lead glass calorimeter in DELPHI [12]. Analog sums of three or four towers are combined by another module (SAD) into 45^o overlapping sectors and the resulting signals are discriminated with two different thresholds. The low-threshold hit patterns are processed by a programmable logic unit (LTS-DB) [13] to create back-to-back Bhabha triggers used in the offline calculation of the luminosity. The high-threshold bits are used as a more selective trigger of Bhabha events for the online luminosity measurement.

The scintillator veto counters are used to trigger on single photon events. In this so-called neutral trigger, the calorimeter signals are combined in 22.5^o sectors and the resulting analog sums are discriminated (SVED) [14]. The signal from the 64 large veto counters are split and sent both to Fastbus ADCs[9] and to discriminators (VDB) [15]. The hit patterns from the calorimeter and the large veto counters are combined in a logic unit to form the neutral trigger. The trigger allows a signal in at most one of the two scintillator planes in front of the shower. Both the veto counter sector directly in front of the shower and its two neighbours are considered, since the edges of the scintillator sectors overlap.

The four signals from the small veto counters are also split to a Fastbus ADC and to a set of discriminators (ADB). If any of these discriminators are set the neutral trigger is inhibited.

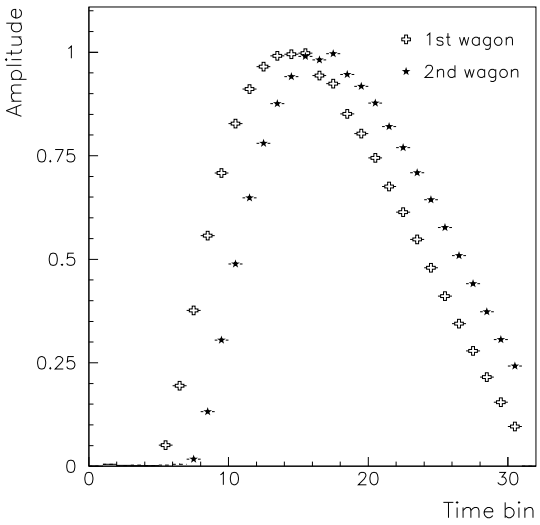

Figure 9. The pulse shape from two different showers produced by different wagons as measured by the FADC. Each bin corresponds to 140 ns.

In 1995, the LEP operation mode changed from colliding beams of eight bunches separated by 11 μs to collisions of four so-called bunchtrains each having up to 4 "wagons" or "minibunches" separated by 247 ns [16]. This entailed a loss of synchronization with the collisions at the level of ±370 ns and a deterioration of the STIC

[9] 1885F, manufactured by LeCroy.

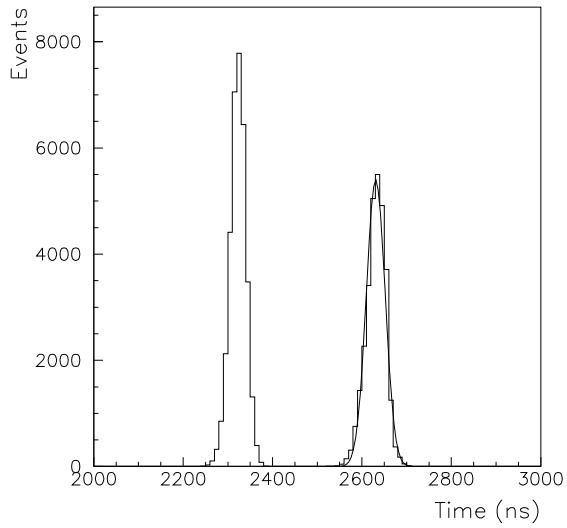

Figure 10. The time distribution of calorimeter signals determined from the pulse shape. The Gaussian fit to the second peak has $\sigma = 21.0$ ns.

energy measurement. The STIC readout was modified to deal with the new situation. By using four sets of discriminators for the veto counter signals (each gated at the arrival time of a different wagon) it was possible to determine which wagon had caused the interaction. The veto counter hit pattern was also used to produce the gate for the calorimeter ADCs. During the periods when LEP was running in bunch train mode, the level of inefficiency (for Bhabha events) of the wagon tagging was negligible, and only 1.7% of the Bhabha online wagon tags were ambiguous. Furthermore, in most of these cases, it was possible to determine offline the true wagon number by comparison of the recorded hodoscope hit patterns with the position of the shower in the calorimeter and thus to correct the measured energy. The fraction of Bhabha events in which the offline wagon determination failed was about 0.3‰ .

The veto counter cannot be used to determine the wagon in single photon events since they are selected on the basis of not having any signals in these detectors. Instead the calorimeter signal itself is digitized 32 times by 8-bits FADCs (ADB) with a sampling interval of 140 ns (Figure 9). From the position of the rising edge of the digitized pulse it was possible to determine the wagon number offline and to correct the energy measurement accordingly. Figure 10 shows the time distribution of calorimeter signals determined from such a pulse shape measurement. A clear separation between electrons from two wagons can be seen and the time resolution obtained with this method is 21 ns.

The FADC values are also used to calculate the radial position of the calorimeter showers in the trigger logic. If the radius is less than 11 cm the neutral trigger is rejected. In this way, a large part of the off-energy electron background is suppressed and the trigger rate is greatly reduced.

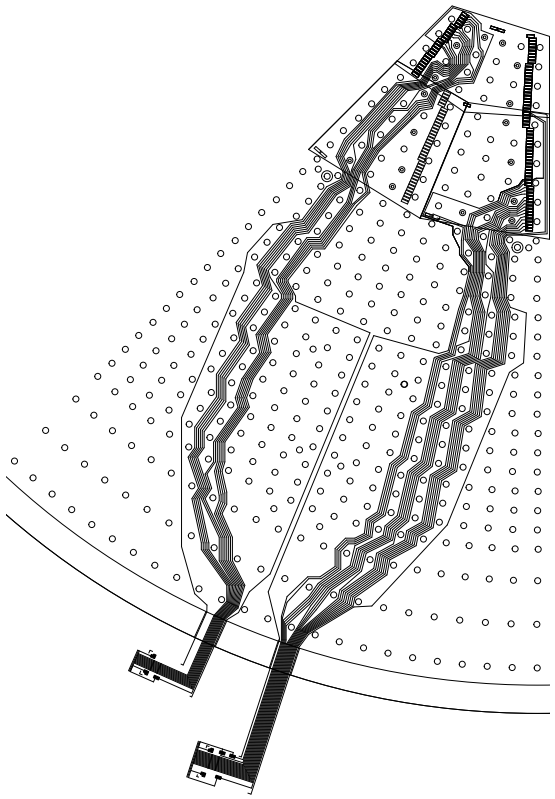

Figure 11. Layout of a 45^o sector of the silicon shower maximum detector with two of its eight Kapton cables shown. The strip structure is not drawn; only the connections to the strips are indicated. Note the holes for the calorimeter fibers which the signal wires have to avoid.

5. THE SILICON STRIP DETECTOR

Each STIC calorimeter was equipped with two planes of silicon shower maximum detectors [17]. The reasons for this were that

- it provides a means to reconstruct the shower axis with ~10 mrad accuracy and this improves the rejection of off-energy electron background;
- it improves the coordinate resolution and the two-shower separation;
- it provides a cross-check in the determination of the STIC calorimeter acceptance in the luminosity measurement.

The silicon planes were installed at depths of 4.0 and 7.4 radiation lengths inside the calorimeter and they cover the angular region between 32.5 and 79 mrad. Radially, the covered region starts at 71.5 mm (73.0 mm) from the beam axis and extends to 174.2 mm (178.3 mm) for the first (second) plane. The two planes are slightly different in order to match the projective geometry of the STIC calorimeter. Each plane consists of 1 mm thick ceramic tiles attached to a 3.5 mm thick aluminum plate and is aligned by three dowels. The silicon detector was attached, with conductive glue, to a metallized area of

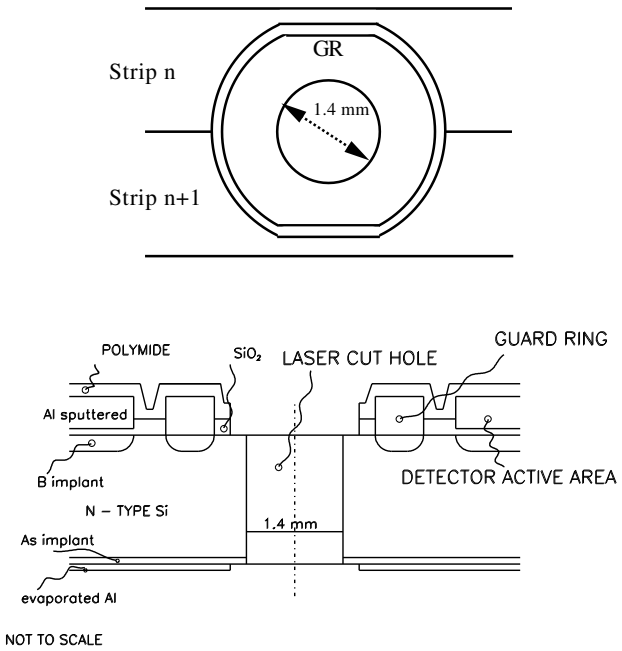

Figure 12. Layout of the region surrounding a fiber hole. Both a top and a side view are shown.

the ceramic which was used to provide the backplane biasing voltage for the diodes.

The detector is made of 300 μm thick, high-resistivity n-type silicon, with p-type strips implanted on the front and an n^+ layer on the back. The circular strips cover 22.5^o in azimuthal angle, i.e., one calorimeter sector, and have a radial pitch of 1.712 mm(1.754 mm) for the first (second) plane. The radial granularity was chosen, following simulation studies [18], to obtain an optimum spatial resolution. In both planes the silicon detectors are arranged in two concentric crowns. Each 45^o sector consists of three silicon wafers with one inner wafer covering two calorimeter sectors and two outer wafers each covering one calorimeter sector. The inner wafers have 2×24 radial strips while the outer wafers have 36 strips (Figure 11).

The main challenge in the detector construction was to make the 1.4 mm diameter holes in the silicon for the passage of the WLS fibers. Three different techniques for making the holes were tested: laser cutting, ultrasonic grinding and chemical etching. All three techniques gave satisfactory mechanical results. However, the best quality to price performance was obtained using laser cutting[10]. The accuracy obtained in the hole diameter was less than 10 μm. The layout of the region surrounding the holes is shown in Figure 12. The implanted strip is protected by a guard region extending to 300 μm from the edge of the hole. The total passive zone around a hole has a diameter of about 3 mm. The holes are always located between two strips, in order to have strip continuity.

In order to evaluate possible damage to the substrate, the strips with holes were compared to those without holes [19]. Figure 13 shows that there was a slight difference in capacitance, due to geometrical effects, between the two sets of strips while the full depletion voltage was the same. A special production of wafers without holes showed leakage currents comparable to those of the detectors with holes.

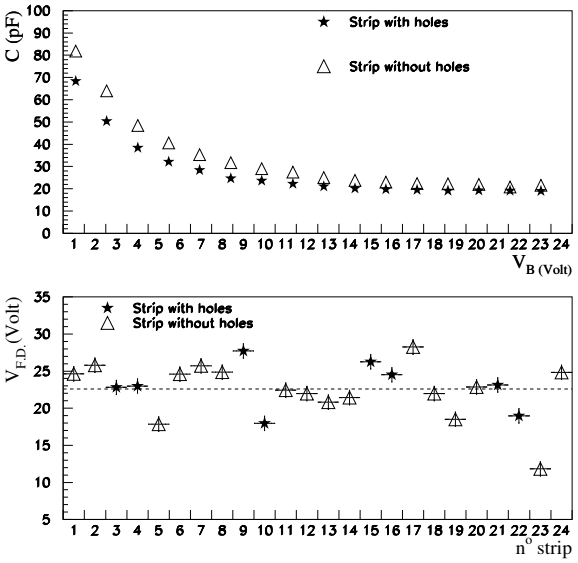

Figure 13. A comparison of the capacitances (top) and of the full depletion voltages (bottom) between strips with and without holes.

The strips were AC coupled to the readout and biased by means of a FOXFET scheme [20]. Each strip acts as an independent source, while the gate and the drain are common. The drain was put at the same voltage as the preamplifier (5 V) in order to avoid current flow in case of damage to the decoupling capacitance. A voltage between 30 V and 50 V (depending on the detector) was applied to the backplane, in order to achieve full depletion and to compensate for the voltage drop between the strip and the drain. An aluminum pad was used for charge collection on each strip. Two aluminum wires, 33 μm in diameter, were used to bond each pad to a copper track[11] deposited on a flexible cable which brings the signals to the outer edge of the calorimeter (Figure 11). The cable was made of a 50 μm Kapton[12] substrate, 35 μm copper tracks and a 50 μm protective coating.

Each 45^o sector of each silicon plane is connected to a Microplex 4 (MX4) charge amplifier with 128 channels and multiplexed output, designed by the Rutherford Appleton Laboratory (UK) [21]. The signals from the strips are sampled and stored twice, once before the LEP beam crossing and once after all the charge in the silicon has been collected, and the difference between the two measurements is sent to a differential amplifier. The technique of double sampling provides a suppres-

[10]MICRON Semiconductor Ltd., UK.

[11]Mipot, Cormons, Italy.

[12]Manufactured by Du Pont.

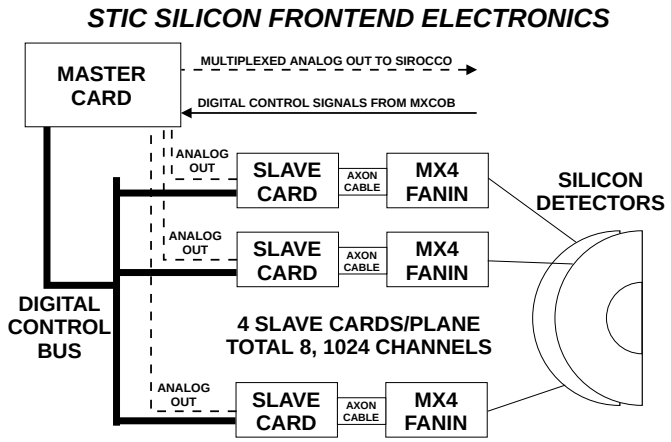

Figure 14. Scheme of the front-end electronics of the silicon detectors for a half cylinder STIC module. The silicon detectors are connected to the MX4 fanin card by flexible Kapton printed circuit cables. The fanins receive the digital control signal from and send the analog differential outputs to the slave cards which amplify the signals. The slave cards are plugged as daughterboards on a PCB on the front of the calorimeter. This same PCB is used to bus the digital and analog signals to a master card, which multiplexes 8-to-1 the analog signals before they are sent to the Fastbus SIROCCO in the counting room for digitization.

sion of common mode spurious signals induced at the detector level.

A special hybrid fanin card[13] matches the 0.5 mm track pitch on the Kapton cables to the 44 μm pitch of the MX4 chip. It consists of a ceramic substrate on which a 1 μm aluminum layer has been evaporated under vacuum and then imprinted by chemical etching. The connections between the Kapton cables and the tracks on the fanin were made by connectors[14] soldered onto the fanin. Given the difficulties of soldering directly on the aluminum tracks, the solder pads were made by evaporating in sequence a layer of titanium (0.05 μm), palladium (0.15 μm) and gold (0.30 μm), after which another layer of gold (3 μm) was added by galvanization. At first only chromium and gold were used, but this led to unstable contacts to 10-15% of the pads.

A block diagram of the full front-end electronics chain is shown in Figure 14. The output signals from the amplifiers (slave cards) are sent to the control room via an 8-to-1 analog multiplexer (master card). The data from each detector are clocked, at a 1 MHz frequency, into a Sirocco IV Fastbus module [22], where they are digitized by a flash ADC.

[13]Designed at CERN and manufactured by Mipot, Cormons, Italy.

[14]ELCO®, series 6200-6201.

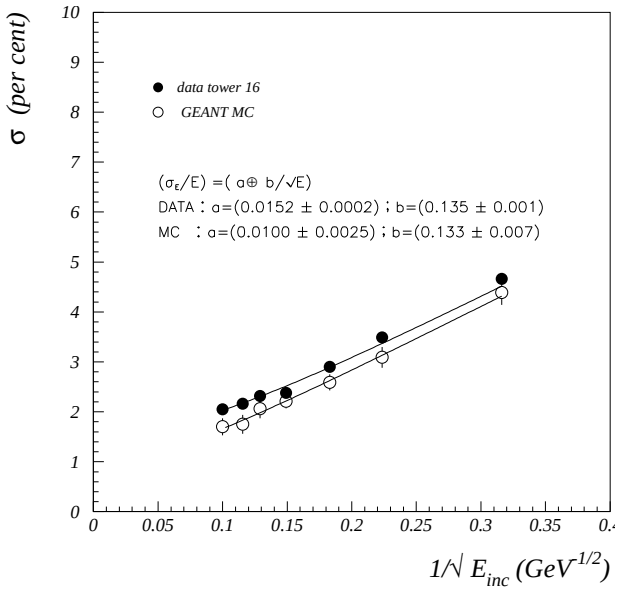

Figure 15. The measured and GEANT simulated energy resolution for electrons from a testbeam going into the center of one tower.

6. PERFORMANCE IN A TESTBEAM

6.1. Studies of the calorimeter

The conceptual design of the STIC detector was studied with a small prototype in 1992, to ascertain the energy resolution, the response uniformity and the accuracy of the position measurement [23]. These measurements were repeated with two different STIC modules in 1993 and the results can be summarized as follows:

- the energy resolution was $\sigma/E(\%) = (1.52 \pm 0.02) \oplus (13.5 \pm 0.1)/\sqrt{E}$;
- the contribution to the resolution from electronic noise was negligible ($\sigma \simeq$90 MeV);
- the energy linearity was within $\pm$ 1%;
- the energy deposited by muons was 4.5σ above the pedestal.

Figure 15 shows a comparison of the measured energy resolution with the results of a GEANT [24] based Monte Carlo simulation [25]. In this simulation photons and electrons in the electromagnetic showers were tracked down to cut-off energies of 50 KeV and 500 KeV, for photons and electrons respectively. The modulation of the energy response due to the presence of the fibers and the leakage of light between neighbouring scintillators was implemented in the GEANT Monte Carlo by means of light collection maps. These give, as a function of the position where the energy is deposited, the fraction of light collected in the same tower and in the neighbouring ones. The light collection maps were computed in a separate fast Monte Carlo program [26] that was tuned to reproduce the test-bench measurements of the fibers and the scintillators [27].

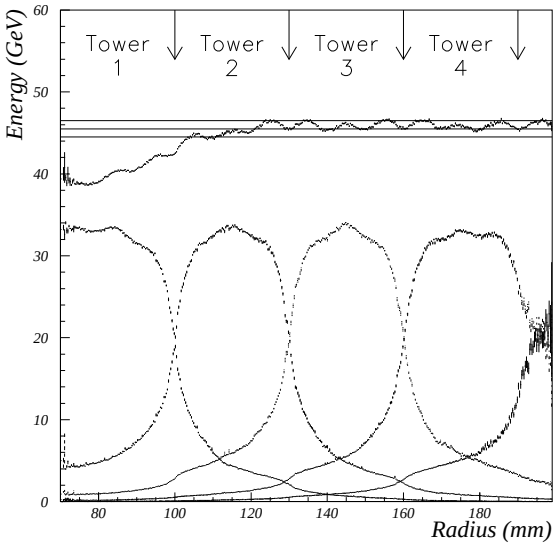

Figure 16. Spatial uniformity of STIC response. The curves in the lower half of the figure correspond to the energy deposited in each tower while the curve in the upper half gives the overall energy deposit. The lines indicate the $\pm 2\%$ interval around the beam energy.

The comparison of the energy resolution formula obtained from the testbeam data and the GEANT simulation shows good agreement between the sampling terms while there is a difference in the constant term. This can most likely be attributed to the difficulties in simulating the light collection mechanism.

The spatial uniformity of the energy response was mapped by scanning the calorimeter radially with an electron beam. The impact point of the particle was measured with an accuracy of <40 μm using an external silicon microstrip telescope. The energy collected by each tower and the overall energy measured by the calorimeter are shown in Figure 16 as a function of the radial impact point. Above tower ring 1, where the energy measurement is not affected by the shower leakage, the response is modulated within a band of $\pm 2\%$. This is due to the increase in light collection when the particle enters the calorimeter close to a fiber. The importance of the continuous absorber used in STIC is apparent in the uniformity of the response as the beam crosses the tower boundaries.

The radial position of a shower was obtained from the energy sharing between rings of calorimeter towers [28]. Radial scans were made of all tower rings and Figure 17 shows one such scan of tower rings 1 and 2 performed with a 45 GeV electron beam and the external silicon microstrip telescope. In this measurement, the ratio of the energy deposited in the two rings is given as a function of the impact point from the telescope. The distance d_k to the border between rings k and $k+1$ was parametrized as a function of the estimator

$$\epsilon = \ln \frac{\sum_{i=1}^{k} E_i}{\sum_{i=k+1}^{N_{rings}} E_i} \qquad (1)$$

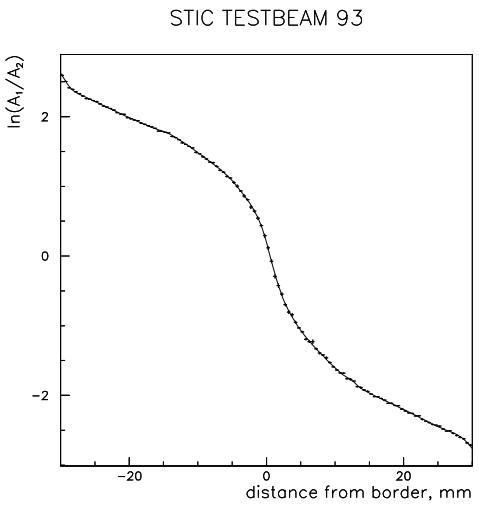

Figure 17. The ratio of the energy measured in tower ring 1 and tower ring 2 versus the impact point measured by the microstrip telescope.

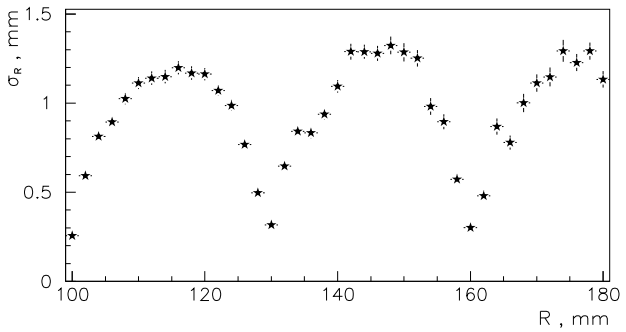

Figure 18. The radial resolution of the calorimeter versus radius.

where E_i is the measured energy in ring i. The quantity $d_k(\epsilon)$ was measured for each border k in the testbeam.

For each shower the distances to the outer and the inner borders of the ring with the maximum energy deposit were calculated. These two measurements were combined to improve the resolution near the center of the rings. Figure 18 shows the measured radial resolution as a function of the radius. It varies from 0.25 mm in a narrow region ($\pm$ 2 mm) around the ring borders to 1.2-1.3 mm in the central regions of the rings.

In the same way as for the radial position, the algorithm reconstructing the azimuthal angle of the shower was based on the measured sharing of shower energy at the border between adjacent calorimeter sectors. The linear distance from the impact point to a border between two sectors was calculated with an estimator similar to (1). Since the towers are larger in the azimuthal direction than in the radial direction the azimuthal resolution is also poorer. The resolution in the azimuthal direction in, for example, ring 4 varies between $\sim$1 mm at the tower sector border and $\sim$4 mm at the tower center.

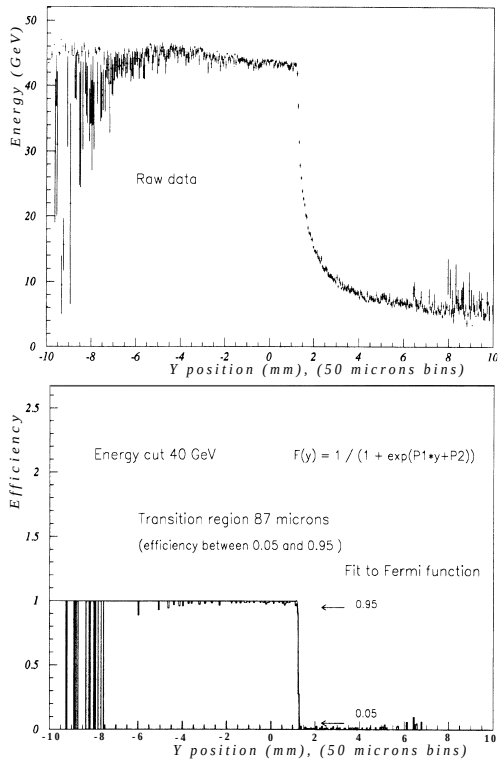

Figure 19. Energy deposited in the calorimeter as a function of the radial impact position (y) (top). The average energy measured by the calorimeter (normalized to 45 GeV) as a function of the radial impact position (bottom). The region $y \geq 1$ mm was covered by a tungsten mask. A fit of a Fermi function to the transition region at the mask border is superimposed.

In a luminosity monitor it is essential to have a good definition of the inner edge of the acceptance. This can be achieved either directly by measuring the energy sharing as described above or by using an accurately machined tungsten mask which translates a cut in energy into a very precise radial measurement [3,23]. The mask method was studied with the prototype calorimeter and a silicon microstrip telescope by scanning the edge of a 6 cm thick piece of tungsten [29]. Using an optimized value for the energy cut (e.g. 40 GeV for 45 GeV electrons), the transition region was measured. The transition region was defined as the region where the fraction of events with a shower energy larger than the energy cut goes from 5% to 95% . The width of this region gives the sharpness of the inner edge of the used acceptance. The measurement, shown in Figure 19, gives a transition region of 87 μm for a fit of a Fermi function and 82 μm for a fit of a step function convoluted with a Gaussian distribution. The latter fit gives $\sigma = 25$ μm which is close to the expected resolution of the measurement of the impact point. Therefore, it was concluded that the mask method defines the inner edge of the acceptance to better than 25 μm.

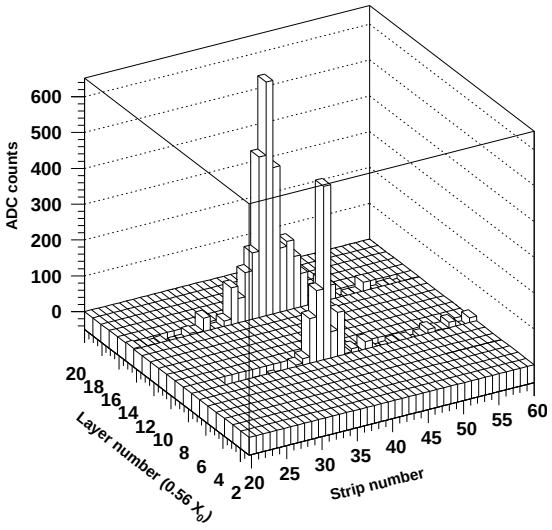

Figure 20. The online pulse height distribution for different strips after pedestal and noise subtraction (for one 45 GeV testbeam electron).

6.2. The silicon shower maximum detectors

In 1994, a STIC calorimeter module equipped with silicon shower maximum detectors was exposed to a 45 GeV electron testbeam. Both the silicon detectors and the readout chain were the same as those used in DELPHI.

The data showed the presence of a coherent noise source that produced a common shift of the baseline. Pedestal runs were taken between the testbeam runs to monitor the noise and to determine correlation coefficients between the various strips. The noise was then subtracted on an event-by-event basis by using the signals from the strips outside a shower and the correlation coefficients.

The measured signal-to-noise ratio in the strip with the maximum energy deposit was about 40 for a 45 GeV electromagnetic shower. Figure 20 shows an example of an online pulse height distribution after pedestal and coherent noise subtraction.

As shown in Figure 21, the transverse profiles of the shower, measured by the two silicon planes, agree well with those of a simulation based on the GEANT program.

The radial position of the incoming particle was estimated, in both silicon planes, by means of a barycenter method applied to the five strips around the shower maximum, without correcting for possible strip-to-strip variations in gain. The distribution of the differences between the radial positions reconstructed by the two silicon planes (Figure 22) provides a measurement of the angular resolution in the reconstruction of the direction of the showering particle. The 0.63 mm FWHM of the distribution translates into an angular resolution of 13 mrad, since the distance between the two silicon planes is 51.7 mm. This resolution is in good agreement with the 10 mrad resolution aimed for in the proposal [4] for the detector.

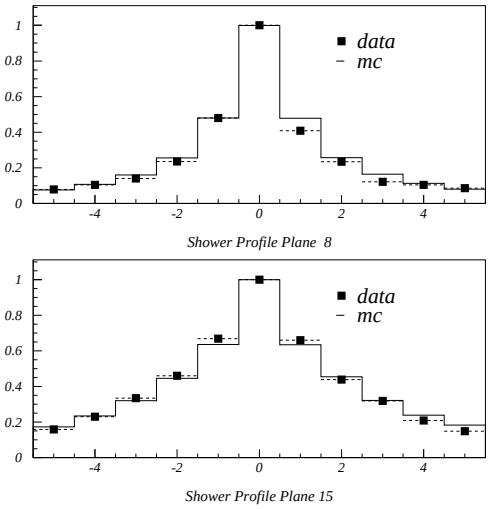

Figure 21. Transverse shower profiles, for 45 GeV electrons, in the first (at 4.0 X_0) and second (at 7.4 X_0) silicon plane. The testbeam data and the results of a GEANT simulation are compared.

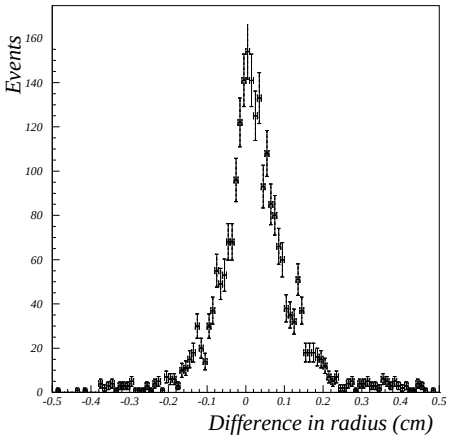

Figure 22. Difference between the radial positions reconstructed in the two silicon planes.

6.3. The veto counters

Two scintillator counters, covering one calorimeter sector, were mounted on a STIC module in a testbeam. They were positioned at approximately the same distance from the calorimeter as in DELPHI and were read out with the same type of photomultipliers and a 10 m long clear fiber cable. The purpose of the test was to measure the response of the counters to minimum ionizing particles (MIPs) and more importantly to determine the loss of photon initiated showers due to shower backsplash from the calorimeter, the so-called "albedo" effect.

The response of the veto counters, measured with 45 GeV electrons, was independent of the position of the impact point and was ~20 photoelectrons per MIP. With a MIP defined by a cut on the pulse height at 3σ above the pedestal, more than 99.7% of the electrons fulfilled the MIP requirement in both counters.

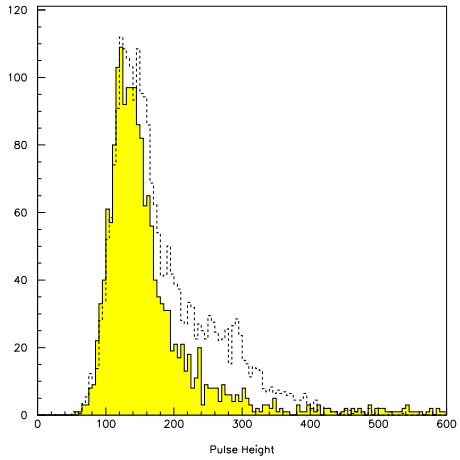

Figure 23. Pulse height distributions for electrons (the dashed histogram) and for pions (the shaded area).

The pulse height distribution for pions was quite different from that of electrons (Figure 23). The distribution for the electrons had a tail at large pulse heights, absent for the pions, and due to the albedo. When the counters were placed at a distance of 2 m in front of the calorimeter, the energy distributions for electrons and for pions were identical.

The most direct way to measure the albedo would be to expose the calorimeter and the veto counters to a photon beam and count the fraction of showers in STIC giving a pulse height in the veto counters consistent with that of a MIP. No photon beam was available, however, and therefore the pulse height from the counters was measured with the electron beam hitting the center of a calorimeter sector adjacent to the one covered by the scintillators or at a distance of one and half sectors away. The albedo was then defined to be the fraction of events identified as MIPs when the electron beam hits STIC but not the veto counters.

The results from a radial scan of two STIC sectors with a 45 GeV electron beam are shown in Figure 24 as a function of the STIC tower ring. The figure shows the albedo for each counter separately and after requiring that both counters give pulse heights consistent with a MIP. In all cases the albedo was independent of the radial position of the impact point. For a single counter the albedo was ~12% when the beam hit the center of the adjacent sector and ~7% when the impact point was one sector further away. When both counters had to satisfy the MIP cut the albedo was reduced to ~5% and $\leq$ 2% respectively.

The energy dependence of the albedo was measured with the beam going into the center of tower ring 5 in the sector next to the scintillators and by varying the energy of the beam. The data showed an increase of the albedo from ~2% at 5 GeV to ~6% at 100 GeV when the presence of a signal in both counters was used to define the albedo.

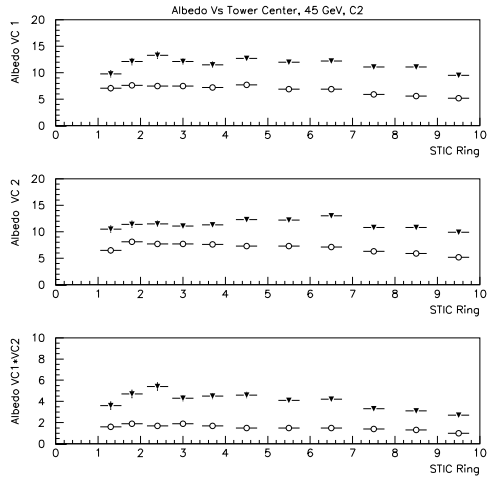

Figure 24. Fraction of events with a pulse height consistent with a MIP when the beam hits a calorimeter sector adjacent to the veto counters (triangles) and when the impact point is one sector further away (circles). The two upper plots show the albedo for each counter separately, and the lower plot is for the coincidence between the two counters.

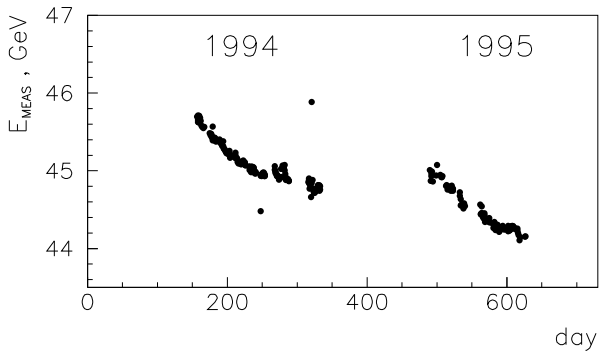

Figure 25. The calorimeter energy response to 45.6 GeV Bhabha electrons versus time.

7. PERFORMANCE AT LEP

7.1. Energy measurement

In order to achieve a good energy resolution, a precise knowledge of the calorimeter characteristics is required. This includes a monitoring of possible changes with time. The time dependence of the energy response of the calorimeter to Bhabha electrons, obtained by using the same set of calibration coefficients for all the data, is shown in Figure 25. A reduction of the measured energy of up to 2% per year has been observed. The origin of this "ageing" effect is not well understood, but radiation damage of the scintillators and/or fibers due to the synchrotron radiation has been ruled out. However, when the fibers were changed in 1996 it was discovered that dust had accumulated on the fibers inside the sampling structure and it is possible that this could cause the observed reduction in light output.

The ageing effect is corrected for by calibrating the

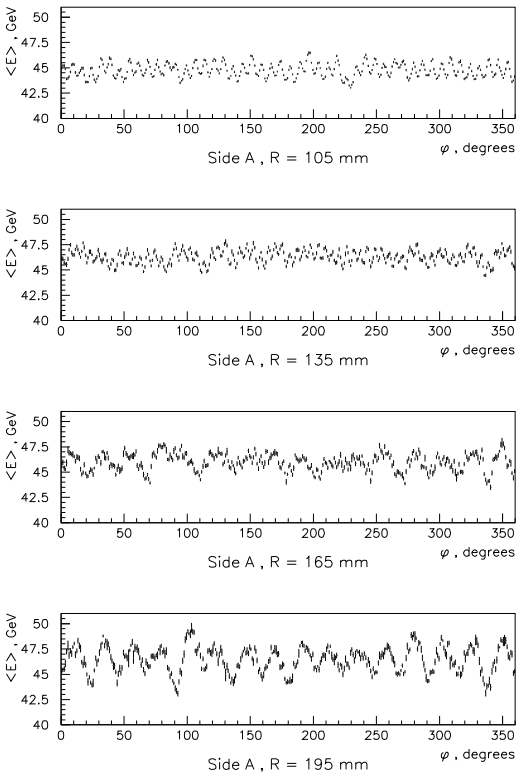

Figure 26. The energy response to 45.6 GeV electrons as a function of the azimuthal angle at four different radii. Kuraray Y7 fibers were use in this measurement.

calorimeter approximately once per month, using a sample of non-radiative Bhabha events, which deposit a known amount of energy in the calorimeter. The calibration coefficients c_j are determined from the raw amplitudes A_{ij} as those minimizing [30] the quantity

$$F = \sum_{i=1}^{N_{events}} (\sum_{j=1}^{N_{towers}} c_j A_{ij} - E_{expected})^2 \quad .$$

The lateral energy leakage, determined from Monte Carlo simulations, is subtracted from the beam energy to give the expected energy $E_{expected}$. The leakage is significant in the inner and the outer parts of the calorimeter, and it has been parametrized as a function of the reconstructed radial position of the shower. The steep radial distribution of Bhabha events, with many more calibration events in the inner rings than in the outer rings, was taken into account by an event-weighting procedure.

The energy response of shashlik-type calorimeters usually depends on the impact point of the incoming particle. Figure 26 shows an azimuthal scan of the energy response using Bhabha electrons and a calorimeter equipped with Kuraray Y7 fibers. In this measurement the impact point was measured by the calorimeter itself. Close to the border between tower rings one and two the fiber structure is clearly visible, and the non-uniformity of the energy response is about ±3%. At higher radii the fiber modulation disappears, due to the

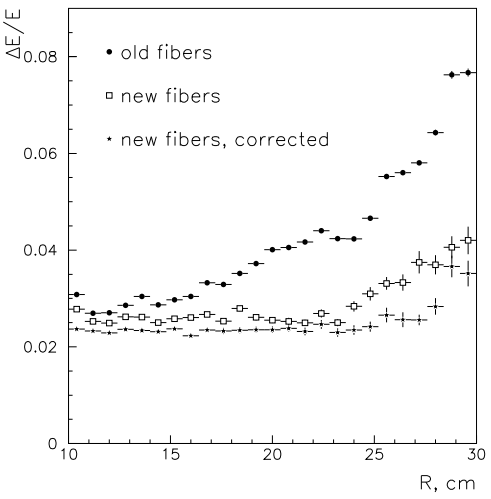

Figure 27. The energy resolution at 45.6 GeV as a function of radius for a calorimeter with the old Y7 and the new Y11 fibers. The resolution with Y11 is shown both with and without the energy-map correction described in the text.

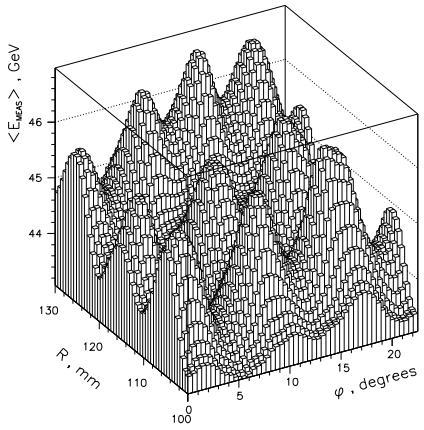

Figure 28. Energy response to 45.6 GeV electrons as a function of the impact point (measured by the calorimeter itself).

poorer azimuthal resolution, and is replaced by a tower modulation causing non-uniformities of ±6% at a radius of 19.5 cm. This modulation is caused by the bending of the fibers at the back of the calorimeter. At high radii the towers are large in the azimuthal direction and the fibers close to the tower sector borders have to be bent more in order to be connected to the phototetrodes.

A measurement of the attenuation length as a function of the fiber bending radius showed that the Y7 fibers begin to crack when the bending radius is smaller than 8 cm. In 1996 therefore, the Kuraray Y7 fibers were replaced with longer Y11 fibers, which are less brittle and less sensitive to bending. The improvement of the resolution due to the fiber change is demonstrated in Figure 27, which shows the energy resolution as a function of radius. At small radii where the non-uniformities are caused mainly by the increased light collection close to the fibers, there is a modest improvement of the resolution. At large radii, however, where the fiber bending is the major cause of non-uniformities, a significant improvement of the energy resolution was observed with the new Y11 fibers.

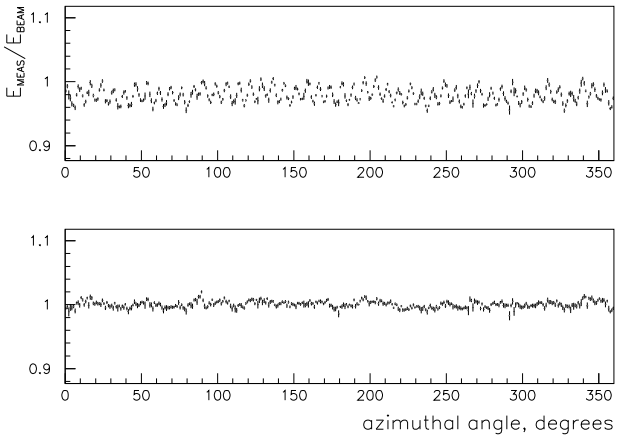

Figure 29. The energy response to 92 GeV electrons as a function of the azimuthal angle, measured with Y11 fibers at a radius of 10.5 cm. Both angles and radii were measured by the calorimeter itself. The upper plot shows the energies before and the lower plot those after energy-map correction.

The non-uniformities are reduced further by mapping the energy response as a function of the impact point. The $R-\phi$ dependence of the energy response of one STIC tower to non-radiative Bhabha events is shown in Figure 28 as a function of the reconstructed position of the shower. The peaks in the distribution correspond to the positions of WLS fibers. Figure 29 shows how the fiber modulations are reduced after applying a correction based on such an energy map. The final energy resolution at small radii after correction is given in Figure 30 as a function of the energy. The resolution predicted by GEANT simulations agrees well with the resolution measured with the new Y11 fibers. The measured resolution was parameterized as

$$\sigma/E(\%) = (0.68 \pm 0.09) \oplus (14.1 \pm 0.4)/\sqrt{E}$$

where the energy E is in GeV. The contribution to the second term from photoelectron statistics was estimated with the LED system to be around 5-6%$/\sqrt{E}$ (see Section 2.4) and the resolution due to sampling fluctuations can thus be estimated to be ~13%$/\sqrt{E}$.

7.2. Position measurement

As mentioned previously, both the radius and the azimuthal angle of the impact point of the shower can be measured on the basis of the sharing of the deposited energy between nearby calorimeter towers. The reconstruction method relies on the testbeam measurements described in Section 6.1. A specially designed platform was used at the testbeam in order to make the beam enter the calorimeter in the same way as at LEP, i.e., following the projective geometry of the calorimeter. However, small discrepancies between the testbeam set-up

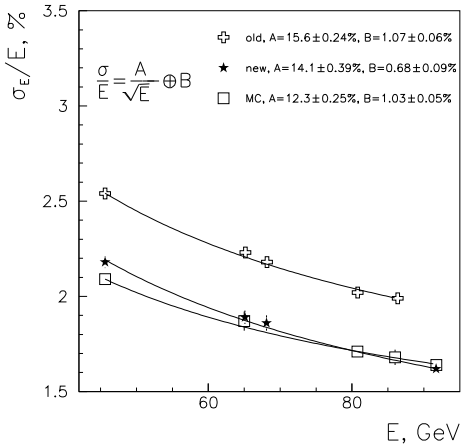

Figure 30. Energy resolution at small radii after energy-map correction with the old Y7 and the new Y11 WLS fibers. The resolution from a GEANT Monte Carlo simulation is also shown.

and the positioning of the calorimeters at LEP together with the strongly varying resolution caused biases in the radial reconstruction. These biases were studied by comparing the measured radial distribution of Bhabha events with what was expected from the Monte Carlo simulation and a correction function was derived [31]. The size of the correction was similar to the radial resolution (0.3-1.0 mm).

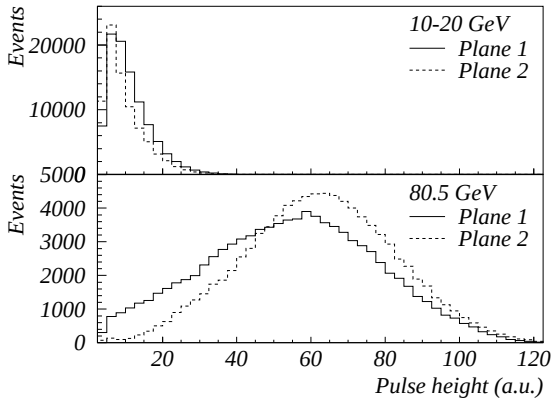

Figure 31. The pulse height distributions of the strips with the maximum signal in the silicon detectors.

The silicon strip detectors can be used to improve the measurement of the radial position and the two-shower separation. In these detectors the strips with the largest signal, after coherent noise subtraction [32], are used as the seed in the shower reconstruction algorithm [33]. The pulse height distributions of the strips with the largest signal are shown in Figure 31 for 80 GeV Bhabha electrons and for electrons with an energy between 10 and 20 GeV.

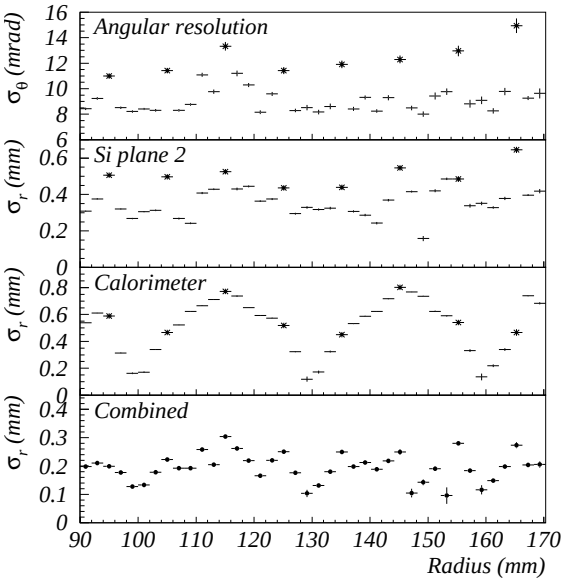

Figure 32. The angular resolution of the two silicon strip planes, the radial resolution of the second silicon strip plane, the radial resolution of the calorimeter and the radial resolution of a weighted average of the radii from the calorimeter and the two silicon planes. Points corresponding to the positions of fiber holes are marked as stars. All measurements were made with 92 GeV electrons.

The radius and the azimuthal angle of a shower in the silicon planes are calculated by taking into account the signals of strips located at most one sector away in azimuth from the strip with the maximum and at most three strips away radially. The radial reconstruction uses the seven radial sums Σ_i of pulse heights over the three sectors. After determining which sum Σ_j is the largest, an estimator based on the logarithm of the fraction $\Sigma_{j-1}/\Sigma_{j+1}$ is used to calculate the radial position. The azimuthal angle is calculated with a two-dimensional barycenter method, where the strips are weighted by pulse height.

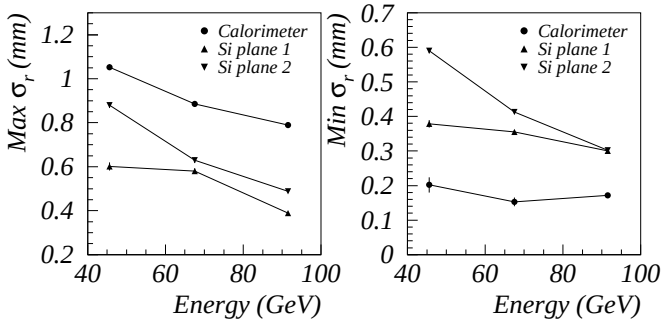

Figure 33. The radial resolution versus energy for the silicon strip planes and the calorimeter. The resolution of the silicon detector at the radii of the fiber holes is given in the leftmost plot together with the resolution of the calorimeter in the center of the towers. The rightmost plot shows the resolution in the regions between the holes in the silicon planes and at the tower borders in the calorimeter.

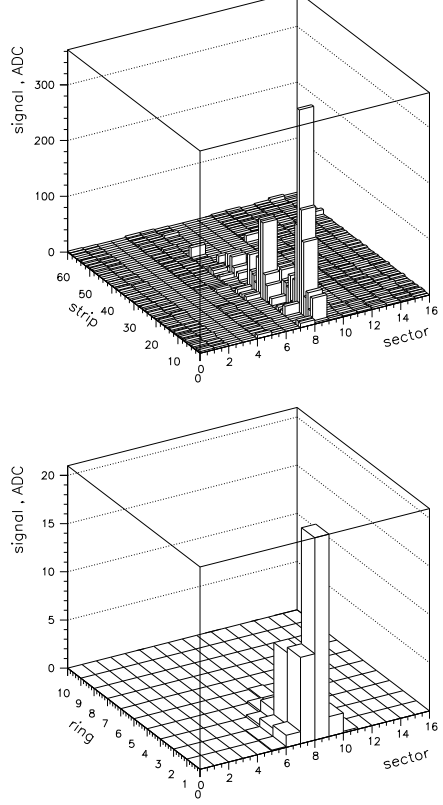

Figure 34. Two close showers are well separated in a silicon plane (top) and not separated in the calorimeter (bottom).

The uppermost plot in Figure 32 shows the angular resolution as a function of radius for 92 GeV electrons at LEP. In this measurement, a large sample of Bhabha electrons was divided into radius bins with a width of 2 mm, and the angular resolution was determined by fitting a Gaussian to the distribution of the differences in reconstructed radius between the two silicon planes for each bin. The resolution plot shows a regular pattern of points, separated by about 1 cm in radius, where the resolution is significantly poorer than elsewhere in the the detectors. These points correspond precisely to the radial locations of the holes that allow the wavelength-shifting fibers to pass through the silicon detectors. The angular resolution at 92 GeV is approximately 9 mrad except in the regions of the holes, where it varies between 11 and 15 mrad. At 45 GeV, the corresponding numbers are 14 mrad and 17-25 mrad.

The three distributions of difference in radius between the two silicon planes and between each of the silicon planes and the calorimeter allowed an approximate calculation of the individual radial resolution of each detector as a function of radius. Figure 32 shows these resolutions for silicon plane 2 and for the calorimeter. While the silicon resolution is poorer in the region of the fiber holes, the calorimeter resolution shows the same behaviour as was observed in the testbeam with minima at the tower borders and maxima at the tower center. A weighted average of the three radius measurements gives a resolution of 100-300 μm.

The resolution of the reconstructed radii in the silicon detectors is energy-dependent and improves with increasing energy. This is shown in Figure 33 which depicts the minimum and the maximum resolution in both the silicon planes and the calorimeter as a function of energy.

In addition to the position measurement, the silicon detectors can be used to improve the two shower separation. An example of this is given in Figure 34. In this radiative Bhabha event ($e^+e^- \rightarrow e^+e^-\gamma$), the two showers from the e^+ and the γ are well separated in the silicon plane, while they are merged to one cluster in the calorimeter.

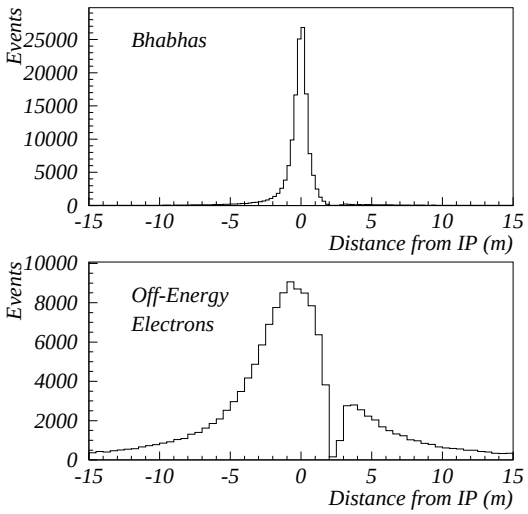

Figure 35. Distribution of reconstructed vertices of Bhabha electrons (top) and of off-energy electrons (bottom).

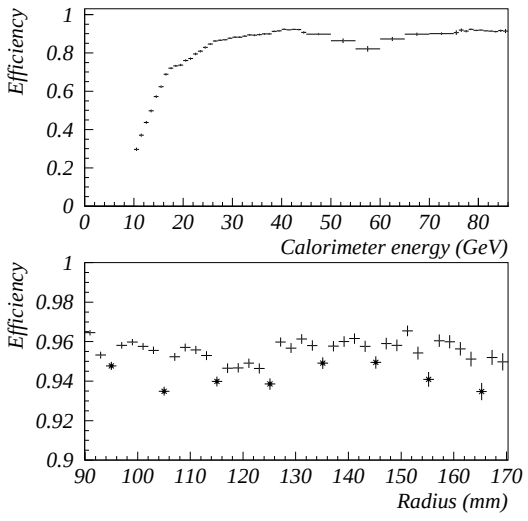

Figure 36. The efficiency of the silicon vertex reconstruction as a function of calorimeter energy (top) and radius (bottom). The points marked with stars indicate the locations of the holes for the wavelength-shifting fibers.

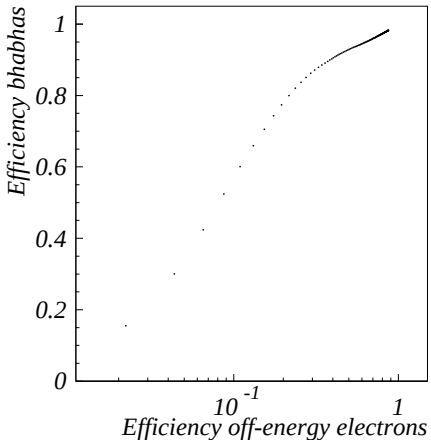

Figure 37. Fraction of Bhabha events surviving a cut on the reconstructed vertex versus fraction of off-energy electrons surviving the same cut. Each point represents an increase by 10 cm of the cut on the vertex, beginning with a cut at ±10 cm near the lower left corner.

7.3. Rejection of off-energy electrons with the silicon strip detectors

Off-energy electrons are created in bremsstrahlung interactions between beam particles and residual gas molecules in the beampipe and may have their origin anywhere in the LEP beamline [34]. They can be rejected by a cut on the vertex reconstructed with the silicon strip detectors [33]. This vertex is calculated by extrapolating the track, formed by the two radial coordinates measured by the silicon, to the beamline. The vertex position is then defined as the distance from the intersection of the track with the beamline to the interaction point. The distributions of reconstructed vertices of a sample of 80 GeV Bhabha electrons and of a sample of off-energy electrons are shown in Figure 35. The vertices of the Bhabha electrons are peaked in a narrow distribution around the interaction point, while the off-energy electrons have a much broader vertex distribution. The "holes" in the distributions of Figure 35, at about 2.5 m from the interaction point, are due to the geometrical acceptance of the silicon detectors which makes it impossible to reconstruct silicon tracks which cross the beamline close to the position of the two silicon planes themselves.

The efficiency of the vertex reconstruction is defined as the fraction of showers detected in both silicon planes. Figure 36 shows this efficiency as a function of energy. It is nearly constant at a level of ∼90% at energies above 25 GeV. However, the efficiency as a function of the radius is not constant since it drops by 1-1.5% at those radii where the holes for the wavelength-shifting fibers are located.

Figure 37 shows the fraction of Bhabha electrons surviving a cut on the reconstructed vertex compared to the fraction of off-energy electrons surviving the same cut. A requirement that all silicon vertices are within ±0.5 m of the interaction point keeps 61% of the Bhabha electrons and rejects 89% of the off-energy electrons. A looser cut at ±1.0 m keeps 80% of the electrons from the interaction point and rejects 79% of the off-energy electrons.

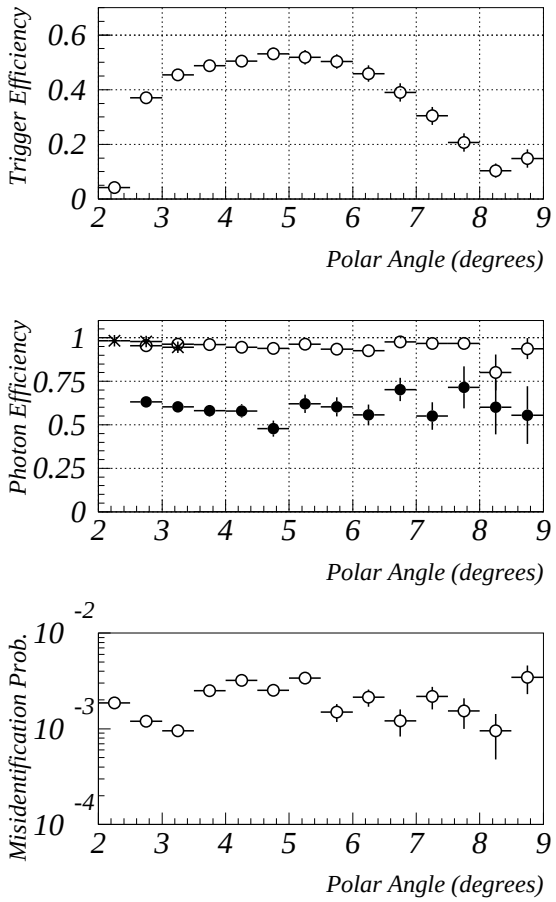

Figure 38. The trigger efficiency for photons (top), the efficiency of the offline photon identification (center) and the probability that an electron will be misidentified as a photon (bottom). In all plots open circles denote a requirement of no hits in at least one scintillator plane, filled circles no hits in either plane and stars the efficiency of the small veto counter.

7.4. Electron-photon separation

The efficiency of the single photon trigger has been studied with a sample of radiative Bhabha scattering events with the photon in STIC, one electron in the beampipe and the other electron in the forward lead glass calorimeter [35]. The selected photons had energies between 60 and 90 GeV. The efficiency of the single photon trigger for this sample is shown in the uppermost plot of Figure 38. The efficiency varies between 54% and 10% depending on the thickness of the material that the photons traverse before reaching the veto counter.

In the offline analysis, additional harder cuts on the veto counter pulse height were made. These had a flat efficiency of 95% (Figure 38 center). The rejection of electrons could be improved further by requiring no signal in either scintillator plane but then 35% of the pho-

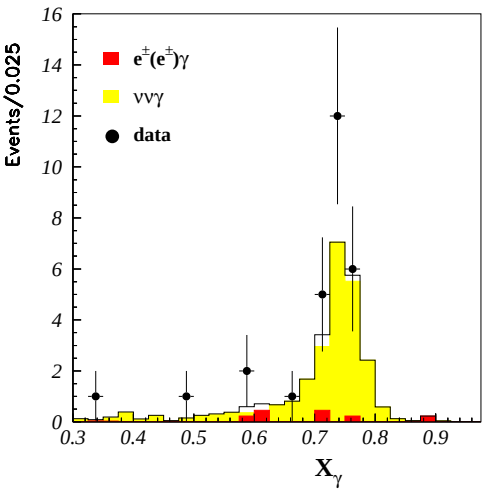

Figure 39. The ratio of the photon energy to the beam energy (X_γ) of single photons in STIC. The dark shaded area is the background from QED processes and the light shaded area is the expected spectrum from $e^+e^- \to \nu\bar{\nu}\gamma$ while the solid line is the sum of both.

tons that survived the trigger requirement and the pulse height cuts were lost (mainly due to albedo effects).

The rejection of electrons was studied with a non-radiative Bhabha sample. The probability that an electron would give a signal in one plane of the veto counter was measured to be 99.8% and the probability that an electron would be wrongly identified as a photon was measured to be $(1-4)\cdot 10^{-3}$ (Figure 38 bottom). Due to the presence of $e^+e^- \to \gamma\gamma$ events in the Bhabha sample, it was not possible to measure directly the rejection by the veto counter when a requirement of no signal in both planes was made. However, from the electron efficiency one can estimate it to be $\sim 4\cdot 10^{-6}$.

Figure 39 shows the energy spectrum in STIC of single photon events at $\sqrt{s}$ =183 GeV [36]. A clear radiative return peak from the process $e^+e^- \to Z^0\ \gamma \to \nu\bar{\nu}\gamma$ is visible.

8. THE LUMINOSITY MEASUREMENT

At LEP the luminosity is measured by counting the number of Bhabha scattering events at low angles:

$$e^+e^- \to e^+e^-(n\gamma) \quad (\theta < 200 \text{ mrad})$$

The Bhabha events are selected by requiring two back-to-back electromagnetic showers at small angles with respect to the beamline and having the same energy as the beams.

A calorimetric event selection is preferred since it reduces the sensitivity of the measurement to the knowledge of the material in front of the luminometer. This selection procedure is also well matched with the theoretical requirements for a precise calculation of the accepted cross section, because it retains both non-radiative and radiative Bhabhas and therefore it reduces the sensitivity to the differential distributions of any emitted photons.

The fiducial region was defined by radial cuts which were asymmetric on the two sides of the experiment (called "the narrow side" and "the wide side" respectively). This choice, common to all the experiments at LEP, minimizes the sensitivity of the measurement to movements of the interaction point and to displacements of the centers of the calorimeters with respect to the beamline [37].

In the following subsection a short summary of the key points in the luminosity determination is given. For more details see [38].

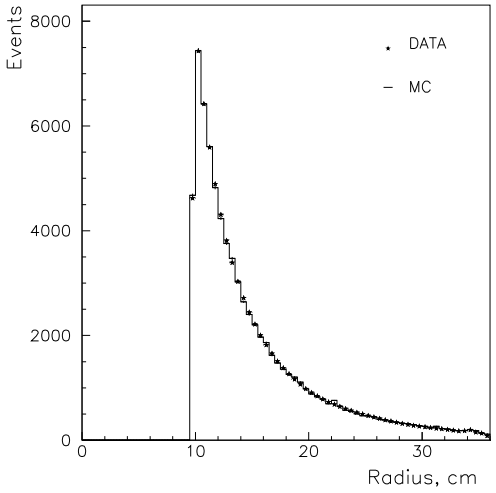

Figure 40. Radial distribution of Bhabha events measured by STIC on the narrow side and from a GEANT Monte Carlo simulation. The sharp cut at R $\simeq$ 96 mm is due to the tungsten ring that defines the acceptance.

8.1. Event selection

The steep angular dependence of the Bhabha cross section is illustrated in Figure 40. Since the differential cross section is proportional to $1/\theta^3$ the most severe requirement for the luminometer is a precise definition of the inner edge of the acceptance on the narrow side. While the other experiments at LEP1 applied a cut on the reconstructed radius of the electromagnetic showers, in DELPHI the first tower ring of the calorimeter was covered on the narrow side with a well machined tungsten ring ("the W nose"), which was 6 cm thick and projective to the interaction point.

As shown in Figure 41, the W nose made it possible to define the inner edge of the acceptance by a simple cut on the energy of the shower, since the electrons which hit the W nose lost most of their energy before reaching the calorimeter.

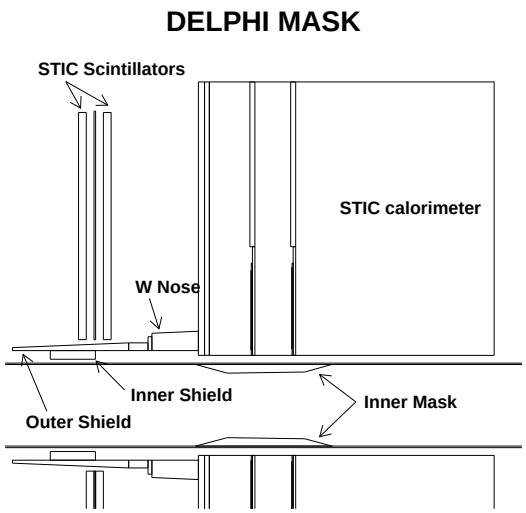

Figure 41. STIC and the tungsten shields at LEP1.

On the side opposite the mask, i.e., on the wide side, cuts were applied to the reconstructed radius of the electromagnetic shower.

The sample of Bhabha events was selected by considering, in both STIC arms, the most energetic cluster. The following selection criteria were applied:

- the energies of both clusters (E_A and E_C) had to be larger than 65% of the beam energy;
- the acoplanarity, i.e., the difference in azimuthal angle between the two clusters, should be $180^o \pm 20^o$;
- the reconstructed radius of the cluster on the wide side (R_A) had to be between 8.2 cm and 28 cm;
- the reconstructed radius of the cluster on the narrow side (R_C) had to be less than 25 cm.

The requirements on energy and acoplanarity rejected background caused by an accidental coincidence between two off-energy electrons. The energy cut also defined the inner edge of the acceptance on the narrow side, while the rest of the acceptance was determined by cuts on the reconstructed radii of the clusters.

8.2. Evaluation of the accepted cross section

The evaluation of the Bhabha cross section accepted in the fiducial volume of STIC was made with Monte Carlo programs in two steps. The events were generated with the BHLUMI 4.03 program [39] and they were then tracked inside the calorimeter by the GEANT program described previously (see Section 6.1).

The total theoretical uncertainty in the calculation of the accepted cross section amounted to $1.1 \cdot 10^{-3}$. It was mainly related to the truncation of the QED perturbative series, and to the technical precision in the Monte Carlo implementation.

The contribution of $e^+e^- \to \gamma\gamma(\gamma)$ events, which in a calorimetric measurement are indistinguishable from Bhabha scattering events, was evaluated with another Monte Carlo program [40]. The contribution of this process was found to be $\sigma_{\gamma\gamma} = 28$ pb, corresponding to $5 \cdot 10^{-4}$ of the visible Bhabha cross section.

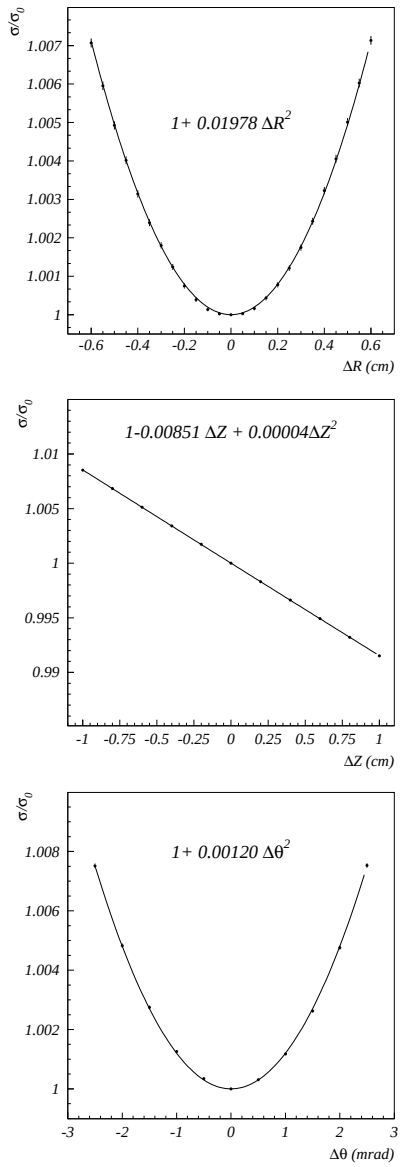

Figure 42. Dependence of the accepted cross section on the transverse position of the IP (top), on its longitudinal position (center) and on tilts of the beam (bottom).

8.3. Effect due to IP displacements

A displacement of the interaction point (IP) with respect to the center of the STIC system changes the cross section accepted inside the detector. This was the largest source of systematic uncertainty in the luminosity measurement.

If D is the distance from the front face of the calorimeter to the interaction point, the inner edge of the acceptance becomes $R'_{min} = R_{min}(1 \pm z_{IP}/D)$ for a movement z_{IP} in the longitudinal direction and

$$R'_{min} = \sqrt{(R_{min}\cos\phi - r_{IP})^2 + (R_{min}\sin\phi)^2}$$

for a movement r_{IP} in the transverse plane along the x direction.

The full 2π coverage of the detector in azimuth cancels out the first order dependence of the visible cross section on a movement r_{IP} in the transverse plane, provided that r_{IP} is smaller than half the difference between the R_{min} cuts on the narrow and the wide side. In this case

$$\sigma(r_{IP}) = \sigma_0 \left(1 + 2\left(\frac{r_{IP}}{R_{min}}\right)^2\right) \qquad (2)$$

where σ_0 is the accepted cross section without a displacement of the IP.

The W nose eliminates the possibility of alternating the wide and the narrow side for each event. Therefore, in the case of a longitudinal displacements (z_{IP}), the first order dependence of the visible cross section does not cancel out:

$$\sigma(z_{IP}) = \sigma_0 \left(1 \mp 2\frac{z_{IP}}{D} + \left(\frac{z_{IP}}{D}\right)^2\right) \approx \sigma_0 \left(1 \mp 2\frac{z_{IP}}{D}\right) . \qquad (3)$$

The above relations are obtained with the assumption of a point-like luminous region and non-radiative Bhabha events. A more precise study was made with Monte Carlo simulations. Figure 42 shows that the result of the simulation of a transverse or a longitudinal displacement follows what is expected from (2) and (3). Only the coefficients in the formulae are slightly different from what is obtained with the Monte Carlo program.

Tilts of the beamline with respect to the calorimeter centerline was also studied with the simulation. As in the case of transverse displacements, it had a dependence which was quadratic in the tilt angle.

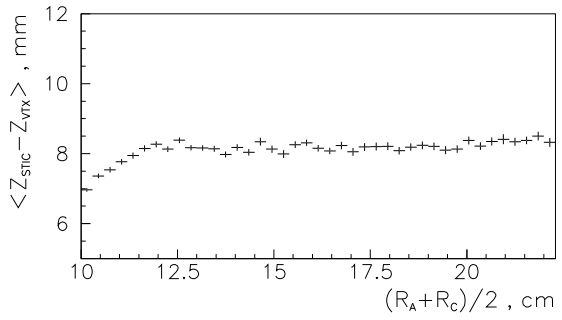

Figure 43. The difference between the positions along the beamline of the IP measured by STIC and by the microvertex detectors versus the average radius measured by the two calorimeters.

8.4. Measurement of the IP

The possibility of a determination of the position of the interaction point by STIC was important in order to reduce the systematic error in the luminosity measurement [31].

The position of the IP was measured by STIC, on a fill by fill basis, with a three dimensional method, by minimizing the quantity $\sum_k d_k^2/\sigma_k^2$, where d_k is the distance from the IP to the straight line connecting the back-to-back showers of the Bhabha event, corrected for the small effect of the magnetic field, while σ_k is the related error.

The statistical accuracy in the reconstruction of z_{IP} using Bhabha events was found to be satisfactory, and the comparison of the IP coordinates measured by STIC and by the DELPHI microvertex detector gave:

$$\begin{aligned} \sigma(x_{IP}^{STIC} - x_{IP}^{MVTX}) &= 22\ \mu m \\ \sigma(y_{IP}^{STIC} - y_{IP}^{MVTX}) &= 61\ \mu m \\ \sigma(z_{IP}^{STIC} - z_{IP}^{MVTX}) &= 280\ \mu m \end{aligned}$$

As discussed above, the largest sensitivity of the accepted cross section to the IP position turned out to be in the longitudinal direction. A variation of 1 mm in z_{IP} produced a 0.9‰ change in the measured luminosity. Since z_{IP} was calculated from radial measurements made by STIC, an accurate control of systematic uncertainties in the radial reconstruction over the full STIC surface was needed. In order to check this, z_{IP} was calculated in narrow intervals in the variable $\bar{R} = (R_A + R_C)/2$ which is the average of the measured radii of the two showers in the Bhabha event. Figure 43 shows the dependence of $z_{IP}^{STIC} - z_{IP}^{MVTX}$ on $\bar{R}$. For the region $\bar{R} > 12$ cm any bias is less than $\pm$ 0.3 mm, corresponding to a systematic uncertainty of $3 \cdot 10^{-4}$ in the luminosity determination. After taking also other biasing effects of the radial reconstruction into account, a total error of $4 \cdot 10^{-4}$ was obtained. In addition, the radial mechanical positioning of the STIC towers was estimated to contribute another $3 \cdot 10^{-4}$ to the luminosity error.

Another source of systematic errors is the position of the two STIC calorimeters with respect to each other. The distance between the two calorimeters was measured to be

$$d_{STIC} = 4400.5 \pm 0.6 \text{ mm}$$

and the 0.6 mm error translates into a systematic uncertainty in the luminosity of $3 \cdot 10^{-4}$. Another uncertainty of the same size stems from temperature variations in the LEP tunnel, which could alter the distance between the two calorimeters. A summary of all contributions to the systematic error from the determination of the interaction point is given in Table 2.

8.5. Evaluation of the systematic errors

The major question in the luminosity analysis is how well the systematic errors in the analysis can be controlled. The estimated systematic errors from all known sources are given in Table 3. The largest source of uncertainty, i.e., the IP position, has already been discussed. Other contributions will be described briefly below.

8.5.1. Energy and acoplanarity cuts

The purpose of the energy and acoplanarity cuts was to reject off-energy electron background. Figures 44 and

Source of systematics	Contribution to $\Delta\mathcal{L}/\mathcal{L}$
distance STIC modules	$= 3 \cdot 10^{-4}$
temperature effects	$= 2 \cdot 10^{-4}$
δz_{IP} (mechanics)	$= 3 \cdot 10^{-4}$
δz_{IP} (reconstruction)	$= 4 \cdot 10^{-4}$
IP position	$= 6 \cdot 10^{-4}$

Table 2. Summary of the contributions to the systematic error due to the uncertainties of the positioning of the calorimeters with respect to the IP.

Source of systematics	Contribution to $\Delta\mathcal{L}/\mathcal{L}$
IP position	$= 6 \cdot 10^{-4}$
Mask technique	$= 4 \cdot 10^{-4}$
MC statistics	$= 3 \cdot 10^{-4}$
R_A^{min} cut	$= 2 \cdot 10^{-4}$
R_A^{max} and R_C^{max} cut	$= 2 \cdot 10^{-4}$
Acoplanarity cut	$= 1 \cdot 10^{-4}$
Energy cut	$= 3 \cdot 10^{-4}$
Background subtraction	$= 2 \cdot 10^{-4}$
Trigger inefficiency	$= 2 \cdot 10^{-4}$
Total experimental	$= 0.9 \cdot 10^{-3}$
Total theoretical	$= 1.1 \cdot 10^{-3}$

Table 3. Summary of the contributions to the systematic error on the luminosity.

45 show the variation of luminosity when the cuts are changed around their chosen values.

A variation of the energy cut between $0.6 \cdot E_{beam}$ and $0.7 \cdot E_{beam}$ translated into a variation of the luminosity of $2 \cdot 10^{-4}$. The luminosity was even less sensitive to variations of the acoplanarity cut, and the contribution to the error was estimated to be less than $1 \cdot 10^{-4}$.

8.5.2. Geometry of the mask

Due to the angular dependence of the Bhabha cross section, a bias δR at the inner edge R_C^{min} of the acceptance on the narrow side translates into a systematic error

$$\frac{\delta L}{L} \simeq \frac{2\delta R_C^{min}}{R_C^{min}} \quad .$$

The goal of a $<1‰$ accuracy in the luminosity determination with $R_C^{min} = 96$ mm therefore leads to a requirement of $\delta R \leq 50$ μm.

The testbeam study of the tungsten mask showed that R_C^{min} could be measured with a resolution better than 25 μm. Consequently, the statistical precision $\delta R_{stat}^{min} \simeq 25\ \mu m/\sqrt{N_{Bhabhas}}$ could, due to the large Bhabha cross section, be neglected.

In order to ensure that mechanical biases did not influence the determination of R_C^{min}, the mask geometry was measured in two different ways:

- a first measurement was made (with an accuracy of 3 μm) of the absolute radius in 18 azimuthal positions;
- a second measurement was made (with an accuracy of 0.1 μm) of deviations from circularity in 24 azimuthal positions.

A conservative estimation of possible biases gave $\delta R_{syst}^{min} \simeq 20$ μm, which translates into an error of $4 \cdot 10^{-4}$ in the luminosity determination.

8.5.3. Radial cuts

The radial cut at the inner border on the wide side ($R_A^{min} = 8.2$ cm) cuts off the radiative tail of the Bhabha scattering distribution and it was evaluated to contribute $2 \cdot 10^{-4}$ to the systematic error. Possible biases in the radial reconstruction of up to $\sim$150 μm at the outer border ($R_C^{max} = 25$ cm and $R_A^{max} = 28$ cm) gave a contribution of $2 \cdot 10^{-4}$ to the systematic uncertainty.

In addition, the mechanical accuracy of the tower positioning in the calorimeter has to be taken into account. This was measured during assembly and found to be better than 50 μm in all layers (see Section 2.1). Assuming that the effective number of samplings contributing to the measurement of the spatial position of each shower is about 20, this translates into mechanical biases of about 10 μm in the position determination. This is negligible compared with the biases coming from the reconstruction method itself.

8.5.4. Energy of the beam

The uncertainty of the measured beam energy enters into the luminosity measurement since the accepted cross section changes with energy due to two different effects:

- the QED part of the cross section has a dependence $\sigma(E_{beam}) \propto 1/E_{beam}^2$;
- the γZ interference strongly depends on the energy (about 7‰ per GeV).

Close to the Z^0 peak a good approximation of the uncertainty in the luminosity is given by the relation

$$\frac{\delta L}{L} \simeq \frac{3\delta E_{cms}}{E_{cms}} \quad .$$

Given that the uncertainty in the absolute energy of the LEP beam is at the level of 1 MeV, the contribution to the systematic uncertainty is negligible.

8.6. Luminosity at LEP2

During data taking at energies above the Z^0 peak most physics channels of interest are statistically limited and there is no need for a very precise knowledge of the luminosity. The W nose used in the luminosity determination was therefore removed before the 1996 LEP run at $\sqrt{s} = 161$ GeV, in order to increase the forward electromagnetic coverage of DELPHI.

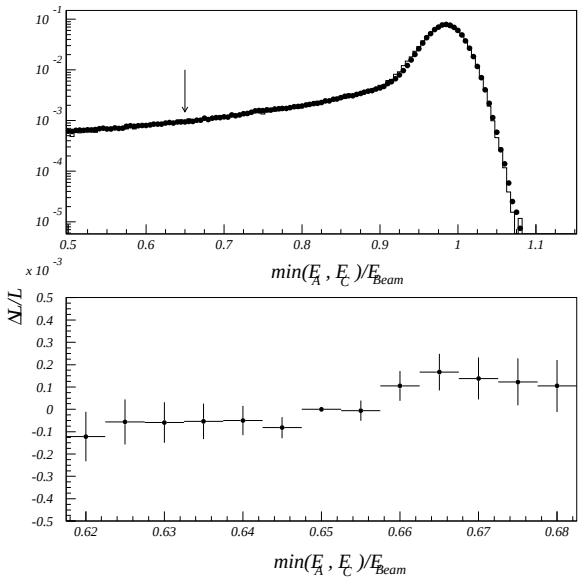

Figure 44. Comparison between data and simulation of the distribution of the energy of the lowest energy shower in Bhabha events (top). The solid line is the Monte Carlo data. The arrow indicates the cut used in the analysis. Variation of the measured luminosity versus the energy cut (bottom).

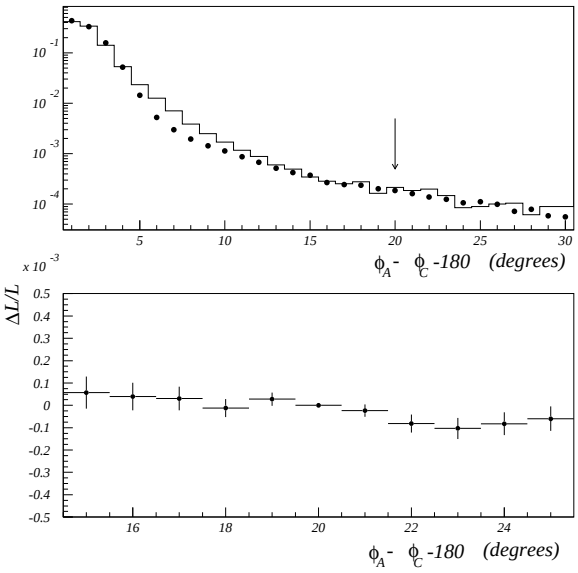

Figure 45. Comparison of the acoplanarity distribution between data and simulation (top). The solid line is the Monte Carlo data. The arrow indicates the cut used in the analysis. Variation of the measured luminosity versus the acoplanarity cut (bottom).

The luminosity analysis was the same as during Z^0 running except that the inner acceptance on the narrow side was defined by a cut on the reconstructed radius ($R > 10$ cm). After the removal of the nose, the two sides of the detector are identical, and it is possible to alternate at each event the narrow and the wide side. This reduces the sensitivity of the measurement to the position of the interaction point.

The overall systematic uncertainty is, however, completely dominated by possible biases in the reconstruction of the radius. During the high precision Z^0 running in 1994, the systematic error in the Monte Carlo due to the uncertainty in the Moliere radius caused an error of $\sim$30 μm in the reconstruction of the radius at a tower border. After comparing the luminosity calculated with the tungsten nose and by a radius cut ($R > 13$ cm) an error of $\delta R_{sys}^{min} \simeq 130$ μm was derived for the method without the nose. This corresponds to a total uncertainty in the luminosity measurement of 2.7‰ .

9. CONCLUSIONS

The STIC calorimeter has been operating as the DELPHI luminosity monitor since 1994 and has met the design criteria by providing a luminosity measurement with a systematic error of 0.9‰ at LEP1.

STIC is a completely hermetic detector which extends the calorimetric coverage of DELPHI both at low angle, thus improving the statistical accuracy of the luminosity measurement by a factor of two and at large angle, thus closing a gap which existed between the old luminometer and the forward electromagnetic calorimeter.

The calorimeter together with the silicon strip detector can measure the radial position of a shower with a resolution of 100-300 μm and the shower direction can be measured with an angular resolution of 14 mrad at 45 GeV and 9 mrad at 92 GeV.

The addition of the scintillator veto system allows DELPHI to measure the invisible Z^0 width using the single photon trigger and it provides an effective e-γ separation that can be used to eliminate possible backgrounds in searches for new particles.

ACKNOWLEDGEMENTS

We would like to thank the technical staff of our home institutes for their excellent work. In particular, we would like to thank M. Boldini, L. Maselli and F. Zuffa of the INFN section of Bologna, J. Pinhao, F. Ribeiro and J. Patriarca of LIP and IST, T. Nilsson of the University of Lund and P. Korobchuk, A. Zhidkikh, V. Brezhnev and L. Timshina of IHEP Serpukov. The assistance of M. Rebut and B. Buisson (CERN, EP division) was extremely valuable in the construction of the veto counters. The support of C. Brand and of the Experimental Assembly section of the Engineering and Construction group of the CERN EP division is also sincerely appreciated. We gratefully acknowledge the help we received from A. Braem (CERN, EP-TA1 section) and from C. Millerin (CERN, EP-PES section) during the fanin production. We also gladly acknowledge the support with the Kapton cable production from A. Gandi and his team at the printed circuit workshop at CERN. We would like to thank O. Runolfsson for letting us use the OPAL microvertex workshop and for his assistance during the MX4 bonding. The help from D. Regin,

T. Taylor and R. Veness of the CERN SL division was essential during the detector installation at LEP. The assistance of the staff of the CILEA computing center in Milano during the Monte Carlo production is gratefully acknowledged.

REFERENCES

1. P. Aarnio et al., NIM **A303** (1991) 233.
2. P. Abreu et al., NIM **A378** (1996) 57.
3. P. Abreu et al., Nucl. Phys. **B367** (1991) 511.
4. The DELPHI Collaboration, "*Proposal for the replacement of the Small Angle Calorimeter of DELPHI*", CERN-LEPC/92-6/P2-Add1.
5. S.J. Alvsvaag et al., Proceedings of *The 5th International Conference on Calorimetry in High Energy Physics*, BNL, USA, September 1994, Ed. by H.A. Gordon and D.Rueger, World Scientific 1995; S.J. Alvsvaag et al., Proceedings of *The Beijing Calorimetry Symposium*, Beijing, China, October 1994, Ed. by H.S. Chen, IHEP, Beijing, 1995.
6. G.S Atoyan et al., NIM **A320** (1992) 144.
7. H. Fessler et al., NIM **A240** (1985) 284; B. Loehr et al., NIM **A254** (1987) 26.
8. M. Bonesini et al., NIM **A387** (1997) 60; M. Bonesini et al.,"*Study of Hamamatsu R2149 phototetrodes in magnetic field*", DELPHI 96-175 CAL 133.
9. Yu. Gouz et al., "*LED monitoring system for the STIC calorimeter*", preprint IHEP 95-108, Protvino 1995; also available as DELPHI 95-56 CAL 126.
10. J. Janoth et al., NIM **A350** (1994) 221.
11. S.J. Alvsvaag et al., IEEE Trans. Nucl. Sci. **42** (4), 478 (1995).
12. I. Lippi et al., NIM **A286**, (1990) 243.
13. S.J. Alvsvaag,"*The SAT local trigger supervisor*", Scientific/Technical report no. 1991-27, Univ. of Bergen, Norway.
14. S.J. Alvsvaag et al.,"*SVED The STIC veto discriminator*", Scientific/Technical report no. 1996-11, Univ. of Bergen, Norway.
15. S.J. Alvsvaag et al.,"*VDB The STIC veto decision box*", Scientific/Technical report no. 1996-06, Univ. of Bergen, Norway.
16. T. Camporesi et al., preprint CERN-LEPC 94-13; T. Camporesi et al., preprint CERN LEPC 94-16.
17. S.J. Alvsvaag et al., IEEE Trans. Nucl. Sci. **42** (4), 469 (1995); S.J. Alvsvaag et al., NIM **A360** (1995) 219.
18. G. Della Ricca, Diploma Thesis, University of Trieste, 1993; G. Della Ricca and M. Prest, "*Simulation of the DELPHI STIC silicon shower maximum detector*", preprint INFN/AE-96/04; also available as DELPHI 96-7 CAL 131.
19. S.J. Alvsvaag et al., Nucl. Phys. B (Proc. Suppl.) **44** (1995) 74; V. Cassio, Diploma Thesis, University of Torino, 1993.
20. M. Laakso et al., NIM **A326** (1993) 214.
21. J.T. Walker et al., NIM **A226** (1984) 200; P.P. Allport et al., NIM **A273** (1988) 630; J. Santon and N. Kurtz,"*An introduction to the MX Chip*", preprint RAL-89-028.
22. M. Burns et al., NIM **A277** (1989) 154.
23. A. Benvenuti et al., IEEE Trans. Nucl. Sci **40**, (1993) 537.
24. CERN Program Library Long Writeup W5013.
25. M. Bonesini et al., "*Simulation of the DELPHI STIC calorimeter*", DELPHI 93-118 CAL 106.
26. M. Espirito-Santo et al., "*Fast simulation of an electromagnetic calorimeter: a two stage approach*", DELPHI 97-42 CAL 136.
27. M. Espirito-Santo et al., "*Experimental tests on scintillator tile light collection efficiency*", DELPHI 97-03 CAL 134.
28. M. Paganoni et al., "*Energy and position reconstruction in the DELPHI Small Angle Tile Calorimeter*", DELPHI 97-07 PHYS 666.
29. A.G. Frodesen et al., "*Analysis of data from the STIC prototype test*", DELPHI 93-114 CAL 104.
30. J. Myrheim et al, NIM **A327** (1993) 539.
31. S.J. Alvsvaag et al., IEEE Trans. Nucl. Sci. **43** (3), 1496 (1996).
32. E. Falk et al., "*Algorithms for reduction of coherent noise in the silicon shower maximum detector of STIC*", preprint INFN/TC-97/33; also available as DELPHI 97-60 CAL 137.
33. E. Falk et al., "*Performance of the STIC Silicon Detectors at LEP2*", DELPHI 98-43 CAL 140.
34. E. Falk et al., "*Simulation of Off-Energy electron background in DELPHI*", preprint CERN SL/97-04(EA); also available as DELPHI 97-12 LEDI 8.
35. P. Ferrari and V. Hedberg, "*Photon and electron identification in the very forward region of DELPHI*", DELPHI 98-49 CAL 141.
36. P. Ferrari et al.,"*Analysis of the single photon channel at LEP2*", DELPHI 98-55 PHYS 780; E. Falk et al.,"*Photon analysis with STIC*", DELPHI 98-147 PHYS 791.
37. G. Barbiellini et al., Atti Accad. Naz. Lincei **44** (1968) 233; J.F. Crawford et al., NIM **127** (1975) 173.
38. M. Bigi, PhD Thesis, University of Torino, 1996; T .Camporesi et al., "*Luminosity measurement in 1994 with the STIC detector*", DELPHI 97-08 PHYS 667.
39. S. Jadach et al., Phys. Lett. **B353** (1995) 362; S. Jadach et al., Phys. Lett. **B353** (1995) 349.
40. F.A. Berends and R. Kleiss, Nucl. Phys. **B186** (1981) 22.

Article II

Analysis of the single photon channel at LEP 2

ICHEP'98 #206
Submitted to Pa 10
Pl 12

DELPHI 98-76 CONF 144
22 June, 1998

Analysis of the single photon channel at LEP 2

Preliminary

DELPHI Collaboration

P. Ferrari [1], **C. Matteuzzi** [1], **E. Falk** [2], **V. Hedberg** [2], **A. Firestone** [3], **P. Checchia** [4], **F. Mazzucato** [4]

Abstract

A study has been made of the production of single photons in the reaction $e^+e^- \to \gamma$ + *invisible particles* at $\sqrt{s} = 183$ GeV. The analysis uses data which correspond to an integrated luminosity of about 50 pb^{-1}, collected with the DELPHI detector. The number of light neutrino families is measured. The absence of an excess of events beyond that expected from Standard Model processes is used to set limits on new physics. The cross sections and masses of supersymmetric particles like neutralinos and gravitinos, for specific model parameters, are investigated. A search for a substructure as described by composite models is carried out.

Paper submitted to the ICHEP'98 Conference
Vancouver, July 22-29

[1] Sezione INFN, Milano, Italy.
[2] Lund University, Lund, Sweden.
[3] Iowa State University, Ames, USA.
[4] Sezione INFN and University of Padova, Italy.

1 Introduction

The process

$$e^+e^- \rightarrow \gamma + \text{invisible particles} \tag{1}$$

receives a contribution within the Standard Model from the radiative production of neutrino-antineutrino pairs through the radiative return to the Z^0 and the t-channel W exchange, with the photon radiated from the beam electron or the exchanged W. Possible contributions to this final state could come from a new generation of neutrinos, from the radiative production of some other neutral weakly interacting particle or from a new particle decaying into a photon. Theories of supersymmetry (SUSY) predict the existence of particles, such as the neutralino, which would give origin to a final state with missing energy and a photon if the lightest neutralino decays into $\tilde{G}\gamma$ with an essentially massless $\tilde{G}$ ($m_{\tilde{G}} < 1$ eV/c^2). Several results have been published on this topic [1] [2].

In the study presented here, the *single* γ + *missing energy* final state at LEPII is used to explore the existence of possible new particles. After the description of the main detectors used in the analysis and the selection criteria of the data samples (Sections 2, 3 and 4), a measurement of the number of neutrino families is made. Limits on physics beyond the Standard Model are presented in the sector on compositeness (preons) [3] and supersymmetric particles [4].

2 The DELPHI detector

The general criteria for the selection of events are based mainly on the electromagnetic calorimeters and the tracking system of the DELPHI experiment [5]. All three major electromagnetic calorimeters in DELPHI, the High density Projection Chamber (HPC), the Forward ElectroMagnetic Calorimeter (FEMC) and the Small angle TIle Calorimeter (STIC), have been used in the single photon reconstruction. The angular coverage of these detectors and the energy resolution are given in Table 1.

	Angular coverage	Energy resolution
STIC:	$2^\circ < \theta < 10^\circ$ and $170^\circ < \theta < 178^\circ$	$\sigma/E = 0.0152 \oplus (0.135/\sqrt{E})$
FEMC:	$10^\circ < \theta < 37^\circ$ and $143^\circ < \theta < 170^\circ$	$\sigma/E = 0.03 \oplus (0.12/\sqrt{E}) \oplus (0.11/E)$
HPC:	$40^\circ < \theta < 140^\circ$	$\sigma/E = 0.043 \oplus (0.32/\sqrt{E})$

Table 1: Polar angle coverage and energy resolution of the electromagnetic calorimeters in DELPHI (E is in GeV).

The barrel region is covered by the HPC, which is a gas sampling calorimeter consisting of 144 modules arranged in 6 rings inside the magnetic field. Each module contains 41 layers of a lead converter with a total thickness of 18 $X_0/sin(\theta)$. In between the converter layers are slots with an argon/methane gas mixture and when ionization is produced in the gas, the detector can measure the position and energy of the shower in the same way

as a time projection chamber. A shower is sampled nine times longitudinally [5].

FEMC is made up of an array of 4532 lead glass blocks in each endcap. The 5 m diameter lead glass walls have a depth of 20 X_0. The blocks are truncated pyramids that give a readout granularity of about 1° both in ϕ and in θ. The Cherenkov light produced in the lead glass by the charged particles from a shower is read out by phototriods. The energy resolution of the calorimeter is degraded by the material in front of it, which causes photon conversions and even preshowers. This degradation is particularly severe at low and high polar angles.

The very forward luminosity monitor STIC consists of two lead-scintillator calorimeters of shashlik type, read out by wavelength-shifting fibers. They are located on either side of the interaction point at a distance of 2.2 m and have a thickness of about 27 X_0. The tower structure is divided into ten rings and sixteen sectors for a total of 160 towers in each calorimeter. An electron veto detector, consisting of two layers of scintillator mounted on the front of each calorimeter together with a smaller ringshaped scintillator mounted directly on the beampipe, is used in the trigger to provide $e - \gamma$ separation.

In addition to the electromagnetic calorimeters, the DELPHI tracking system, which is made up of several independent detectors, is used to reject events in which charged particles are produced. The main tracking devices are the Time Projection Chamber (TPC) and the microVertex silicon Detector (VD) and its extension into the forward region, the so-called Very Forward Tracker (VFT). The two latter detectors are also used for electron/photon separation by vetoing photon candidates which can be associated with hits in these detectors.

Finally, the hadron calorimeter (HCAL) is used to reject cosmics and to provide photon/hadron separation.

2.1 The single photon trigger

Three different triggers are used in DELPHI to select the single photon events. It is essential for the analysis that the performance and the efficiency of these triggers are well understood.

The HPC trigger for purely neutral final states uses a plane of scintillators inserted into one of the HPC sampling gaps at a depth of around 4.5 X_0. A second level trigger decision is produced from the signals of analog electronics and is based on a coincidence pattern inside the HPC module. The trigger efficiency [6] has been measured with radiative events ($\mu\mu\gamma$ and $ee\gamma$) and Compton events. It is strongly dependent on the photon energy up to ~12 GeV (Figure 1) and it varies from 40% to 80% in the interval 4 to 30 GeV and is $(89.0 \pm 2.5)\%$ for $E_\gamma > 40$ GeV . This efficiency does not include losses due to the cracks between modules of the HPC detector.

The FEMC trigger requires an energy deposition of at least 2.5 GeV. The efficiency increases with energy and is ~97% at 18 GeV. Correlated noise in several adjacent channels

causes fake triggers, but these can be rejected offline with high efficiency by algorithms that take into account the lead glass shower pattern.

The STIC trigger requires an energy deposition of at least 15 GeV and reaches full efficiency at 30 GeV. An online angular cut to reject off-energy background restricts the acceptance to $2.6° < \theta < 9.0°$, where θ is the angle with respect to the beamline. Since the scintillator layers in front of the calorimeters are used in anti-coincidence with the calorimeter signal, electrons are rejected by the trigger. This means that photons that convert are not included in the STIC single photon sample. The trigger efficiency has been measured with a sample of photons from $e^+e^-\gamma$ events with one of the electrons seen in FEMC and the microvertex detectors and the other electron lost in the beampipe. The efficiency varies between 54% and 21% if the angular region is limited to $3.8° < \theta < 8.0°$ (Figure 1).

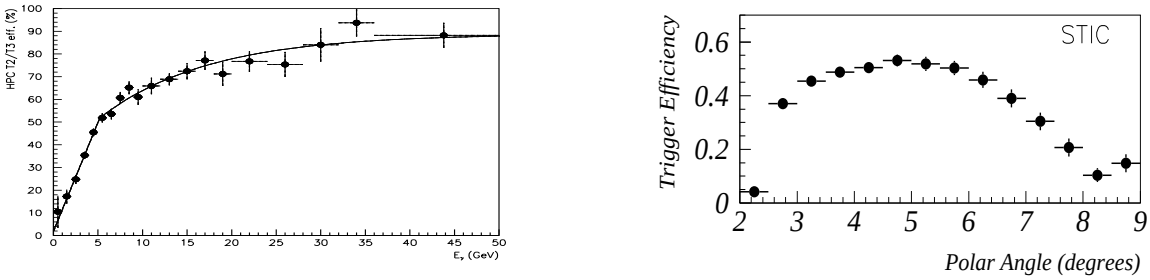

Figure 1: *LEFT* : HPC single photon trigger efficiency as a function of the photon energy. The losses due to the HPC cracks are not included. *RIGHT* : The STIC single photon trigger efficiency as a function of the polar angle.

3 Event and photon selection

The basic selection criteria of events are the same for the three electromagnetic calorimeters: no charged tracks detected and no electromagnetic showers apart from the shower from the single photon candidate. However, the details of the selection vary for the different electromagnetic calorimeters.

3.1 Photons in the HPC acceptance

Events with a photon in the HPC were selected if there were no charged particles coming from the interaction point detected in the the Time Projection Chamber. The presence of tracks in the forward region of the detector and of tracks in the TPC not coming from the interaction point was used to veto events due to background from beam gas and cosmic rays. In order to reject the background from radiative Bhabha events and Compton events, no energy deposit larger than 1 GeV in the STIC was allowed. It was also required that no other electromagnetic showers were present in the forward electromagnetic calorimeters and a second shower in the HPC was accepted only if it was within 20° of the first one. The hadronic calorimeter was used to reject cosmic events. The

event was rejected if there were two hadronic showers recorded in the HCAL. If only one shower was present, the event was retained if the HCAL shower was consistent with being caused by punch-through of the electromagnetic shower. A constraint on the γ direction was imposed, requiring that the line of flight and the shower direction measured in the calorimeter coincided within 15°.

Only showers having an energy above 6 GeV and a polar angle in the interval $45° < \theta < 135°$ were considered. They were required to satisfy some conditions meant to define good electromagnetic shape. A shower therefore had to start in the first three rows (that is, within the first 2.0 X_0) and have at least three rows filled and no more than one empty row until the end of the shower development. The polar angle of the shower axis had to be outside the range 88° to 92°, where the HPC has a dead region. Finally, the shower direction had to be consistent with the z coordinate, accounting for the fact that $z < 0$ is on the $\theta > 90°$ side, and $z > 0$ is on the $\theta < 90°$ side.

The photon identification efficiency depends on the criteria applied to require a good electromagnetic shower. It has been determined on the basis of a Monte Carlo sample of events passed through the complete simulation of the DELPHI detector [7]. The identification efficiency depends on the photon energy as shown in Figure 2. It ranges from ∼45% at low E_γ to ∼78% for $E_\gamma > 15$ GeV. Figure 2 also includes the inefficiency due to the dead regions of the HPC detector.

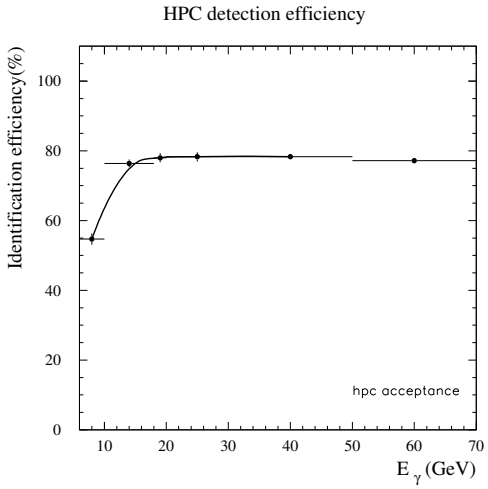

Figure 2: Efficiency of the single photon selection criteria in the HPC.

3.2 Photons in the FEMC acceptance

Events were preselected if they had at least one shower in FEMC with an energy above 10 GeV and a polar angle in the intervals $11° < \theta < 30°$ or $150° < \theta < 169°$. Showers in the lower and upper parts of FEMC were discarded because of the large amount of material in front of FEMC due to the STIC and the TPC detectors. In order to separate electrons from photons, the FEMC shower was extrapolated to the interaction point and the event was rejected if hits in the silicon microvertex detectors (VD and VFT) could be

associated with the shower.

The next step in the analysis was to require no charged tracks or additional electromagnetic showers in the event. However, the large amount of material in front of FEMC meant that about half of the photons preshowered before reaching the calorimeter. Most of the preshower was contained in a cone of about 12° around the largest shower and the selection took this into account by requiring no charged tracks, no electromagnetic showers (in STIC, FEMC and the HPC) and no hadronic showers outside a 12° cone. If there were no charged tracks inside the cone either, i.e., the photon had not preshowered, it was required that only one FEMC shower was present in the event. If, on the other hand, charged tracks were present in the cone, more than one FEMC shower were allowed and their momentum vectors were added to that of the largest shower.

The requirement of no electromagnetic showers outside the cone greatly reduced the background of radiative Bhabha and Compton events by rejecting events that had one or both electrons in the acceptance of the experiment. Events with hadrons and cosmics were rejected by the requirement of no hadronic showers outside the cone. In addition, it was required that the ratio of electromagnetic to electromagnetic plus hadronic energy inside the cone was larger than 0.95 .

Most reconstruction and event selection efficiencies in the analysis were taken into account by using Monte Carlo samples passed through the extensive detector simulation package of DELPHI [7]. Some efficiencies, however, were determined from data. In particular, the requirements of no electromagnetic or hadronic showers and no charged tracks were studied. A sample of events triggered at random and a sample of back-to-back Bhabha events with the electrons in STIC were used for this purpose. It was found that noise and machine background caused showers and tracks which would veto about 13% of the good single photon events.

3.3 Photon selection in the STIC acceptance

Single photons in STIC were selected by requiring one shower with an energy of at least 20 GeV in one of the two STIC calorimeters and no other electromagnetic showers in STIC, nor in FEMC or the HPC. No charged tracks in any of the tracking systems in DELPHI and no showers in the hadron calorimeter were allowed in the event. It was furthermore required that all single-photon candidates had satisfied the STIC single photon trigger and that there was no signal in at least one of the two large scintillator planes in front of the shower. A requirement of no signal in the small scintillators mounted on the beampipe made it possible to reject some of the radiative $ee\gamma$ background. In spite of the scintillator requirements, the huge background of off-energy electrons made it necessary to introduce the energy cut shown as a dashed line in Figure 3.

The trigger efficiency in the STIC acceptance was discussed in Section 2.1 . The offline photon identification and reconstruction resulted in an additional loss of 5% of the photons. The selection of events with no shower in STIC and no tracks introduced similar losses as those in the FEMC analysis and were estimated with the same methods.

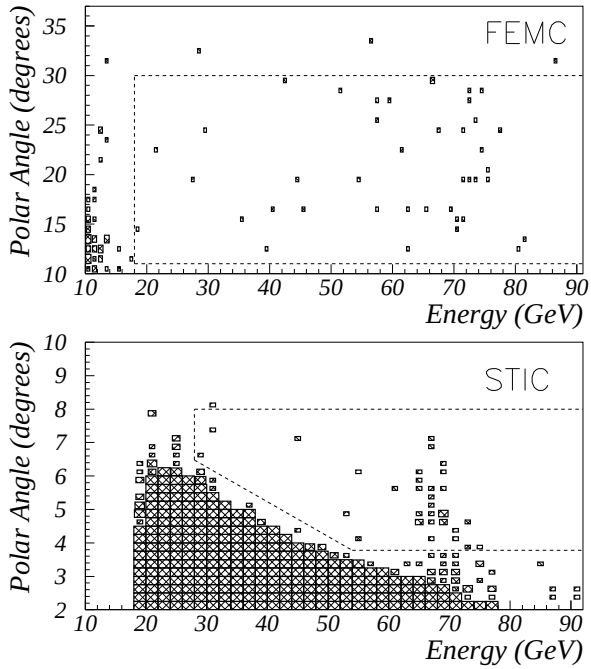

Figure 3: The polar angle versus energy distribution of photon candidates in FEMC and STIC (a full box contains five or more entries). Photons in both endcaps are shown with $\theta = 180° - \theta$ for $\theta > 90°$. The dashed lines indicate the regions used in the final analysis.

4 Background and data sample

The main source of background is the QED process $e^+e^- \to e^+e^-\gamma$ where the two electrons escape undetected along the beampipe or the electrons are lost by not being detected by the experiment. This process has a very high cross section [8], decreasing rapidly when E_γ and the photon polar angle increase. In Figure 3, the events in FEMC at low energy and low polar angle are all due to this process. The behaviour of this QED background together with the rapidly varying efficiencies at low energies are the reasons why different energy cuts had to be applied for photons in the three calorimeters. In the final analysis it was required that $x_\gamma > 0.06$ (HPC), $x_\gamma > 0.2$ (FEMC) and $x_\gamma > 0.3$ (STIC), where x_γ is the photon energy in units of the incident beam energy.

The critical parameter in the rejection of the $e^+e^-\gamma$ background is the polar angle at which the electrons start being detected by the experiment, i.e., seen in the STIC detector. This detector reconstructs electrons down to $\theta = 38$ mrad and in addition the scintillator counters mounted on the beampipe can be used to reject events with electrons down to 31 mrad. Simulations have shown that even at lower angles (down to 17 mrad) a large fraction of the electrons are detectable because they interact with a tungsten shield mounted inside the beampipe. Since the electrons have a high energy and the shield is thin, the electromagnetic showers leak enough energy into the STIC to make it possible

to reject the events.

The remaining background from the $e^+e^-\gamma$ process in the acceptance of the STIC and FEMC detectors was calculated with a Monte Carlo program [9] and two different event topologies were considered. Either both electrons were below the STIC acceptance or one or both of the electrons were in the DELPHI acceptance but were not detected by the experiment.The first topology gives background at low photon energy while the second one contributes photons at higher energy. The estimated number of $e^+e^-\gamma$ events with the energy cuts described previously are given in Table 2. In the HPC acceptance an analytical calculation [8] showed that the $e^+e^-\gamma$ background was negligible.

	HPC		FEMC		STIC	
x_γ:	0.06-0.60	$\geq$0.60	0.20-0.60	$\geq$0.60	0.30-0.60	$\geq$0.60
$N_{observed}$:	16$\pm$4.0	38$\pm$6.2	15$\pm$3.9	43$\pm$6.5	4$\pm$2.0	24$\pm$4.9
$N(e^+e^- \to e^+e^-\gamma)$:	0	0	0.57$\pm$0.22	2.51$\pm$0.43	0.20$\pm$0.04	0.41$\pm$0.41
$N(e \to e\gamma)$:	0	0	0	0	0.23$\pm$0.23	1.38$\pm$0.56
$N(e^+e^- \to \nu\bar{\nu}\gamma)$:	23.9$\pm$0.7	35.6$\pm$1.0	12.1$\pm$1.0	36.0$\pm$1.7	2.5$\pm$0.2	22.2$\pm$0.9
$N^{total}_{expected}$:	23.9$\pm$0.7	35.6$\pm$1.0	12.7$\pm$1.0	38.5$\pm$1.8	2.9$\pm$0.3	24.0$\pm$1.1

Table 2: The observed and expected number of events for different processes. All errors are statistical only.

A background seen only in STIC is the single electron background produced by interactions between the beam particles and residual gas molecules in the LEP beampipe. In these $e \to e\gamma$ events the photons are always lost in the beampipe while the off-energy electrons are bent into the STIC acceptance by the low-beta quadrupoles close to DELPHI. The rate of this background is so large that in the sample of events triggered by the STIC photon trigger there were several thousands of misidentified off-energy electrons for each photon from a $\nu\bar{\nu}\gamma$ event. It was not possible to provide a $\gamma - e$ separation powerful enough to eliminate completely this background.

A detailed study (including a simulation) of off-energy electrons has been made [10]. This study showed that the off-energy background is created in different parts of LEP and then focused by the magnets into different azimuthal sectors of STIC giving rise to different radius and energy distributions depending on the origin in LEP of the $e \to e\gamma$ process. The rate of this background depends on the vacuum pressure in the LEP ring and since this vacuum pressure is not known in detail a reliable estimation of the number of background events by a simulation is not possible. Instead a background sample was collected with a trigger similar to the photon trigger but without the requirement of an absence of signal in the scintillator vetocounter. With the exception of the scintillator requirement, all cuts in the photon analysis were applied to this background sample, which contained about twice the number of events compared to the number of photon candidates. From this analysis it was established that a clean photon sample could be obtained by removing showers at low energy and low polar angle as indicated by the dashed line in

Figure 3. The remaining background in the accepted region was estimated to be 1.6±0.6 events.

Other backgrounds, such as $\gamma\gamma$ collisions, $e^+e^- \to \gamma\gamma$ and cosmic events, were found to be negligible.

The $\nu\bar{\nu}\gamma$ process was simulated by the KORALZ [11] and NUNUGPV [12] programs. The final number of expected and observed events are given in Table 2. In total, 140±12 single photon events were observed in the three calorimeters, with 138 events expected from known sources, all at 183 GeV. The energy spectrum of the selected events is shown in Figure 4 together with the expected contributions from background and $\nu\bar{\nu}\gamma$.

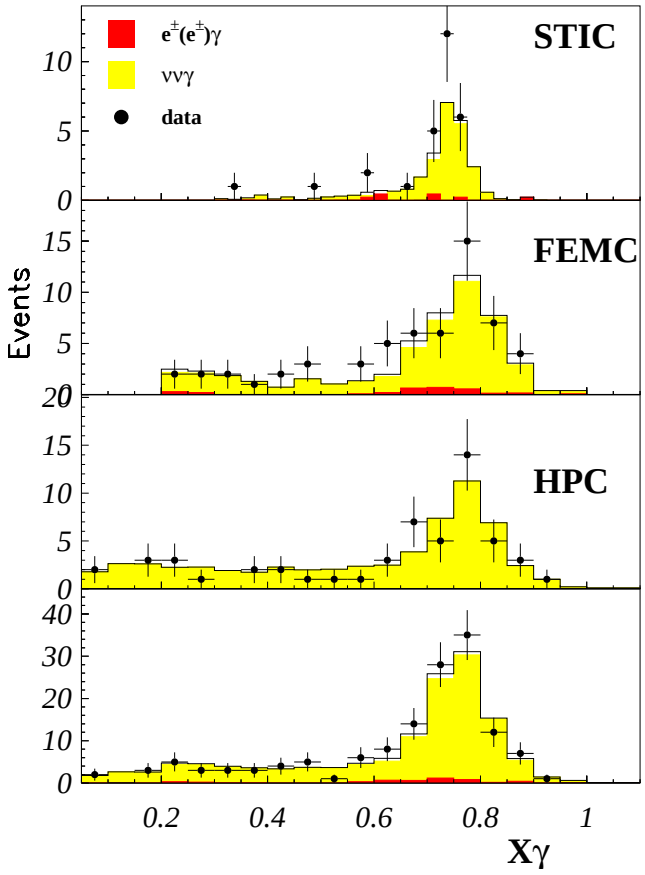

Figure 4: $x_\gamma = E_\gamma/E_{beam}$ of selected single photons in STIC, FEMC, HPC and for all calorimeters combined. The dark shaded area is the background from QED processes and the light shaded area is the expected spectrum from $e^+e^- \to \nu\bar{\nu}\gamma$ while the histogram is the sum of both.

Where relevant for the analysis, the samples in the HPC consisting of 10 events at 161 GeV and 11 events at 172 GeV were also considered (the total collected luminosity was 19.9 pb^{-1}). At these lower energies the number of expected events from Standard Model sources was 15.1 and 10.8 at the two energies respectively [13].

5 Analysis of the single photon sample

5.1 Cross sections

The cross sections at $\sqrt{s} = 183$ GeV after correcting for background and efficiencies are given in Table 3. Events with more than one photon contribute to the measured cross section if the other photons are at low angle ($\theta_\gamma < 38$ mrad), low energy ($E_\gamma < 1.5$ GeV) or within 3, 12 and 20 degrees with respect to the highest energy photon in STIC, FEMC and HPC respectively.

	HPC	FEMC	STIC
θ_γ:	$45° - 135°$	$11° - 30°$, $150° - 169°$	$3.8° - 8.0°$, $172° - 176.2°$
x_γ:	$\geq$0.06	$\geq$0.20	$\geq$0.60
Luminosity:	50.2 pb^{-1}	44.3 pb^{-1}	52.0 pb^{-1}
$\sigma(\gamma + inv.)$	1.85$\pm$0.25$\pm$0.15 pb	2.26$\pm$0.31$\pm$0.18 pb	1.09$\pm$0.21$\pm$0.12 pb
$\sigma(\nu\bar{\nu}\gamma)$ for $N_\nu = 3$	2.04 pb	1.96 pb	1.12 pb
N_ν	2.7$\pm$0.4$\pm$0.2	3.5$\pm$0.5$\pm$0.3	2.9$\pm$0.6$\pm$0.3

Table 3: The corrected cross section for $e^+e^- \to \gamma + invisible$ and the calculated cross section for $e^+e^- \to \nu\bar{\nu}\gamma$. The first error quoted is statistical and the second systematic. N_ν is the number of light neutrino generations.

The contribution from various sources to the systematic error is given in Table 4. The dominant uncertainty comes from the estimation of trigger and detection efficiencies. The total systematic error is taken as the individual errors added in quadrature.

	HPC		FEMC		STIC	
Source	Variation	$\Delta\sigma$	Variation	$\Delta\sigma$	Variation	$\Delta\sigma$
Luminosity	$\pm$1%	$\pm$1%	$\pm$1%	$\pm$1%	$\pm$1%	$\pm$1%
Trigger efficiency	$\pm$5%	$\pm$5%	$\pm$2%	$\pm$2%	$\pm$6%	$\pm$6%
Identification efficiency	$\pm$5%	$\pm$5%	$\pm$6%	$\pm$6%	$\pm$7%	$\pm$7%
Calorimeter energy scale	$\pm$5%	$\pm$4%	$\pm$5%	$\pm$5%	$\pm$0.5%	$\pm$1%
Background	$\pm$25%	$\pm$1%	$\pm$50%	$\pm$3%	$\pm$75%	$\pm$6%
Total		$\pm$8%		$\pm$8%		$\pm$11%

Table 4: Contribution to systematic errors of the cross section measurement $e^+e^- \to \gamma + invisible$.

A measurement of the cross section of the process $e^+e^- \to \nu\bar{\nu}\gamma$ makes it possible to calculate the number of light neutrino generations (N_ν). DELPHI has previously reported

a value of $N_\nu = 2.89 \pm 0.32$ from LEPI data only [14]. A similar study has now been carried out with the LEPII data. In this analysis, a Monte Carlo method [12] was used to calculate the expected values of the cross section of the process $e^+e^- \to \nu\bar{\nu}\gamma$. The cross section was calculated inside the acceptance of each of the three detectors used in the analysis. Figure 5 shows the expected behaviour of the cross section, calculated with $NUNUGPV$, for three neutrino families compared with the values measured with the HPC detector at different LEP energies.

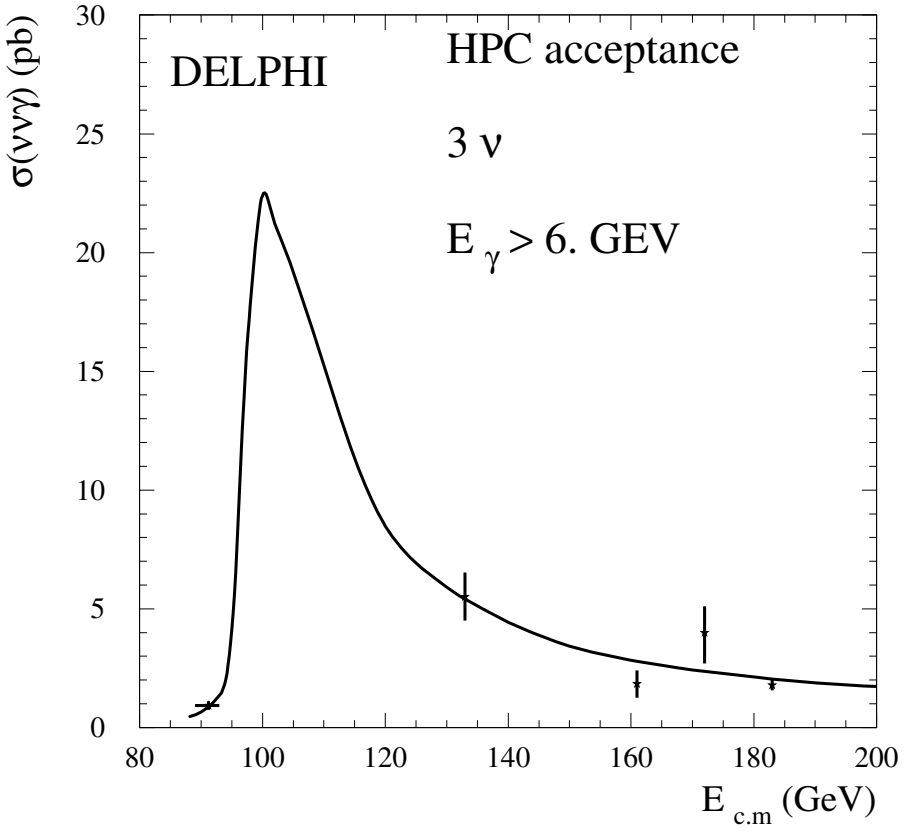

Figure 5: The measured cross sections at 91, 133, 161, 172 and 183 GeV compared to the expected $\sigma(\nu\bar{\nu}\gamma)$ as a function of $\sqrt{s}$ (for three neutrino generations).

The number of neutrino generations deduced from the cross section measurements are given in Table 3. Averaging the three independent measurements from the different calorimeters, and including also the data from the HPC at 161 and 172 GeV ($N_\nu = 2.6 \pm 0.6 \pm 0.4$), the number of light neutrino generations becomes:

$$N_\nu = 2.92 \pm 0.25(stat) \pm 0.14(syst)$$

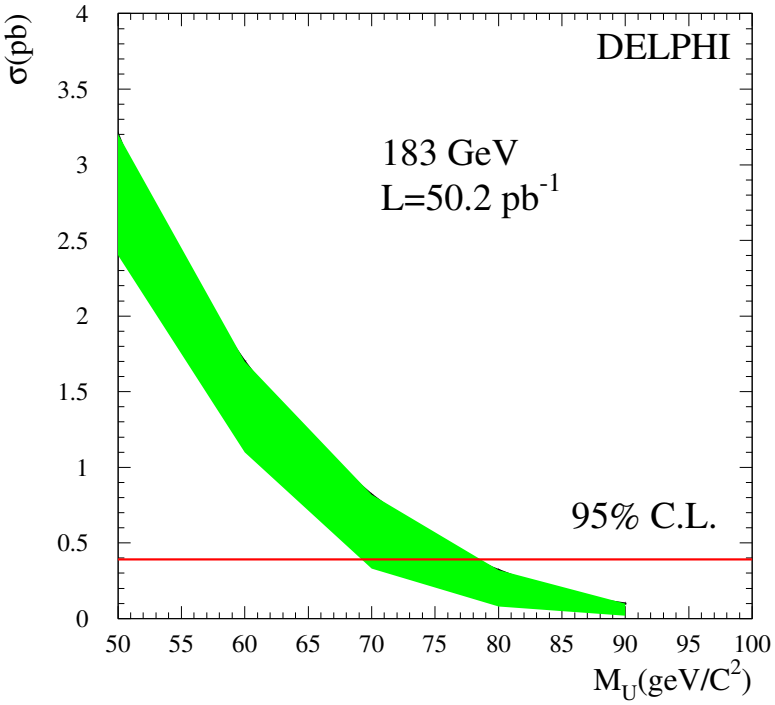

Figure 6: Limit at 95% C.L. for the mass of the W-type U boson.

5.2 Limits on compositeness

Compositeness models predict several new particles which do not exist in the Standard Model. A specific Preon Model is considered in this analysis [3]. This model considers leptons, quarks and weak bosons as composite particles. Some of the predicted new particles contribute to the cross section of the process $e^+e^- \to \gamma + inv$. At a relatively light mass scale, it predicts the existence of objects connected with neutrinos ($l_S, \bar{l}_S$), with down quarks (q') and with W bosons ($U^{\pm}$, U^0). It also requires a new vector boson D, which could be as heavy as several times the Z^0 mass. The U^0 boson decays invisibly and can be produced in the reaction $e^+e^- \to U^0\bar{U^0}\gamma$, contributing to the process $e^+e^- \to \gamma + inv$. Also pairs of $l_S\bar{l}_S$ could be produced through $U^{\pm}$ exchange and contribute to $e^+e^- \to \gamma + inv$.

Calculating the cross sections with the hypothesis that a composite boson D exists with mass between $M_D = 5 \cdot M_{Z^0}$ and $M_D = 7 \cdot M_{Z^0}$ and summing the contributions to the cross sections coming from direct production of $U^0\bar{U}^0$ pairs and the exchange of $U^{\pm}$, a limit can be obtained on M_U from the measured $\sigma(e^+e^- \to \gamma + inv.)$ after subtracting the contribution expected from neutrino production in the Standard Model. The limit calculated from the HPC and FEMC data is shown in Figure 6 and it ranges between

$$M_U > 68 - 78 \text{ GeV/c}^2 \quad \text{at 95\% C.L.}$$

varying M_D in the range indicated above. Weaker limits have been determined at lower LEPII energies [2].

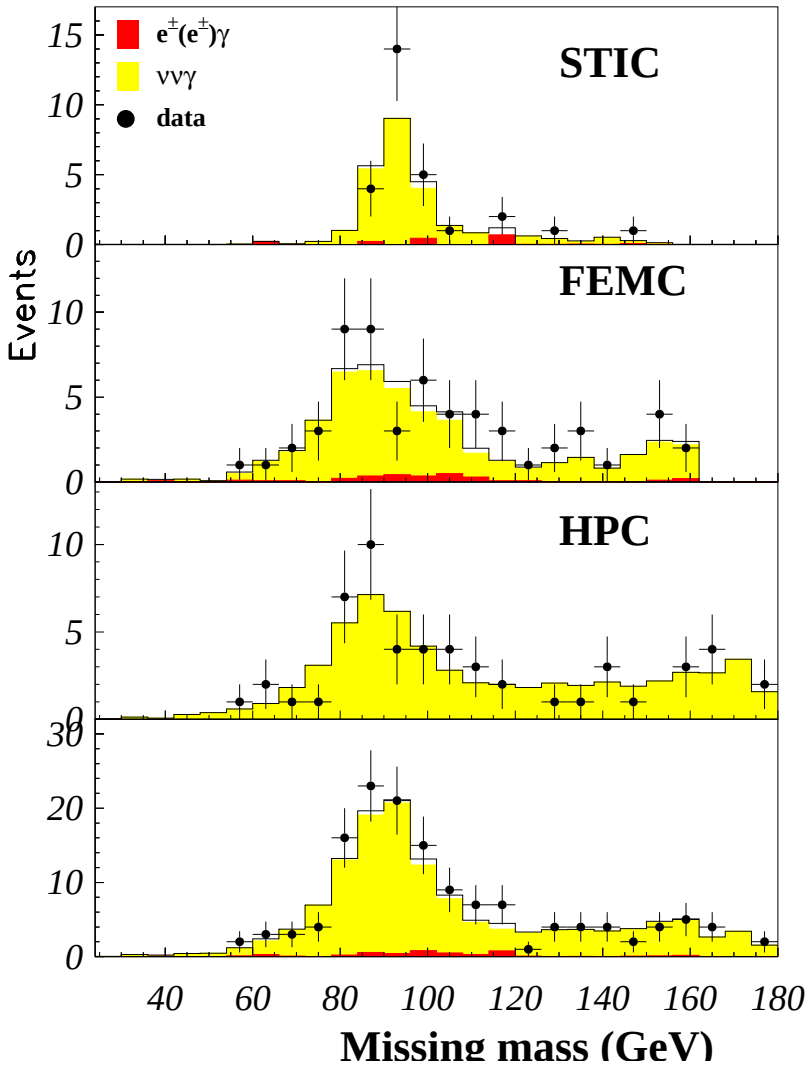

Figure 7: Distribution of the recoiling mass against the detected photon. The dark shaded area is the background from QED processes and the light shaded area is the expected spectrum from $e^+e^- \to \nu\bar{\nu}\gamma$ while the histogram is the sum of both.

5.3 Limits on the production of an unknown neutral state

In many previous analyses [2] [14] [15] one has used the observed candidates to set a limit on the probability of the existence of a new particle, X, produced in association with a photon and being stable or decaying to invisible decay products. The limit is calculated from the recoil mass distribution (Figure 7) of the 140 single γ in the angular region $3.8^\circ < \theta < 176.2^\circ$ and taking into account the expected background. The limit is valid when the intrinsic width of the X particle is negligible compared to the detector resolution (the recoil mass resolution varies between 10 GeV at the Z^0 peak to 1 GeV at high masses). The upper limit at the 95% confidence level of the cross section for $e^+e^- \to \gamma$+X is given in Figure 8 for photons in the HPC region and in all three calorimeters. In the latter case an assumption of an ISR-like photon angular distribution has been made to correct for losses between the calorimeters.

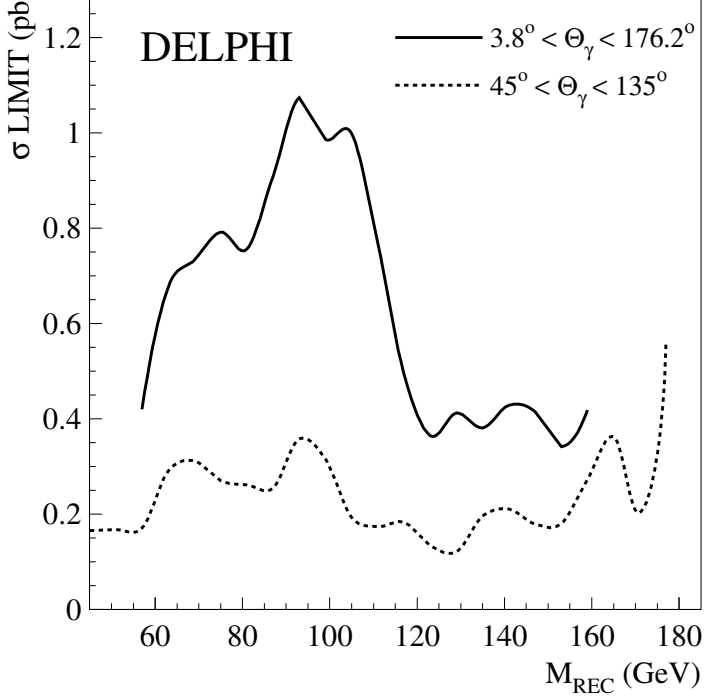

Figure 8: Limit at 95% C.L. for the production of a new unknown stable neutral object.

5.4 SUSY particles

5.4.1 Limits on the gravitino mass

Recently, the possibility of detecting a light gravitino in accelerator experiments was studied in detail [16] and the cross section for the process $e^+e^- \to \tilde{G}\tilde{G}\gamma$ was computed under the assumption that all other supersymmetric particles are too heavy to be produced. The radiative double differential cross section $d^2\sigma/(dx_\gamma, dcos\theta_\gamma)$, where x_γ and θ_γ are the fraction of the beam energy carried by the photon and the photon polar angle with respect to the electron direction, is given in [16] for the radiative production ($e^+e^- \to \tilde{G}\tilde{G}\gamma$) of an undetectable gravitino pair. The total cross section can be written as:

$$\sigma = \frac{\alpha_s^3}{320\pi^2|F|^4} \cdot I, \tag{2}$$

where $|F|^{\frac{1}{2}}$ is the supersymmetry-breaking scale which is related to the gravitino mass by $|F| = \sqrt{3/8\pi} \cdot G_N^{-\frac{1}{2}} \cdot m_{3/2}$ and I is an integral over the photon energy and polar angle. The largest sensitivity is obtained with photons at low energy and/or low polar angle, as illustrated by Figure 9.

Single photon final states from the Standard Model process $e^+e^- \to \nu\bar{\nu}\gamma$ have a polar angle distribution similar to the signal, except for the enhanced characteristic peak due to the radiative return to the Z^0, at $x_\gamma = 1 - {M_Z}^2/s$. Therefore, the optimal kinematical region in which to look for the signal is in the low region of the photon energy spectrum. Since the signal cross section (2) grows as the sixth power of the center-of-mass energy, the highest sensitivity is found at the highest beam energy. For this reason, the data taken in 1997 at $\sqrt{s} = 183$ GeV provide the best sample in which to look for the $e^+e^- \to \tilde{G}\tilde{G}\gamma$

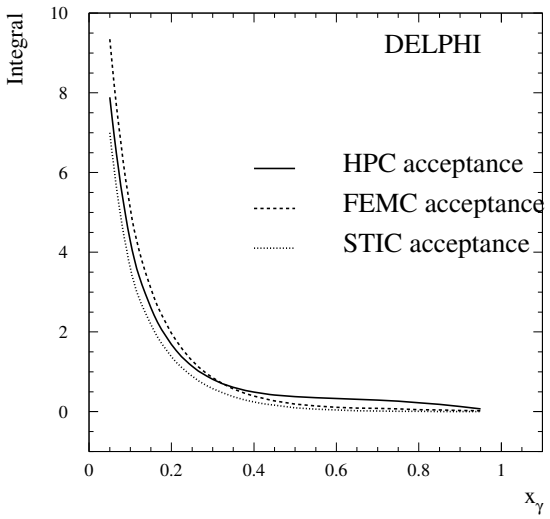

Figure 9: The behaviour of the integral I (used in equation (3)) as a function of x_γ.

signal. The lower limit on the gravitino mass can be extracted from the upper limit σ_0 on the production cross section (2) through:

$$m_{3/2} > 3.8 \cdot 10^{-6} eV \left[\frac{\sqrt{s}(GeV)}{200}\right]^{3/2} \left[\frac{I}{\sigma_0}\right]^{1/4} \tag{3}$$

All the three DELPHI calorimeters, STIC, FEMC and the HPC, were used in this analysis. The sensitivity was optimized for each of them, maximizing the value of the function I given in Figure 9. The different energy regions with the corresponding expectations from the Standard Model are summarised in Table 5.

Detector	HPC	FEMC	STIC
x_γ	0.06-0.60	0.20-0.60	0.30-0.60
$N_{observed}$	16	15	4
σ_0	0.30 pb	0.52 pb	0.37 pb
$m_{3/2} >$	$6.9 \cdot 10^{-6}$ eV	$4.6 \cdot 10^{-6}$ eV	$3.2 \cdot 10^{-6}$ eV

Table 5: The limits on $m_{3/2}$ (as defined by equation (3)), calculated with the data from the three calorimeters.

The upper limit at 95% confidence level is calculated according to [17]. Combining the three calorimeters, one obtains the limit

$$\sigma_0 < 0.50 \text{ pb} \quad \text{at } 95\% \text{ C.L.} \tag{4}$$

The total kinematical region corresponds to $I = 7.7$ and the lower limit on the gravitino mass from equation (3) then becomes

$$m_{3/2} > 6.6 \cdot 10^{-6} \text{ eV/c}^2 \quad \text{at } 95\% \text{ C.L.} \tag{5}$$

which correspond to a SUSY breaking energy scale $|F|^{\frac{1}{2}} > 166$ GeV. The effect of the systematic uncertainties on this limit is negligible. This limit is weaker than those obtained at $p\bar{p}$ machines [18] and by astrophysical constraints [19] and it is at the same level as those set by $(g-2)_\mu$ [20]. However, it has the feature of being valid when all the masses in the SUSY models are very large.

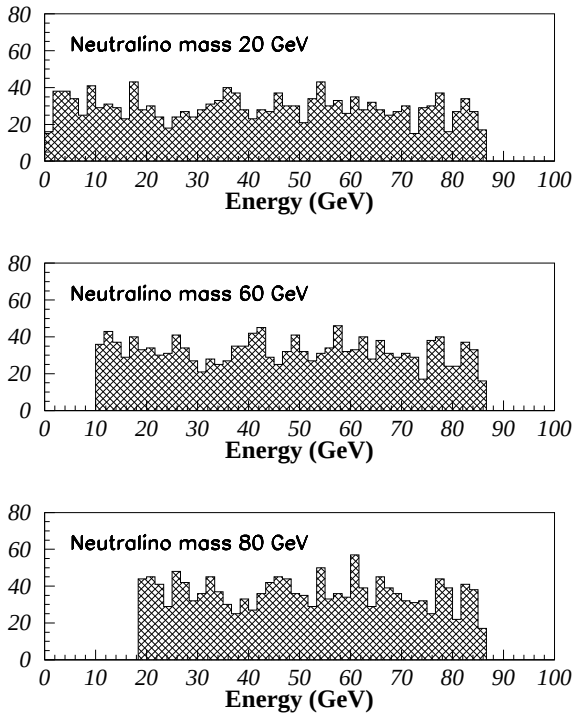

Figure 10: Energy distributions of the photon from neutralino decays produced in the process $e^+e^- \to \tilde{G}\chi \to \tilde{G}\tilde{G}\gamma$. The plots have been produced at $\sqrt{s}$ =172 GeV.

5.4.2 Limits on neutralino production

The production of a neutralino $\tilde{\chi}^0$ together with a gravitino $\tilde{G}$ through $e^+e^- \to \tilde{G}\tilde{\chi^0} \to \tilde{G}\tilde{G}\gamma$ has also been considered. The limit is calculated from the energy distribution of the expected events, generated with $SUSYGEN$ [21] and the observed 75 single photon events (at 161, 172 and 183 GeV) in the angular region $45° < \theta < 135°$, after taking into account the expected background from $\nu\bar{\nu}\gamma$. Figure 10 shows the expected photon energy distributions for neutralinos with different masses. The cut on E_γ was made in such a way as to keep at least 90% of the signal. The resulting overall efficiency including both the energy cut and the geometrical acceptance was 66%. The calculated upper limit for the cross section of the process $e^+e^- \to \tilde{G} + \tilde{\chi^0}$ is given in Figure 11 for the data at 183 GeV.

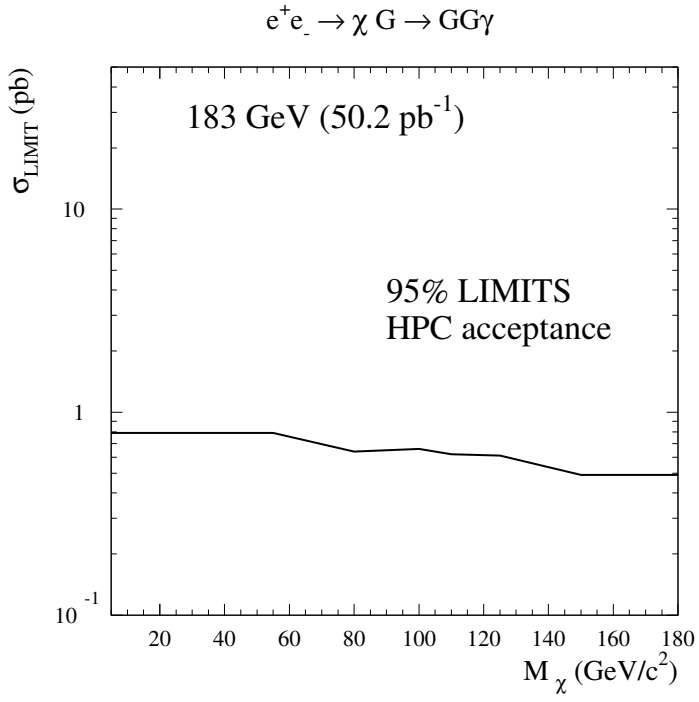

Figure 11: Upper limits for the cross section of the process $e^+e^- \to \tilde{G}\tilde{\chi} \to \tilde{G}\tilde{G}\gamma$ at 95% C.L.

6 Conclusions

With the 50 pb^{-1} of data collected by DELPHI in 1997 at a center-of-mass energy of 183 GeV a study has been made of the production of events with a single photon in the final state and no other visible particles.

The measured cross sections are in agreement with the expectations from the Standard Model process $e^+e^- \to \nu\bar{\nu}\gamma$ and a calculation of the number of light neutrino families gives the result:

$$N_\nu = 2.92 \pm 0.25(stat) \pm 0.14(syst)$$

The absence of an excess of events has been used to set limits on the production of a new unknown model-independent neutral state, a W-type U-boson as described by a compositeness model, a light gravitino and neutralinos.

References

[1] ALEPH Collaboration, R. Barate *et al.*, Phys. Lett. **B420** (1998) 127.
L3 Collaboration, M. Acciarri *et al.*, Phys. Lett. **B411** (1997) 373;
OPAL Collaboration, K. Ackerstaff *et al.*, Eur. Phys. J. C2(1998) 607.

[2] DELPHI Collaboration, P. Abreu *et al.*, Phys. Lett. **B380** (1996) 471.

[3] H. Senju, Prog. Theor. Phys. **95** (1996) 455 and references therein.

[4] S. Ambrosanio and B. Mele, Phys. Rev. **D52** (1995) 3900;
S. Ambrosanio *et al.*, Nucl. Phys. **B478** (1996) 46.

[5] DELPHI Collaboration, P. Abreu *et al.*, Nucl. Inst. and Meth. **A378** (1996) 57;
DELPHI Collaboration, P. Aarnio *et al.*, Nucl. Inst. and Meth. **A303** (1991) 233.

[6] D. Gillespie and T. Malmgren, DELPHI 94-46 CAL 155;
S. Paiano and A. Perrotta, DELPHI 98-37 CAL 139.

[7] DELPHI Collaboration, DELPHI 89-67 PROG 142;
DELPHI Collaboration, DELPHI 89-68 PROG 143.

[8] M. Caffo, R. Gatto and E. Remiddi, Phys. Lett. **B173** (1986) 91;
M. Caffo, R. Gatto and E. Remiddi, Nucl. Phys. **B286** (1987) 293.

[9] D. Karlen, Nucl. Phys. **B289** (1987) 23.

[10] E. Falk, V. Hedberg and G. von Holtey, CERN SL/97-04(EA) and DELPHI 97-12 LEDI 8.

[11] S. Jadach *et al.*, Comp. Phys. Comm. **66** (1991) 276;
S. Jadach *et al.*, Comp. Phys. Comm. **79** (1994) 503.

[12] G. Montagna *et al.*, Nucl. Phys. **B452** (1995) 161.

[13] DELPHI Collaboration, P. Abreu *et al.*, Eur. Phys. J. C1(1998) 1.

[14] DELPHI Collaboration, P. Abreu *et al.*, Z. Phys. **C74** (1997) 577.

[15] OPAL Collaboration, R. Akers *et al.*, Z. Phys. **C65** (1995) 47.

[16] A. Brignole, F. Feruglio and F. Zwirner, Preprint hep-ph/9711516.

[17] R.M. Barnett *et al.*, Phys. Rev. **D54**, 1 (1996) 166.

[18] D. Dicus and S. Nandi, Phys. Rev. **D56** (1997) 4166;
A. Brignole *et al.*, Preprint hep-ph/9801329.

[19] J.A. Grifols, Preprint hep-ph/9804225.

[20] F. Ferrer and J.A. Grifols, Phys. Rev. **D56** (1997) 7466;
T. Li, J.L. Lopez and D.V. Nanopoulos, Preprint hep-ph/9704439.

[21] S. Katsanevas and P. Morawitz, Preprint hep-ph/9711417.

Article III

Photon Analysis with STIC

DELPHI Collaboration DELPHI 98-147 PHYS 791
3 August 1998

Photon Analysis with STIC

E. Falk, V. Hedberg
Department of Physics, University of Lund, Lund, Sweden
P. Ferrari, C. Matteuzzi
Sezione INFN, Milano, Italy

Abstract

The calorimeter STIC has been used, for the first time, to identify and analyse events with a photon in the very forward region of DELPHI. Samples of single-photon events were analysed for the reaction $e^+e^- \to \gamma +$ invisible at center-of-mass energies of 161, 172 and 183 GeV. The single-photon events were used to explore the possibilites of using STIC to identify photons while maintaining control over difficult background situations, caused by large amounts of misidentified off-energy electrons and of photons from radiative Bhabha scattering and Compton scattering. In particular, two subdetectors of STIC were used for this purpose: the veto counters, which were used to distinguish photons from electrons, and the silicon-strip detectors, which were tested as a means of rejecting off-energy electron background. The measured cross sections were used to count the number of neutrino generations.

1 Introduction

The calorimeter STIC has been used, for the first time, to analyse events with a photon in the very forward region of DELPHI. The aim of the analysis was to explore the possibilities of using STIC to identify photons and to investigate the means to maintain control over difficult background situations. The analysis was carried out on single-photon events, i.e., for the reaction $e^+e^- \to \gamma +$ invisible, where the photon had entered STIC. Data taken at center-of-mass energies of 161, 172 and 183 GeV were used.

Within the Standard Model, the process $e^+e^- \to \gamma +$ invisible receives contributions from radiative production of neutrino-antineutrino pairs through radiative return to the Z^0 and from t-channel W exchange, with the photon radiated from the beam electron or from the exchanged W. Therefore, single-photon events can be used to count the number of light neutrino generations, N_ν. Although the cross section for radiative neutrino production is rather small, it is very sensitive to N_ν, and this method of measuring the number of neutrino families provides a complement to the so-called lineshape method used at LEP1. Possible contributions to the single-photon final state could also come from some other neutral weakly interacting particle or from a new particle decaying into a photon. Hence, the $\gamma +$invisible final state also provides a tool to explore the possible existence of new particles.

The measured cross sections for the process $e^+e^- \to \gamma +$ invisible in the present analysis were used to count the number of neutrino families, under the assumption that the only contribution to the single-photon final state comes from the reaction $e^+e^- \to \gamma\nu\bar{\nu}$. Searches for new particles are not reported here. Instead, the analysis of the data at $\sqrt{s} = 183$ GeV is part of a larger analysis, which does include searches for new particles, and in which all three DELPHI calorimeters, STIC, FEMC and HPC, were used [1]. Measurements of this type have been made previously with the HPC calorimeter, for center-of-mass energies between the Z^0 peak and 172 GeV [2]. It is, however, the first time that such measurements have been performed with STIC.

The single-photon data recorded at small polar angles contain large amounts of background in the form of misidentified off-energy electrons, produced in interactions between beam particles and residual gas molecules in the beam pipe, and from radiative Bhabha scattering and Compton scattering, where the electrons escape detection. Even after an event selection defining events with the appropriate single-photon configuration had been carried out, the data samples contained several thousand background events for every true single-photon event. The principal challenge of the single-photon analysis with STIC was to reduce the large background to a level where a meaningful identification of single-photon events became possible. Two subdetectors of STIC were specifically used as tools to reject background: the veto counters, a set of scintillator counters, were used to distinguish photons from electrons; and the silicon-strip detectors were tested as a means to reduce off-energy electrons.

2 The STIC Detector

2.1 The Calorimeters

The luminosity monitor STIC in DELPHI consists of two lead-scintillator calorimeters of shashlik type, read out by wavelength-shifting fibers. These are located on either side of the interaction point at a distance of 2.2 m and have a thickness of about 27 radiation lengths (see Figure 1). Each calorimeter is divided into 10 rings and 16 sectors in such a manner that they form 160 towers that point to the interaction region. The calorimeters are usually referred to as arm A and arm C, according to the DELPHI convention of calling the side of incoming electrons side A and that of positrons side C. For a complete description of these detectors, see [3].

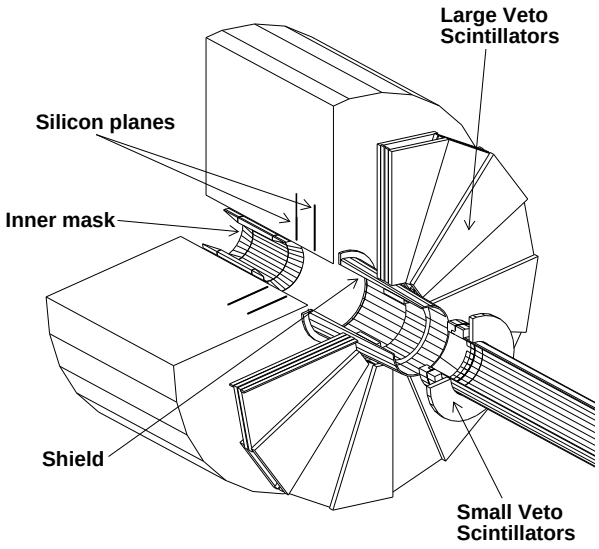

Figure 1: Outline of a STIC calorimeter. The planes of silicon-strip detectors inserted into the calorimeter are shown in the drawing. Placed in front of the calorimeter are the scintillators of the veto-counter system. The inner, or synchrotron, mask, and the shield are tungsten rings that protect the TPC from synchrotron radiation.

The calorimeters extend radially from 65 mm to 417.5 mm, measured from the beam line. This corresponds to a polar-angular acceptance of 29 to 188 mrad (1.7°–10.8°). In reality, however, the inner acceptance is determined by a system of tungsten masks and shields mounted in front of STIC. Some of these were used to define the acceptance in the luminosity measurements at LEP1; others protect the TPC from synchrotron radiation. The configuration of these masks and shields has varied from year to year [4]. For the period covered by this analysis, the inner acceptance was at a radius of 84 mm (2.2°).

2.2 The Veto Counters and the STIC Triggers

A veto system consisting of a set of scintillators is mounted in front of each arm of STIC. This veto system is part of a neutral trigger that provides electron-photon separation. Photons are identified by the absence of signals in the scintillators in front of the point where a showering particle entered STIC.

The scintillator counters are made up of two parts: the main detector, called the large veto counters, and an extension to cover small polar angles, the so-called small veto counters. The large veto counters consist of two layers of scintillator mounted in front of each arm of STIC and covering radii from 96 to 412 mm. The scintillator planes are divided into 16 sectors that match the segmentation of the calorimeters. The small veto counters consist of one layer of scintillator divided into two half-rings that are mounted directly on the beam pipe on either side of the interaction point, in front of the large veto counters. The small veto counters extend radially from 56.5 mm to 130 mm.

STIC provides a so-called single-arm trigger, which requires an electromagnetic shower in one of the arms of STIC, with an energy deposit $E \geq 0.16 E_{\mathrm{beam}}$, where E_{beam} is the beam energy, and with the showering particle entering at a radius $r > 10$ cm. This trigger is used to select and monitor off-energy electron background. The neutral trigger requires the same conditions to be fulfilled as in the case of the single-arm trigger. In addition to this, there is a requirement for the absence of any signal in at least one of the scintillator planes in the region in front of the point where the showering particle entered the calorimeter. In the large veto counters, this region is confined to the sector in which the particle entered STIC, and the two adjacent sectors. In the region of the small veto counters, there is no matching between the scintillator half-rings and the calorimeter sectors, and in order to fulfill the requirements for the neutral trigger, neither half may register a signal. The neutral trigger is fully efficient for energies above 35 GeV [4].

2.3 The Silicon-Strip Detectors

Each calorimeter has been equipped with two planes of silicon-strip detectors with which the direction of a shower can be measured. The purpose of this tracking device is to improve rejection of off-energy electron background. The silicon detectors consist of planes of circular strips replacing one lead-scintillator layer at a depth of 4.0 radiation lengths and another at 7.4 radiation lengths in each of the two arms of STIC, thus giving a total of four silicon planes (see Figure 1). The silicon planes cover 32–77 mrad in polar angle (71.5–174.2 mm and 73.2–178.4 mm in radius respectively). Each silicon plane is divided into 16 sectors that follow the sector geometry of the calorimeter. For a more detailed description of these detectors, see [5].

3 Event Selection

The analysis of single-photon events was performed on data taken at center-of-mass energies of 161, 172 and 183 GeV, with integrated luminosities of 10.02, 9.97 and 52.0 pb^{-1} respectively. The event selection was divided into two steps. The first step involved selecting events having

the appropriate configuration, with a single shower in STIC and no signal in any other DELPHI subdetector. The second step consisted of using the veto counters to identify the showering particle in STIC as a photon.

3.1 Selection of Single-Photon Events

The selection of events with a single-photon candidate was based on the requirement that the events have exactly one electromagnetic shower in STIC and no signal anywhere else in DELPHI. The shower was required to have an energy E of at least 20 GeV. The absence of a signal anywhere else in DELPHI was established through the following criteria:

- There were no showers, other than the single-photon candidate, with an energy $E > 0.5$ GeV detected in STIC;
- There were no showers with an energy $E > 0.1$ GeV reconstructed in FEMC or in HPC;
- No charged-particle tracks had been reconstructed by any of the DELPHI tracking detectors;
- There were no showers with an energy $E > 0.5$ GeV detected in the hadronic calorimeter, HAC.

The efficiency of this event selection was 88% for the 183 GeV data sample, 97% for 172 GeV, and 95% GeV for 161 GeV. The efficiencies were estimated with a set of non-radiative Bhabha events in STIC. They were also estimated with a set of events triggered by the DELPHI random trigger; these efficiencies were slightly lower. This difference in efficiency between the two samples was taken into account in the estimation of the systematic errors. The efficiency at 183 GeV is lower than that of the other two energies because of a higher noise level in the HAC detector in 1997.

3.2 Identification of Photons

Once the single-photon candidates had been selected, further requirements were imposed on each event in order to identify the showering particle in STIC as a photon. Hence, it was required that the candidate event should have fired the neutral trigger. The trigger decision made on-line (see Section 2.2) is based on a set of discriminated signals from the veto counters. Off-line, ADC readings from the veto counters are also available, and these were used to refine the cut based on the neutral trigger.

The off-line cut was based on the same requirements as those of the neutral trigger, i.e., a shower in STIC in conjuntion with the absence of any signal in at least one of the scintillator planes in front of the shower, with the exception that both the ADC values and the discriminator values were used to identify a signal in the scintillators. A cut requiring the absence of any signal in either scintillator plane was tried, but this cut was found to veto many photons that had caused a backsplash (the so-called albedo) when entering the calorimeter.

The efficiency of the photon identification depends on the radius, and decreases at higher radii. This is due to the additional material, e.g., the TPC laser boxes, located there. The efficency ϵ has been parametrised as a function of polar angle [4], and is given by

$$\epsilon = -0.2475 + 0.3176 \cdot \theta - 0.03347 \cdot \theta^2,$$

where θ is measured in degrees. Due to the low photon-identification efficiency at high polar angles ($\epsilon \leq 0.10$ at $\theta \geq 8.2°$), an upper cut at $\theta = 8°$ was introduced in the analysis. The requirement of $r > 10$ cm in the neutral trigger sets a lower limit in polar angle at about $\theta = 2.8°$ ($r \simeq 11$ cm).

4 Background

As mentioned already, the main type of background entering the single-photon sample is misidentified off-energy electrons. They are created in bremsstrahlung interactions between beam particles and residual gas molecules, and may have their origin anywhere in the beam line. Different methods to eliminate this background were studied; these are discussed in Section 4.1 below.

After the off-energy electrons, the largest contribution to background in the single-photon sample comes from the QED process $e^+e^- \to e^+e^-\gamma$, where the photon enters STIC and both electrons are lost in the beam pipe. This type of background is discussed further in Section 4.2 below.

A different configuration of radiative Bhabha scattering that likewise contributes to the background is that in which one of the electrons enters DELPHI and remains undetected. A brief account of this type of background is given in Section 4.3.

Other sources of background that were investigated but found to be of less or of no importance are cosmic events, Compton scattering on thermal photons, synchrotron radiation and detector noise. They are briefly discussed in Section 4.4.

4.1 Off-Energy Electron Background

Bremsstrahlung interactions between beam particles and residual gas molecules in the beam line create an abundance of electrons and photons. The photons produced in these interactions never reach DELPHI, but the electrons are bent into the STIC acceptance by the low-beta quadrupoles. The rate of this background is so high that, despite the fact that the veto counters have a rejection factor of ~ 1000, a large amount remained in the event samples after the event selection described above.

The off-energy electron background has been studied extensively elsewhere [6]. It was shown that the off-energy electrons are focused by the LEP quadrupoles into different azimuthal sectors of STIC in a very characteristic pattern. One horizontal and two vertical components can be distinguished. Each component has its own specific distributions in radius and in

energy. The horizontal component is confined to radii below 11 cm, whereas the vertical components extend to well over 20 cm in radius. The energy distributions scale linearly with the beam energy; they extend to about 50 GeV at $\sqrt{s} = 136$ GeV, and remain below 70 GeV at $\sqrt{s} = 183$ GeV. Figure 2 shows the two-dimensional radius-energy distributions of this background at $\sqrt{s} = 136$ GeV.

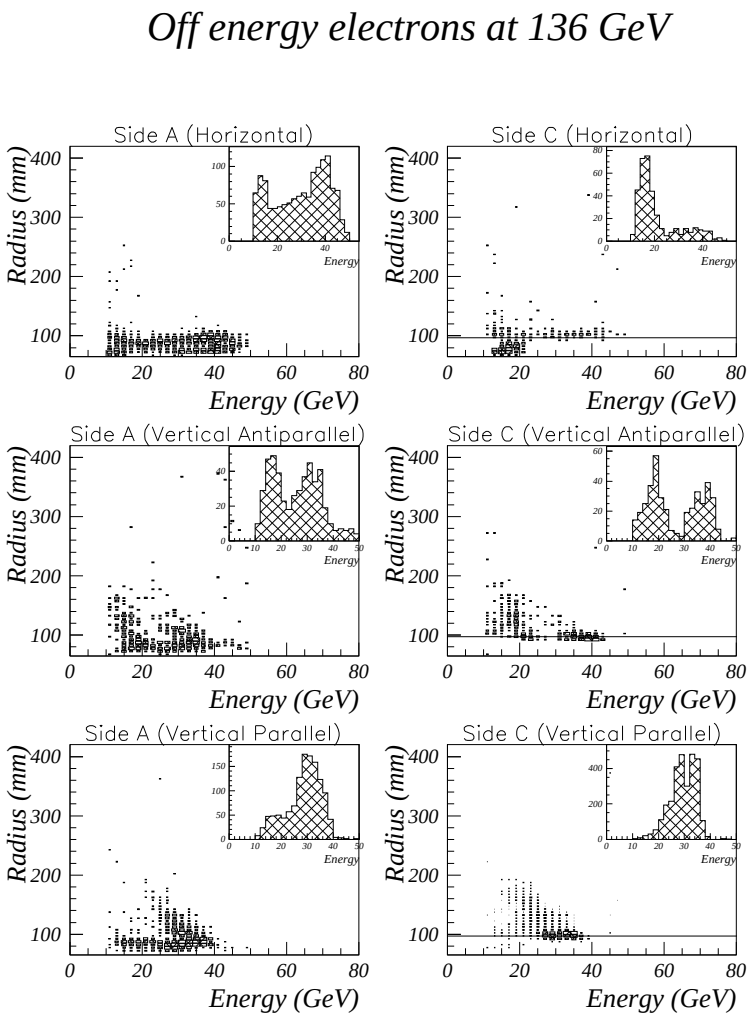

Figure 2: Distribution of radius *vs.* energy for off-energy electrons in STIC, at $\sqrt{s} = 136$ GeV. The three different components (horizontal, vertical antiparallel and vertical parallel) are shown for each calorimeter arm separately. The names "antiparallel" and "parallel" refer to the fact that these two components are deflected in a direction parallel or antiparallel to the direction of the electrostatic field that creates the vertical separation for the different bunches of the bunch trains in LEP. The C side was covered by a tungsten nose, extending to a radius $r = 97$ mm, during the 136 GeV data-taking. The edge of the tungsten nose is indicated by a line in the histograms.

The simulations in [6] showed good qualitative agreement with data. However, the Monte Carlo program used to simulate the off-energy electron events could not be used to estimate the

background quantitatively; its rate is highly dependent on the vacuum pressure in LEP, and this is generally not known to a good precision. Therefore, both the study of possible methods to eliminate this background, and the estimation of any remaining such background in the final data sample, were carried out with specially selected data samples consisting of single-electron events.

The single electrons were selected in a procedure similar to that of the single photons, but the veto counters were used to identify the showering particle as an electron. Hence, events were selected only if the neutral trigger had *not* been fired, and the off-line cut on the veto-counter ADCs and discriminators required a hit in both scintillator planes in the region around the entrance point of the showering particle (or, for the small veto counters, in at least one of the two scintillator halves); all other criteria were identical to those of the selection of single photons.

4.1.1 Methods to Remove the Off-Energy Electron Background

A polar-angular cut rejecting events below approximately 3° ($\simeq 12$ cm in radius) removes essentially all of the horizontal component of the off-energy electron background, and a good fraction of the vertical components as well. Two different methods to remove the remaining background in the vertical plane were tested: One was to combine the polar-angular cut with a cut on the vertex reconstructed by the silicon-strip detectors and with a cut in the $r-\varphi$ plane, where r is the radius and φ the azimuthal angle; the other was to tighten the cut on the polar angle.

The silicon-strip detectors have a reconstruction efficiency of about 90% [7]. A cut on the vertex at 75 cm on either side of the interaction point rejects 88% of the reconstructed off-energy electrons and keeps 73% of the particles originating from the interaction region. Choosing to retain particles whose vertices were not reconstructed, one obtains a total rejection of 79% and an efficiency of 76%. This cut is illustrated in Figure 3. Since the acceptance of the silicon detectors is limited to 17 cm in radius, it was necessary to introduce a cut in the $r-\varphi$ plane in order to remove background at higher radii. The cut was chosen to have, in the $x-y$ plane, the shape of two semi-ellipses joined along the horizontal axis. The horizontal axis of both ellipses is 6 cm, whereas the vertical axis is 22 cm in one case and 24 cm in the other; the reason for this is that the radial distributions are different for the two vertical background components. The $r-\varphi$ cut is illustrated in Figure 4. This combination of cuts removes nearly all of the background events that have an energy above a fraction $x_\gamma \simeq 0.4$ of the beam energy, but it necessitates further cuts in the low-energy region.

Using a combination of a cut on the reconstructed vertex and a cut in the $r-\varphi$ plane has the disadvantage of limiting the acceptance used for the cross section measurement, and also of yielding a lower efficiency in the region of the silicon detectors. If, however, these cuts are not carried out, one is obliged to tighten the polar-angular cut from $\sim 3^\circ$ to $\sim 4^\circ$ in order to remove the off-energy electron background.

At low energies, the QED background where both electrons were lost in the beam pipe eventually required a tighter cut than was necessary in order to remove the remaining off-energy

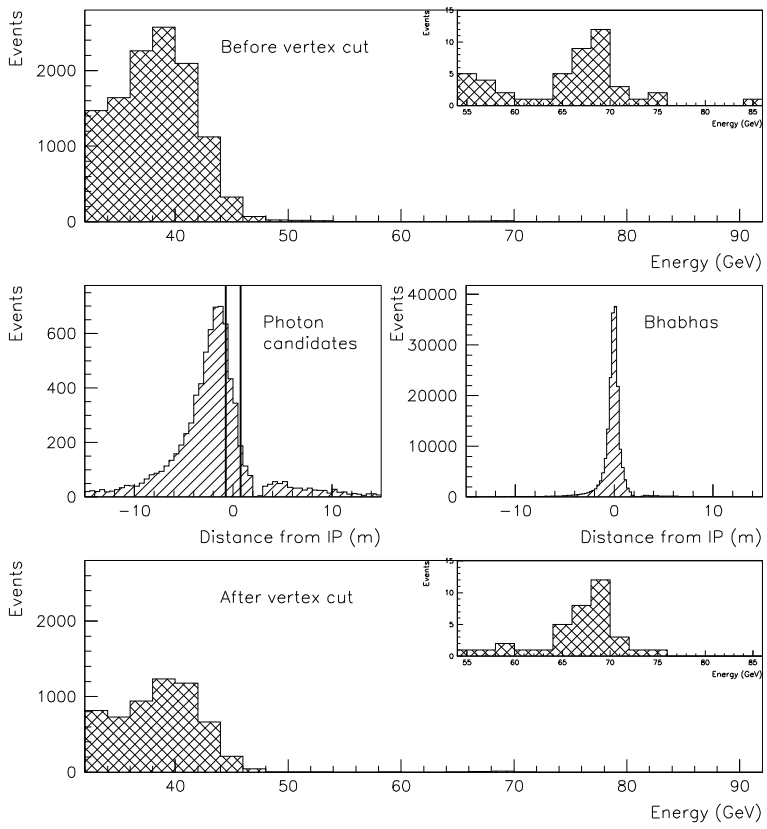

Figure 3: Illustration of the cut on the vertex reconstructed by the silicon-strip detectors. The figures in the center row show the distribution of reconstructed vertices for the sample of photon candidates at $\sqrt{s} = 183$ GeV, as well as that of a sample of Bhabha events, which are known to originate from the interaction point. Lines mark the cut at ± 75 cm on the vertices of the photon candidates. The top and bottom figures show the energy distributions of the photon candidates before and after the vertex cut.

electron background; this is discussed further in Section 4.2. Therefore, the best solution was to use a linear cut in the $x_\gamma - \theta$ plane in the region $0.3 \leq x_\gamma < 0.6$ and to omit entirely the region $x_\gamma < 0.3$, where it was not possible to obtain a satisfactory background rejection and where the efficiency of the neutral trigger was low. The two different methods developed into the following sets of cuts:

- Alternative 1: In the region $0.3 \leq x_\gamma < 0.6$, one uses the polar-angular acceptance $\theta_0 \leq \theta < 8.0°$, where θ_0 lies on the straight line between the points ($x_\gamma = 0.3$, $\theta = 6.5°$) and ($x_\gamma = 0.6$, $\theta = 4.2°$). Above $x_\gamma > 0.6$, one uses the polar-angular acceptance $4.2° - 8.0°$. These two areas will henceforth be called Region 1. In addition, Region 2 is defined by the cuts $x_\gamma > 0.6$ and $3.2° \leq \theta < 4.2°$. Region 1 has so little background contamination that it can be used without the vertex cut and the cut in the $r - \varphi$ plane. These cuts are, however, applied to Region 2.

- Alternative 2: Region 1 as described above is enlarged slightly for $\sqrt{s} = 183$ GeV and 172 GeV: the lower acceptance at $\theta = 4.2°$ is moved to $\theta = 3.8°$. For $\sqrt{s} = 161$ GeV, however, it remains at $\theta = 4.2°$. Region 2 is not used.

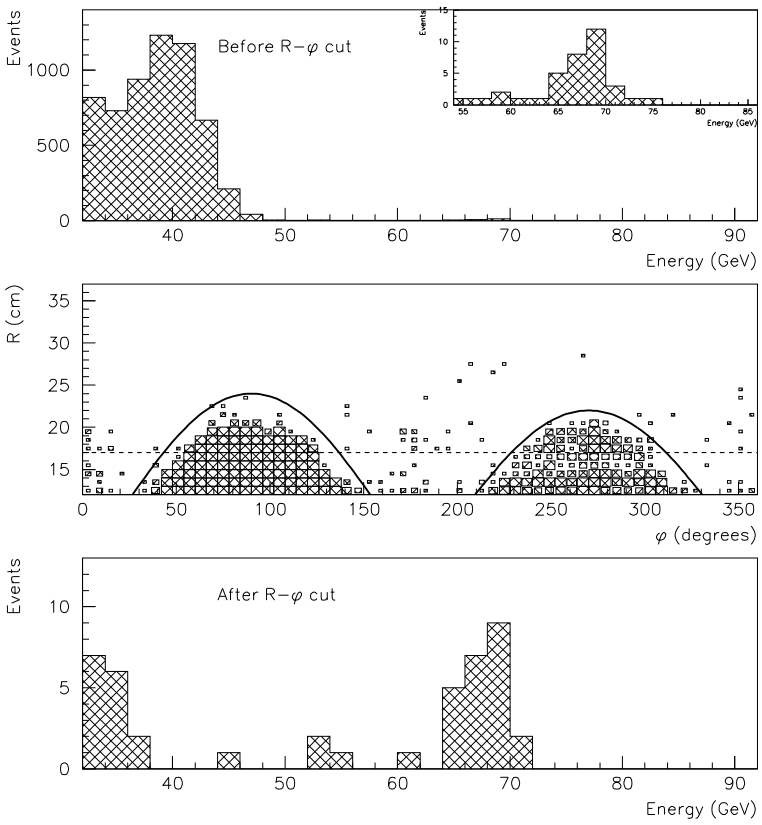

Figure 4: Illustration of the elliptical cut in the $r - \varphi$ plane. The center figure shows the two-dimensional distribution of the photon candidates in the $r - \varphi$ plane, for $\sqrt{s} = 183$ GeV. The curves drawn in the figure mark the cut. The dashed line shows the position of the outer edge of the silicon-strip detectors. The top and bottom figures show the energy distributions of the photon candidates before and after the $r - \varphi$ cut.

These two sets of cuts are illustrated in Figure 5.

4.1.2 Remaining Off-Energy Electron Background

The remaining off-energy electron background in the single-photon samples was estimated from the number of single-electron events surviving all of the selection cuts of the single-photon analysis, with the exception of the photon identification. This number was multiplied by a normalisation factor relating the size of the single-electron sample to the size of the single-photon sample. This factor was taken to be the ratio of single-photon candidates to single-electron events *inside* the ellipse described above; in both samples, the events in this region should come predominantly from off-energy electron background. At 183 GeV, the single-electron sample contained five times as many off-energy electrons as the single-photon sample. The final number of off-energy electron events contaminating the single-photon sample is shown, for each center-of-mass energy and each of the two analysis alternatives, in Table 1.

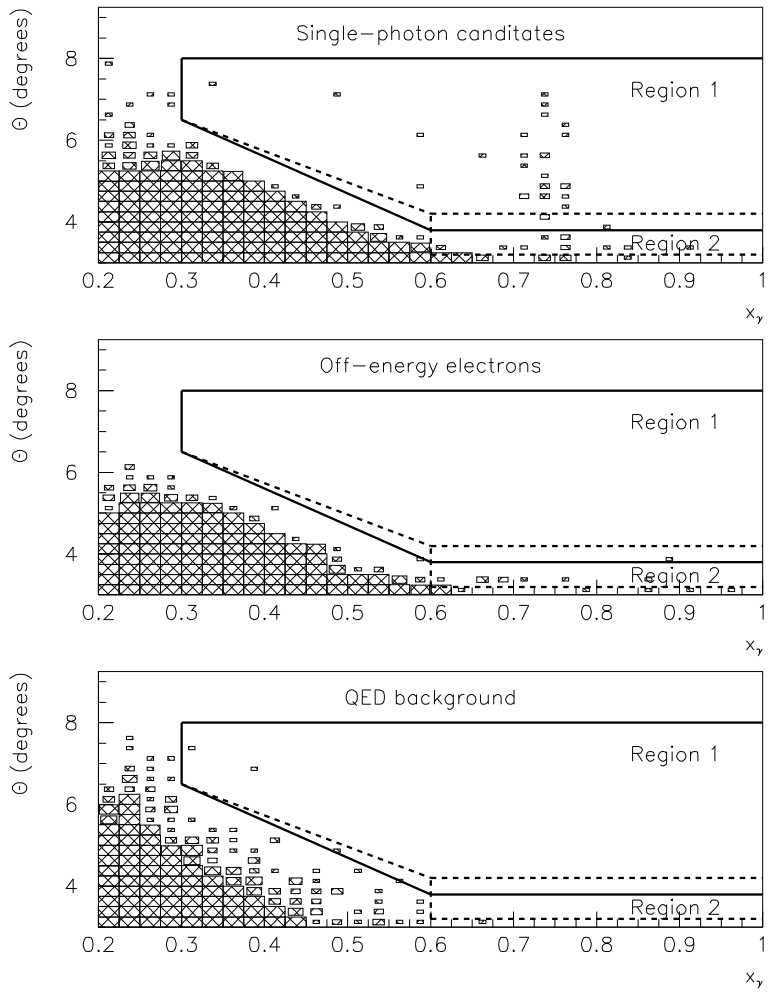

Figure 5: Polar angle *vs.* fraction of beam energy carried by the photon, for single-photon candidates (top), off-energy electron background (center), and simulated QED background (bottom), at $\sqrt{s} = 183$ GeV, after event selection and photon identification. The solid lines mark the boundaries of Region 1 used in the analysis without the silicon-strip detectors, i.e., in the final analysis. The dashed lines mark the boundaries of Region 1 and of Region 2 used in the analysis with the silicon-strip detectors. The number of events in each histogram corresponds to the integrated luminosity used in the analysis. A full box contains 10 events or more.

4.2 Background from QED with Both Electrons Lost in the Beam Pipe

The main source of photon background comes from the QED process $e^+e^- \to e^+e^-\gamma$, where the two electrons escape undetected along the beam pipe. One sometimes discriminates between radiative Bhabha scattering and Compton scattering, where Compton scattering indicates that the momentum transfer $q^2 \to 0$, i.e., the exchanged photon is (quasi)real and the scattering angle of one of the electrons is ~ 0.

The estimation of the QED background where the electrons are lost in the beam pipe was

CMS Energy	Analysis with Si-Strip Detectors		Analysis without Si-Strip Detectors	
	$0.3 \leq x_\gamma < 0.6$	$x_\gamma \geq 0.6$	$0.3 \leq x_\gamma < 0.6$	$x_\gamma \geq 0.6$
161 GeV	0	0	0	0
172 GeV	0	0	0	0
183 GeV	0	0.69 ± 0.40	0.23 ± 0.23	1.38 ± 0.56

Table 1: Number of events of off-energy electron background estimated to remain in the final data sample, for the three different center-of-mass energies and the two different analysis methods. The errors quoted are statistical.

done in two steps. DELSIM, the DELPHI detector simulation package [8], was used to establish the probability that an electron entering STIC would be detected, and hence that a QED event would be rejected, as a function of the polar angle at which it entered STIC. Radiative Bhabha scattering and Compton scattering events were then modeled with the Monte Carlo event generator TEEGG [9], which simulates the process $e^+e^- \to e^+e^-\gamma(\gamma)$ at low q^2. In this step, the detector response was not simulated; instead, the photon energy was smeared with a radius-dependent energy resolution corresponding to that measured previously with data.

The DELSIM studies, the results of which are shown in Figure 6, showed that the probability of detecting electrons at small polar angles varies considerably with the polar angle. Electrons entering the synchrotron mask inside the beam pipe, for instance, have a high probability of being detected due to energy leakage into the calorimeter. Electrons going through the tungsten shield have a probability of being detected varying from 0.1 to 1.0, depending on where they enter the shield and thus on the amount of material along their trajectories. Therefore, for the 183 GeV data, another cut was introduced, based on the data from the small veto counters in front of the tungsten shield. This required that no hits should have been recorded anywhere in the small veto counters, on either side. This cut removed some of the QED background at lower energies. A problem with corrupted discriminator/ADC information from the small veto counters prevented a similar cut in the 161 and 172 GeV analyses.

The simulations based on TEEGG showed that the energy spectrum of the photons coming from QED background of the type discussed here is highly dependent on the polar-angular region, and becomes softer with increasing polar angles. The two-dimensional $x_\gamma - \theta$ distribution of the simulated background is shown in Figure 5. This distribution has an almost triangular shape. The core of this type of QED background is confined to energies below $x_\gamma = 0.45$, and to polar angles below $\theta = 6.0°$. However, small parts of it extend to high energies at low polar angles ($x_\gamma \simeq 0.7$ at $\theta \simeq 3°$) and to large polar angles at low energies ($\theta \simeq 8°$ at $x_\gamma \simeq 0.2$).

It was mainly the QED background that made it necessary to omit the region $x_\gamma < 0.3$. It was also, as mentioned in Section 4.1, the QED background that determined the linear cut in the $x_\gamma - \theta$ plane in the region $0.3 \leq x_\gamma < 0.6$. These two cuts removed most, but not all, of the QED background.

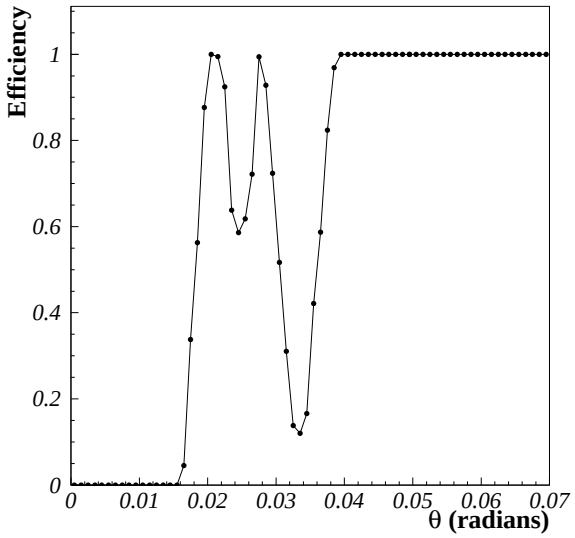

Figure 6: Probability of an electron being detected by STIC, as a function of the polar angle at which it enters the calorimeter. The electrons have an energy of 91.5 GeV, and the threshold for detection is 0.5 GeV. The peak in the efficiency at 0.020 comes from electrons showering in the synchrotron mask inside the beam pipe and leaking energy into STIC. The dip at 0.024 is due to electrons escaping below the calorimeter, whereas the peak at 0.027 is created by electrons entering STIC from below. The dip around 0.034 is caused by electrons entering the tungsten shield placed in front of STIC.

4.2.1 Remaining QED Background

The number of QED events with both electrons lost in the region below STIC that remained in the single-photon sample, after all cuts (including those of the two different methods described in Section 4.1) had been applied, was estimated with the TEEGG Monte Carlo samples. The results are shown in Table 2.

CMS Energy	Analysis with Si-Strip Detectors		Analysis without Si-Strip Detectors	
	$0.3 \leq x_\gamma < 0.6$	$x_\gamma \geq 0.6$	$0.3 \leq x_\gamma < 0.6$	$x_\gamma \geq 0.6$
161 GeV	0.10 ± 0.01	0.022 ± 0.005	0.10 ± 0.01	0
172 GeV	0.12 ± 0.02	0.005 ± 0.002	0.16 ± 0.02	0
183 GeV	0.12 ± 0.01	0.059 ± 0.008	0.20 ± 0.01	0.006 ± 0.002

Table 2: Estimated number of QED background events with both electrons escaping undetected that remain in the final data sample, for each of the three different center-of-mass energies and the two different analysis methods. The errors quoted are statistical.

4.3 Background from QED with One Electron Escaping Undetected in DELPHI

Radiative Bhabha scattering where one of the electrons enters DELPHI without being detected and the other is lost in the beam pipe also contributes to the background in the single-photon sample. This case was likewise studied with Monte Carlo simulations. TEEGG was used to generate $e^+e^-\gamma$ events with the photon in the STIC acceptance, the electron entering DELPHI above STIC ($\theta \geq 9^\circ$), and the positron escaping in the beam pipe. The electron (but not the photon) was then used as input to DELSIM. This configuration was seen to leave a contribution to the background in the region $x_\gamma \geq 0.6$. The quantitative estimate of the remaining background of this type in the different data samples is dealt with in Section 6, where the measured cross sections are discussed.

4.4 Other Sources of Background

Background types other than those discussed above were also investigated, but they were found to be of little or no importance to the single-photon analysis. They include cosmic events, Compton scattering on thermal photons, synchrotron radiation and detector noise.

Cosmic events sometimes give rise to single-photon candidates with a photon energy larger than the beam energy. These events were almost entirely eliminated by the requirement that no showers had been detected in HAC (see Section 3.1), and were assumed not to contribute to the background after that.

Compton scattering of beam particles on thermal photons in the beam pipe have been studied extensively at LEP [10]. These studies suggest that the average energy of the scattered photons is 2.2% of the beam energy at LEP2. This energy is too small for the photons to be seen in the analysis.

Photons originating from synchrotron radiation in the dipole and quadrupole fields of the LEP magnets have also been studied elsewhere [11], and have been found to have energies in the keV range. They are therefore of no concern to this analysis.

Detector noise has been observed to create fake events in STIC. The phototetrodes reading out the calorimeter occasionally generate large pulses, which give rise to clusters in the off-line shower reconstruction. These fake clusters were removed in the event selection by a requirement that a photon candidate should have a signal in at least nine adjacent towers. The efficiency of this selection criterion was estimated with data and Monte Carlo samples of hadronic radiative-return events ($e^+e^- \to \gamma + \text{hadrons}$) at 172 GeV. The efficiencies obtained were $96 \pm 2\%$ (data) and $99.0 \pm 0.1\%$ (Monte Carlo).

5 Comparison of Methods and Final Cuts

The two different sets of cuts discussed in the previous section gave very similar results in terms of number of events detected. The energy distributions, after imposing the cuts of each

method in turn, are shown in Figure 7. The rejection of off-energy electrons obtained with the cut on the vertex reconstructed by the silicon detectors was not sufficient to improve the analysis significantly. The rate of this type of background remained high even after the most seriously affected parts of the detector acceptance had been excluded with the $r-\varphi$ cut. It was not possible to enlarge further the region of phase space included in the analysis after the vertex and $r-\varphi$ cuts, and so the gain obtained by using the silicon detectors in the analysis was limited.

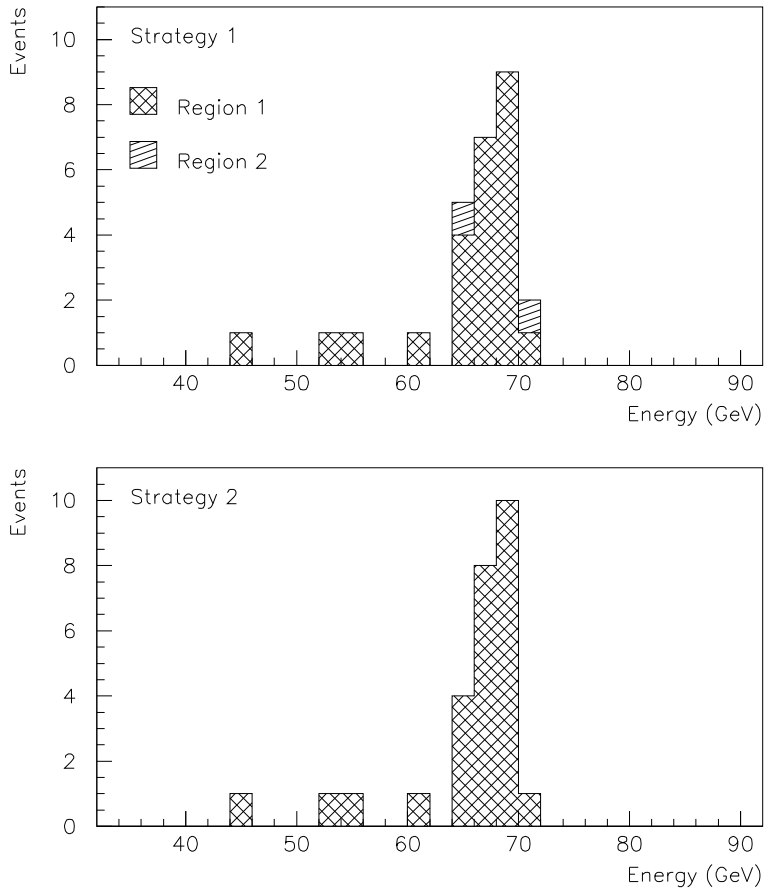

Figure 7: Energy distributions of single photons remaining when all cuts have been performed, for Regions 1 and 2 in the analysis with the silicon-strip detectors (top) and for Region 1 in the analysis without the silicon-strip detectors (bottom). $\sqrt{s} = 183$ GeV.

The total efficiencies of Regions 1 and 2, taking into account the efficiencies of the neutral trigger, the event selection, and the photon identification, and for Region 2 also the efficiencies of the vertex cut and of the $r-\varphi$ cut, depend on the photon energy and on the polar angle. An example, for a photon energy of 70 GeV, is shown in Figure 8. Due to the low efficiency of the cuts used in Region 2, one may argue that it is better to adopt the alternative using Region 1 only. This was the method chosen in a combined single-photon analysis at $\sqrt{s} = 183$ GeV, where STIC was one of the detectors used [1]. It is also the method used in the remainder of the analysis discussed here. The final cuts for each of the center-of-mass energies are listed in Table 3. The energy distributions of the final single-photon samples are shown in Figure 9.

CMS Energy	$0.3 \leq x_\gamma < 0.6$	$x_\gamma \geq 0.6$
161 GeV	$(6.5^\circ - 4.2^\circ) \cdot \frac{(x_\gamma - 0.6)}{(0.6-0.3)} + 6.5^\circ \leq \theta \leq 8.0^\circ$	$4.2^\circ \leq \theta \leq 8.0^\circ$
172 GeV	$(6.5^\circ - 3.8^\circ) \cdot \frac{(x_\gamma - 0.6)}{(0.6-0.3)} + 6.5^\circ \leq \theta \leq 8.0^\circ$	$3.8^\circ \leq \theta \leq 8.0^\circ$
183 GeV	$(6.5^\circ - 3.8^\circ) \cdot \frac{(x_\gamma - 0.6)}{(0.6-0.3)} + 6.5^\circ \leq \theta \leq 8.0^\circ$	$3.8^\circ \leq \theta \leq 8.0^\circ$

Table 3: Final cuts in the $x_\gamma - \theta$ plane, where x_γ is the fraction of the beam energy carried by the photon and θ the polar angle, for the different center-of-mass energies.

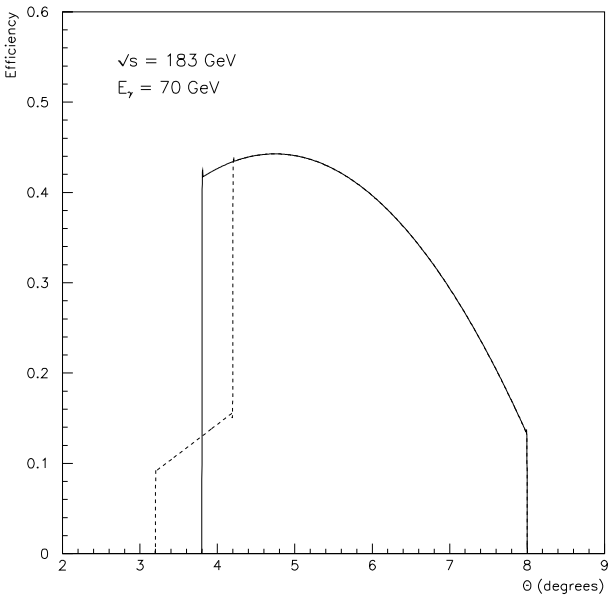

Figure 8: Total efficiency of the full selection procedure as a function of azimuthal angle measured by the calorimeter. The efficiency is shown for a photon energy of 70 GeV and a center-of-mass energy of 183 GeV. The continuous line shows the efficiency for Region 1 as defined in the final analysis, and the dashed line shows the efficiency for the modified Region 1 and the added Region 2. The total efficiency includes the efficiencies of the neutral trigger, the event selection, and the photon identification. For Region 2, it also includes the efficiencies of the vertex cut and the elliptical cut in the $r - \varphi$ plane.

6 Cross Sections

Events where the photon carries a fraction of the beam energy $x_\gamma \geq 0.6$ were selected for a measurement of the cross section in the radiative-return region. The measured efficiencies and background contributions were summed and used to calculate the cross section $\sigma(e^+e^- \to \gamma + \text{invisible})$ for each of the four center-of-mass energies. The results are shown in

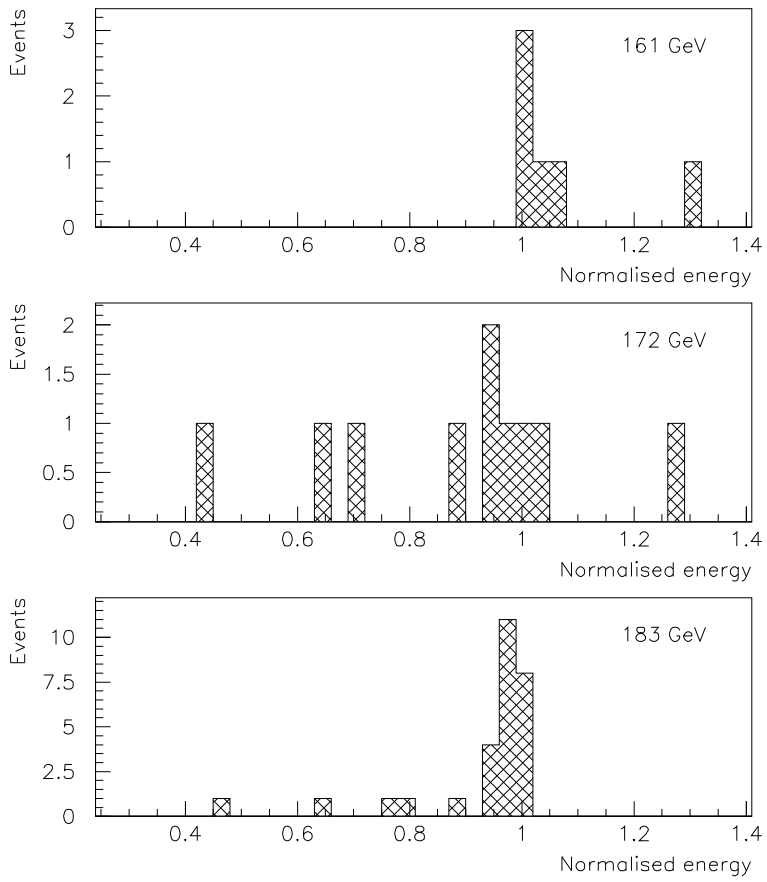

Figure 9: Energy distributions of the final single-photon samples (Region 1 only) for the different beam energies used in the analysis. The energy was normalised to that of the radiative-return peak for each data sample.

Table 4.

The systematic error of the measured cross sections is 11%. The dominant uncertainty comes from the estimation of identification and trigger efficiencies (7% and 6% respectively), together with the estimation of the remaining background (6%). Other sources of uncertainty are the luminosity (1%) and the energy scale of the calorimeter (1%). The individual errors were added in quadrature. They were considered to be the same for all three center-of-mass energies.

7 The Number of Neutrino Families

The cross sections measured for the single-photon production were compared to the theoretical cross sections for the process $e^+e^- \to \gamma\nu\bar{\nu}$. The number of neutrino families, N_ν, was calculated, under the assumption that the only contribution to the single-photon final state comes from neutrino production. The cross section for the process $e^+e^- \to \gamma\nu\bar{\nu}$ is directly proportional to the number of neutrino species.

CMS Energy	161 GeV	172 GeV	183 GeV
Int. Luminosity (pb^{-1})	10.02	9.97	52.0
Events	6 ± 2.4	7 ± 2.6	24 ± 4.9
Events/Efficiency	16.3 ± 6.6	17.1 ± 6.4	59.0 ± 12.0
Off-Energy Background	0	0	1.38 ± 0.56
QED Background I	0	0	0.006 ± 0.001
QED Background II	0.09 ± 0.09	0.09 ± 0.09	0.45 ± 0.45
Corr. Cross Section (pb)	1.60 ± 0.66	1.69 ± 0.65	1.08 ± 0.23

Table 4: Corrected cross sections for $e^+e^- \to \gamma +$ invisible in STIC at different center-of-mass energies. Only the region $x_\gamma \geq 0.6$ was used. QED Background I refers to the configuration in which both electrons are lost in the beam pipe, and QED Background II refers to that with one electron lost in the beam pipe and the other escaping undetected above STIC. The errors quoted are statistical.

The theoretical cross sections corresponding to the existence of three neutrino families were calculated with two different Monte Carlo event generators, NUNUGPV [12] and KORALZ [13]. The measured and the expected cross sections for the region $x_\gamma \geq 0.6$ of each center-of-mass energy are shown in Table 5. The cross sections calculated with KORALZ for this region are consistently lower than those calculated with NUNUGPV. A comparison of the energy distributions of the photon shows that the reason for this is that the distributions generated with KORALZ have a lower radiative-return peak with wider tails than the corresponding distributions generated with NUNUGPV. This difference is due to different ways in which the contribution from processes such as $e^+e^- \to \gamma\gamma\nu\bar{\nu}$, where one photon escapes undetected along the beam pipe, is calculated in the two event generators. The distributions generated with NUNUGPV seem to be in better agreement than those of KORALZ with the true photon distributions. A comparison between the energy distribution of the final event sample at $\sqrt{s} = 183$ GeV and the distribution predicted by NUNUGPV is shown in Figure 10.

NUNUGPV was used to determine the theoretical production cross sections for two, three and four neutrino families respectively. A straight line was fitted to the three points, and the number of neutrino families was determined from this line in combination with the corresponding measured cross section. This is illustrated in Figure 11. The number of neutrinos obtained at each center-of-mass energy is shown in Table 5. Averaging the number of neutrinos measured at the different center-of-mass energies, one obtains

$$N_\nu = 3.2 \pm 0.5 \pm 0.4.$$

The number of neutrino families calculated from the measurements with STIC at different center-of-mass energies are shown in Figure 12. For comparison, results obtained from other measurements with the FEMC and HPC calorimeters [1] are also shown. The significance of the STIC measurement is seen to be compatible with those from FEMC and HPC, despite the constraints imposed on the STIC analysis by the difficult background conditions.

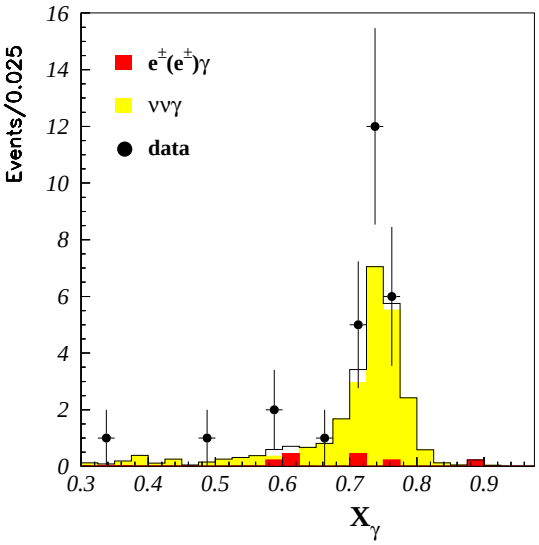

Figure 10: Energy distribution of the final event sample, together with the expected contribution from the process $e^+e^- \to \gamma\nu\bar{\nu}$ as calculated with NUNUGPV, and also with the contribution from the various background sources. $\sqrt{s} = 183$ GeV.

CMS Energy	Measured and Corrected Cross Section (pb)	Expected Cross Section (pb) NUNUGPV	KORALZ	Number of Neutrino Species
161 GeV	1.85 ± 0.76	1.46 ± 0.03	1.35 ± 0.03	3.80 ± 1.56
172 GeV	1.69 ± 0.65	1.26 ± 0.03	1.21 ± 0.03	4.02 ± 1.55
183 GeV	1.08 ± 0.23	1.09 ± 0.02	1.06 ± 0.03	2.97 ± 0.63

Table 5: Measured and expected cross sections for $e^+e^- \to \gamma\nu\bar{\nu}$, and the corresponding number of neutrino families, for the different center-of-mass energies. Only the region $x_\gamma \geq 0.6$ was used. The cross section at $\sqrt{s} = 161$ GeV is given for the same acceptance as the one at 172 and 183 GeV.

8 Conclusions

The calorimeter STIC has been used, for the first time, to identify and analyse events with a photon in the very forward region of DELPHI. Samples of single-photon events, where the photon had entered STIC, were analysed for center-of-mass energies of 161, 172, and 183 GeV. The single-photon events were used to explore the possibilites of using STIC to identify photons while maintaining control over the difficult background situation caused by the large number of off-energy electrons and by radiative Bhabha scattering.

A satisfactory background rejection was obtained with a set of cuts on the polar-angular acceptance and on the fraction of the beam energy carried by the photon. A combination of a cut on the vertex reconstructed by the STIC silicon detectors and a cut in the $r - \varphi$ plane was

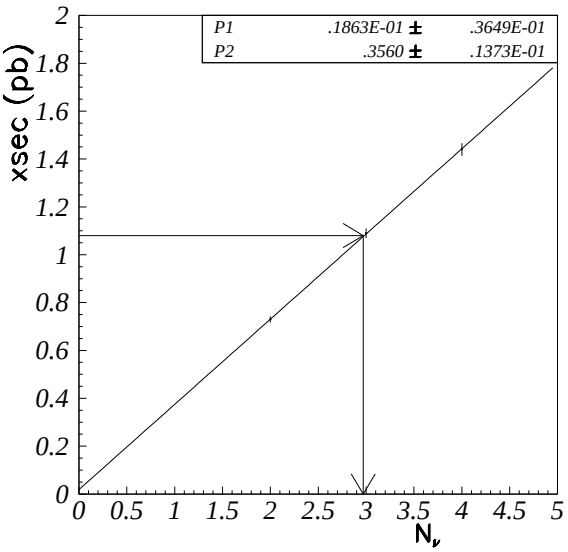

Figure 11: Theoretical cross section, as a function of the number of neutrino families, N_ν, for $\sqrt{s} = 183$ GeV. The cross sections for two, three and four neutrino families were calculated with NUNUGPV, and a straight line was fitted to the points. As the arrows indicate, the measured cross section, 1.09 pb, corresponds to $N_\nu = 2.97$.

tried and would have allowed the use of a somewhat larger region of phase space. However, the added region did not improve the significance of the analysis.

The measured cross sections for single-photon production were compared with the theoretical predictions for the process $e^+e^- \to \gamma\nu\bar{\nu}$ of two different Monte Carlo event generators, NUNUGPV and KORALZ. NUNUGPV was found to have a somewhat better agreement with data and was used to calculate the number of neutrino families.

The results of the measurement of the number of neutrino families were compared with those obtained from single-photon analyses carried out with the FEMC and HPC calorimeters. The results from STIC were competitive with those of FEMC and HPC, despite the very difficult background situation.

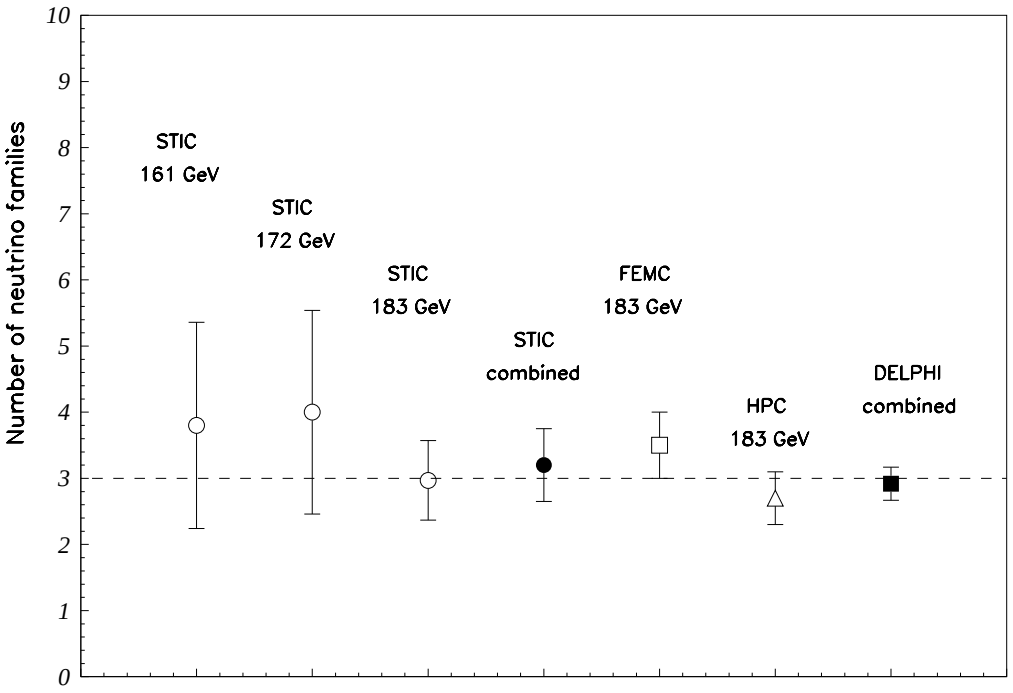

Figure 12: Number of neutrino families measured with STIC at different center-of-mass energies, together with the result of the individual measurements combined. For comparison, results obtained from measurements with the FEMC and HPC calorimeters, as well as the number obtained from combining all measurements with the three calorimeters, are also shown.

References

[1] E. Falk *et al.*, DELPHI 98-55 PHYS 780.

[2] DELPHI Collaboration, P. Abreu *et al.*, Eur. Phys. J. C1 (1998) 1;
DELPHI Collaboration, P. Abreu *et al.*, Phys. Lett. B380 (1996) 471;
DELPHI Collaboration, P. Abreu *et al.*, Z. Phys. C74 (1997) 577.

[3] S.J. Alvsvaag *et al.*, Nucl. Phys. B, Proc. Suppl. 44 (1995) 116; also available as DELPHI 95-12 CAL 119;
S.J. Alvsvaag *et al.*, IEEE Trans. Nucl. Sci. 42 (4) (1995) 478; also available as DELPHI 94-157 CAL 120;
S.J. Alvsvaag *et al.*, in H.A. Gordon and D. Rueger, eds., "Proceedings of the 5th International Conference on Calorimetry", World Scientific Publishing Co., Singapore 1995; also available as DELPHI 94-148 CAL 118;
S.J. Alvsvaag *et al.*, in H.S. Chen, ed., "Proceedings of the Beijing Calorimetry Symposium", IHEP, Beijing 1995; also available as DELPHI 95-14 CAL 123.

[4] P. Ferrari and V. Hedberg, DELPHI 98-49 CAL 141.

[5] S.J. Alvsvaag *et al.*, Nucl. Inst. and Meth. A360 (1995) 219; also available as DELPHI 94-126 CAL 117;
S.J. Alvsvaag *et al.*, IEEE Trans. Nucl. Sci. 42 (4) (1995) 469; also available as DELPHI 94-158 CAL 121;
S.J. Alvsvaag *et al.*, DELPHI 95-13 CAL 122; contribution to the 4th International Conference on Advanced Technology and Particle Physics, Como, Italy, October 1994.

[6] E. Falk, V. Hedberg and G. von Holtey, DELPHI 97-12 LEDI 8; also available as CERN SL/97-04 (EA).

[7] E. Falk, V. Hedberg and I. Gouz, DELPHI 98-43 CAL 140.

[8] DELPHI collaboration, DELPHI 89-67 PROG 142;
DELPHI collaboration, DELPHI 89-68 PROG 143.

[9] D. Karlen, Nucl. Phys. B289 (1987) 23.

[10] V.I. Telnov, Nucl. Inst. and Meth. A260 (1987) 304;
B. Dehning *et al.*, Phys. Lett. B249 (1990) 145;
C. Bini *et al.*, Phys. Lett. B262 (1991) 135;
C. Bini *et al.*, Nucl. Inst. and Meth. A306 (1991) 467;
H. Burkhardt, SL note 93-73;
G. von Holtey *et al.*, CERN-SL/97-40 (EA).

[11] G. von Holtey, CERN SL/95-29 (EA).

[12] G. Montagna *et al.*, Nucl. Phys. B452 (1995) 161.

[13] S. Jadach *et al.*, Comp. Phys. Comm. 66 (1991) 276;
S. Jadach *et al.*, Comp. Phys. Comm. 79 (1994) 503.

Article IV

Simulation of Off-Energy Electron Background in DELPHI

DELPHI Collaboration DELPHI 97-12 LEDI 8
24 February 1997

Simulation of Off-Energy Electron Background in DELPHI

E. Falk, V. Hedberg
Department of Physics, University of Lund, Lund, Sweden
G. von Holtey
CERN

Abstract

Monte Carlo simulations of off-energy electron background in the DELPHI luminometer STIC are reported. The study simulates the running conditions at 68 GeV with and without bunch trains. The electrostatic separators, which create the vertical separation bumps for the bunch trains, cause a high concentration of background in the vertical plane. The simulations are compared to LEP data taken under similar running conditions. A comparison between the simulated running conditions at 68 GeV and those of the new LEP2 beam optics at 80.5 GeV is made. Moreover, the study investigates background components entering STIC elsewhere than through the front of the detector, and a significant portion is found to enter either from the back or from below. Possible improvements of the background situation are also discussed.

EUROPEAN ORGANIZATION FOR NUCLEAR RESEARCH

European Laboratory for Particle Physics

CERN - SL DIVISION

CERN SL/97-04(EA)

Simulation of Off-Energy Electron Background in DELPHI

E. Falk, V. Hedberg
Department of Physics, University of Lund, Lund, Sweden
G. von Holtey
CERN

Abstract

Monte Carlo simulations of off-energy electron background in the DELPHI luminometer STIC are reported. The study simulates the running conditions at 68 GeV with and without bunch trains. The electrostatic separators, which create the vertical separation bumps for the bunch trains, cause a high concentration of background in the vertical plane. The simulations are compared to LEP data taken under similar running conditions. A comparison between the simulated running conditions at 68 GeV and those of the new LEP2 beam optics at 80.5 GeV is made. Moreover, the study investigates background components entering STIC elsewhere than through the front of the detector, and a significant portion is found to enter either from the back or from below. Possible improvements of the background situation are also discussed.

Geneva, Switzerland
February 1997

1 Introduction

A simulation study of off-energy electron background in the DELPHI luminometer STIC has been carried out. The purpose of the simulation was to gain a better understanding of phenomena seen in data taken during the third running period (P3) of 1995. During this period, which took place in November 1995, LEP was operated at 68 GeV in bunch-train mode (albeit with only one and two wagons). This running period was the first in which the DELPHI experiment used a trigger aimed at selecting single-photon events in STIC. This so-called neutral trigger, which provides $e-\gamma$ separation, requires an energy deposit in one of the two STIC calorimeters in conjunction with an absence of signals in the scintillator planes in front of the calorimeters. It was immediately apparent that this trigger was very sensitive to off-energy electron background. Not only did off-energy electrons that entered STIC without passing the scintillation counters fire the trigger, but also electrons that arrived from the front did so because of counter inefficiencies.

Previously, the OPAL experiment reported an increase in off-energy electron background in their luminosity analysis when LEP began operating in bunch-train mode at 45 GeV [1]. A simulation of this background showed that an increase of the background in the vertical plane was due to the electrostatic separators that create the vertical separation bumps for the bunch trains of the counter-rotating beams in LEP.

In DELPHI, this background does not enter the sample of Bhabha events used in the luminosity measurement, because in this analysis only high-energy back-to-back electron-positron pairs are taken into account. The radial distribution of off-energy electrons is very steep, and since the inner acceptance for Bhabha electrons is at a larger radius in DELPHI than it is in OPAL, DELPHI also has a lower acceptance for off-energy electrons.

In single-photon analysis, however, DELPHI typically triggers on several thousand off-energy electrons for every true single-photon event. For this reason, a study of this background in DELPHI together with a simulation of off-energy electrons was carried out in order to investigate what the optimal running conditions of LEP may be, and also to determine whether the neutral trigger might be improved. The simulations were done at beam energies of 68 GeV and 80.5 GeV, imitating the running conditions of the third LEP period (P3) in 1995 and the first period (P1) in 1996.

2 STIC

The luminosity monitor STIC consists of two lead-scintillator calorimeters of shashlik type, read out by wavelength-shifting fibers. These are located on either side of the interaction point at a distance of 2.2 m [2]–[5]. The two calorimeters are usually referred to as arm A and arm C, according to the DELPHI convention of calling the side of incoming electrons side A and that of positrons side C; see Figure 1.

Each of the STIC calorimeters is equipped with two planes of silicon-strip detectors with which the direction of a shower can be measured. The purpose of this tracking device is to

improve rejection of off-energy electron background. A veto system consisting of two layers of scintillator is mounted in front of each arm of STIC. This veto system is part of the neutral trigger discussed above.

Several tungsten masks and shields are mounted on and near STIC. A so-called tungsten nose is mounted on the front face of the calorimeter on side C (but not on side A), and is used to define the acceptance for Bhabha electrons in luminosity measurements. A synchrotron radiation mask is mounted underneath each arm of STIC, inside the beam pipe, and these masks protect the DELPHI TPC from synchrotron radiation. Furthermore, a "tungsten shield", mounted on the tungsten nose, provides additional radiation protection to the TPC.

Figure 2 shows an outline of a STIC calorimeter with the silicon planes and the veto counters marked. The location of masks, nose and shields are also indicated. Each calorimeter is divided into 10 radial rings and 16 azimutal sectors, thus giving a total of 160 towers which point to the interaction region (see Figure 3). The dimensions of some of the beam-pipe components, the tungsten masks and the detectors are given in Table 1.

3 Simulation Program

The simulations were carried out with the CERN library program Decay Turtle [6], which simulates beams of charged particles through transport systems. It was modified both to include decay calculations that handle bremsstrahlung on residual gas molecules and to incorporate electrostatic separators in the beam transport line. A length of approximately 650 m of the LEP beam line was simulated, beginning at the quadrupole QF23 that lies 640 m upstream of the DELPHI interaction point. The program does not simulate energy loss in material, and any interaction with material results in full interception in this study.

The program assumes constant vacuum pressure (10^{-9} Torr) along the beam line. In reality, the vacuum pressure is known to differ between different sections of LEP and also within sections over time. Unfortunately, it is not possible to find out retroactively what the actual vacuum pressures were during a certain running period. The rate of off-energy electron background is proportional to the vacuum pressure.

The simulations were carried out at a beam energy of 68 GeV, with bump amplitudes of 50%, 80% and 100% of maximum amplitude of the vertical separation bump. (Maximum amplitude is obtained at voltages of 260 keV, 57 keV and 190 keV on the electrostatic separators ES.QS2, ES.QS4 and ES.QS7 respectively.) These conditions correspond to the LEP operating modes of fills 3182, 3183 and 3186 of November 1995, which are the fills that have been used for comparisons of the simulations with data. Simulations were also made with a beam energy of 80.5 GeV and a bump amplitude of 100%. This resembles the running conditions of period P1 of July–August 1996. 100% bump amplitude at 68 GeV beam energy corresponds to a maximum vertical displacement of the beam by 8.4 mm at the location of the quadrupole QS4. (The maximum beam displacement is inversely proportional to the beam energy and hence decreases for higher energies.) For comparison, simulations were also made without vertical separation bumps, again at 68 GeV. The layout of the vertical separation bump is shown in Figure 4.

The simulation set-up was chosen to imitate the electron beam coming in toward interaction point 8. The impact on the front plane of arm C of STIC was studied, both with and without the tungsten nose in front of the calorimeter; again, see Figures 1 and 2. This set-up corresponds to a negative bump polarity with a vertical axis pointing upwards. The opposite, *i.e.,* a positive bump polarity, is true for the positron beam hitting arm A, and the simulation of off-energy electron background of this arm is simply reversed with respect to the vertical axis compared to that of arm C.

Throughout the study, a cut was used to eliminate particles of energy less than 10 GeV. A similar cut was imposed on the STIC trigger, where events with reconstructed shower energies below 10 GeV were discarded.

4 Simulation: Comparison Between No Bump and Full Bump Amplitude

A comparison of the results of the 68 GeV simulations at zero and 100% bump amplitude shows several interesting features which appear when the electrostatic separators creating the bumps are switched on. Figure 5 shows plots of the shower energy deposited in the different calorimeter sectors for these two cases.

Without a vertical bump, the vast majority of the background is located in the horizontal plane. The energy spectrum shows a peak around 45 GeV with a tail towards lower energies. When the electrostatic separators are switched on, a large part of the background is shifted from the horizontal plane into the vertical plane. Peaks appear around 20 GeV in the lower part of the calorimeter and around 35 GeV in the upper part. Moreover, the background is clustered in a few relatively distinct groups. This grouping is related to where in the beam transport system the background was created, which will be discussed below. In order to facilitate a comparison with data, the following classification, illustrated in Figure 5 and in Table 2, was made: Particles entering sectors 1, 8, 9 and 16 belong to the horizontal group; particles entering sectors 11–14 belong to the vertical parallel group; and particles entering sectors 3–6 belong to the vertical antiparallel group. The names parallel and antiparallel refer to the direction of the deflection of the particles of these two groups with respect to that of the first deflection of the bunch-train bump. The vertical parallel group enters arm C in the upper part of the calorimeter and arm A in the lower part; the opposite is true for the antiparallel group.

4.1 Energy Distribution

The energy distributions with no bump and with full bump are shown for each of the three groups in Figure 6. These plots confirm the peaks that appear in Figure 5b when the electrostatic separators are switched on. They are centered at 46 GeV in the horizontal plane, at 22 GeV in the vertical antiparallel group and at 36 GeV in the vertical parallel group. A second peak at approximately 35 GeV also appears in the antiparallel group, as well as a long tail of

horizontal background with energies down to 10 GeV.

The two latter background components are clearly different from the main peaks of the horizontal and the vertical antiparallel groups respectively. Therefore, these two azimuthal groups were divided into a low-energy and a high-energy subgroup, with the division between the two at 25 GeV.

The high-energy component of the horizontal background seems relatively unaffected by the electrostatic separators, while the horizontal background swept into the vertical plane by the separators is mainly of lower energy.

4.2 Origin of Background

Each of the five groups described above originates from a specific part of the beam line upstream of the interaction point. Figure 7 shows the distances from the interaction point at which the backgrounds are created. The particles of the high-energy horizontal group are created beyond a distance of 106 m, or upstream of the quadrupole QS6. The high-energy vertical antiparallel group also originates from this part of the beam line, mainly immediately upstream of QS6. The low-energy horizontal group is created in the section between the interaction point and the electrostatic separator ES.QS2, located 24 m upstream of the interaction point. The low-energy antiparallel group originates from the region between ES.QS2 and the quadrupole pair QS3 and QS4, located 58.0 m and 64.2 m respectively upstream of the interaction point. Finally, the vertical parallel group is created in the section between QS3/QS4 and QS6.

4.3 Radial Distribution

The radial distribution also reveals interesting differences between the various groups, as Figure 8 shows. The radii are measured on the front face of the calorimeter. The distributions for the two horizontal groups extend from the inner edge of the calorimeter at 65 mm to approximately 110 mm, where the distributions are sharply cut. This is true both for a full vertical bump and for no bump at all. The sharp cut is the shadow of the synchrotron radiation mask *upstream* of the interaction point, *i.e.,* of the mask located inside the *opposite* arm of STIC. Simulations show that the radial distributions of the horizontal groups would extend to about 250 mm were it not for this mask.

The vertical groups, on the other hand, are not affected by the synchrotron radiation mask. The low-energy antiparallel group extends radially to over 200 mm, as does the parallel group. The upper radial limit for the high-energy antiparallel group is at approximately 150 mm.

The upper limit for the radial distribution is hardly affected by the presence of the vertical bump. The main difference in radial distribution is the relative occupancy of the different groups, the principal effect of the bump separators on the background being the transition from the horizontal to the vertical plane.

5 Comparison Between Data and MC

The simulated background has been compared to data taken during the 1995 P3 run at 136 GeV center-of-mass energy. Three fills have been studied, numbers 3182, 3183 and 3186, with bump amplitudes of 50%, 80% and 100% respectively. The last fill contains a small number of events, and the comparison presented here will concentrate on the other two fills. As discussed in Section 3, no interactions between the off-energy electrons and material were simulated. Detector effects causing a smearing in the energy and position measurements have also been ignored. All off-energy electrons in the simulation enter the calorimeter from the front, while in the data they may also enter STIC from behind or from below (*i.e.,* inside the hole for the beam pipe). This will be discussed further in Section 6. In addition, possible variations of the vacuum pressure during and between the data-taking periods have not been taken into account.

Despite the limitations of the Monte Carlo study, the data show clear evidence for all three major background components predicted by the simulation, as seen in Figures 9 and 10. The low-energy and the high-energy parts of the horizontal and the vertical antiparallel components are also present in the data, but, for the reasons given above, not necessarily with the same relative magnitude as in the simulation.

5.1 The Horizontal Background Component

In Section 4.3 it was pointed out that the Monte Carlo simulation has a sharp cut in the radial distribution at a radius of 110 mm due to the synchrotron mask. This cut is also clearly visible in the data (see Figures 11 and 12).

The histograms of the data from side C show many events having a reconstructed radius less than that of the tungsten nose and with an energy around 15 GeV. These events are of course not present in the simulation. A closer analysis of the data shows that these background electrons leave signals neither in the veto counter in front of the calorimeter nor in the silicon-strip detectors inside the calorimeter. Therefore, it is most likely that they enter STIC from behind or from below.

The two regions in the Monte Carlo energy distribution which are caused by electrons being created in different parts of LEP are also observed in the data. However, the high-energy peak seems to be less significant in the data than in the simulation. In the data, the low-energy peak overlaps with the peak from electrons coming from below and from behind; this background is peaked at a somewhat lower radius than the electrons entering from the front.

In the data from side A, which has no tungsten nose, there are many electrons with energies between the two peaks. Data from the veto counters show that these events typically have hits in a third or more of the sectors of the counters. This is an indication that these electrons come from the front, and that they have pre-showered before entering the calorimeter. Electrons entering STIC at low radii go through a very thick beam pipe (68 mm for electrons entering at the inner acceptance of STIC), and they also pass through a 44 mm thick beam-pipe flange and part of the beam-pipe bellows located nearby, which electrons entering STIC at higher radii do not (see Table 1). It is therefore likely that part of the high-energy background interacts with

the material at low angles and is detected in STIC at lower energies.

5.2 The Vertical Antiparallel Background Component

The simulation of the vertical antiparallel background shows distinct low-energy and high-energy groups in the radius-energy histograms, giving rise to two peaks in the energy distribution (see Figure 12). These groups are, as pointed out earlier, produced in different parts of LEP. These bands are also seen in the data (see Figure 11), where they are wider, probably because of the finite detector resolution. The relative number of events in the low- and the high-energy groups are different in data and in Monte Carlo, but this could be explained by the assumption of a constant vacuum pressure in LEP in the simulation. A higher pressure in a particular section of the beam line would give rise to more background electrons being created in that section.

Another difference between Monte Carlo and data is the presence in the latter of a low-radius band on side A (but not on side C). These events have multiple hits in the veto counters and are probably, as in the horizontal case, produced through interactions between high-energy electrons and material at low angles.

5.3 The Vertical Parallel Background Component

For the vertical parallel background component, the simulation predicts one band in the radius-energy plots with a broad peak at 30 GeV. This is in good agreement with the data (see Figures 11 and 12).

There is also a low-radius band with many veto-counter hits in the data from side A, and again, these events are most likely to be caused by interactions in and around the beam pipe.

6 Off-Energy Electrons Entering STIC Elsewhere than Through the Front

The sharp shadow of the upstream synchrotron radiation mask seen in simulations as well as in data indicates the possibility that off-energy electrons enter STIC upstream of the interaction point, *i.e.,* from behind. Electrons entering the calorimeter from behind would not leave a signal in the veto counters, and they would thus incorrectly fire the neutral trigger discussed in Section 2. Therefore, the radial distribution of each of the background groups was studied in detail at certain points along the beam line. The points were chosen as illustrated with arrows in Figure 13, so that they would correspond to: particles entering arm A either from behind or from below; particles entering arm C either from the front face or from below; particles escaping through the gap between STIC and the synchrotron radiation mask on side A and then hitting the front face of arm C; and particles being stopped by one of the two synchrotron radiation masks. Particles reaching the front face of arm C were treated separately depending on the radius being larger or smaller than that of the tungsten nose. The simulations were carried

out with a beam energy of 68 GeV, at 50% and 100% bump amplitudes, and the results are illustrated in Figures 13 and 14 respectively.

6.1 Background Entering STIC From the Front

With a bump amplitude of 50%, about 84% of the particles entering STIC enter from the front. Of these, 8% enter STIC in the hole for the beampipe, *i.e.,* below the tungsten nose. With all groups combined, 45% of the particles entering STIC enter the front face in the region covered by the tungsten nose. Most of these belong to the horizontal groups, which are concentrated below 110 mm in radius due to the shadow of the synchrotron radiation mask. As a result, the horizontal background on side C is almost entirely stopped by the tungsten nose, and the vertical background becomes dominant instead.

6.2 Background Entering STIC From the Back

Most of the particles entering from the back, about 3/4 at 50% bump amplitude, belong to the high-energy horizontal group. No particles of the high-energy antiparallel group and hardly any of the parallel group enter STIC in this way. Particles that enter STIC in ways other than through the front face do not follow the projective geometry of STIC. When this happens, the energy is not necessarily correctly reconstructed in the off-line data processing; in fact, the calculated energy may well be too low. Since a large part of the background concerned comes from the high-energy horizontal group, this could account for some of the difference in quantity between data and simulation seen in the low-energy horizontal group.

About 6% of the particles entering STIC pass between the calorimeter and the synchrotron radiation mask on side A and enter the front face of arm C at a radius of approximately 150 mm, *i.e.,* above the tungsten nose.

6.3 The Synchrotron Radiation Mask

In addition to the above, about 18% as many particles as enter STIC hit the synchrotron radiation mask from the back and about 30% hit the mask from the front at 50% bump amplitude. Those being stopped by the mask on side A belong almost exclusively to the horizontal groups, and simulations without the mask show that they would all have entered the front of side C had the mask not been there. On the other hand, those particles which are stopped by the mask on side C would not have entered the calorimeter in the absence of the mask. However, it is possible that some of the energy of these particles leaks into the calorimeter from underneath; due to the limitations of the simulations, it is beyond the scope of this study to resolve this question.

7 LEP2

Between 1995 and 1996, LEP underwent major upgrades, and the beam energy was increased from 68 GeV at the end of 1995 to 80.5 GeV during the first running period of 1996. The effects of these machine modifications to the background situation were investigated through simulations of the new beam optics with a beam energy of 80.5 GeV. The only significant effect observed is an increase of the background energy, which scales linearly with the beam energy for each of the different background groups (see Figure 15). The qualitative behavior of these groups, and in particular, their radial distributions, remain practically unaltered.

8 Can the Off-Energy Electron Background be Reduced?

8.1 LEP Running Conditions

The exposure of STIC to off-energy electrons can be reduced by closing the nearest collimators, vertical COLV.QS1 and/or horizontal COLH.QS1, and by changing the amplitude of the vertical separation bump.

Closing the vertical collimator COLV.QS1 would reduce the vertical parallel and the vertical antiparallel high-energy background below a collimator half-opening of 40 mm, as shown in Figure 16. The standard setting used for COLV.QS1 in 1995 was 33 mm, which reduced the background rates from these two groups by approximately 30%. In 1997, this collimator will be moved from its present location at 8.5 m from the interaction point upstream to a new location at 15 m from the interaction point, where it will be called COLV.QS2. The effect of closing the collimator in its new location is shown in Figure 17. Here, the collimator must be closed to below 20 mm before it begins to have any effect on the rate of vertical background. On the other hand, the beam is also much narrower, and it would be possible to close the collimator to perhaps 13 mm. This would reduce the rate of vertical background by about 50%. (In order to ensure that the collimators do not scrape the tails of the beam, they should not be closed further than to 30 σ_y. The beam size σ_y is 0.8 mm at the old location of the collimator and will be 0.41 mm at the new location, assuming an emittance of 3.3 nm.)

The amount of high-energy horizontal background begins to decrease at a half-opening of collimator COLH.QS1 of 35 mm and is reduced by 50% at a half-opening of about 17 mm, as shown in Figure 18. The setting used in 1995 was 32 mm. In this case it does not seem possible to reduce the background by closing the collimator.

At a beam energy of 68 GeV, the amplitude of the vertical separation bump must be below about 50% in order to decrease the amount of high-energy vertical background significantly, as shown in Figure 19. Reducing the bump amplitude of course also increases the horizontal background, since the bump amplitude does not affect the amount of background created (or even that reaching STIC), but only the fraction swept into the vertical plane. In the case of the vertical parallel background, which is the most disturbing kind in the physics analysis, the amplitude must be less than 20% for a reduction of a factor of two in rate. At present, it

is not known how small a bump amplitude can be used without beam-beam effects becoming disturbing, but the bump amplitude is probably not an effective tool in the fight against this background.

One issue which is of great importance is the quality of the vacuum in LEP and in particular in those regions in which the high-energy vertical background is produced, *i.e.,* in the regions between the quadrupoles QS7 and QS3. During 1996, for example, the rate of vertical background in the 172 GeV running period was ten times lower than that in the previous 161 GeV running period. It is most likely that this was due to an improved vacuum during the later part of the year, because the beam itself slowly cleans the vacuum. The vacuum was broken in the section between the quadrupoles QS2 and QS4 during the winter shutdown of 1996-1997. This is the section where low-energy vertical antiparallel background is produced, and one may therefore expect a higher rate of such background at the startup in 1997.

8.2 Improvements of STIC

From the radius-energy distributions in Figures 11 and 12 it is clear that an effective method to reduce the background is to apply a radial cut. With a cut at a radius of 12 cm, all horizontal and most of the vertical background is removed. The energy of the remaining vertical background is less than 35 GeV, which is about half the beam energy.

Since a radial cut reduces the background very efficiently, the STIC neutral trigger was modified in 1996 between the 161 GeV and the 172 GeV running periods to allow for a crude radius measurement to be made on-line and used in the trigger decision.

New scintillation counters, so-called small veto counters, covering low angles were also added to the experiment in 1996, and were incorporated in the neutral trigger in order to reduce the trigger rate further and to close a hole which appeared in the old veto-counter system when the tungsten nose was replaced by a smaller tungsten shield in 1996.

One possible additional improvement would be to cover part of the back of the calorimeter with some shielding in order to reduce the amount of horizontal background entering this way. The space available at the back is limited, however, and this type of background is easily rejected off-line with the silicon-strip detectors discussed in Section 2. The new on-line radius cut should also reduce the trigger rate.

9 Summary and Conclusions

The results of the simulation of off-energy electron background in STIC can be summarized in the following way:

- The background appears in distinct groups. This grouping is related to where in the beam line the background has its origin, and the behavior of the groups depends on the amplitude of the vertical bunch-train bump created by the electrostatic separators. Five different groups have been defined: two groups which enter STIC in the horizontal plane,

one of which is of higher energy (peaked around 45 GeV at a beam energy of 68 GeV) and one of lower energy (10–25 GeV); a vertical group deflected in the direction parallel to that of the bunch-train bump, which enters STIC in the upper part of side A and in the lower part of side C and which is peaked in energy around 35 GeV; and two vertical groups antiparallel to the bump, one of higher energies (peaked at 35 GeV) and one of lower energies (peaked at 15 GeV).

- There is good agreement between the Monte Carlo and data taken during P3 in 1995. All five groups identified above are seen in the data. The groups have similar energy and radius distributions. The shadow of the synchrotron radiation mask is very sharp both in simulations and in the data. The radius-energy distributions (Figures 11 and 12) show that there is a low-radius band of electrons in the data from side A which is not present in the simulations. This band is most likely to be caused by interaction with material traversed by electrons entering STIC at low angles. Moreover, the simulations do not agree with the data on the relative population of the different groups. A possible explanation for these discrepancies lies in the differences in vacuum pressure between different parts of the beam line, which are not accounted for in the simulation.

- A significant portion (some 25%) of the off-energy electron background which hits STIC enters the detector elsewhere than through the front. Most of this background enters from the back, and a large fraction thereof comes from the high-energy horizontal group. Since these particles do not follow the projective geometry of STIC, their energy is not necessarily correctly reconstructed in the off-line data processing. This could account for some of the relative abundance of low-energy horizontal background seen in data but not in Monte Carlo.

- The modifications of the beam optics for LEP2 that were made between 1995 and 1996 have not altered the qualitative behavior of the off-energy electron background. The energy of the background scales linearly with the beam energy.

- It is possible to reduce the rate of vertical high-energy background by closing the vertical collimator COLV.QS1. In 1997, when this collimator is placed at a new location further upstream, one may be able to reduce this background by 50% by closing it to 13 mm. On the other hand, closing the horizontal collimator COLH.QS1 enough to reduce the rate of horizontal background is not possible. Nor is reducing the bunch-train bump amplitude an efficient tool to improve the situation. The most important factor concerning operation of LEP, however, is the quality of the vacuum in the region of the electrostatic separators. Due to an opening of the section between quadrupoles QS2 and QS4, the rate of low-energy vertical antiparallel background is expected to increase at the startup of 1997.

- The STIC neutral trigger was improved during 1996 by the addition of new low-angle scintillator counters and the inclusion of a radius requirement in the trigger decision. However, the off-energy background remains the most serious problem in single-photon analysis.

10 Acknowledgements

The authors wish to thank I. Belokopytov, M. Lamont and E. Migliore, who helped us retrieve information from the DELPHI and LEP databases for P3 1995. We also appreciate fruitful discussions with T. Camporesi.

References

[1] G. von Holtey, *Off-Energy Electron Background with Bunch Trains in LEP,* CERN SL/95-86 (EA).

[2] S. J. Alvsvaag et al., *The Small Angle Tile Calorimeter project in DELPHI,* DELPHI 95-12 CAL 119, Contribution to the 4th International Conference on Advanced Technology and Particle Physics, Como, Italy, October 1994.

[3] S. J. Alvsvaag et al., *The DELPHI Small Angle Tile Calorimeter,* DELPHI 94-157 CAL 120, Contribution to the IEEE 1994 Nuclear Science Symposium and Medical Imaging Conference, Norfolk, USA, October 1994.

[4] S. J. Alvsvaag et al., *The new small angle calorimeter in DELPHI,* DELPHI 94-148 CAL 118, Contribution to the 5th International Conference on Calorimetry, Brookhaven, USA, September 1994.

[5] S. J. Alvsvaag et al., *The DELPHI Small Angle Tile Calorimeter,* DELPHI 95-14 CAL 123, Contribution to the Beijing Calorimetry Symposium, Beijing, China, October 1994.

[6] K. L. Brown, Ch. Iselin, *DECAY TURTLE—A Computer Program for Simulating Charged Particle Beam Transport Systems, Including Decay Calculations,* CERN 74-2.

Component	Radial coverage (in mm)	Polar angular coverage (in mrad)
Aluminium beam pipe	$53 \leq r \leq 55$	$\theta \leq 30$
Steel beam pipe	$53 \leq r \leq 55$	$\theta \geq 29$
Beam-pipe bellows	$55 \leq r \leq 66$	$26 \leq \theta \leq 35$
Beam-pipe flange	$55 \leq r \leq 73$	$29 \leq \theta \leq 40$
Synchrotron mask	$41 \leq r \leq 53$	$17 \leq \theta \leq 23$
Tungsten nose	$60 \leq r \leq 96.173$	$29 \leq \theta \leq 44.1$ [1]
Veto counters	$87.8 \leq r \leq 379$	$44 \leq \theta \leq 185$
STIC scint. planes	$65 \rightarrow 76 \leq r \leq 417.5$ [2]	$29.5 \leq \theta \leq 188 \rightarrow 161$ [3]
STIC lead planes	$65 \leq r \leq 417.5$ [4]	$29 \rightarrow 25 \leq \theta \leq 188 \rightarrow 161$ [3]
Si strip planes	$71.5 \rightarrow 73.2 \leq r \leq 174.2 \rightarrow 178.4$ [5]	$32 \leq \theta \leq 77$

Table 1: The dimensions of beam-pipe components, tungsten masks and STIC detectors.

AZIMUTHAL REGION	SIDE A		SIDE C	
	STIC sectors	Azimuthal angle	STIC sectors	Azimuthal angle
Horizontal	1+16 8+9	0°±22.5° 180°±22.5°	1+16 8+9	0°±22.5° 180°±22.5°
Vertical parallel	3+4+5+6	90°±45°	11+12+13+14	270°±45°
Vertical antiparallel	11+12+13+14	270°±45°	3+4+5+6	90°±45°

Table 2: Definitions of horizontal, vertical parallel and vertical antiparallel azimuthal regions. The azimuthal angle is defined in a coordinate system with the x axis pointing to the center of LEP, the y axis upwards and the z axis in the direction of the electron beam (*i.e.,* towards calorimeter C). The numbering of STIC sectors is such that sectors 1 and 16 are on the side nearest the LEP center, sectors 3-6 are in the upper half of the calorimeters and sectors 11-14 in the lower half.

[1] This corresponds to a radius $\leq$ 97.019 mm at the first scintillator plane.
[2] The inner radius is given for the first and the last scintillator plane in the calorimter.
[3] The value before the arrow refers to the first sandwich plane and the value after the arrow to the last plane.
[4] All the lead converter plates have the same size.
[5] The value before the arrow refers to the first Si strip plane and the value after the arrow to the last plane.

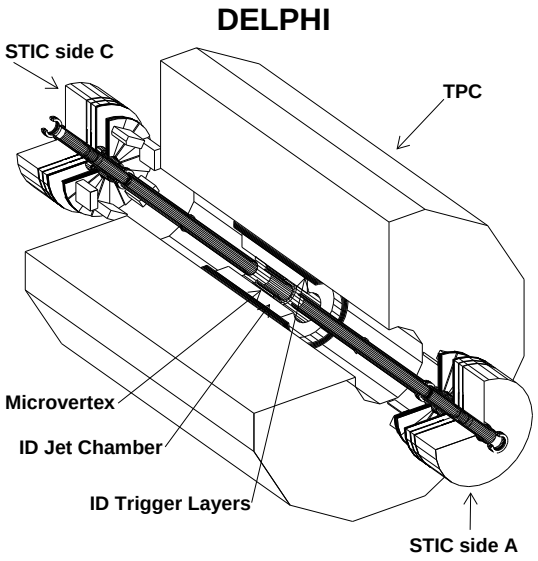

Figure 1: Location of STIC inside DELPHI. The STIC calorimeters are placed at a distance of 2.2 m on either side of the interaction point. Side A is that of the incoming beam of electrons; side C that of the incoming positrons. The electron beam has negative separation-bump polarity at this interaction point, and the positron beam has positive polarity.

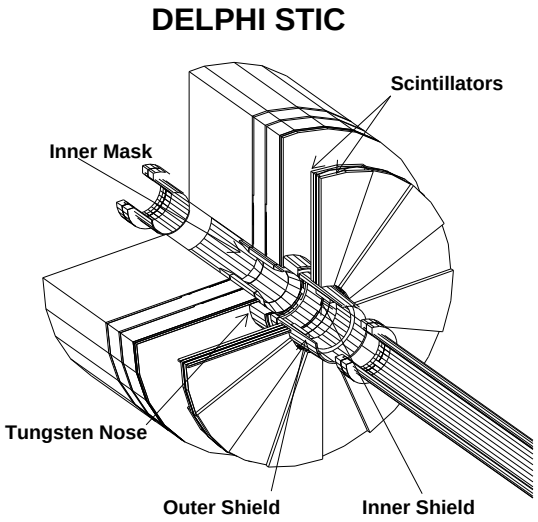

Figure 2: Outline of a STIC calorimeter showing the two scintillator planes of the veto counters in front of the calorimeter and the two planes of silicon detectors inside it. The tungsten nose and the synchrotron radiation mask, or inner mask, are marked. The position of the synchrotron radiation mask indicated here is that of 1994; in 1995 it was placed further back.

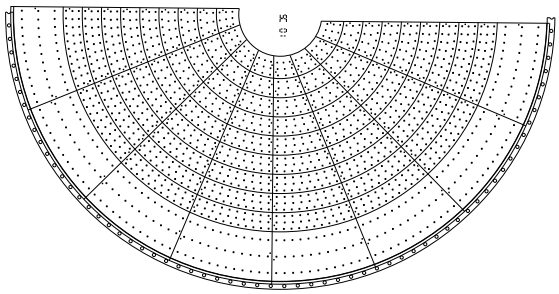

Figure 3: One half of the first STIC sandwich layer. Each calorimeter is divided into 10 radial rings and 16 azimuthal sectors, giving a total of 160 towers which point to the interaction region. The convention in numbering the calorimeter sectors is to use numbers 1–16 starting just above the horizontal plane on the inside of the LEP ring, and passing via the upper half of the calorimeter through the outside of the ring and onto the lower calorimeter half.

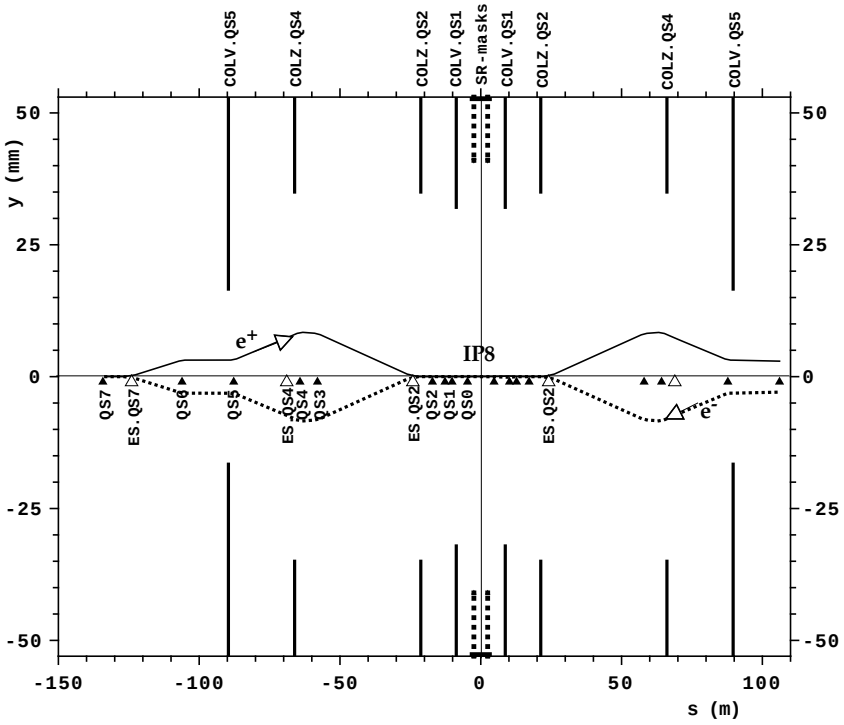

Figure 4: Layout of the vertical separation bump at the DELPHI interaction point (IP8). The bump amplitude reaches its maximum at quadrupole QS4 and is 8.4 mm for a beam energy of 68 GeV.

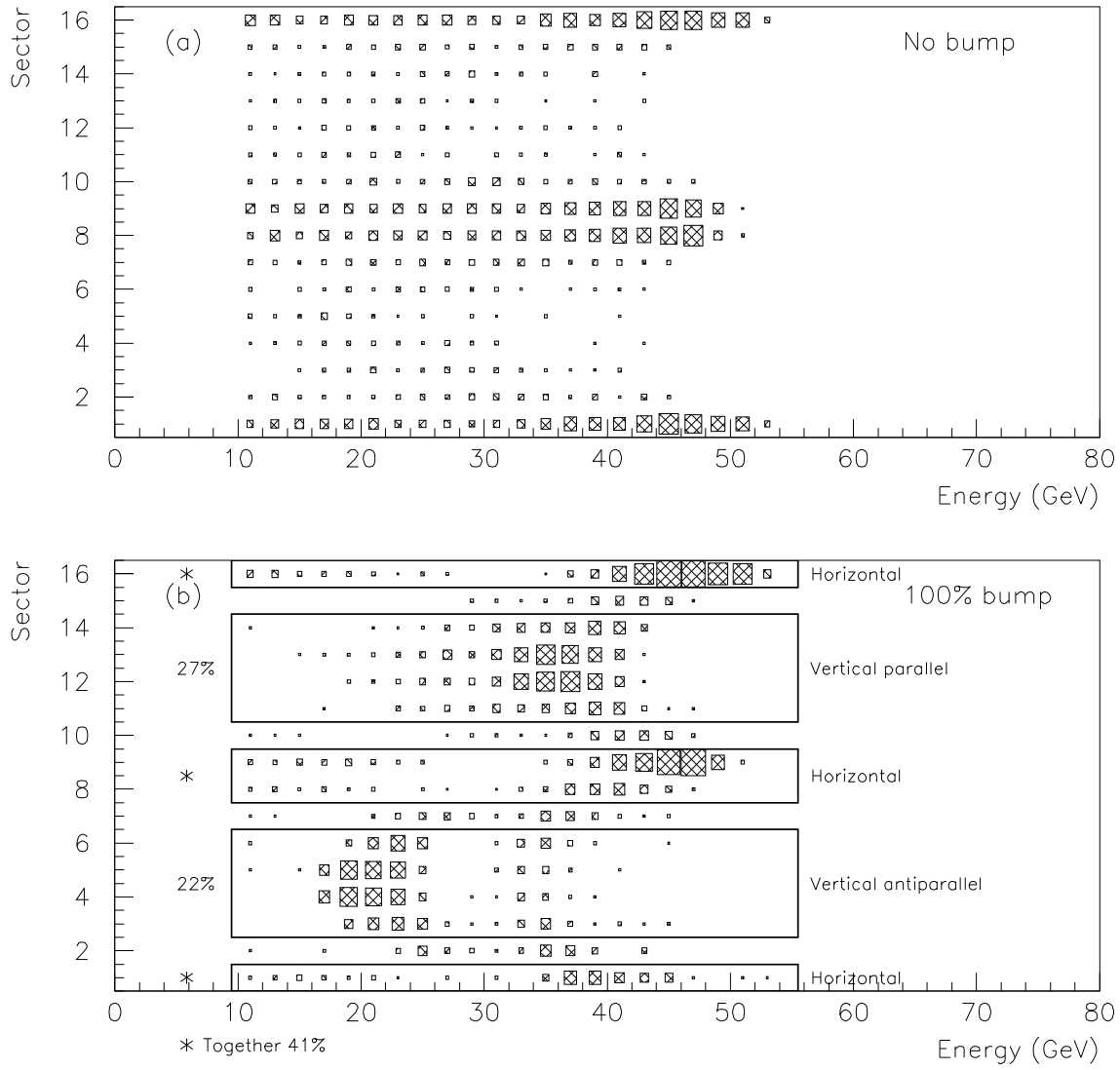

Figure 5: Comparison between (a) simulation with no separation bump and (b) simulation with 100% separation bump at 68 GeV beam energy for arm C without the tungsten nose. The histograms show calorimeter sectors *vs.* calorimeter energy. The areas of the boxes are proportional to the number of entries in the corresponding histogram bin. The names "parallel" and "antiparallel" refer to the direction of the deflection of the particles of these two groups with respect to that of the first deflection of the bunch-train bump.

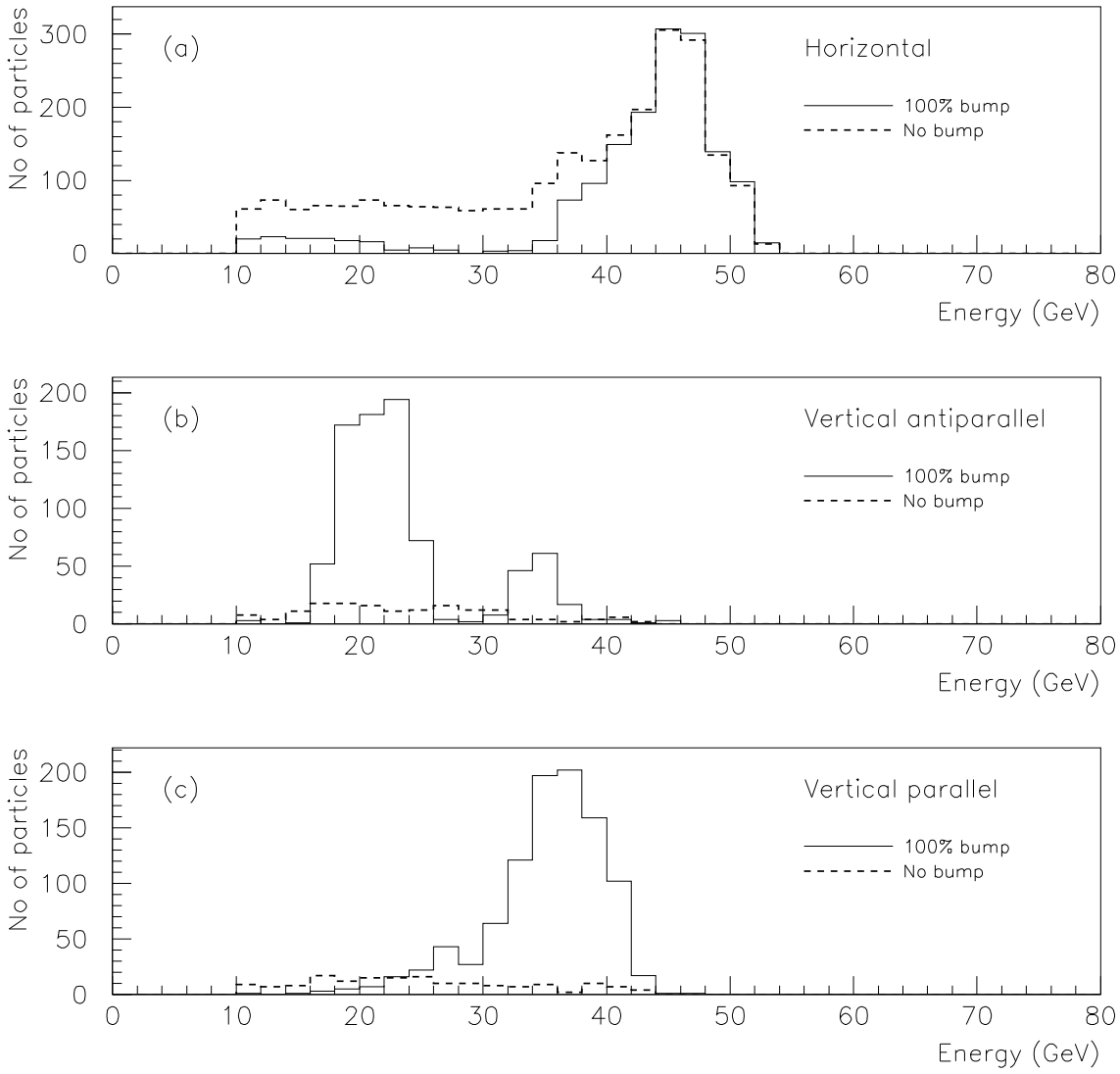

Figure 6: Simulated energy distributions with and without bunch-train bump at 68 GeV for (a) the horizontal group, (b) the vertical antiparallel group, and (c) the vertical parallel group.

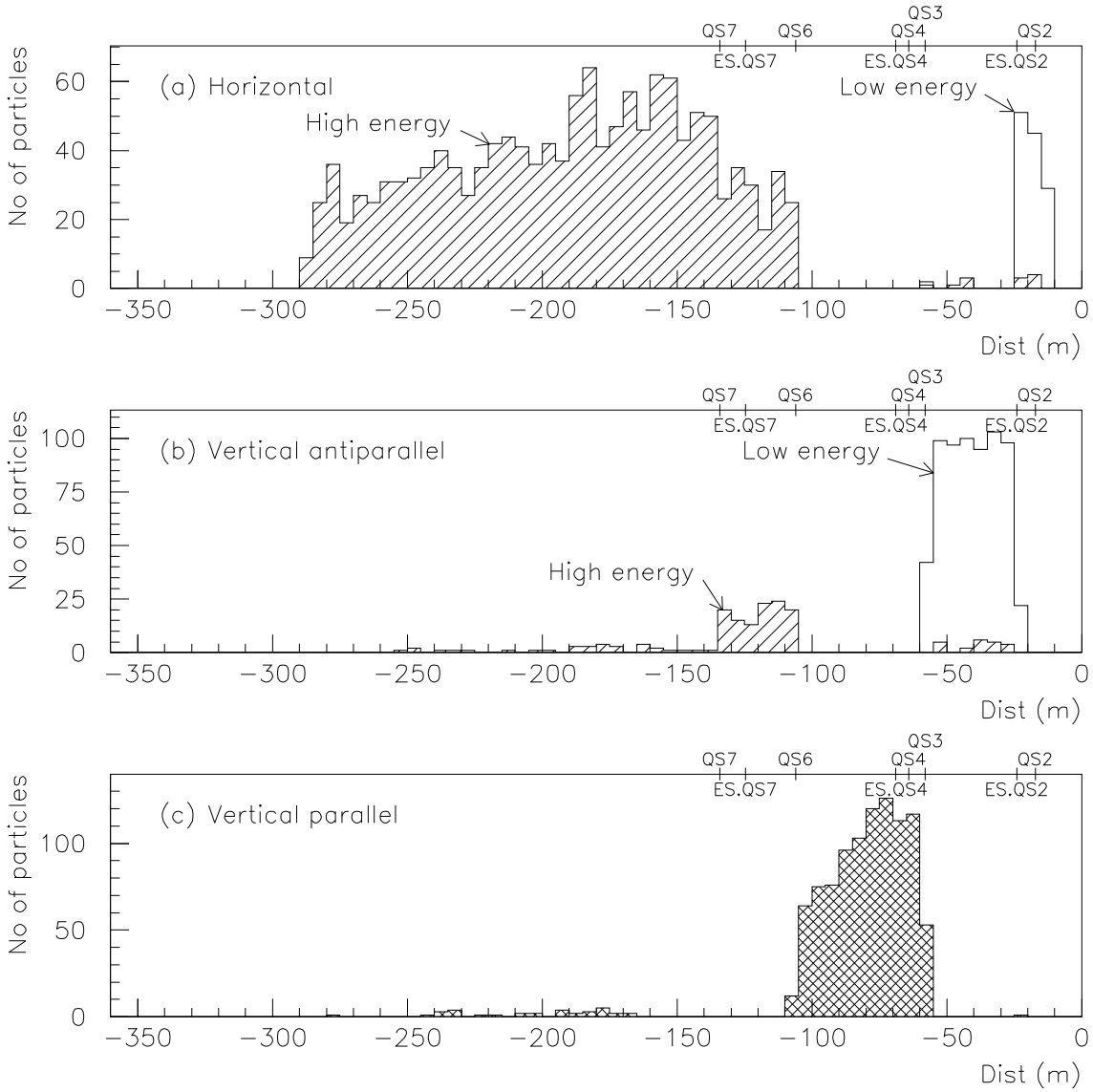

Figure 7: Distance from interaction point at which background was created for different background groups. The simulation was made with 100% bump amplitude at 68 GeV. The locations of the electrostatic separators (ES.QS2, ES.QS4 and ES.QS7) and nearby quadrupoles (QSn) are marked.

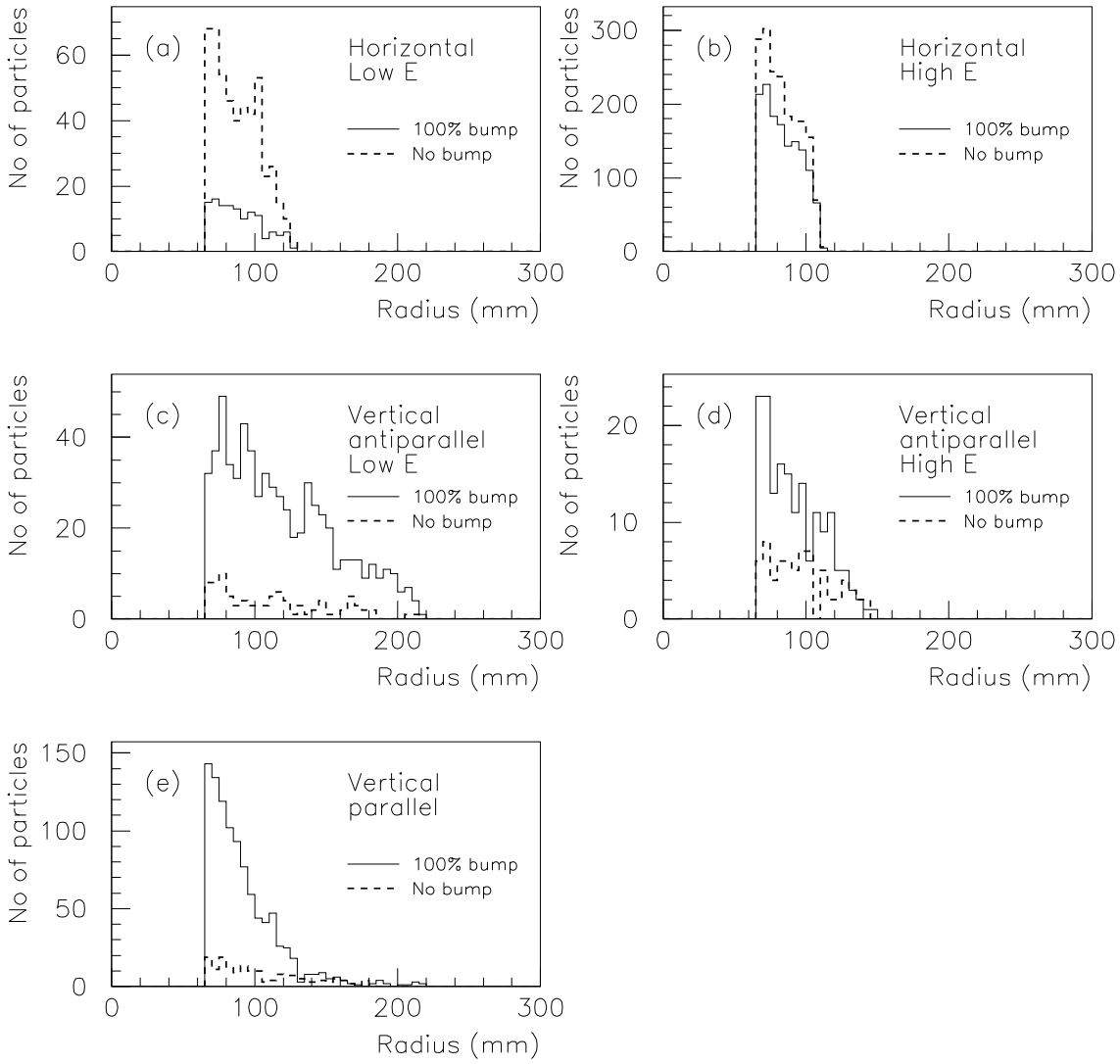

Figure 8: Radial distribution of different background groups at the front face of arm C, without the tungsten nose, both with and without the bunch-train bump. STIC extends radially from 65 mm to 417.5 mm. Note the sharp shadow of the synchtrotron radiation mask at 110 mm in the horizontal groups.

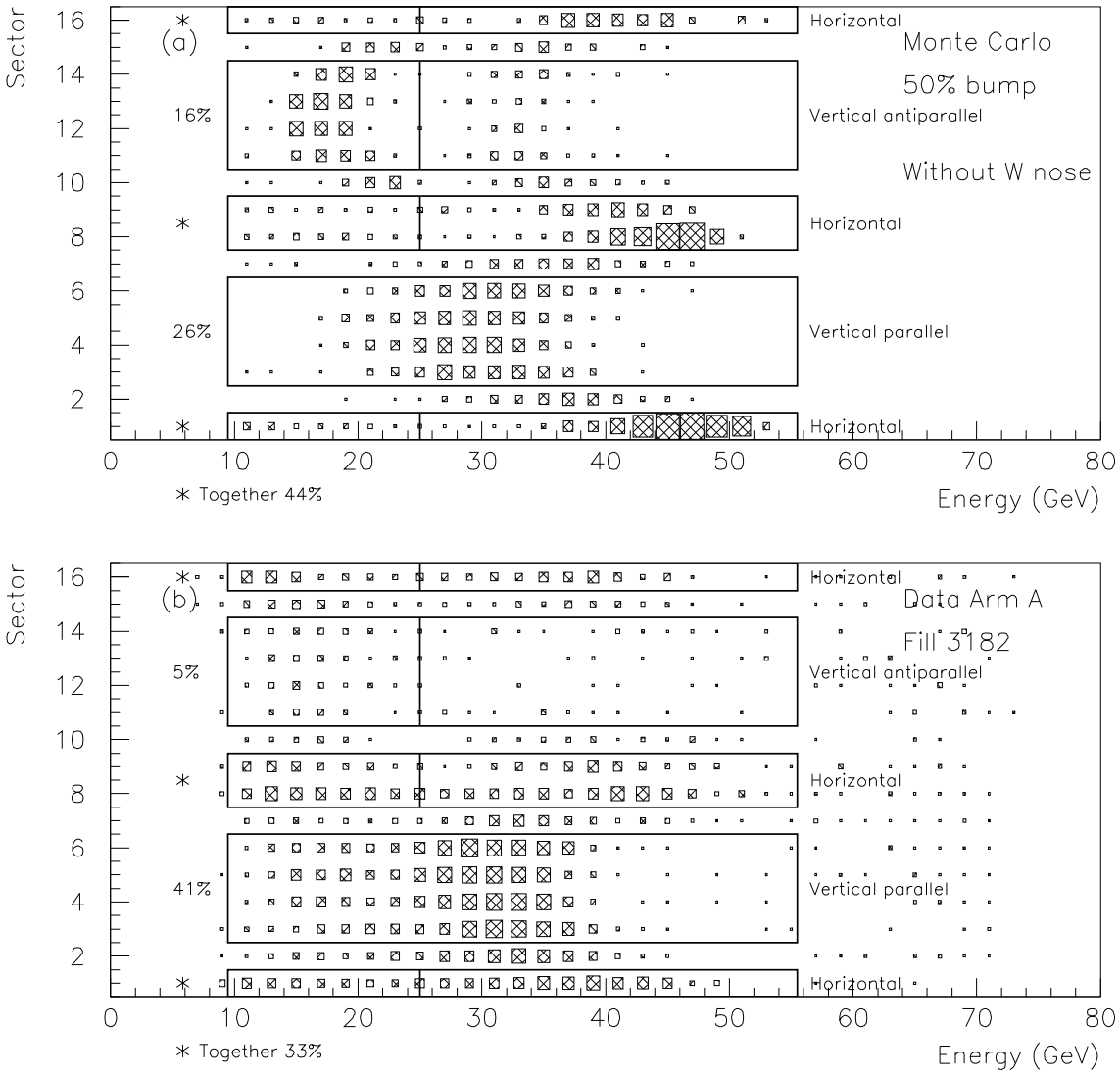

Figure 9: Comparison of calorimeter sector *vs.* energy between (a) Monte Carlo without the tungsten nose, and (b) data for arm A at 68 GeV beam energy and 50% bump amplitude. The vertical lines mark the division between low-energy and high-energy groups. The histograms have been normalized to have the same number of entries.

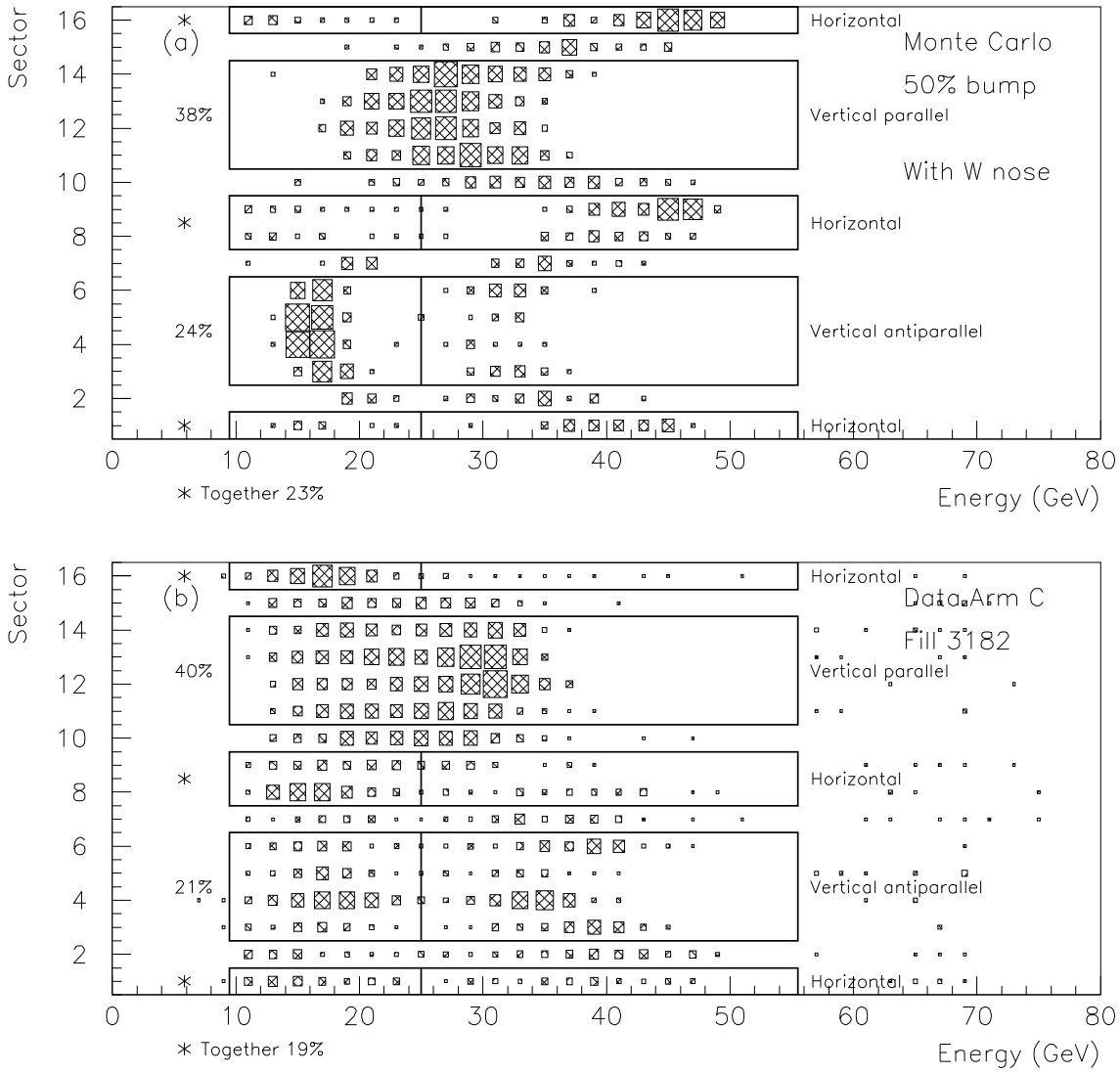

Figure 10: Comparison of calorimeter sector *vs.* energy between (a) Monte Carlo with the tungsten nose, and (b) data for arm C at 68 GeV beam energy and 50% bump amplitude. The vertical lines mark the division between low-energy and high-energy groups. The histograms have been normalized to have the same number of entries.

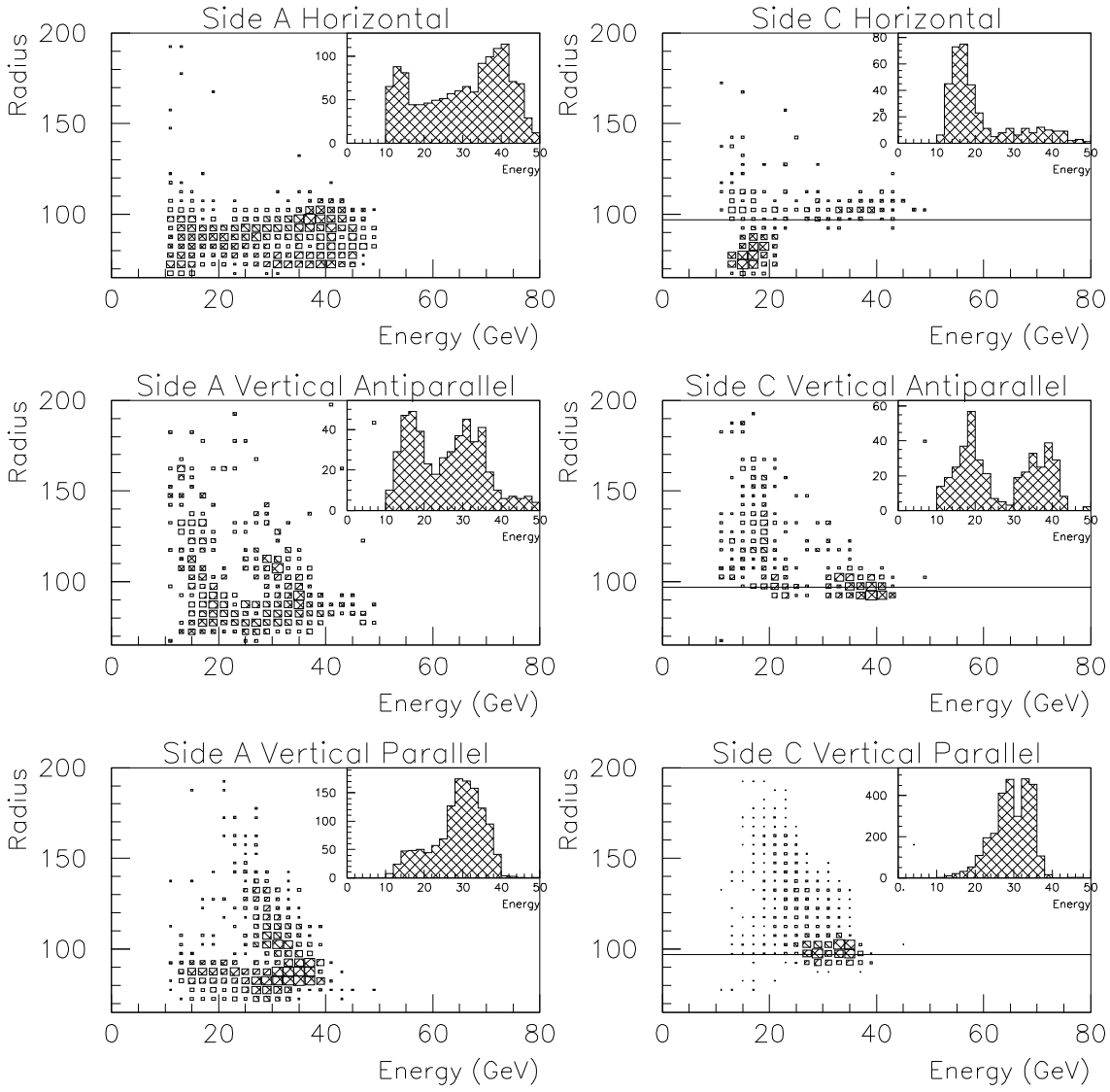

Figure 11: Distribution of radius *vs.* energy of off-energy electrons in data at an energy of 68 GeV per beam and at a bump amplitude of 80% for different background groups. The horizontal line in the histograms for side C indicates the position of the edge of the tungsten nose.

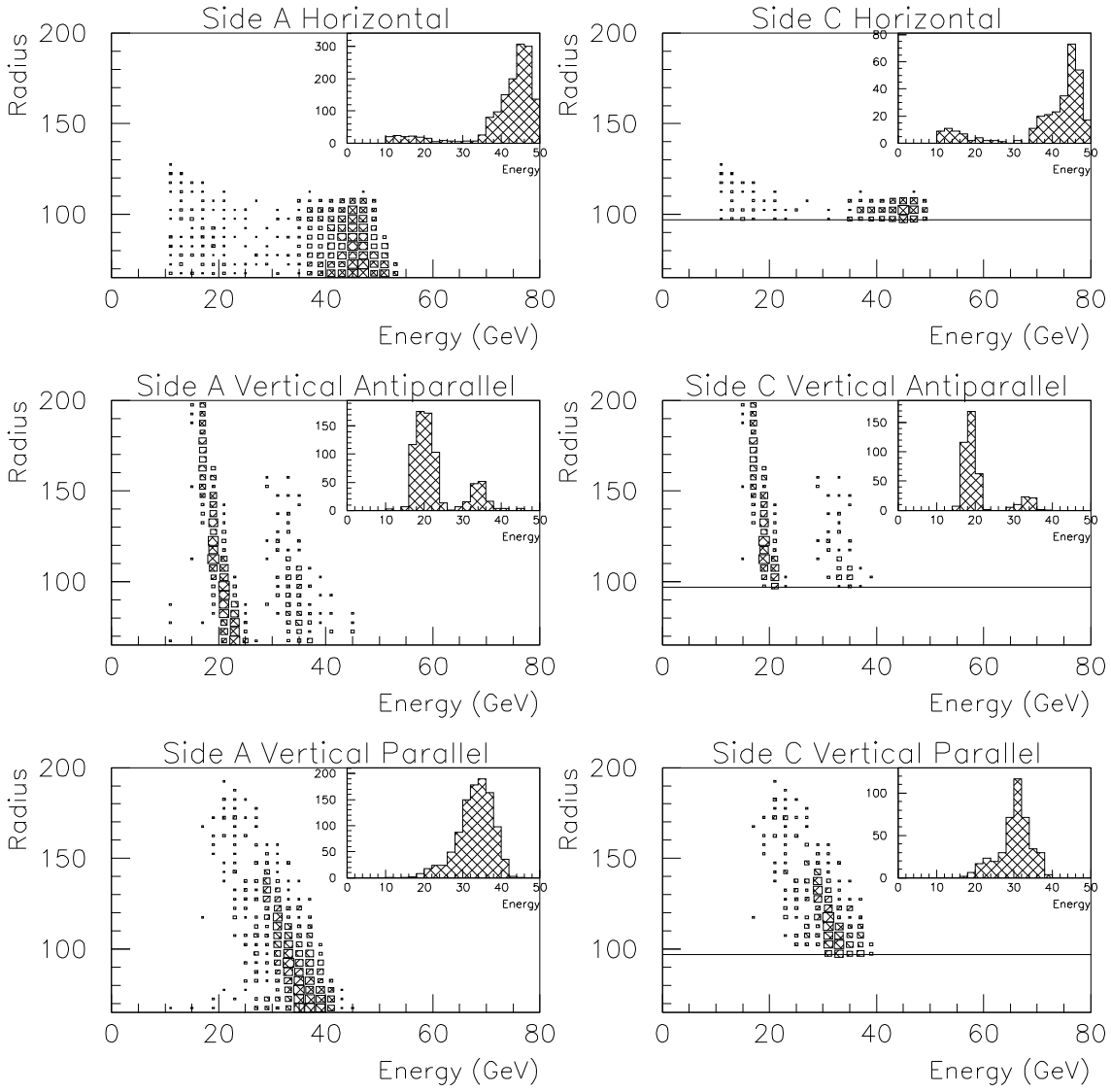

Figure 12: Simulated distribution of radius *vs.* energy of off-energy electrons at an energy of 68 GeV per beam and at a bump amplitude of 80% for different background groups. The horizontal line in the histograms for side C indicates the position of the edge of the tungsten nose.

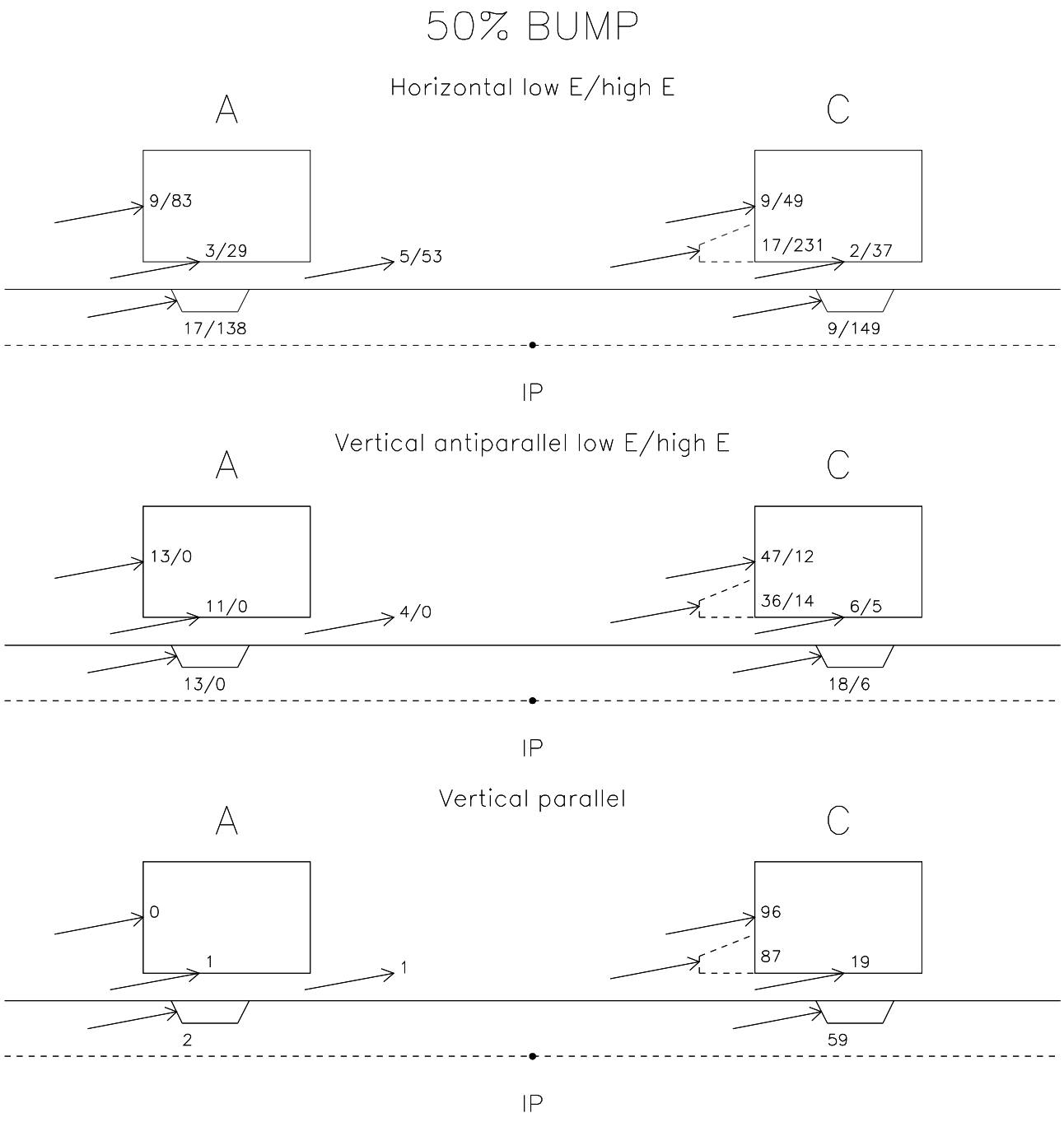

Figure 13: Different entry points for off-energy electrons entering STIC. (Only the electron beam was simulated.) The numbers in the figure show the number of particles entering at each point from each background category at 68 GeV beam energy and at 50% bump amplitude and normalized to a total of 1000 particles *entering* STIC. Particles hitting the synchrotron radiation masks are thus in addition to these 1000 particles. However, the sum of the number of particles entering STIC from each of the groups in the figure is not 1000; this is due to the definition of the groups, which leaves out certain calorimeter sectors.

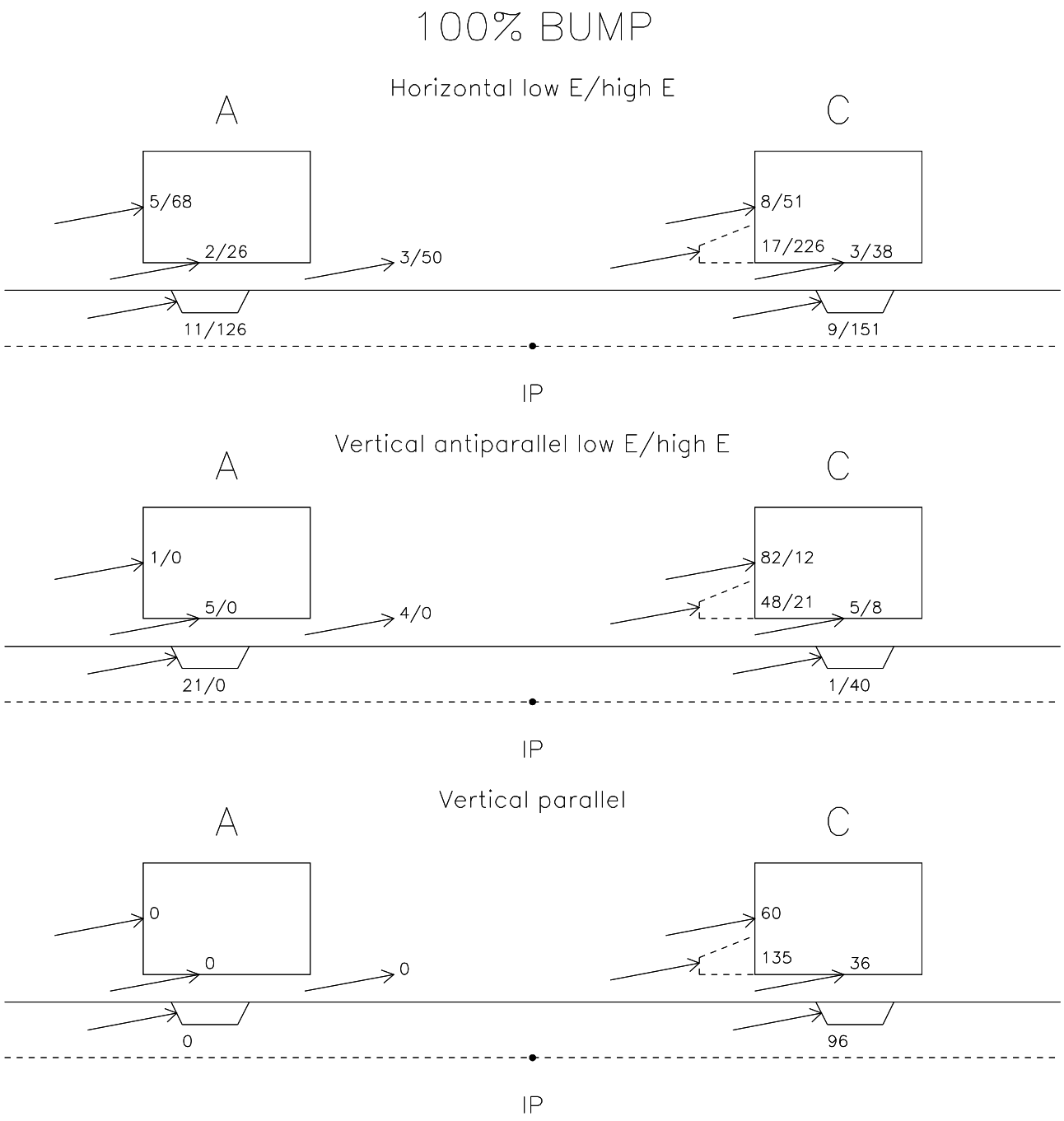

Figure 14: Different entry points for off-energy electrons entering STIC. The numbers in the figure show the number of particles entering at each point from each background category at 68 GeV beam energy and 100% bump amplitude and normalized to a total of 1000 particles *entering* STIC.

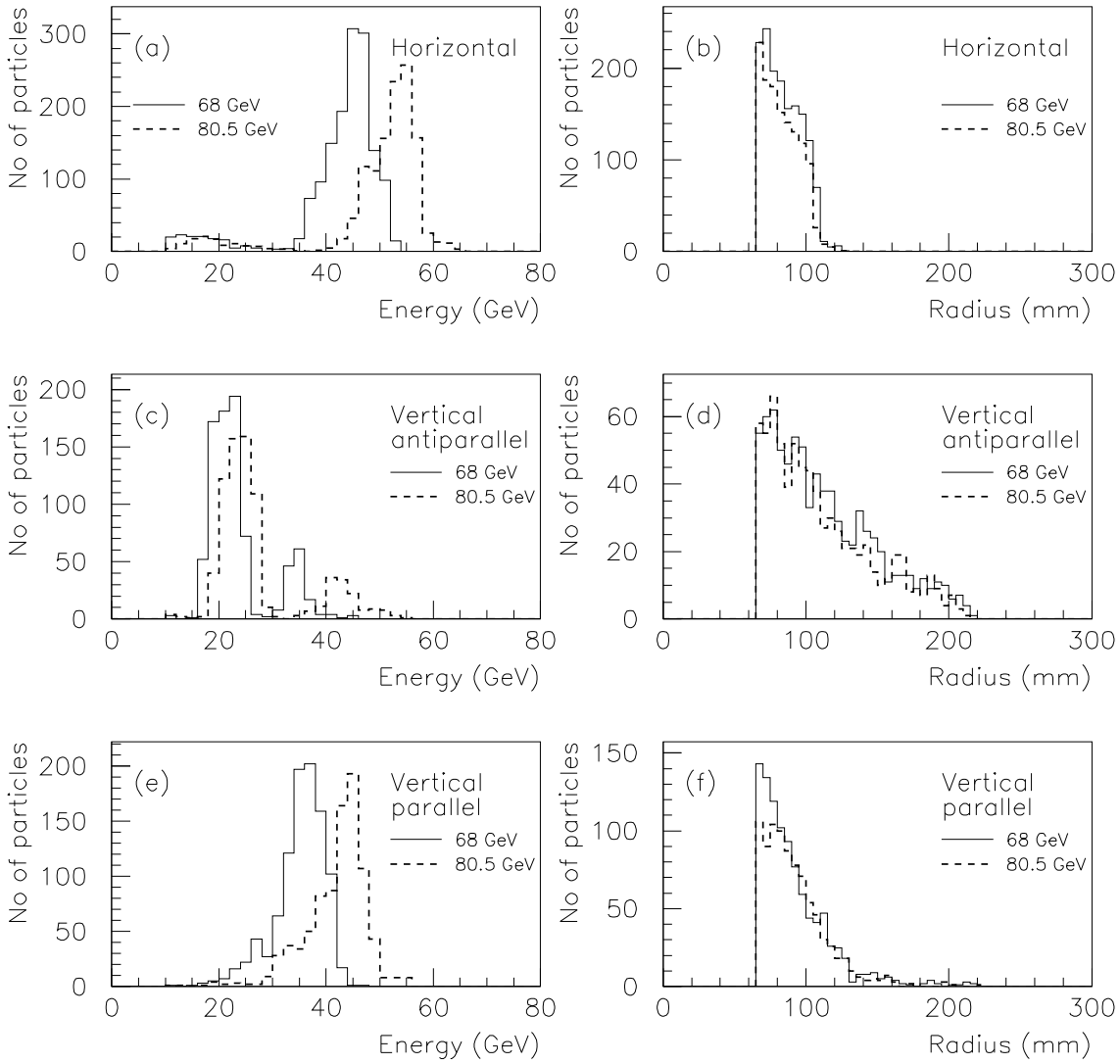

Figure 15: Comparison of simulated energy distributions and radial distributions between the beam optics of 1995, with a beam energy of 68 GeV, and that of 1996, with a beam energy of 80.5 GeV, for different background groups.

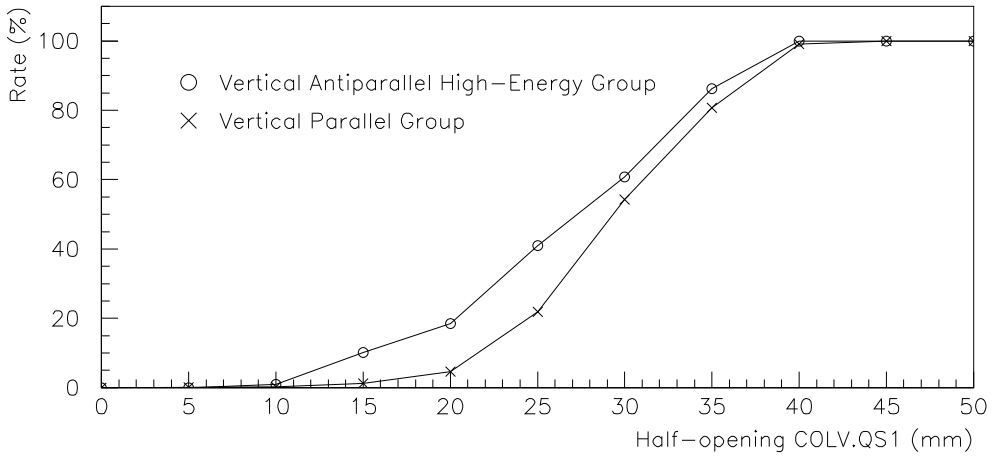

Figure 16: Rate of background of the vertical antiparallel high-energy group and of the vertical parallel group as a function of the half-opening of the vertical collimator COLV.QS1. The standard half-opening used in 1995 was 33 mm. The rates are normalized to those of a half-opening of 50 mm.

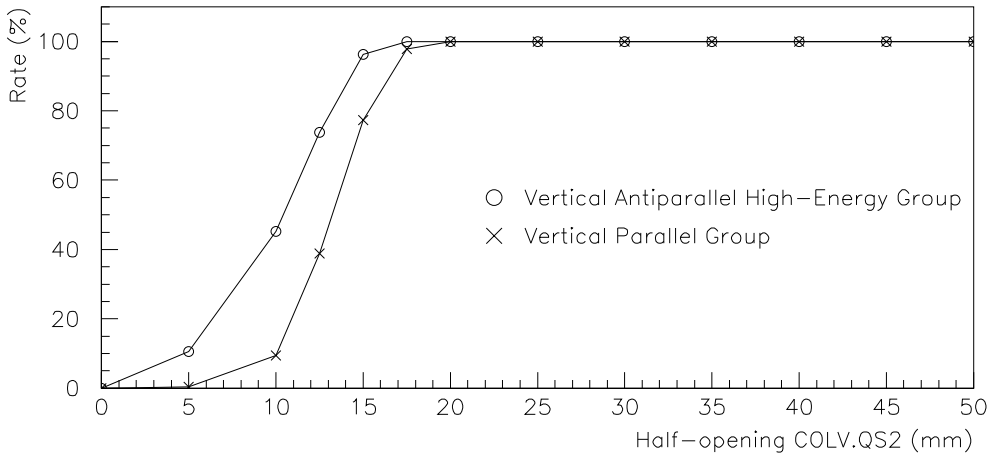

Figure 17: Rate of background of the vertical antiparallel high-energy group and of the vertical parallel group as a function of the half-opening of the old vertical collimator COLV.QS1 in its new position for 1997, where it will be called COLV.QS2. The rates are normalized to those of a half-opening of 50 mm.

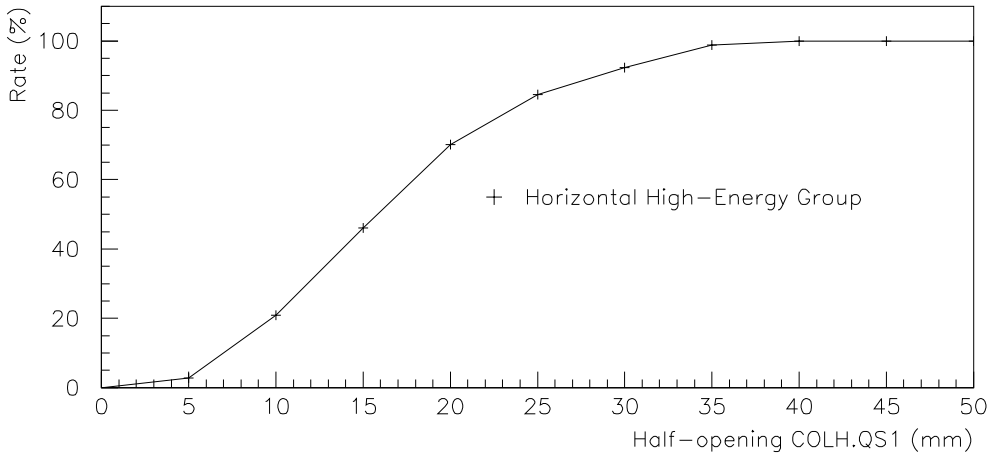

Figure 18: Rate of background of the horizontal high-energy group as a function of the half-opening of the horizontal collimator COLH.QS1. The standard half-opening used in 1995 was 32 mm. The rate is normalized to that of a half-opening of 50 mm.

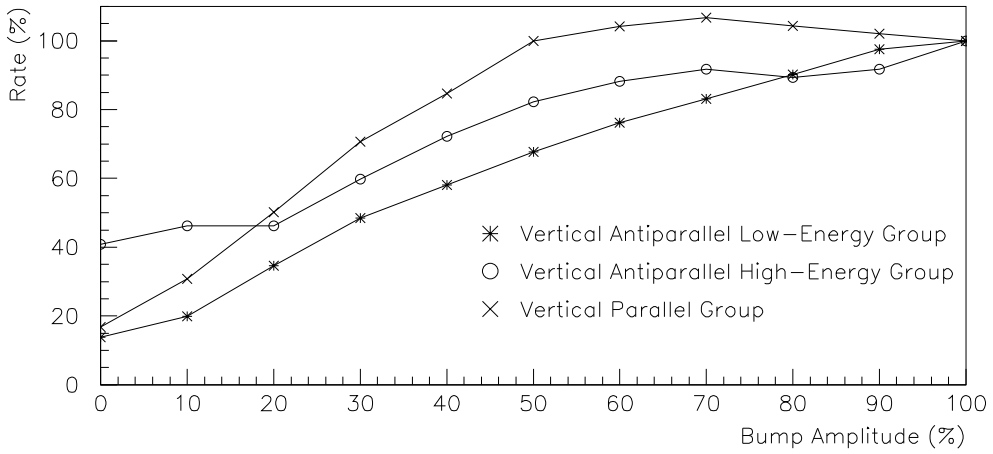

Figure 19: Rate of background in the vertical plane as a function of the amplitude of the vertical separation bumps for different background groups. The bump amplitude is given as a percentage of maximum amplitude at 68 GeV beam energy. The rates are normalized to those of 100% bump amplitude.

Article V

Performance of the STIC Silicon Detectors at LEP2

DELPHI Collaboration DELPHI 98-43 CAL 140
4 May 1998

Performance of the STIC Silicon Detectors at LEP2

E. Falk, V. Hedberg
Department of Physics, University of Lund, Lund, Sweden
I. Gouz
Institute for High Energy Physics, Protvino, Russia

Abstract

The luminosity monitor STIC in DELPHI is equipped with two planes of silicon-strip shower maximum detectors providing a tracking facility that makes it possible to measure the direction of calorimeter showers. These detectors were installed as part of STIC in 1994 but did not become fully operational until 1996. A short description of the software treatment of the silicon-strip data is given, together with an evaluation of the performance of these detectors during their first two years of operation.

1 Introduction

The luminosity monitor STIC in DELPHI consists of two lead-scintillator calorimeters of shashlik type, read out by wavelength-shifting fibers and placed on either side of the interaction point [1]-[7]. Each calorimeter has been equipped with two planes of silicon-strip shower maximum detectors, providing a tracking facility, the main purpose of which is to reject off-energy electron background [3]-[7]. These detectors were installed as part of STIC in 1994 but did not become fully operational until 1996.

The performance of these detectors during their first two years of operation is reported here. A short description of the software treatment of the silicon-strip data is also given. The hardware has been described in several previous reports (see [3]-[7]) and will be only briefly outlined here.

2 Geometry and Readout of the Silicon Detectors

The two calorimeters of STIC, located one on either side of the interaction point at a distance of 2.2 m, are made up of lead-scintillator sandwich layers, which are divided into 10 rings and 16 sectors. They are usually referred to as arm A and arm C, according to the DELPHI convention of calling the side of incoming electrons side A and that of positrons side C. The silicon detectors consist of planes of circular strips replacing one lead-scintillator layer at a depth of 4.0 radiation lengths and another at 7.4 radiation lengths in each of the two arms of STIC, thus giving a total of four silicon planes (see Figure 1). The silicon planes cover 32–77 mrad in polar angle (71.5–174.2 mm and 73.2–178.4 mm in radius respectively), whereas the STIC calorimeters have a polar-angular coverage of 29–188 mrad (65–417.5 mm in radius). Each silicon plane is divided into 16 sectors that follow the sector geometry of the calorimeter, and each sector contains 60 strips and thus makes up a 22.5° segment of 60 concentric circles. Two such sectors in a plane are read out by one Microplex MX4 amplifier chip with an input capacity of 128 channels. The strips are connected to the MX4 by eight Kapton[1] cables (see Figure 2), which are matched to the input of the MX4 by a hybrid fan-in card.

3 Data Treatment

The off-line reconstruction of shower parameters from the silicon-strip data became fully implemented in 1997. The information from the reconstruction is available on DELANA processings 1996F and 1997D and those made thereafter.

The treatment of the data from the silicon-strip detectors is divided into three logical parts. First, a certain amount of basic processing of the raw data takes place. This first treatment includes pedestal subtraction and correction for coherent noise. For a description of these steps, see [8]. Starting in 1997, this data treatment is carried out on-line. The pulse height of each signal is also converted to an energy, and strips with pulse heights below a certain threshold are

[1] Registered trademark of DuPont

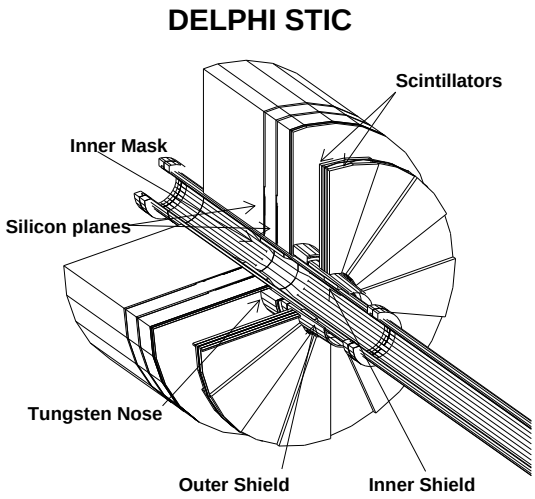

Figure 1: Outline of a STIC calorimeter, showing the location of the two planes of silicon detectors inside it. Also shown in the drawing are the scintillators of a veto-counter system for $e-\gamma$ separation, and a set of masks and shields providing radiation protection for the DELPHI TPC.

discarded. Second, there is a search for showers in the silicon-strip data, and the geometrical parameters (radius as well as polar and azimuthal angles) are calculated for the showers that were found. Finally, there is a matching of the showers that were found in the two silicon-strip planes to those that were found previously in the STIC calorimeter.

3.1 Reconstruction of Showers

A pool is made of all the strips that pass the pulse-height cut of the first data treatment. Showers are then built of strips from this pool in the following way: The pool is searched for the strip with the largest signal. If this strip passes a certain threshold, it is removed from the pool and considered to be a shower seed. All other strips that are located in the same arm and plane and which fall within a certain window in polar and azimuthal angle of the seed strip are also removed from the pool and set up to form a cluster together with this strip. The pool is then searched for a new seed, and the procedure is repeated as long as seeds can be found. When no more strips in the pool pass the threshold, the remaining strips are checked against the constructed clusters. If they are located near one, they are incorporated in this cluster; otherwise, they are ignored.

When all of the clusters have been built, the radius and the azimuthal and polar angles are calculated for each one.

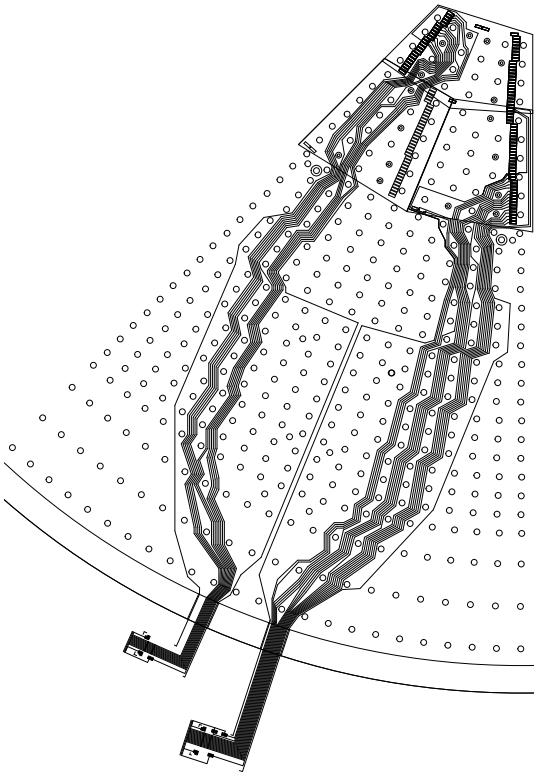

Figure 2: A 45° wedge (two 22.5° sectors) of the silicon shower maximum detector, with two of its eight Kapton cables shown. The strip structure within the sectors is not indicated. Note the many holes for the calorimeter fibers, which the signal wires have to avoid.

3.1.1 Reconstruction of Azimuthal Angle

The azimuthal angle is calculated with a two-dimensional barycenter method. Included in the calculation are all strips belonging to the same cluster and located at most one sector away from the cluster seed in azimuth and at most three strips away radially. Hence, a total of 21 strips, including the seed itself, are used in the calculation. The strips are weighted by energy, and the azimuthal angle of the shower is defined to be the barycenter thus calculated.

3.1.2 Reconstruction of Radius and Polar Angle

The 21 strips that are used to calculate the azimuthal angle are also used to calculate the radius and the polar angle. First, the energies of the three strips located at the same radial level but belonging to different sectors are summed for each of the seven radial steps. Then, the location of the maximum of these seven sums is determined. Thereafter, the radial location of the shower is determined. A logarithmic method can be used to determine the radius, on condition that the maximum sum is not located at the outermost nor at the innermost step in the cluster. Furthermore, the maximum sum and the two neighboring sums must all be greater than zero. The logarithmic method determines the radius by fitting two identical but mirror-imaged exponential functions to three points, i.e., that of the maximum sum and its two

neighbors. The intersection of the two fitted functions defines the radial position of the shower. The polar angle is then calculated from the radius. If the conditions mentioned above are not fulfilled, the same barycenter method that was used to calculate the azimuthal angle is used to calculated the polar angle, from which the radius is then calculated.

3.2 Shower Association

The showers found in the silicon-strip detectors are associated with those of the calorimeter in the following way: For each calorimeter shower, a search is made in the first silicon plane for the highest-energy shower that falls within a window of ± 1 sector in azimuth and ± 5 mrad in polar angle. If such a shower is found, it is associated with the calorimeter shower. A similar search is then carried out in the second silicon plane for a shower that falls within the same window.

4 Status of the Silicon Strips

Each silicon plane is divided into 16 sectors, each containing 60 strips. This yields a total of 3840 strips. About 280 of these, or 7.3%, were not operational in 1996. The malfunctioning strips were divided into different categories, depending on their type of fault: strips whose readout yields underflow or overflow; open strips (i.e., strips with a faulty connection); noisy strips; and strips belonging to a "dead", i.e., improperly connected, Kapton cable. The distribution of faulty strips in these categories is shown in Table 1. The largest contribution comes from open strips, which account for about half of the malfunctioning strips. One Kapton cable on side A was dead in 1996, but it was repaired before the startup in 1997. Unfortunately, however, a whole fan-in card (two sectors) on side A was out of order in 1997.

STIC Arm	Underflow	Overflow	Open	Noisy	Dead Kapton	Total
A	0.5%	1.7%	4.0%	0.4%	2.2%	8.8%
C	0.8%	0.5%	4.0%	0.5%	0%	5.8%
Both	0.6%	1.1%	4.0%	0.5%	1.1%	7.3%

Table 1: Fraction of silicon strips that were faulty in 1996. The malfunctioning strips are divided into different categories: strips whose readout yields underflow or overflow; open strips (i.e., strips with a faulty connection); noisy strips; and strips belonging to a "dead", i.e., improperly connected, Kapton cable. The "dead" Kapton cable on side A was repaired before the startup in 1997. However, a whole fan-in card (two sectors) on side A was out of order in 1997.

5 Performance of the Silicon-Strip Detectors

The reconstruction of vertices with the silicon-strip detectors was examined in different steps: The dependence of the maximum pulse height in the silicon detectors upon the shower energy

recorded by the calorimeter was studied. The radius reconstruction was cross-checked against that of the calorimeter, and the polar-angular resolution of the silicon-strip detectors was calculated. The vertex reconstruction was verified with data samples of Bhabha events, which originate from the interaction point, and compared to the vertex reconstruction of off-energy electron events. The reconstruction efficiency was calculated, and its dependence on energy and radius was studied. The efficiency of events from the interaction point *vs.* the efficiency of off-energy electrons for different vertex cuts was also determined.

5.1 Distribution of Maximum Silicon Signal

The maximum signal, i.e., the first shower seed (see Section 3.1), found in the silicon strips was studied for different calorimeter energies. The distributions of the maximum signal for different energy slices are shown in Figure 3. The magnitude of the maximum signal in the silicon detectors increases with the energy of the showering particle, although the fluctuations of the shower development inside the calorimeter cause a large spread within each distribution. At low energies, the distributions of maximum pulse heights are not well separated from the pedestal, but the separation improves with increasing energies, as expected.

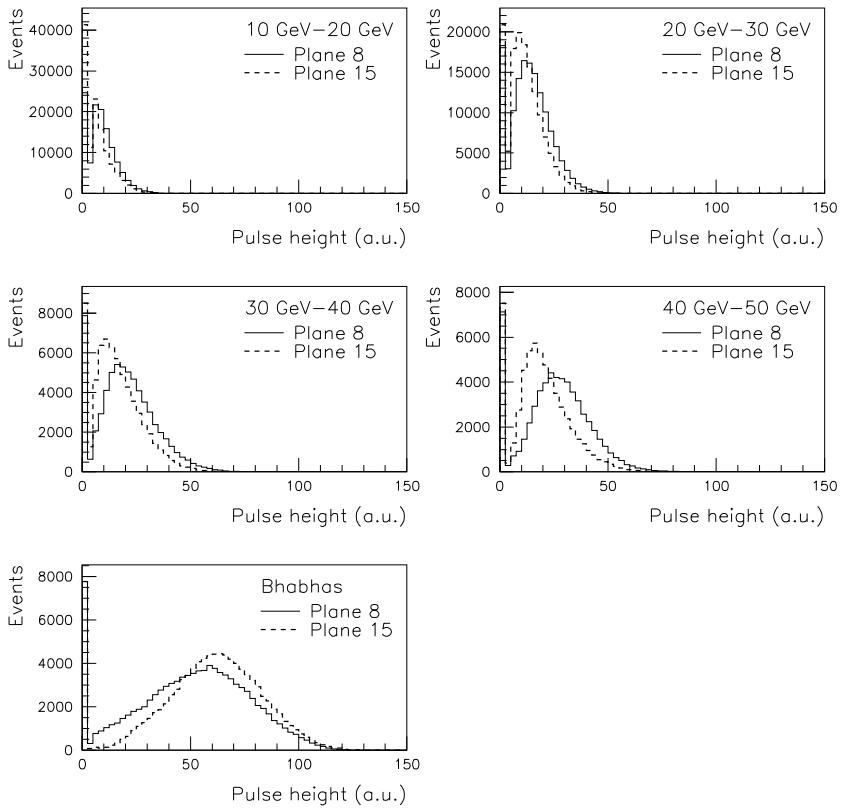

Figure 3: Distributions of maximum pulse height for different energy slices for the two silicon planes of arm C ($\sqrt{s} = 161$ GeV). The two silicon planes are referred to as plane 8 and plane 15, because they replace lead-scintillator layers 8 and 15 of the calorimeter.

5.2 Reconstructed Radii

The radius reconstructed in each silicon plane was compared to that of the calorimeter shower to which it was associated. For this purpose, a sample of Bhabha events, where the particles are known to originate from the interaction point, was selected. The radii reconstructed in the silicon planes were scaled with a factor d_{ff}/d_{Si}, where d_{ff} is the distance from the interaction point to the front face of STIC and d_{Si} the distance from the interaction point to the silicon plane, in order to allow a comparison with the calorimeter radii, which are measured on the front face of STIC. Figure 4 shows that the radii reconstructed in the silicon planes match well with those reconstructed in the calorimeter. The lines in the plots show the windows within which the association between calorimeter and silicon showers takes place (see Section 3.2).

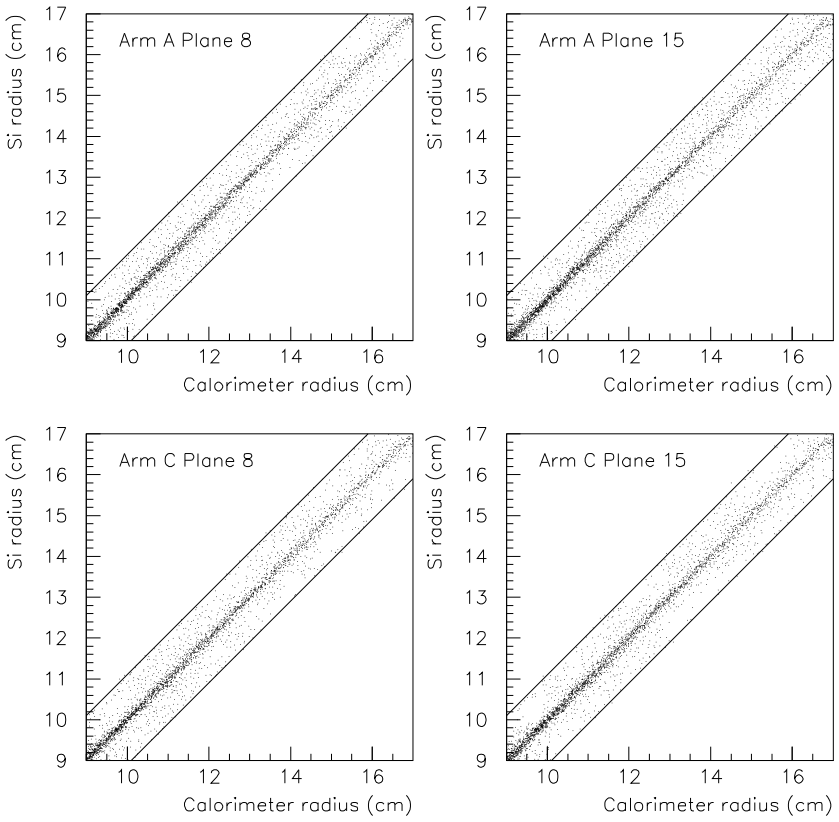

Figure 4: Comparison between radii reconstructed in silicon planes and associated calorimeter radii. A sample of Bhabha events, where the particles are known to originate from the interaction region, was used for the comparison ($\sqrt{s}$ = 161 GeV). The radii reconstructed in the silicon planes were scaled with a factor d_{ff}/d_{Si}, where d_{ff} is the distance from the interaction point to the front face of STIC and d_{Si} the distance from the interaction point to the silicon plane, in order to allow a comparison with the calorimeter radii, which are reconstructed on the front face of STIC. The lines in the plots show the windows within which the association between calorimeter and silicon showers takes place.

5.3 Resolution

The resolution of the reconstructed radii in the silicon detectors is energy-dependent, and it improves with increasing energy. Figure 5 shows the resolution in polar angle as a function of radius at a beam energy of 91.5 GeV. The angular resolution was determined through a fit of a Gaussian to the distribution of the difference in reconstructed radius between the two silicon planes in different radius regions (see Figure 6). The difference in radius was taken from a sample of Bhabha events; hence, ideally, this difference should be zero. The angular resolution as a function of radius shows a regular pattern of points, separated by about 1 cm in radius, where the resolution is significantly poorer than in the surrounding points; these points correspond precisely to the radial locations of the holes that allow the wavelength-shifting fibers to pass through the silicon detectors. The angular resolution at 91.5 GeV is approximately 9 mrad except in the regions of the holes, where it varies between 11 and 15 mrad. At 45 GeV, the corresponding numbers are 14 mrad and 17 to 25 mrad at the holes.

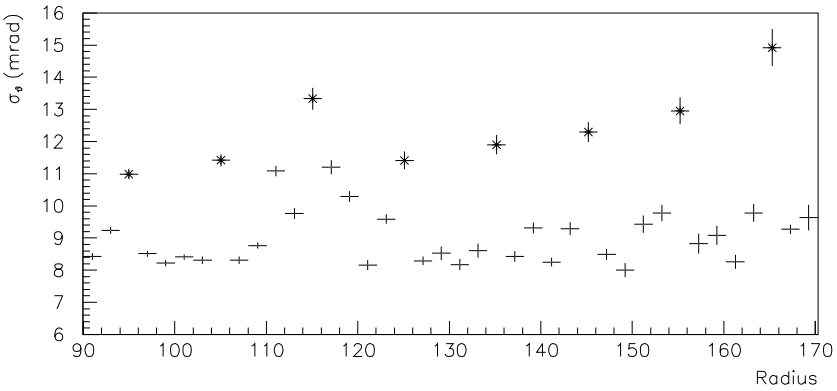

Figure 5: Angular resolution of the silicon-strip detectors for 91.5 GeV electrons. The points marked with stars indicate the locations of the holes for the wavelength-shifting fibers.

The difference in reconstructed radius between the calorimeter and each of the two silicon planes was also determined, and Gaussian fits were made to the distributions for different radius regions. The sigmas of these fitted Gaussians, together with those of the fits to the difference in radius between the silicon planes, allowed an estimation of the individual radial resolutions of the two silicon planes and of the calorimeter as a function of radius. Figure 7 shows these individual resolutions at 91.5 GeV. The calculated calorimeter resolution reproduces well what has been determined previously in independent radial-resolution measurements for the calorimeter at a testbeam (see [9]; the calorimeter has its best resolution near the ring borders and its poorest resolution in the center of the rings). The largest and the smallest resolution of the individual silicon planes and of the calorimeter for three different energies are shown in Figure 8. This figure illustrates the fact that the resolution of the silicon planes, as well as that of the calorimeter, improves with increasing energy; the exception, however, being the calorimeter ring borders, where the resolution is not improved significantly.

The resolution of the radius reconstruction in STIC in the region 90 to 170 mm can be improved if one combines the information from the calorimeter and the silicon planes. An av-

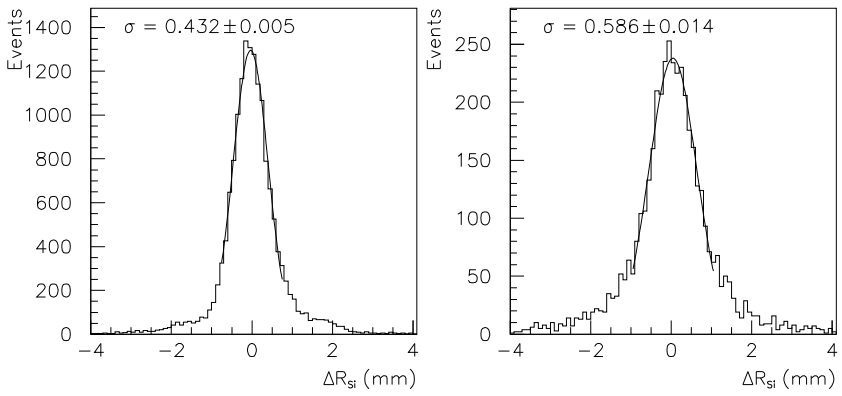

Figure 6: Distribution of difference in reconstructed radius between the two silicon planes for two different radius regions. A Gaussian was fitted to each of the distributions; the non-Gaussian tails of the distributions were left out of the fit. The wider distribution (right) shows a radius region where holes for the wavelength-shifting fibers are located; the narrower distribution (left) shows a region without holes.

erage of the three radii, where they are weighted by their respective resolutions, yields a radius determination with a resolution of 150 to 300 μm. This is illustrated in Figure 7.

5.4 Vertex Reconstruction

The straight line connecting a shower's radial coordinates in the two silicon planes is used to calculate the vertex of the showering particle: the line is extrapolated to the point where it intercepts the beamline, and the vertex is defined to be the distance between this point and the interaction point. The distribution of reconstructed vertices of a sample of Bhabha events as well as that of a sample of off-energy electrons are shown in Figure 9. The vertices of the Bhabha events are peaked in a narrow distribution around the interaction point, as expected. The off-energy electrons are created in bremsstrahlung interactions between beam particles and residual gas molecules anywhere in the beamline [10]. The vertex distribution of the single-arm events, which are dominated by off-energy electrons, is therefore much broader than that of the Bhabha events. Figure 9 confirms that this is the case.

The "holes" in the distributions of Figure 9, at about 2.5 m from the interaction point, are located at the position of the silicon detectors. They are caused by the geometrical acceptance of the two silicon planes, which makes it impossible to reconstruct tracks that intercept the beamline below the silicon detectors.

5.5 Efficiencies

The reconstruction of a vertex requires one reconstructed shower in each silicon plane to be associated with a shower in the calorimeter. The efficiency of the vertex reconstruction for the silicon detectors is defined to be the number of calorimeter showers having associated with them

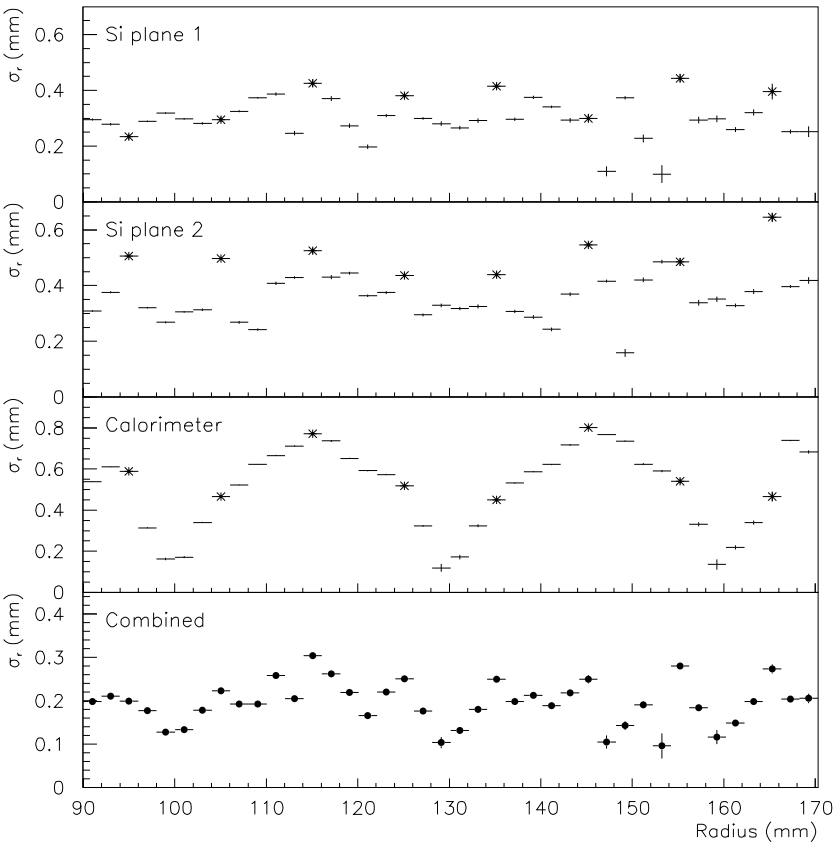

Figure 7: Radial resolution of (top to bottom) silicon plane 1; silicon plane 2; the calorimeter; and of a weighted average of the radii from the calorimeter and the silicon planes. The points marked with stars indicate the locations of the holes for the wavelength-shifting fibers. The measurements were made with 91.5 GeV electrons.

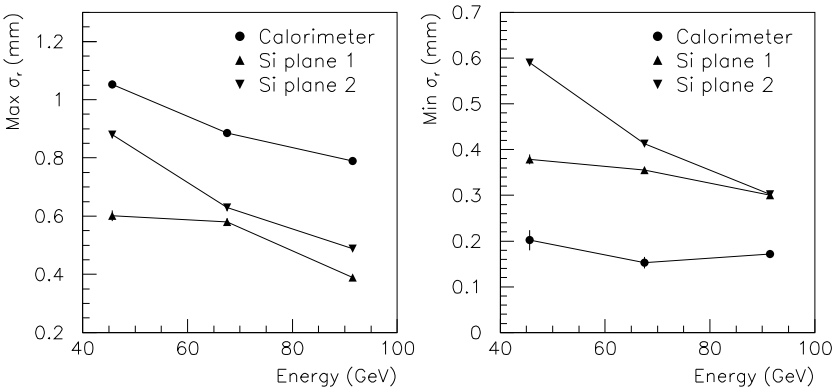

Figure 8: The largest and the smallest radial resolution of the individual silicon planes and of the calorimeter, at beam energies of 45, 65/68 and 91.5 GeV.

one reconstructed shower in each silicon plane divided by the total number of calorimeter showers passing through the silicon region. Figure 10 shows the energy distributions of calorimeter

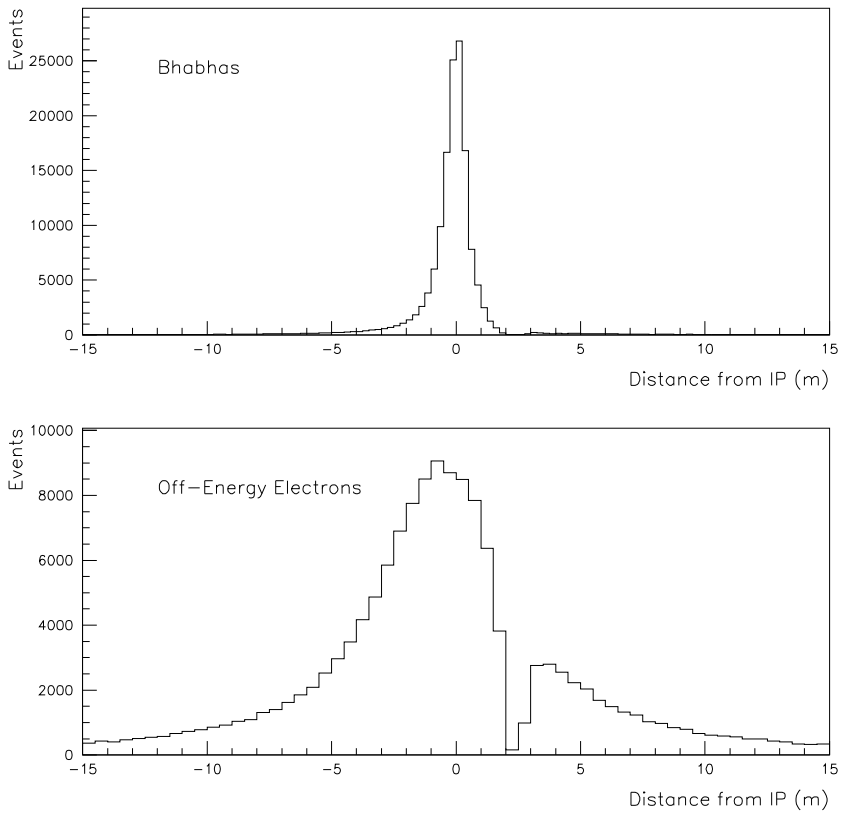

Figure 9: Distribution of reconstructed vertices of Bhabha events and of single-arm events (i.e., events with a shower detected in only one of the two STIC arms) respectively; $\sqrt{s} =$ 161 GeV. The sample of single-arm events nearly exclusively consists of off-energy electrons, which originate mainly elsewhere than from the interaction point; therefore, this distribution is much broader than that of the Bhabha events.

showers before and after imposing the requirement of two associated silicon showers, as well as the corresponding efficiency plot. Bhabha events show up as a clear, isolated peak just above 90 GeV, whereas the single-arm events appear in the region below 50 GeV. The region between 50 and 80 GeV contains hardly any data at all. The efficiency of the vertex reconstruction is nearly constant at a level of approximately 95% down to energies of about 30 GeV, where it begins to decrease. It decreases rapidly below 20 GeV, and it reaches a level of 30% at 10 GeV.

The efficiency as a function of radius was also studied. Taking into account the fact that the radial distributions are much different for different energy ranges, the data sample was divided into five different energy groups: 10-20 GeV; 20-30 GeV; 30-40 GeV; 40-50 GeV and Bhabha events. The radial distributions before and after requiring two reconstructed silicon showers for each calorimeter shower, as well as their corresponding efficiency plots, are shown in Figures 11 and 12. The efficiencies remain fairly independent of the radius within each group. However, at the radii where the holes for the wavelength-shifting fibers are located, there is a small decrease in efficiency. It drops by only 1-1.5%, but the effect is clearly visible in Figure 13.

The aim of the silicon-strip detectors is to allow rejection of off-energy electrons. Therefore,

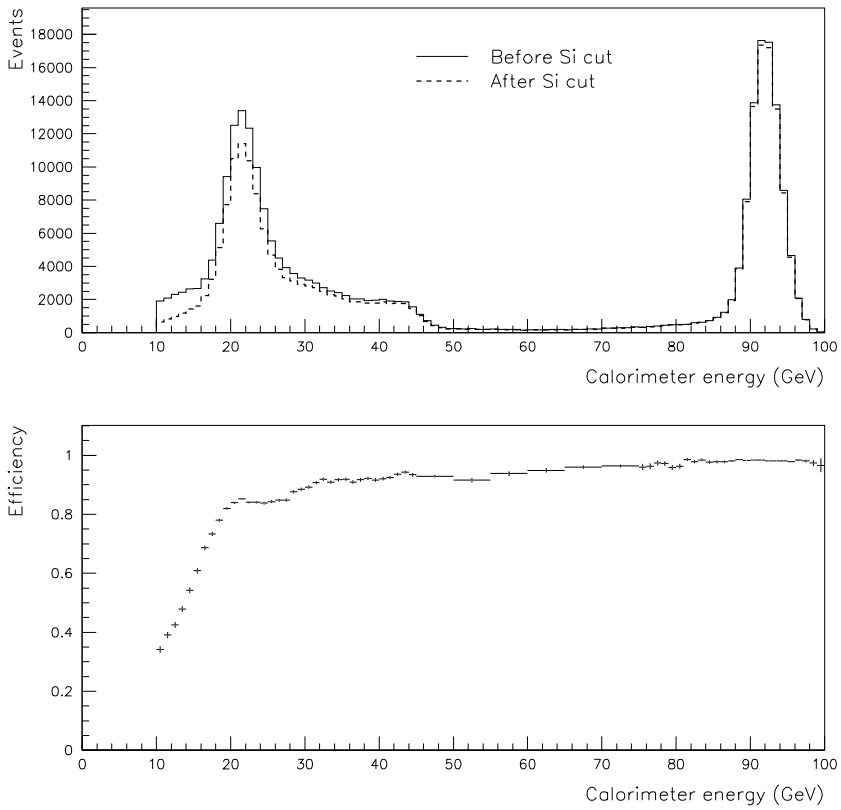

Figure 10: Energy distributions of STIC calorimeter showers ($\sqrt{s} = 183$ GeV) before and after imposing the requirement that each calorimeter shower has one reconstructed shower per silicon plane associated with it, and the corresponding efficiency plot.

the fraction of Bhabha events surviving a cut on the reconstructed vertex was studied and compared with the fraction of off-energy electrons surviving the same cut. The result is shown in Figure 14. Each point in the figure represents an increase by 10 cm of the cut on the vertex, starting with a cut at ± 10 cm. Only calorimeter showers having silicon showers in both planes associated with them were used. A cut at ± 0.5 m keeps 61% of events originating from the interaction point and rejects 89% of the off-energy electrons, whereas a cut at ± 1.0 m keeps 80% of the events from the interaction point and rejects 79% of the off-energy electrons.

6 Summary and Conclusions

Silicon-strip detectors were installed as part of STIC in 1994, in order to make it possible to measure the direction of calorimeter showers. These silicon-strip detectors became fully operational in 1996 and meet their design criteria. They cover 32–77 mrad in polar angle. Their angular resolution is approximately 9 mrad at 91.5 GeV and about 14 mrad at 45 GeV, except in the regions of the holes for the wavelength-shifting fibers, where the resolution is poorer. The vertex-reconstruction efficiency is about 90% at energies above 25 GeV. A vertex cut at ± 0.5 m on successfully reconstructed vertices keeps 61% of events originating from the interaction point

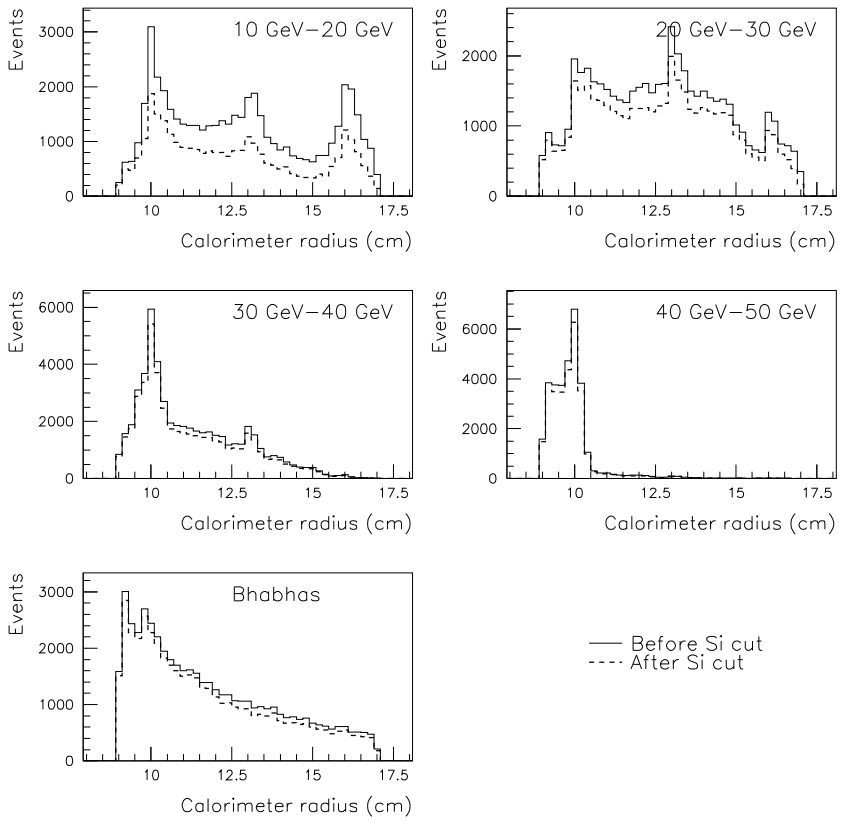

Figure 11: Distributions of reconstructed calorimeter radius for different energy groups in arm A, before and after imposing the requirement that each calorimeter shower has one reconstructed shower per silicon plane associated with it. $\sqrt{s} = 161$ GeV.

and rejects 89% of the off-energy electrons. The resolution of the radius reconstruction in STIC in the region 90 to 170 mm can be improved if one calculates a weighted average of the radii from the two silicon planes and from the calorimeter. One can thus obtain a radius determination with a resolution of 150 to 300 μm.

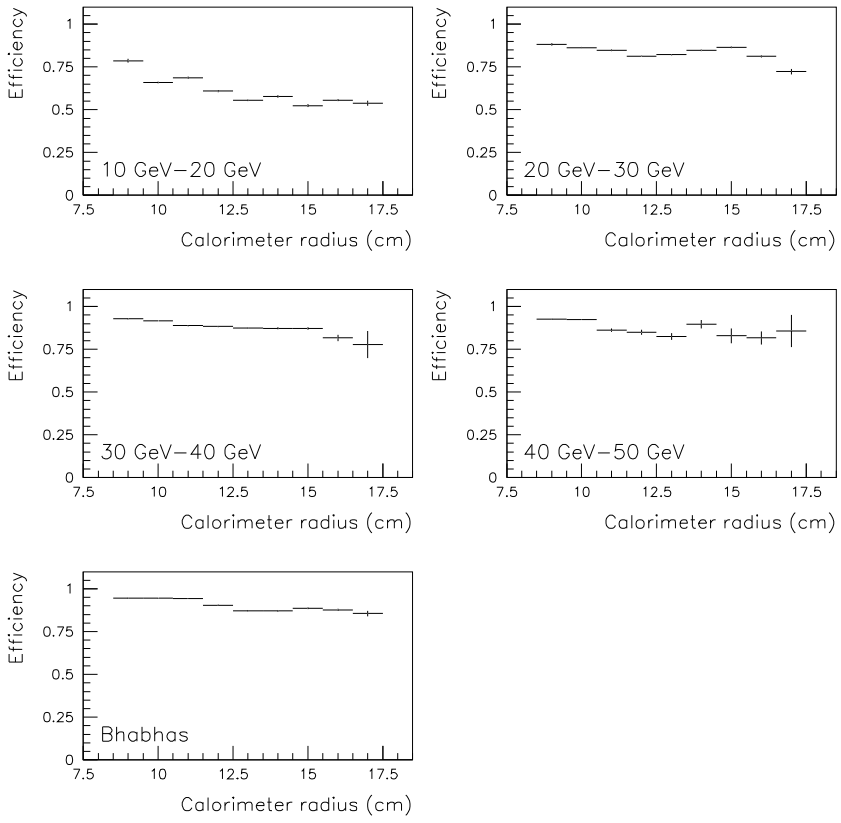

Figure 12: Efficiencies of cut requiring two reconstructed silicon showers for each calorimeter shower *vs.* reconstructed calorimeter radius for different energy groups in arm A. $\sqrt{s} = 161$ GeV.

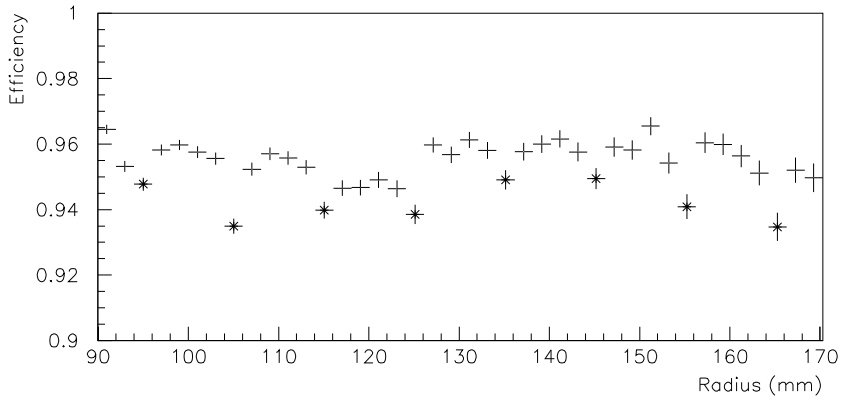

Figure 13: Vertex-reconstruction efficiency *vs.* radius ($\sqrt{s} = 183$ GeV). The points marked with stars indicate the locations of the holes for the wavelength-shifting fibers.

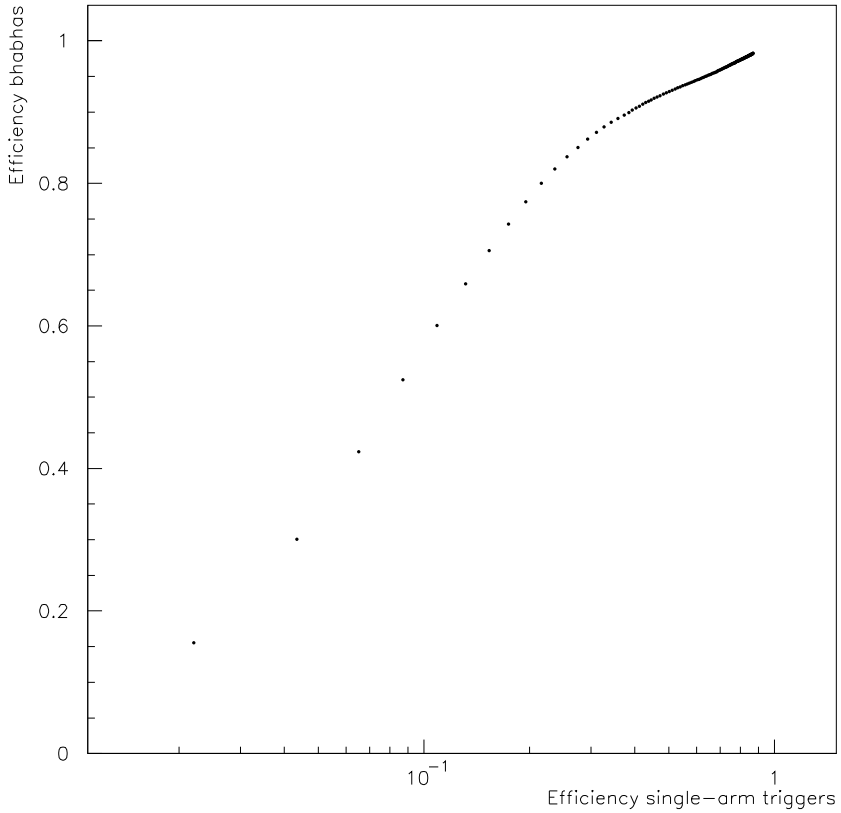

Figure 14: Fraction of Bhabha events surviving a cut on the reconstructed vertex *vs.* fraction of single-arm events surviving the same cut. Each point represents an increase by 10 cm of the cut on the vertex, beginning with a cut at ± 10 cm near the lower left corner. Only calorimeter showers with one reconstructed shower per silicon plane were used before imposing the vertex cut.

References

[1] S. J. Alvsvaag *et al.*, *The Small Angle Tile Calorimeter project in DELPHI,* DELPHI 95-12 CAL 119, contribution to the 4th International Conference on Advanced Technology and Particle Physics, Como, Italy, October 1994.

[2] S. J. Alvsvaag *et al.*, *The DELPHI Small Angle Tile Calorimeter,* DELPHI 94-157 CAL 120, contribution to the IEEE 1994 Nuclear Science Symposium and Medical Imaging Conference, Norfolk, USA, October 1994.

[3] S. J. Alvsvaag *et al.*, *The new small angle calorimeter in DELPHI,* DELPHI 94-148 CAL 118, contribution to the 5th International Conference on Calorimetry, Brookhaven, USA, September 1994.

[4] S. J. Alvsvaag *et al.*, *The DELPHI Small Angle Tile Calorimeter,* DELPHI 95-14 CAL 123, contribution to the Beijing Calorimetry Symposium, Beijing, China, October 1994.

[5] S. J. Alvsvaag *et al.*, *The Silicon Shower Maximum Detector for the STIC,* DELPHI 94-126 CAL 117, contribution to the 6th Pisa Meeting on Advanced Detectors, Elba, Italy, May 1994.

[6] S. J. Alvsvaag *et al.*, *A silicon pad shower maximum detector for a "Shashlik" calorimeter,* DELPHI 94-158 CAL 121, contribution to the IEEE 1994 Nuclear Science Symposium and Medical Imaging Conference, Norfolk, USA, October 1994.

[7] S. J. Alvsvaag *et al.*, *A Silicon Pad Shower Maximum Detector for a Shashlik Calorimeter,* DELPHI 95-13 CAL 122, contribution to the 4th International Conference on Advanced Technology and Particle Physics, Como, Italy, October 1994.

[8] E. Falk, V. Hedberg, I. Gouz, G. Della Ricca, *Algorithms for Reduction of Coherent Noise in the Silicon Shower Maximum Detector of STIC,* DELPHI 97-60 CAL 137; also available as INFN/TC-97/33.

[9] S. J. Alvsvaag *et al.*, *The Performance of the DELPHI STIC Detector at LEP,* contribution to the VI International Conference on Calorimetry in High-Energy Physics, Frascati, Italy, June 1996.

[10] E. Falk, V. Hedberg, G. von Holtey, *Simulation of Off-Energy Electron Background in DELPHI,* DELPHI 97-12 LEDI 8; also available as CERN SL/97-04 (EA).

Article VI

Algorithms for Reduction of Coherent Noise in the Silicon Shower Maximum Detector of STIC

DELPHI Collaboration DELPHI 97-60 CAL 137
24 June 1997

Algorithms for Reduction of Coherent Noise in the Silicon Shower Maximum Detector of STIC

E. Falk, V. Hedberg
Department of Physics, University of Lund, Lund, Sweden
I. Gouz
Institute for High Energy Physics, Protvino, Russia
G. Della Ricca
Dipartimento di Fisica, Università di Trieste and INFN, Trieste, Italy

Abstract

Three algorithms to reduce coherent noise in the silicon shower maximum detector of the DELPHI luminosity monitor STIC are described. The simplest method is fast enough to be used on-line in the readout chain. This would allow one to select the channels to be read out and hence a great reduction of the volume of data. The results of tests of the efficiency and the accuracy of this algorithm are presented, as well as a comparison with the other two methods that also have been proposed for coherent-noise correction.

1 Introduction

The luminosity monitor STIC in DELPHI consists of two lead-scintillator calorimeters of shashlik type, read out by wavelength-shifting fibers and placed on either side of the interaction point [1]-[7]. Each calorimeter has been equipped with two planes of silicon-strip shower maximum detectors, providing a tracking facility, the main purpose of which is to reject off-energy electron background [3]-[7]. Reduction of coherent noise in data read out from these silicon detectors is an essential step in the data processing in order to ensure accurate reconstruction of the energy and the position of the shower. In addition, it is important to have a tool to reduce the amount of information to read out from the silicon detectors, which consist of approximately 4000 channels. A fast algorithm to reduce coherent noise on-line would permit localization of showers and thereafter readout of only a small selection of silicon-strip channels in the vicinity of these showers.

We present a fast and simple, yet accurate, method to reduce coherent noise from the STIC silicon detectors, a method which meets both of the above requirements. It needs no information from any other detector and could be implemented at an early stage of the readout chain, *i.e.,* in the Sirocco IV Fastbus modules, where the signals from the silicon-strip detectors are digitized, and which are equipped with digital signal processors (DSPs) [3]-[7]. A description of the algorithm itself is given, together with the results of an evaluation thereof and a comparison with two other proposed methods to reduce coherent noise.

2 Geometry and Readout of Silicon Detectors

The two calorimeters of STIC are made up of lead-scintillator sandwich layers, which are divided into 10 rings and 16 sectors. They are usually referred to as arm A and arm C, according to the DELPHI convention of calling the side of incoming electrons side A and that of positrons side C. The silicon detectors consist of planes of circular strips replacing one lead-scintillator layer at a depth of 4.0 radiation lengths and another at 7.4 radiation lengths in each of the two arms of STIC, thus giving a total of four silicon planes. Each silicon plane is divided into 16 sectors that follow the sector geometry of the calorimeter; each sector contains 60 strips and thus makes up a 22.5° segment of 60 concentric circles [3]-[7]. Two such sectors in a plane are connected to one Microplex MX4 amplifier chip with an input capacity of 128 channels. The strips are connected to the MX4 by Kapton[1] cables (see Figure 1), which are matched to the input of the MX4 by a hybrid fan-in card. The Kapton cables have a capacity of either 12 or 20 channels. The 24 innermost strips of each sector are read out by two 12-channel Kapton cables and the other 36 strips by two 20-channel Kapton cables. The outermost cable reads out only 16 strips and thus leaves four empty channels connected to the MX4 [3]-[7].

[1]Registered trademark of DuPont

3 Background and Motivation

The method for coherent-noise reduction that is proposed here processes raw silicon-strip data event by event in only two steps in order to allow the possibility of on-line implementation, which would be critical in both processing time and memory requirements. The first step subtracts pedestals, and the second step calculates and subtracts coherent noise.

3.1 Pedestals

Pedestals can be calculated on-line with good accuracy using only a small subsample of events and without use of any external trigger or calorimeter information. Due to sampling conditions (*i.e.,* a positive baseline for the digitization of strip signals) which are altered at the beginning of each physics run, the pedestals must be calculated for each new run. However, one need not use STIC triggers to do this; one may use any DELPHI trigger in order to establish new pedestals as quickly as possible at the beginning of the run. If, amongst these triggers, there are STIC showers for which one does not wish to lose information from the silicon detectors, one can simply read out all silicon-strip channels for these events and process them off-line.

3.2 Coherent Noise

The origin of the coherent noise in the silicon-strip detectors of STIC is not entirely understood. One possible source is electromagnetic pick-up from external devices. Another possibility is noise being generated internally by the front-end electronics (preamplifiers etc.) due to a parasitic electrical coupling between inputs and outputs. It is clear, however, that there is correlation in the noise between channels of the same Kapton cable. There is also noise correlation between channels of adjacent Kapton cables, *i.e.,* cables which belong to the same fan-in card and which emerge from the detector along the same path and are placed on top of one another. Other patterns of coherence are also present, but they are less important. It is necessary to make use of the correlation between channels that are located some distance apart in order to find coherent pulse-height shifts over strip areas larger than a shower, which is typically wider than 20 strips; otherwise, one would not be able to determine the amplitude of the coherent noise at the location of the shower.

Our method makes use of the correlation between Kapton cables. The same pattern of correlation applies to most, but not all, fan-in cards. Therefore, look-up tables are used to store the correlations. There is one such table for each fan-in card, and the table contains 8×8 entries, one for each pair of Kapton cables of the fan-in card in question. For simplicity, each entry is either 1 or 0, depending upon whether or not there is strong correlation with a slope near unity. At present, correlations other than those with a slope near 1 are not included, although such exist and some of them can be relatively strong. The tables have been established manually after a study of plots of the correlation of the average pulse height for each pair of Kapton cables within a fan-in card and over a large number of events. Examples of such correlation plots are shown in Figure 2. For reasons not fully understood, the correlations vary slightly from year to year, so the correlation tables must be updated occasionally and checked a few times per year.

4 Algorithm

As mentioned in the previous section, the method proposed here processes data in two steps; first, pedestals are subtracted, and then coherent noise is calculated and subtracted. The algorithm consists of two separate parts; one performed at the beginning of each new physics run in order to establish pedestal values for each silicon strip, and one for the rest of the run which carries out pedestal and coherent-noise correction.

4.1 Calculation of Pedestals On-line

The first 100 DELPHI triggers at the beginning of a physics run are used to calculate pedestals in two steps: *i)* The signal of each of the first 50 events is added for each individual strip, and then one calculates the mean, p'_i, and RMS, r'_i, for each strip i. *ii)* The operation is repeated for the following 50 events, but for each strip one now includes only those events for which the signal passes the cut $a_i \leq p'_i + 2r'_i$, where p'_i and r'_i are those obtained from the first 50 events. This selection is made in order to minimize the influence of showers. The mean, p_i, and RMS, r_i, obtained after the second calculation are those that will be used as pedestal values for the remainder of the run.

Optionally, this procedure can be repeated on every set of 100 events and the pedestal values used only for the following 100 events instead of for the remainder of the run. This would take care of any sudden jumps in the pedestals during a run. (This phenomenon occurred a few times during the datataking of 1995 and has not been explained.)

4.2 Calculation of Pedestals Off-line

The calculation of the coherent-noise correction is independent of the way in which the pedestal values are calculated and may well be used together with pedestals calculated according to a different method. In order to evaluate the accuracy of the on-line pedestal algorithm, an off-line method was also used.

The off-line method calculates pedestal values using most, but not all, of the events of a physics run. Reconstructed calorimeter clusters are used to discard events with more than one shower per arm. For events with zero calorimeter clusters in one of the arms, all the strips of that arm are used. For events with one cluster, only the strips of the sector located opposite the one through which the shower passed are used; see Figure 3 for an illustration of the selection procedure. This minimizes the influence of showers without restricting the event selection to "empty" events only. The pedestal mean and RMS for each strip are defined to be the mean and RMS of the pulse heights of the selected events.

4.3 Correction for Pedestals and Coherent Noise

After the first 100 triggers of a run, each event is treated as follows: The pedestal mean value obtained at the beginning of the run (or, optionally, at the latest pedestal calculation) is subtracted from the raw data of each strip, a_i, *i.e.,*

$$a_i' = a_i - p_i.$$

Thereafter, one calculates, for each Kapton cable k, the average pulse height $< a >_k$ of all the Kapton cables that are correlated to k (according to the look-up table discussed above). In this calculation only those strips are included which fulfil

$$a_i' \leq n r_i,$$

where n is a constant which is typically 2–3. The purpose of this cut is once again to exclude showers. The value obtained is the estimate of the coherent noise for the group of strips belonging to the Kapton cable in question. This is subtracted from each channel of the Kapton cable, so that one obtains a corrected pulse height for each strip, a_i'':

$$a_i'' = a_i' - < a >_k \ .$$

After having applied the above correction to all Kapton cables, one reads out only those strips for which the pulse height passes a suitably chosen threshold.

5 Evaluation

In order to obtain a good understanding of the performance of the coherent-noise correction method, the coherent-noise correction itself and the calculation of pedestals were evaluated separately.

The evaluation described below, as well as the development of the algorithm itself and the comparison with other algorithms, were performed on data from LEP run 61020 taken at 45 GeV in July 1995. The silicon detectors were read out only for Bhabha-triggered events at that time. Not all of the recorded events were used, but a subsample containing approximately 14000 events from the beginning of the run were used as test data.

5.1 Evaluation of Coherent-Noise Correction

The signal amplitudes obtained after coherent-noise correction were compared in two ways to those obtained before correction (but after pedestal subtraction). First, the pulse heights were plotted for the strips of each fan-in card before and after correction. Two examples, one for each arm, are shown in Figures 4 and 5. As expected, the data that have been corrected for coherent noise show a much narrower distribution around zero ADC counts than the data that are only pedestal-corrected; the coherent-noise correction clearly reduces the spread around zero. Moreover, after coherent-noise correction, hardly any events populate the region below the band where the bulk of the events are concentrated, which indicates that the tables of

correlations between Kapton cables have been established correctly.

Second, the pulse-height distributions of all the strips of each fan-in card were studied for two different cases: In the first case, events were selected when a shower passed through one of the two sectors read out by the fan-in card in question. In the second case, the selection was made for events where the shower went through one of the sectors opposite those of the fan-in card. This selection was made to minimize the influence of showers, since the data sample used contained only Bhabha-triggered events. The selection procedure is illustrated in Figure 3. As in the calculation of off-line pedestals, the determination of the location of showers was based upon reconstructed clusters in the calorimeter arms. The distributions were compared to those obtained before coherent-noise correction but after pedestal subtraction. Figure 6 shows one example of each case from each arm. The coherent-noise correction was found to reduce greatly the width of the pulse-height distribution for all fan-in cards. The peak of the distribution after correction is at zero ADC counts. In the presence of showers, the distribution has a long tail towards higher values, as one would expect.

It is important to ensure that the calculation of the average pulse height used to correct the pedestal-subtracted signals in the vicinity of a shower is not biased by the shower itself. The correction applied to a signal by the coherent-noise correction algorithm was studied for two different cases, which are similar to those described above. The calorimeter was used to locate the sector through which a shower had passed. In one case, the strip with the maximum amplitude in this sector was selected, whereas in the other case, the corresponding strip in the sector opposite the one through which the shower had passed was selected; again, see Figure 3. The correction applied to these two strips is the difference between their pulse heights before and after coherent-noise correction. The average correction for each Kapton cable over all the events in the data sample was plotted for each of these two cases; a sample from each arm is shown in Figures 7(a) and (b). If there is no bias of the correction close to a shower, the average corrections must be the same with and without showers. There is indeed good, albeit not perfect, agreement between the two cases. However, in comparison with the width of the correction distributions, this difference is small and the bias negligible; see Figure 8 for an example of correction distributions in the presence and in the absence of showers.

The RMS cut in the calculation of $< a >_k$ was determined after a study of the way in which different cuts affect the pulse-height distribution after coherent-noise correction. If the cut is set too low, some of those strips which are not part of the shower but which populate the upper end of the pedestal distribution are excluded from the calculation of $< a >_k$. This results in an under-correction of the signal, and the pulse-height distributions far away from a shower will no longer be centered around zero. Too high a cut, on the other hand, includes strips which are indeed part of the shower in the calculation of $< a >_k$, and hence it yields an over-correction of the pulse height in the vicinity of the shower. Results of a very soft cut at $10r_i$ are shown in Figures 7 (c) and (d) as an illustration of the effects of over-correction when parts of showers are included in the coherent-noise calculation. The biased pulse-height correction in the presence of showers is clearly visible in Figure 7. Figure 9 compares pulse-height distributions of all the strips of a fan-in card in the absence and in the presence of showers for cuts at $10r_i$ and $2r_i$. The higher cut produces very good pedestal distributions in the absence of showers, whereas the lower cut results in a slight "overpopulation" of the tail on the positive side. This is due to fluctuations of the pedestal above the $2r_i$ cut. When several strips in the calculation of the

coherent noise fluctuate above the cut, the calculated value becomes an underestimate of the noise, resulting in a tail in the pedestal distribution. In the presence of showers, however, a cut at $10r_i$ leads to many strips with a signal from the shower entering the noise calculation. The consequence is an overestimated noise value and an over-corrected pedestal with a tail towards negative values. In this case, the cut at $2r_i$ behaves better. In the end, a cut at $3r_i$ was chosen.

An estimate of how many strips would remain to be read out after coherent-noise correction was obtained through a count of the number of strips with pulse heights $a_i > 3r_i$ after coherent-noise correction. For the bulk of events with one reconstructed cluster, *i.e.,* one shower, in the calorimeter arm, there remain less than 50 channels to read out on side A and less than 70 on side C. The corresponding numbers for the few events in the data sample with no shower in the calorimeter are 30 and 10 channels respectively. These distributions are shown in Figure 10. The fraction of events with one calorimeter cluster and no silicon strips to read out is 3%.

The coherent-noise correction method where a correction factor is calculated and applied in one step thus succeeds in reducing coherent noise without over-correcting the signal in the vicinity of a shower, and it permits a great reduction in the number of strips to be read out for each event.

5.2 Evaluation of On-Line Pedestal Algorithm

Pedestals calculated off-line according to the method described in Section 4.2 were used as reference pedestals to which those calculated on-line were compared. Results obtained after coherent-noise reduction, where the two different sets of pedestals had been used prior to noise correction, were also compared.

The number of events needed to calculate pedestals at the beginning of a run was determined after a study of the difference between pedestal mean values of the two methods as a function of the number of events. The mean values calculated without cuts fluctuate somewhat with the number of events used, due to the influence of showers. The second step, however, where a cut on the RMS (obtained in the first step) is applied, seems rather insensitive to these fluctuations. With 50 events used to calculate the first set of pedestals, the second set seem to be reasonably stable after less than 50 additional events. The choise was therefore made to use $50+50$ events at the beginning of each run to calculate pedestals. An example of the difference between the on-line and off-line pedestal mean and RMS values after the second iteration as a function of the number of events is shown in Figure 11.

The quality of the RMS values obtained using $50+50$ events was verified through a comparison of the distributions of the RMS values of the two pedestal methods. These distributions agree very well, as can be seen in Figure 12. 100 events is thus sufficient to obtain good RMS values.

In the previous subsection, the average pulse-height corrections calculated and applied by the coherent-noise reduction algorithm were discussed. These corrections were also studied when the reference pedestals had been used before coherent-noise correction. It was found that the two pedestal methods produce very similar results, as can be seen in Figure 13.

Finally, the optional method of recalculating the pedestals on each set of 100 events was compared to that of calculating them only once at the beginning of a new run. The average pulse-height corrections applied, as well as the pulse heights of all strips after coherent-noise correction, are very similar for the two methods.

These tests thus show that only 100 events are needed to calculated adequate pedestal mean and RMS values for the whole run with the proposed two-step scheme. This makes it possible to calculate pedestals on-line, which is necessary for on-line coherent-noise correction.

6 Comparison with Other Methods for Reduction of Coherent Noise

The tests described above were also performed on the other two methods for coherent-noise reduction, which were developed primarily for off-line use, and the results of the three algorithms were compared. For the sake of simplicity, we will refer to these two methods as methods B and C respectively and to the method described above as A.

6.1 Method B

The principle of method B is as follows: The coherent-noise correction is preceded by a conventional pedestal subtraction; pedestals which have been computed off-line at a previous stage are subtracted from the signal of each strip. Then the coherent noise is calculated and subtracted in four steps. First, the average pulse height of all strips is calculated. This value is subtracted from each strip. This procedure is carried out a second time, but now only strips which have a signal of less than 100 ADC counts are included. Then, individual fan-in cards are treated separately; the average signal of all strips of a fan-in card, without cuts, is calculated and subtracted from each of its strips. The last step treats groups of Kapton cables within each fan-in card: the four 12-channel Kapton cables reading out the 24 innermost strips of the two sectors of a fan-in card make up one group; the 20 following strips of each sector, read out by two 20-channel cables, make up a second group; the 16 last strips of the two sectors, also read out by two 20-channel cables, make up a third; and the four empty channels of these two cables make up a fourth group. The average pulse height of each group, where only strips which have a signal less than its RMS are included, is calculated. This is subtracted from all the strips of the group. The value that is then obtained for each strip is the coherent-noise corrected pulse height.

6.2 Method C

In method C the coherent-noise correction is done using individual noise-correlation coefficients for every strip. Only the noise correlations between strips of one sector are taken into account. To a good approximation, these coefficients are the components of the eigenvector corresponding to the largest eigenvalue of the noise covariance matrix for the strips of the sector. Since

the largest eigenvalue in each sector is much larger than all of the others, the noise is clearly dominated by the coherent component, and this approximation is therefore valid. The correlation coefficients are calculated together with pedestals in a separate run prior to the data processing. The noise RMS with and without the coherent-noise correction and quality flags for the strips are determined in the same run.

During the data processing, the coherent-noise correction procedure is carried out after the conventional pedestal subtraction. The correction procedure operates on individual sectors and consists of subtraction from each signal a_i within the sector the value proportional to its noise correlation coefficient v_i :

$$\begin{aligned} a_i' &= a_i - \kappa_s v_i \ , \quad \text{where} \\ \kappa_s &= \frac{\sum_i a_i v_i}{\sum_i v_i^2}. \end{aligned}$$

In the calculations of κ_s only those strips can be included which do not contain signals from showers. The calculations are therefore done iteratively, repeating the subtraction procedure three times. After each time the average RMS r_s for the sector is calculated,

$$r_s = \sqrt{\frac{1}{N}\sum a_i^2} \ ,$$

where N is the number of accepted strips, and those strips for which $a_i > 3r_s$ are then excluded from the calculation of κ_s in the next iteration.

6.3 Comparison

The signal amplitudes after coherent-noise correction by the three methods are shown in Figures 14 and 15. All three methods reduce the spread in the band around zero with respect to the situation previous to coherent-noise correction; see Figures 4 and 5. In general, methods A and C have very little occupancy below the band around zero ADC counts; in some cases it is smaller for method A, whereas in others it is smaller for method C. Method B, however, shows certain regions, which correspond to Kapton cables, where there is a relatively large occupancy below this band. This could be an indication of incorrectness in the assumption on correlation between some Kapton cables in this method.

Examples of the pulse-height distributions of all the strips of a fan-in card in the absence and in the presence of showers are shown on both linear and logarithmic scales in Figure 16. In the absence of showers, method C produces distinctly narrower distributions around zero ADC counts than the other two methods. In the presence of showers, the body of the distribution of method C is often asymmetric around zero, with a larger occupation of negative values. In certain cases it even extends below the pedestal distribution. This might indicate that the calculation of the correction by method C is somewhat influenced by the presence of showers.

A comparison of the pulse-height corrections applied by the three methods, studied in the same fashion as earlier, can be found in Figure 17. It shows that all three methods apply average corrections very near zero ADC counts in the absence of showers. A count of the number of strips remaining after a cut at $3r_i$ performed on methods B and C yields practically identical

results to those of method A.

The three methods thus produce similar results, with the exception of method C which gives narrower pedestals than the other two in the absence of showers and perhaps over-corrects the pulse height somewhat in the presence of showers. Methods B and C are not directly applicable on-line, since they make use of data calculated off-line, such as pedestals, but they could be modified for on-line use, for instance by implementing the on-line pedestal algorithm proposed here. In the view of the complexity of the algorithms, however, method A should be better suited than the other two to meet on-line constraints.

7 Conclusions

The method for coherent-noise correction for the STIC silicon detectors described here is simple enough to be used on-line in order to reduce the amount of data to read out from these detectors. After pedestal subtraction, a coherent-noise term is defined to be the average pulse height of correlated Kapton cables, with a cut on the RMS of each strip in order to limit the influence of showers. This value is then subtracted from the pedestal-corrected signal. This procedure reduces coherent noise without over-correcting the pulse height of a shower. Tests show that pedestals can be calculated for each LEP run with good accuracy using about 100 events at the beginning of the run or, optionally, using sets of 100 events throughout the run. Comparisons with two other algorithms proposed for reduction of coherent noise show that the least complex method performs as well as the other two in terms of accuracy and should be well suited for on-line use.

8 Acknowledgements

The authors gladly acknowledge the many fruitful discussions and ideas contributed by T. Camporesi. We would also like to thank E. Migliore for shedding light on the readout of the silicon-strip detectors.

References

[1] S. J. Alvsvaag et al., *The Small Angle Tile Calorimeter project in DELPHI,* DELPHI 95-12 CAL 119, Contribution to the 4th International Conference on Advanced Technology and Particle Physics, Como, Italy, October 1994.

[2] S. J. Alvsvaag et al., *The DELPHI Small Angle Tile Calorimeter,* DELPHI 94-157 CAL 120, Contribution to the IEEE 1994 Nuclear Science Symposium and Medical Imaging Conference, Norfolk, USA, October 1994.

[3] S. J. Alvsvaag et al., *The new small angle calorimeter in DELPHI,* DELPHI 94-148 CAL 118, Contribution to the 5th International Conference on Calorimetry, Brookhaven, USA, September 1994.

[4] S. J. Alvsvaag et al., *The DELPHI Small Angle Tile Calorimeter,* DELPHI 95-14 CAL 123, Contribution to the Beijing Calorimetry Symposium, Beijing, China, October 1994.

[5] S. J. Alvsvaag et al., *The Silicon Shower Maximum Detector for the STIC,* DELPHI 94-126 CAL 117, Contribution to the 6th Pisa Meeting on Advanced Detectors, Elba, Italy, May 1994.

[6] S. J. Alvsvaag et al., *A silicon pad shower maximum detector for a "Shashlik" calorimeter,* DELPHI 94-158 CAL 121, Contribution to the IEEE 1994 Nuclear Science Symposium and Medical Imaging Conference, Norfolk, USA, October 1994.

[7] S. J. Alvsvaag et al., *A Silicon Pad Shower Maximum Detector for a Shashlik Calorimeter,* DELPHI 95-13 CAL 122, Contribution to the 4th International Conference on Advanced Technology and Particle Physics, Como, Italy, October 1994.

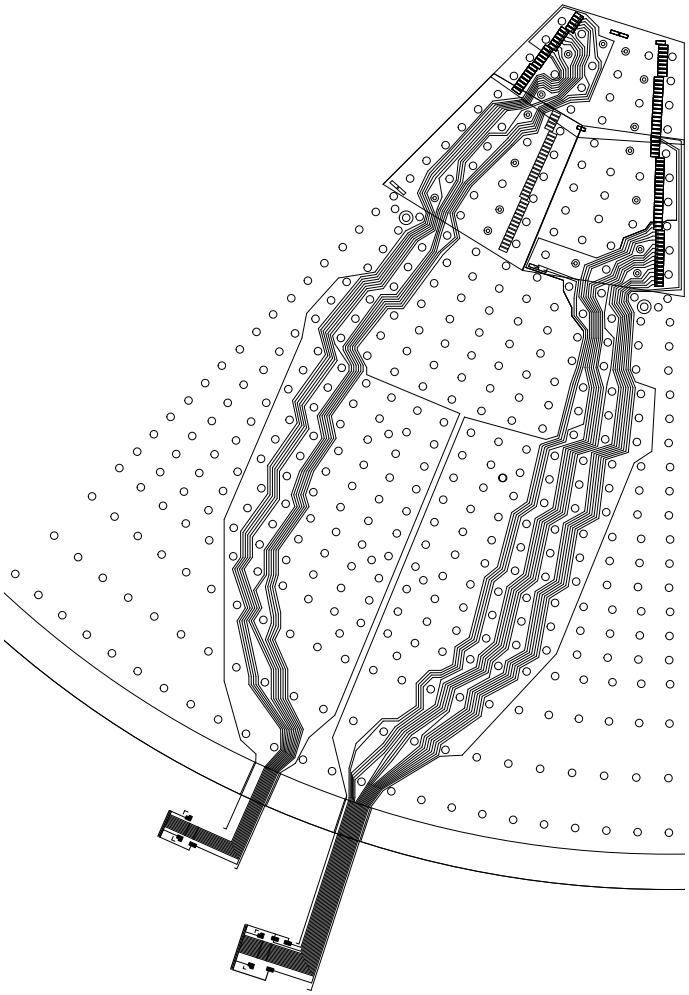

Figure 1: A 45° wedge (two 22.5° sectors) of the silicon shower maximum detector, with two of its eight Kapton cables shown. The strip structure within the sectors is not indicated. Note the many holes for the calorimeter fibers, which the signal wires have to avoid.

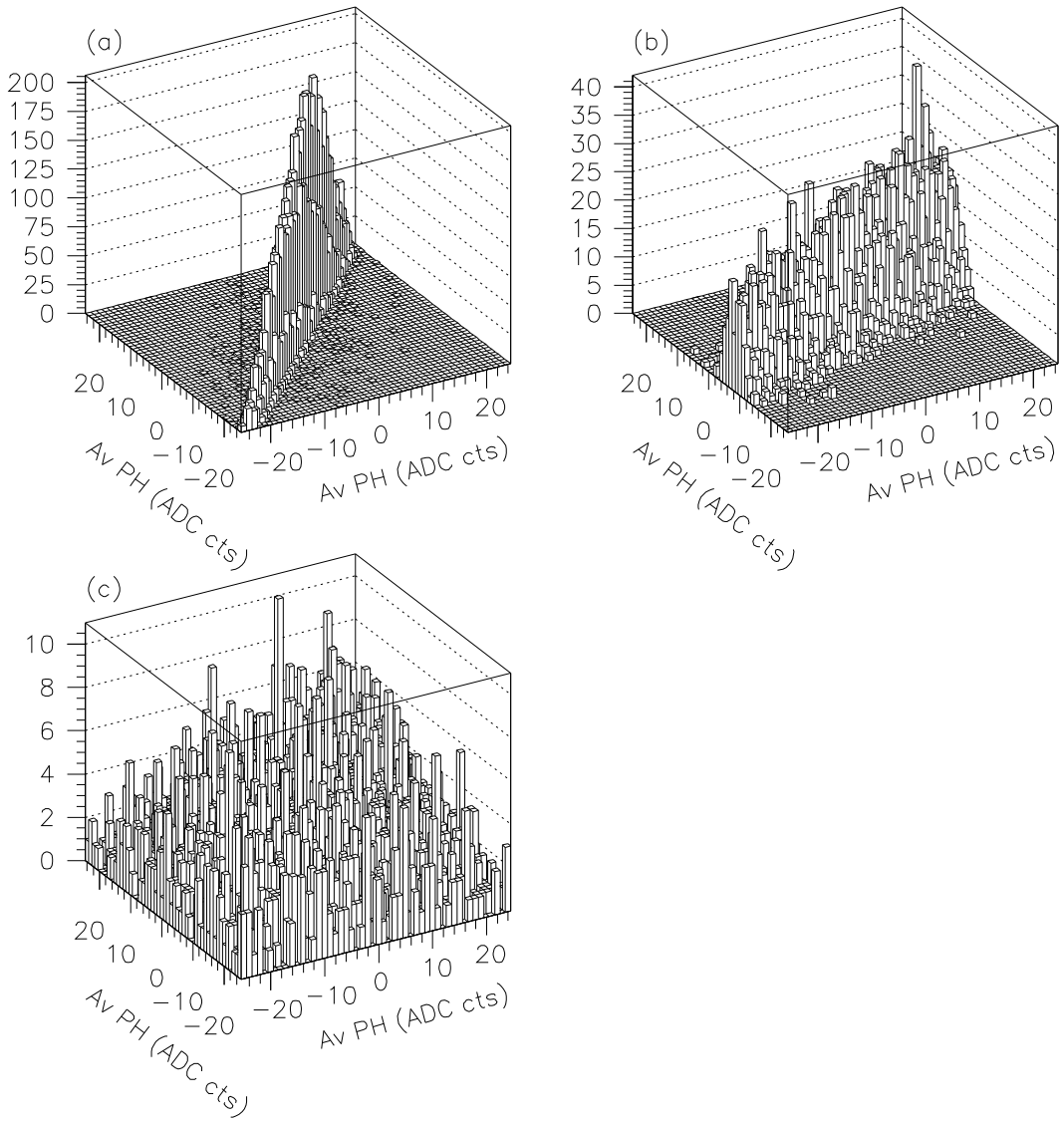

Figure 2: Examples of (a) "strong" correlation, (b) "weak" correlation, and (c) "no" correlation between the average pulse heights of pairs of Kapton cables.

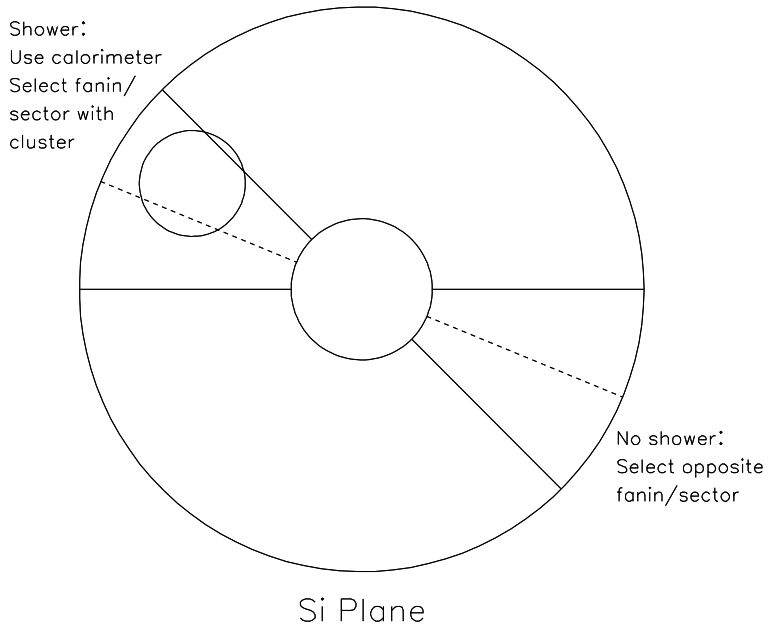

Figure 3: Selection of fan-ins/sectors, with and without showers.

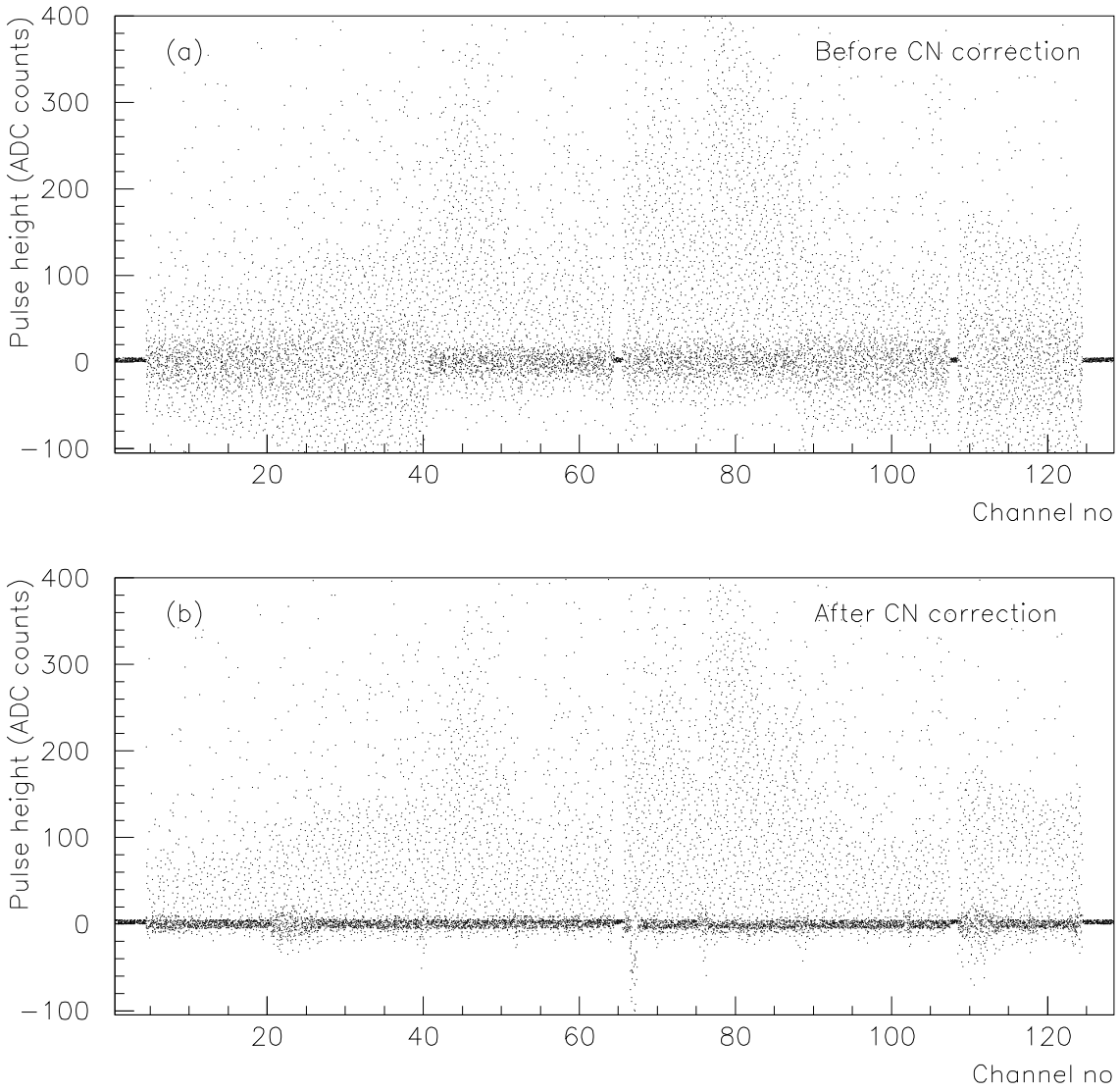

Figure 4: Pulse heights of the strips of a fan-in card reading out side A, (a) before and (b) after coherent-noise correction.

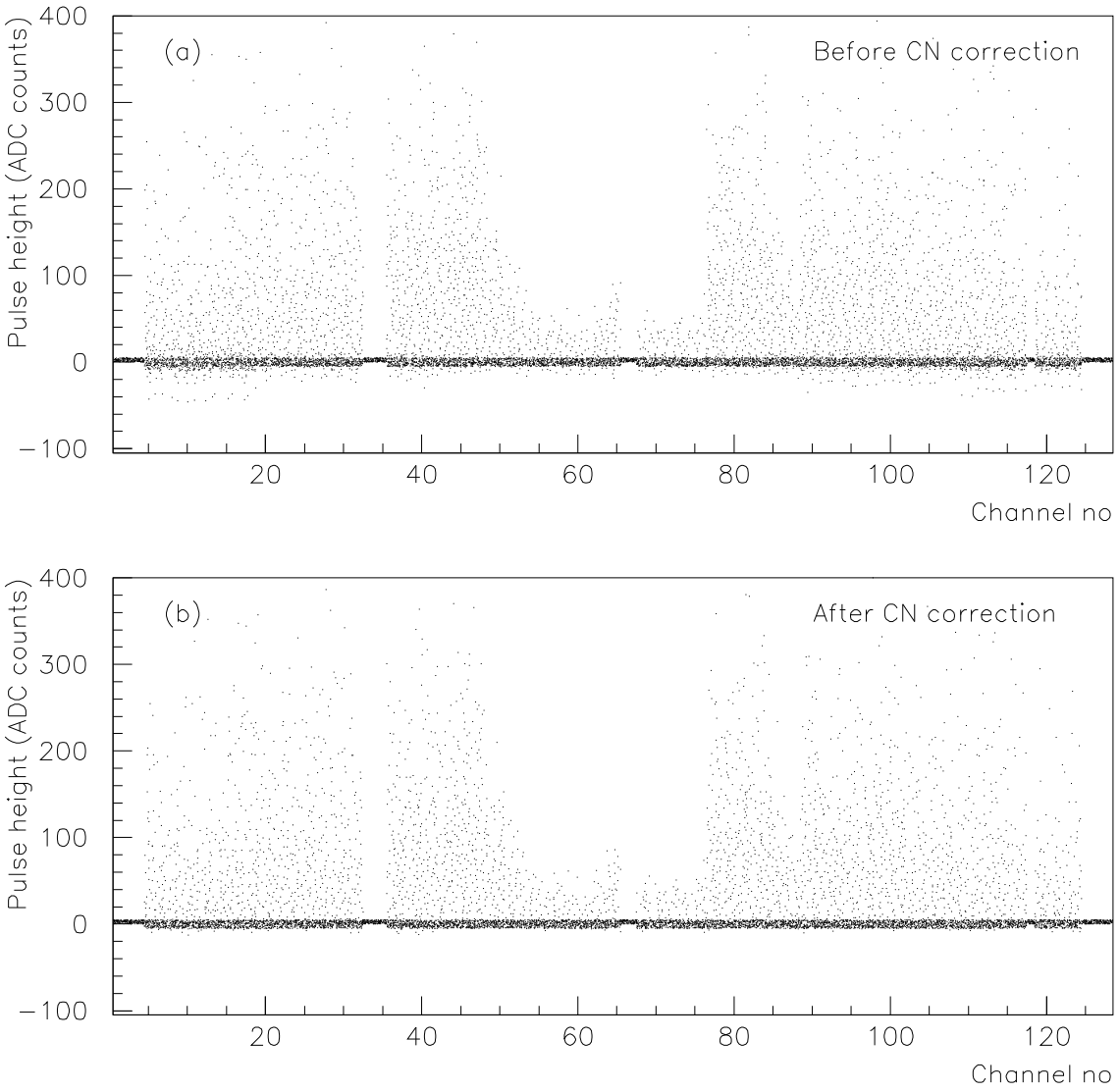

Figure 5: Pulse heights of the strips of a fan-in card reading out side C, (a) before and (b) after coherent-noise correction.

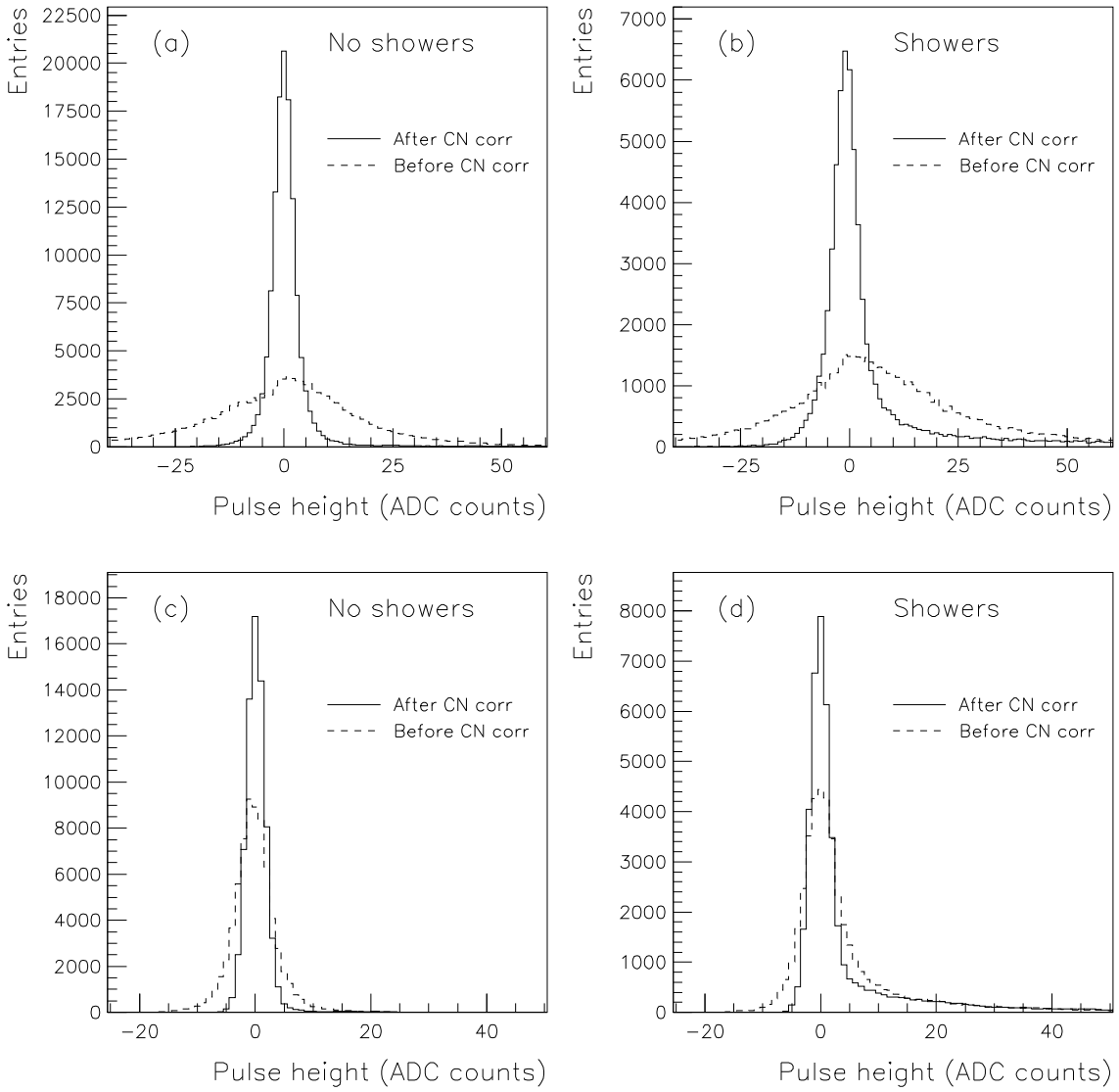

Figure 6: Pulse-height distributions of all strips of a fan-in card before and after coherent-noise correction, for a fan-in card of side A (a) without and (b) with showers and one of side C (c) without and (d) with showers.

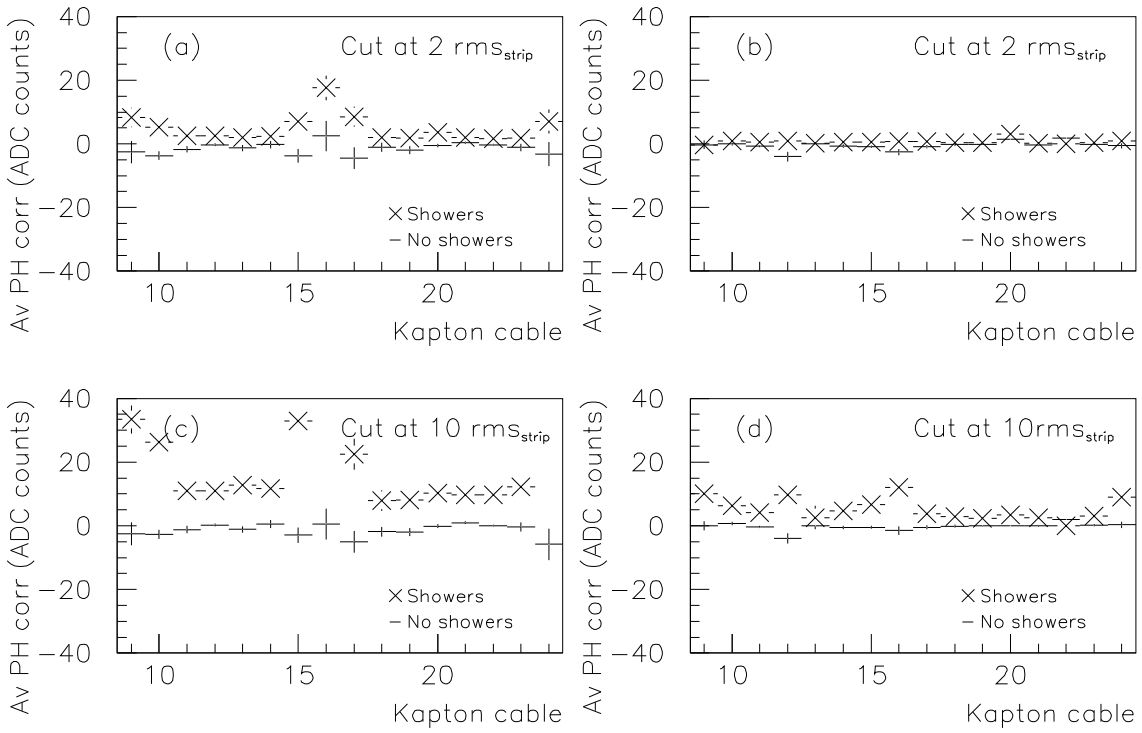

Figure 7: Average pulse-height correction in the presence and in the absence of showers for some Kapton cables. (a) and (b) show examples from side A and side C respectively, when a cut at $2r_i$ was used in the calculation of $< a >_k$. (c) and (d) show the same Kapton cables when a cut at $10r_i$ was used instead.

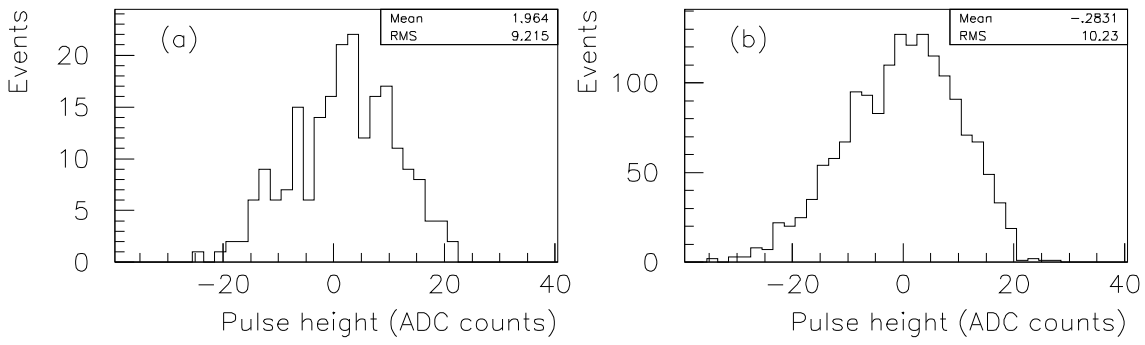

Figure 8: Examples of distributions of pulse-height correction (a) in the presence and (b) in the absence of showers for a Kapton cable of side A and with a cut at $2r_i$ in the calculation of $< a >_k$.

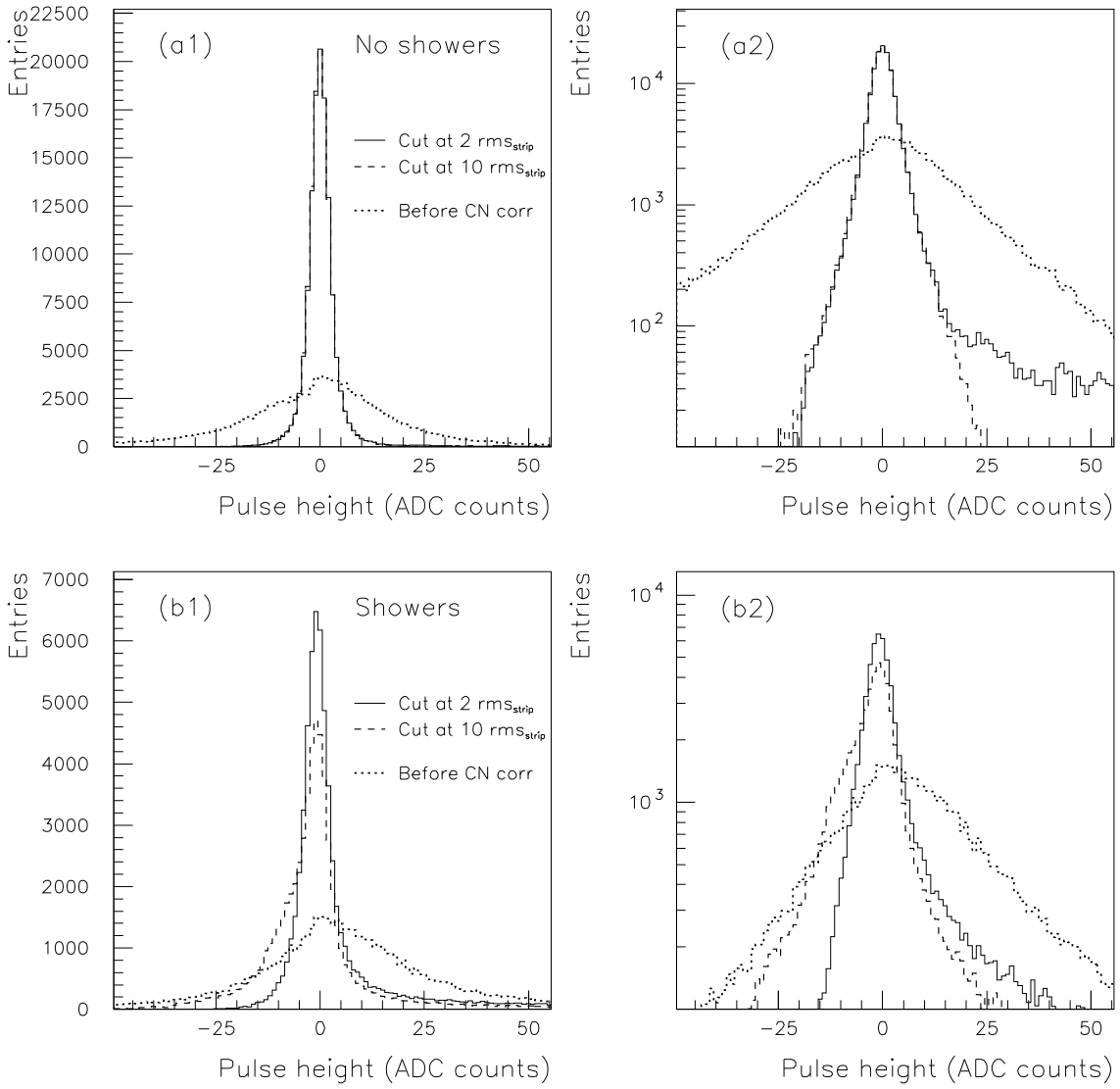

Figure 9: Pulse-height distributions of all strips of a fan-in card of side A after coherent-noise correction; cut at $10r_i$ *vs.* cut at $2r_i$ in the calculation of $< a >_k$. (a1) and (a2) show the distributions in the absence of showers, on linear and logarithmic scales respectively, whereas (b1) and (b2) show the distributions in the presence of showers, also on linear and logarithmic scales.

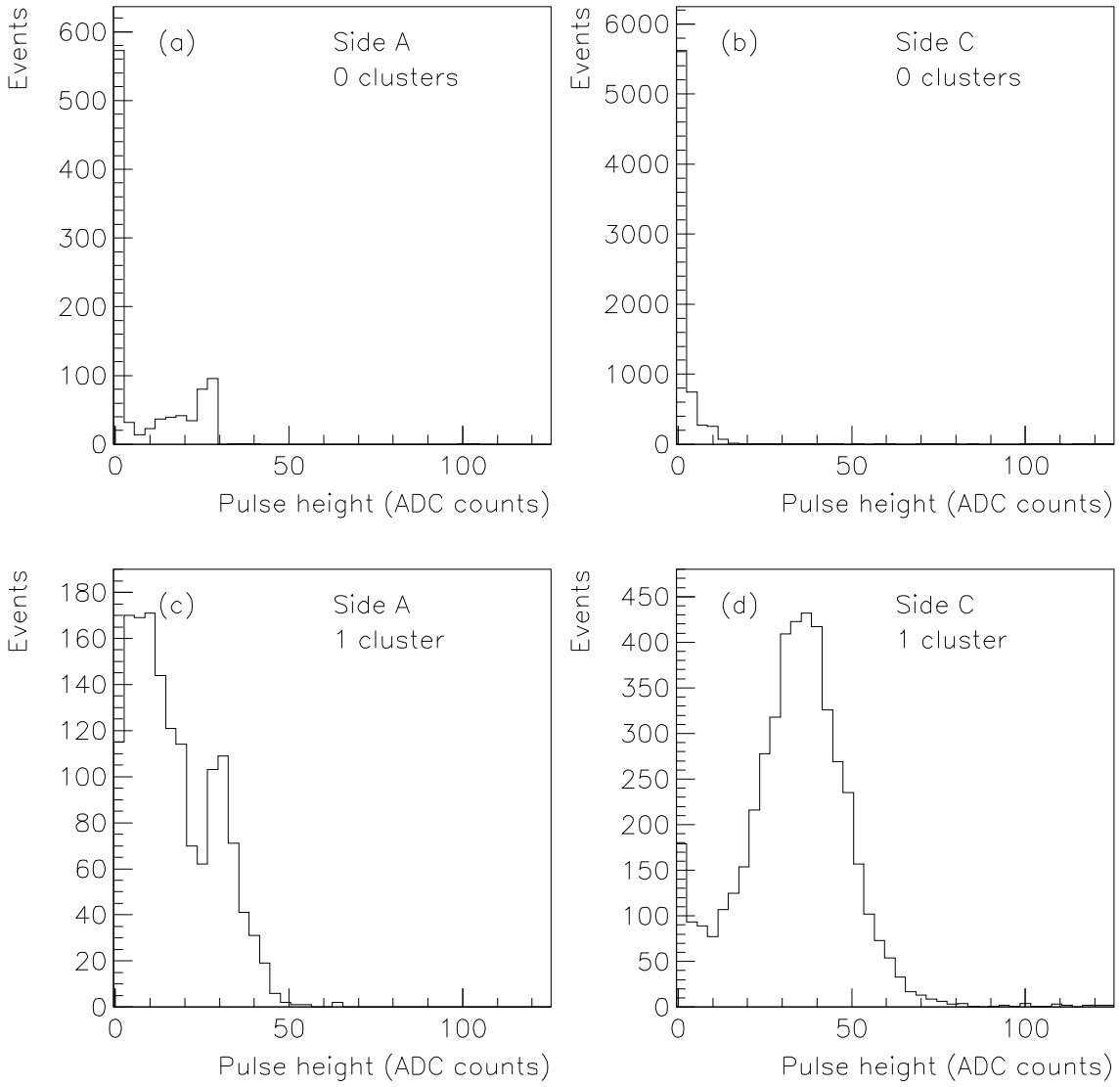

Figure 10: Example of number of strips to read out after a cut at $3r_i$ for sides A and C, with the calorimeter indicating 0 and 1 clusters (showers) respectively.

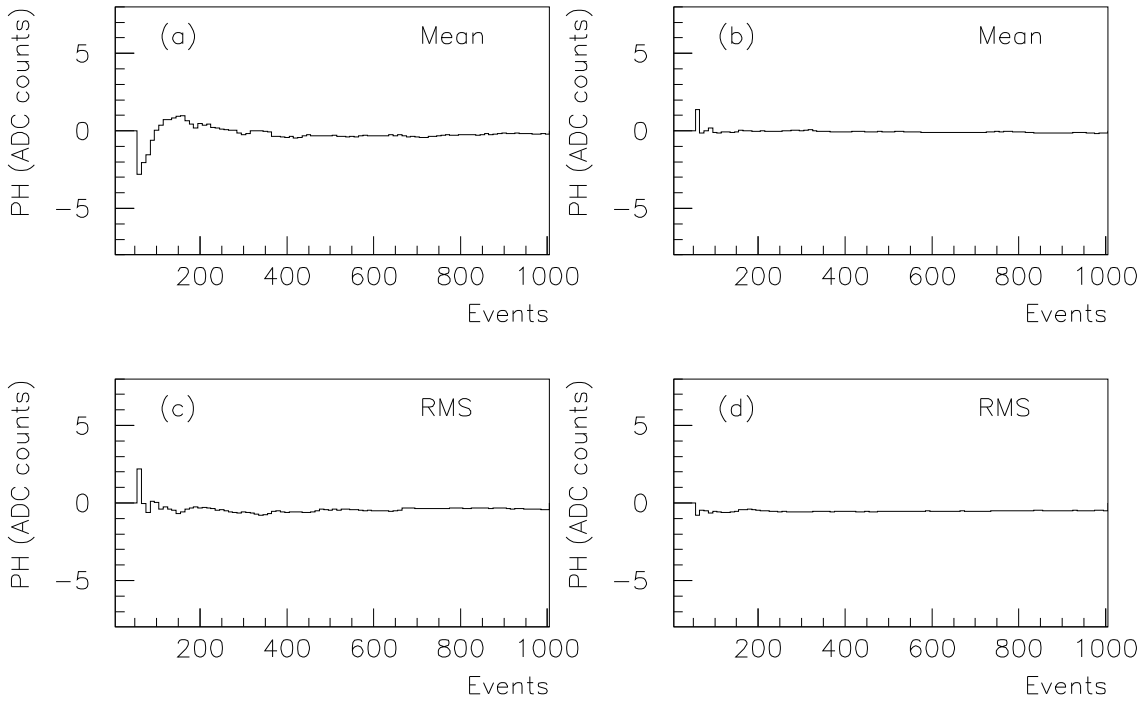

Figure 11: Examples of difference in mean and in RMS between pedestals calculated on-line and those calculated off-line as a function of the number of events. (a) and (c) show a strip from side A, and (b) and (d) show a strip from side C. The first 50 events were used to calculate preliminary pedestals according to the first step of the algorithm.

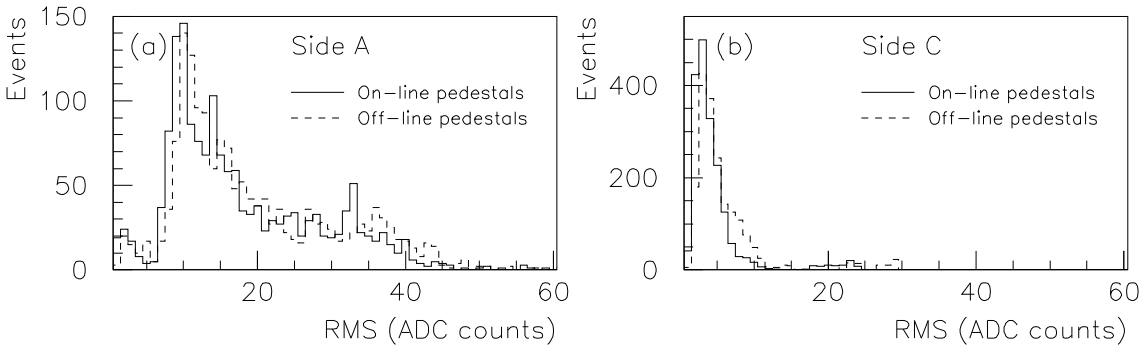

Figure 12: Comparison between RMS distributions of pedestals calculated on-line and off-line respectively for side A and side C. (Each strip provides one entry in the histograms.)

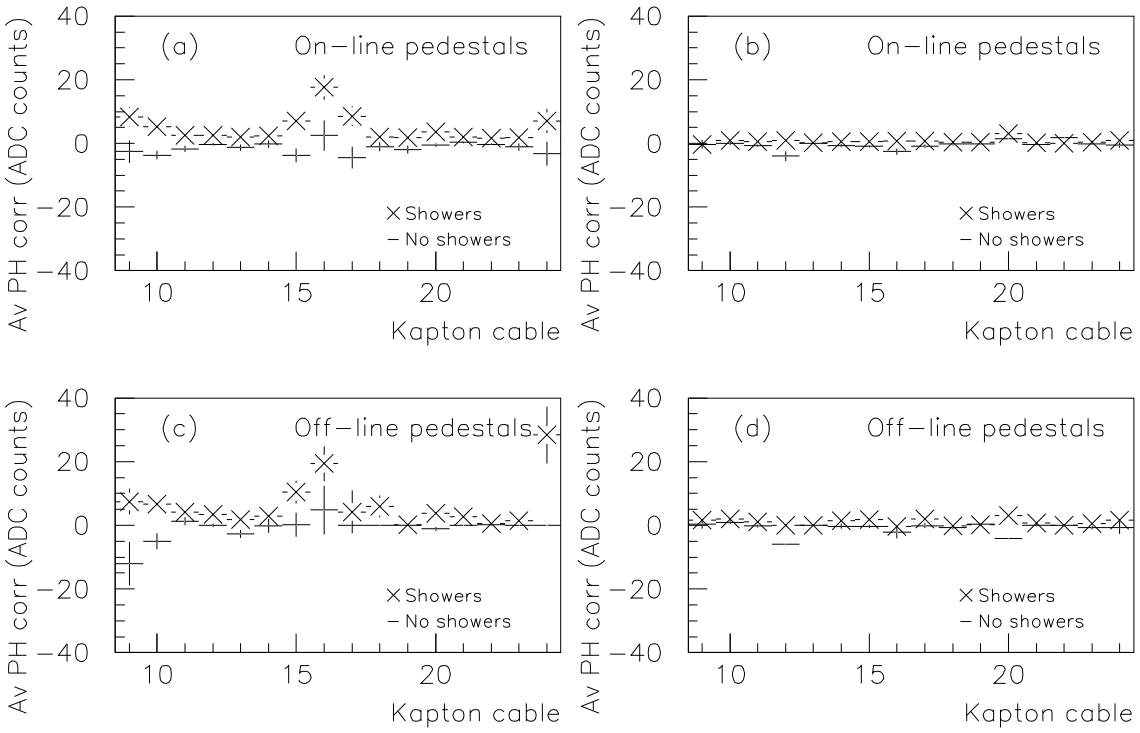

Figure 13: Example of average pulse-height correction using on-line pedestals, (a) side A and (b) side C, and off-line pedestals, (c) side A and (d) side C.

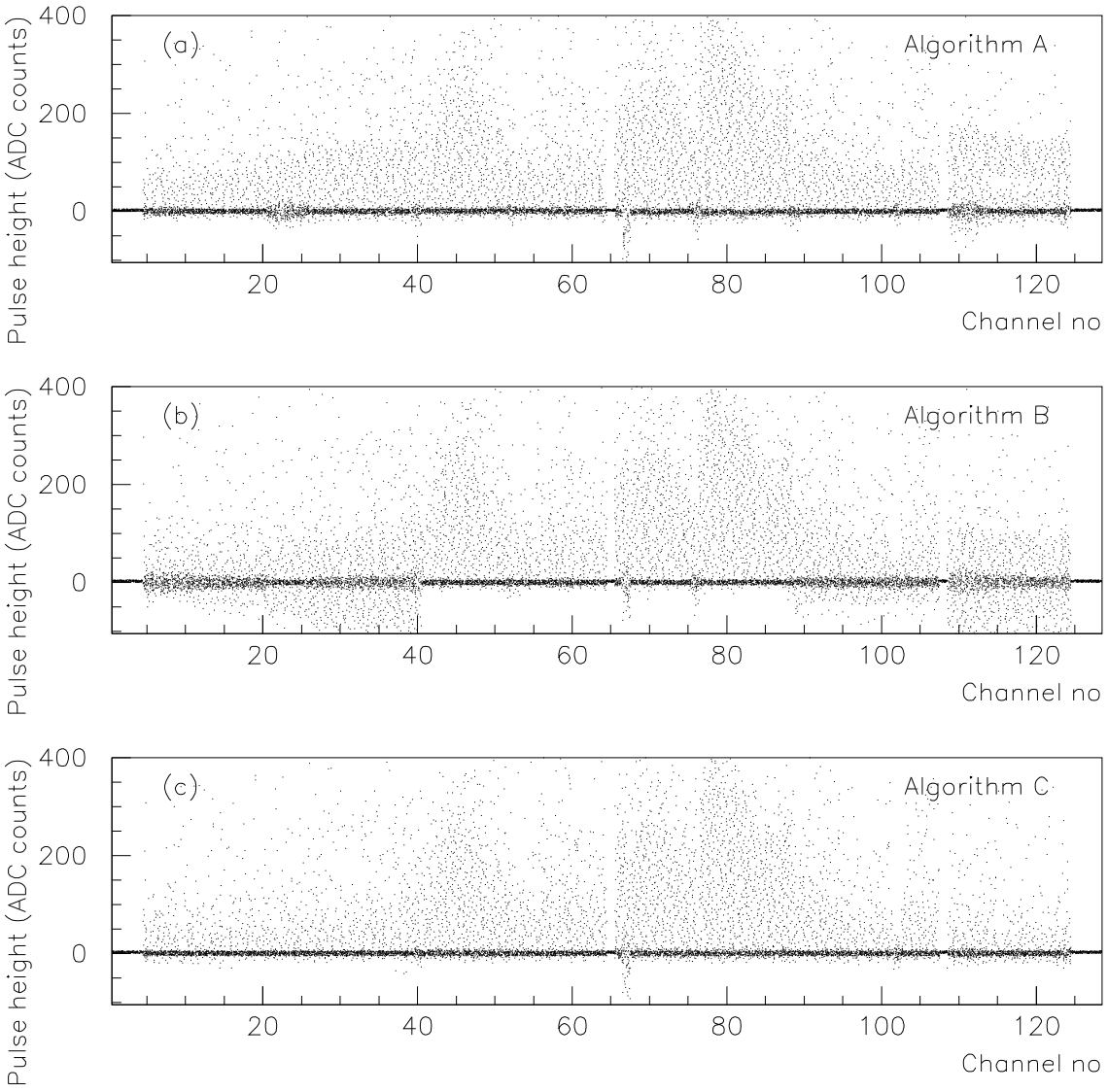

Figure 14: Pulse heights after coherent-noise correction of a fan-in card of side A for the three methods.

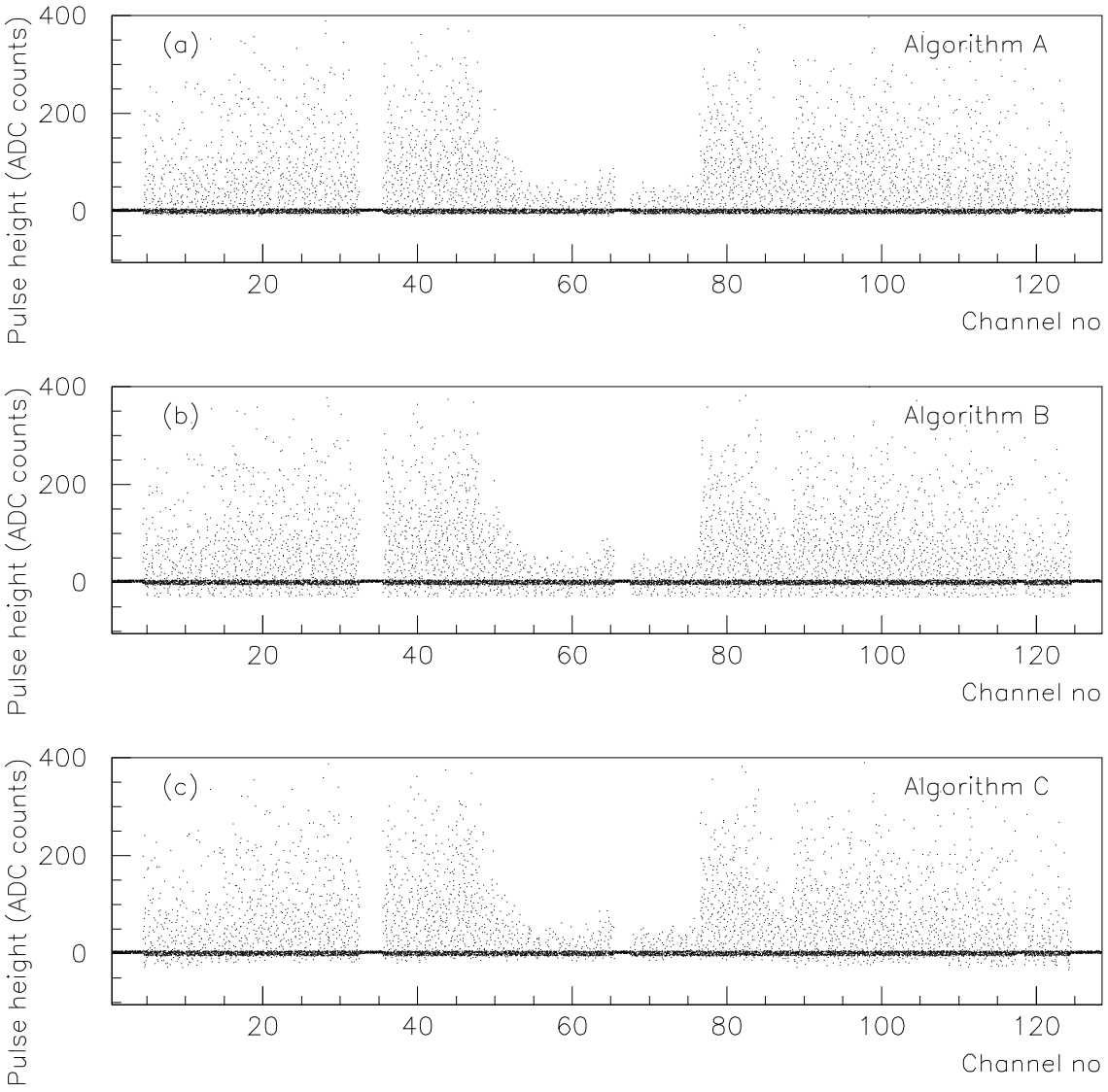

Figure 15: Pulse heights after coherent-noise correction of a fan-in card of side C for the three methods.

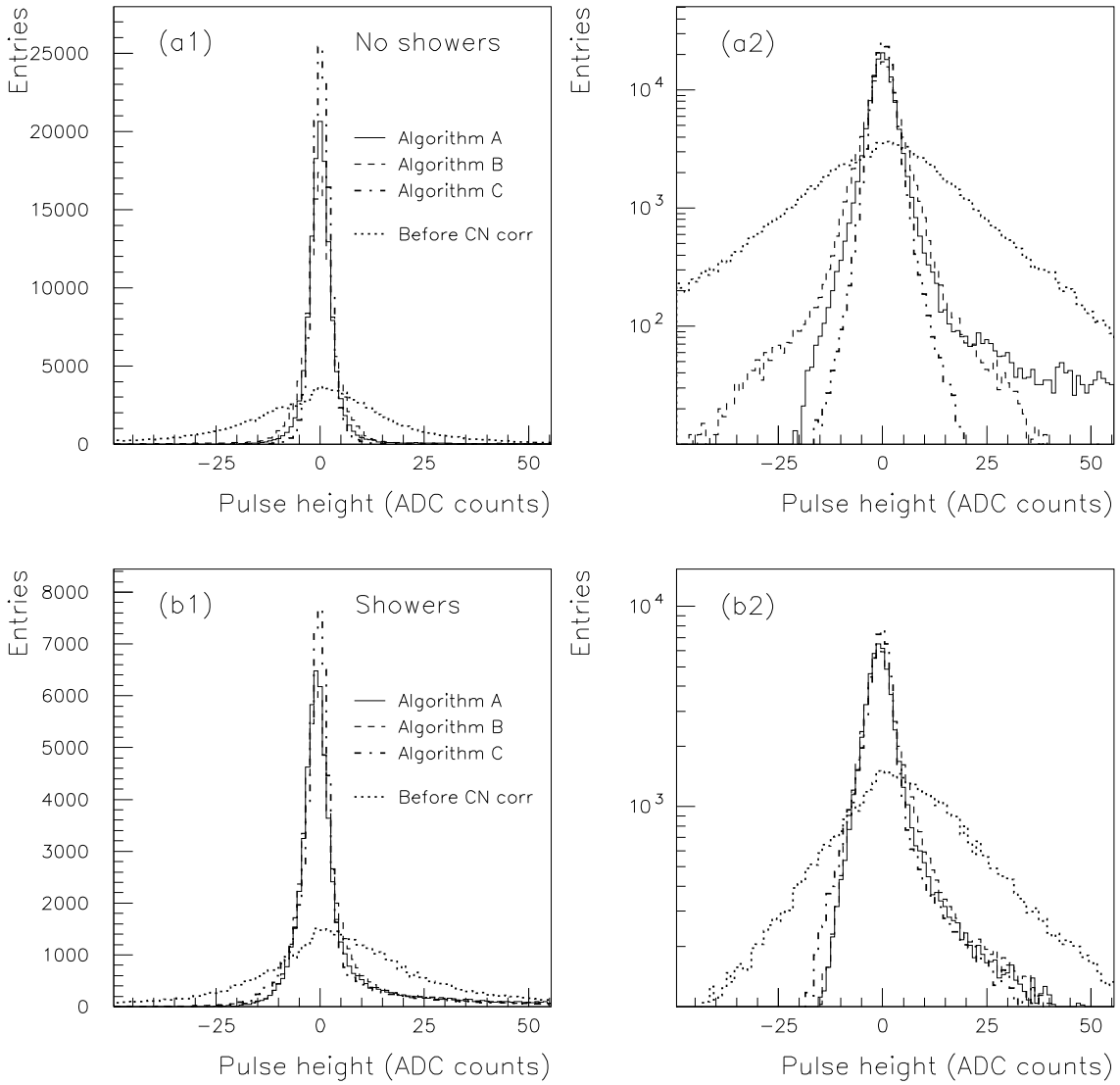

Figure 16: Pulse-height distributions after coherent-noise correction of all strips of a fan-in card of side A for each one of the three algorithms. (a1) and (a2) show the distributions in the absence of showers, on linear and logarithmic scales respectively, whereas (b1) and (b2) show the distributions in the presence of showers, again on linear and logarithmic scales.

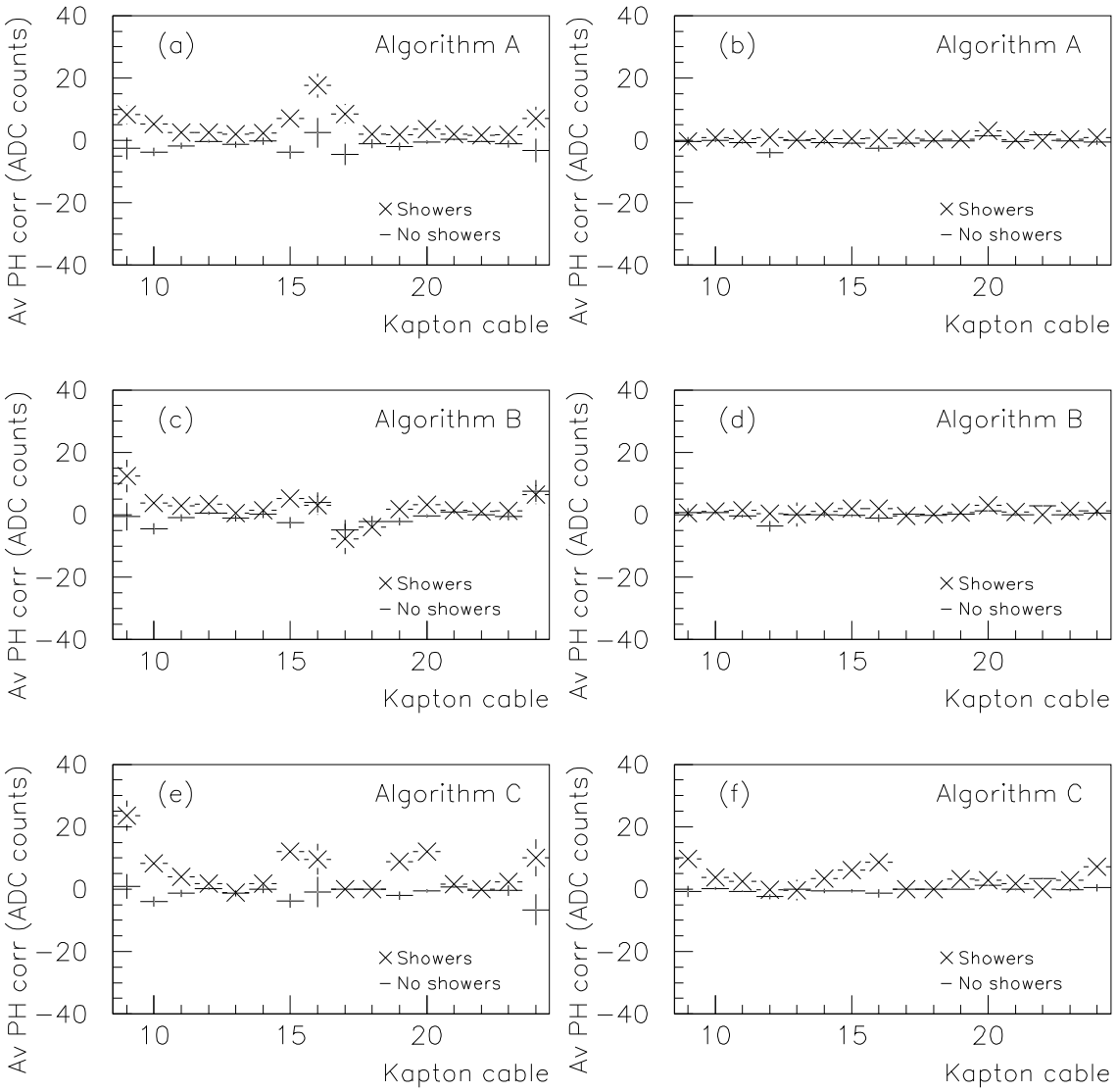

Figure 17: Example of average pulse-height correction for the three different algorithms; (a), (c) and (e) side A and (b), (d) and (f) side C.

Article VII

The Fast Wire Scanner of the CERN PS

EE

CERN-PS-95-06-BD-OP

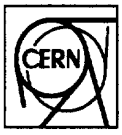

EUROPEAN ORGANIZATION FOR NUCLEAR RESEARCH

CERN - PS DIVISION

CERN/PS 95-06 (BD/OP)

THE FAST WIRE SCANNER OF THE CERN PS

V. Agoritsas, E. Falk, F. Hoekemeijer, J. Olsfors, Ch. Steinbach

Abstract

The Fast Wire Scanners of the PS measure the horizontal and vertical profile of the circulating beam and are important instruments for obtaining beams of high performance, in particular those destined for the LHC.

The system has been upgraded over the last few years. Two new units were built, for improved availability in case of wire breakage, and, through new technology, to provide much longer wire life time, higher precision of measurement, and greater ease of operational use. After the success of the new units, the old ones were upgraded to the same standard. Carbon strands, made of twisted fibres, cross the beam at velocities of up to 20 m/s. Secondary particles, created by the collision of beam particles with the carbon nuclei, are detected with scintillators coupled to photo-multipliers. Their signals are acquired simultaneously with the wire position.

This report describes the physics underlying the method; the mechanism; the electronics; and the software for control, data acquisition and treatment, and display of results.

Geneva, Switzerland
27/3/95

The Fast Wire Scanner of the CERN PS

V. Agoritsas, E. Falk, F. Hoekemeijer, J. Olsfors, Ch. Steinbach

1. Introduction

To attain highest energies, particle accelerator are nowadays cascaded, one injecting into the next with the last stage often being a collider. The chain from the first injector to the collision ring must be optimised for maximum luminosity. Accurate measurement of the beam profile and transverse emittances in circular accelerators has therefore become a primary concern. One of the most reliable instruments is the fast wire beam scanner, now installed in several machines throughout the world. At the CERN PS, a first version was developed almost ten years ago [1]. Two units were installed, one for each plane to measure the proton and antiproton beams destined to the SPS in collider mode. They were thus limited to beams of low intensity. Their reliability was poor and the precision questionable so that an improvement project was launched in 1991. Two new devices were installed and first used as prototypes during the tests of the PS as LHC injector in December 1993 [2]. The installation was completed when the two old ones were upgraded in March 1994. The system became fully operational and integrated in the controls system by the end of the year 1994. The total of four devices, two for each horizontal and vertical plane profiles, are designed to measure all beams available in the PS at present: protons, antiprotons, ions, electrons and positrons, in the energy range of 1 to 25 GeV (for protons) and intensities from 10^9 to 2×10^{13} particles per pulse (ppp).

2. Physics of the system

2.1 Principle

A wire is stretched between the two prongs of a fork, perpendicular to the beam and moved rapidly through the circulating beam (Fig.1). Secondary particles, produced by the interaction of the circulating particles with the wire material, hit a detector, which consists of a scintillator and photo multiplier. The output signal is sampled together with the wire transversal position. The projected beam profile is thus obtained, and also the emittance assuming the β function, the dispersion and momentum spread are known at the device location.

2.2 Multiple scattering

The beam blow-up of the 2σ emittance due to multiple scattering after one traversal is given by [3]:

$$\Delta\varepsilon_x = \frac{\pi}{2}\frac{\beta_x d^2}{v\tau X_o}\left(\frac{15}{\beta p}\right)^2$$

where β_x is the local Twiss amplitude parameter in the measurement plane, d the wire diameter, v the projected transverse wire velocity, τ the revolution period of the particles around the machine, X_0 the radiation length in the wire material, β the particle velocity in units of c, and p the particle momentum (in MeV/c).

In order to minimise the blow-up, the following measures are taken:

- the largest feasible velocity (20 m/s) is aimed at, particularly at injection energy. At higher energies, a lower velocity can be chosen to reduce strain on the mechanism.
- the wire diameter is chosen as small as strength and reliability permit (30 μm).
- Carbon was chosen as wire material replacing the previously used Beryllium, since it has a larger radiation length for the same mechanical strength.

The resulting blow-up factors at three typical PS energies are given in Table 1.

Table 1: Emittance blow-up at 20 m/s velocity

Energy or momentum	Blow-up in meas. plane	Blow-up in other plane	Normalised blow-up in meas. plane	Normalised blow-up in other plane
1 GeV (injection)	0.11	0.20	0.19	0.36
3.5 GeV/c (intermediate)	0.025	0.046	0.094	0.173
26 Gev/c (maximum energy)	0.0005	0.0008	0.013	0.023

2.3 Interaction and temperature rise

The wire scanner must be able to measure the highest beam intensities achieved at present in the PS. Due to interaction with the circulating beam, the temperature of the wire increases during traversal of the beam. Beam traversal is so fast that conduction along the wire and heat radiation are negligible. While measuring the emittance ε_x, the temperature rise is then [3]:

$$\Delta T = \frac{k}{C_v} \frac{dE}{dx} \frac{\beta N}{v \tau} \sqrt{\frac{3}{p \beta_z \varepsilon_z}}$$

where k is the fraction of ionisation loss converted into heat, C_v the heat capacity of the wire material, dE/dx the ionisation loss of the particles in the wire, N the number of particles and ε_z the emittance in the other transverse plane.

The coefficient k has been estimated [4] to 1/3, so that, for an intensity of 2×10^{13} ppp à 26 GeV/c and a normalised emittance of $\varepsilon_z = 30\ \pi$ µrad:

for v = 20 m/s $\quad T \cong 530°C$

for v = 10 m/s $\quad T \cong 1060°C$

The tensile strength of the Carbon wire remains good up to 1300 °C [5], so that one can be confident that the measurements can be made on the highest intensity beams possible today in the PS (2.7×10^{13} ppp).

2.4 The monitor

2.4.1 Choice of scintillator and Photomultiplier

As mentioned in paragraph 2.1, the projected beam distribution is obtained by observing the nuclear interactions of the moving wire material with the circulating beam.

The monitor consists of a small scintillator made of NE110, a long air light guide, a set of optical filters, and a new mesh-type photomultiplier (PM).

The chosen PM, Hamamutsu R2238, has 12 stages of proximity mesh dynodes. The tri-alkalide photocathode can deliver up to 600 mA. The gain varies from 10^3 for an anode voltage of 500V up to 4×10^5 at 1500V. Linearity is good, as shown later.

Two monitors are installed for each wire scanner. One detects the secondaries at small angles in the forward direction of clockwise circulating positively charged particles, the other one looks at the negatively charged particle rotating anticlockwise.

The monitors are designed to detect secondaries with the same efficiency for all possible beam sizes and to keep the background to signal ratio as low as possible. There are optical filters to adjust the photon flux hitting the photocathode. They are neutral grey filters with transmission factors from 0.2 to 100 %, mounted on a Carousel assembly allowing an easy selection. The PM can thus be chosen to obtain a linear response along the whole dynamic range of particle energies and intensities. The optical filters also allow to check the linearity of the PM's for various anode voltages.

2.4.2 Sensitivity

The beam intensities vary from almost 3×10^{13} ppp down to a few 10^9, and the momentum ranges from 0.6 to 26 GeV/c, leading to large differences in secondary particle production rates. Moreover, the dynamic range must include the density variation between the core of the beam and its tails.

The PM dynamic range of a factor 500, given by the manufacturer, is thus not sufficient and a set of optical filters was introduced between scintillator and PM to enlarge it.

The PM sensitivity needs to be described for automatic setting of the filters and PM voltage. The semi-empirical approximate formula is:

$$S \cong K\, p\, I_p\, (1+50T)\, V^8$$

where S is the signal in ADC bits, p the momentum in GeV/c, I_p the beam intensity in 10^{10} ppp, T the transmission factor of the optical filter and V the PM voltage.

The linear dependence on the beam momentum was checked experimentally between 1.7 and 24 GeV/c (Fig. 2). The sensitivity law of V^8 was found from experimental data (Fig. 3) where laws in V^7 and V^8 are compared using a beam intensity around 18×10^{11} ppp, a 20% filter, at 24 GeV/c, with a PM voltage varying from 600 V to 950 V.

2.4.3 Linearity

Linearity is essential for the measurement precision. It was experimentally checked in two ways:

a) By varying the beam intensity: At two different energies, the proton intensity was changed at the PS Booster injection energy of 50 MeV by the standard procedure of varying the number of injected turns. The integral of the output signal over the whole scan is plotted versus intensity on Figure 4. The linearity was found to be better than 5 % up to 3×10^{12} ppp. But this method, in fact, involves a much larger scale since the integration applies also to the tails of the beam where the density is low.

b) By observing the beam at low energy and intensity first (1.7 GeV/c and 9 10^{12} ppp), then at higher energy and intensity (14 GeV/c and 900 10^{10} ppp), with various optical filters (Figs. 5 and 6.). By this method, which is more rigorous than the previous one, the linearity is found to be 2%. One notes that for zero transmission (a blank instead of a filter), one still observes a signal due to direct radiation on the PM.

3. Mechanism

The mechanical assembly consists of three parts (Fig. 7 and 8):

1) An electric motor with a crankshaft and a connecting rod.

2) A push-pull device connecting by bellows the motor in air to the fork in vacuum.

3) A fork with the wire strung between the prongs, hinged along the axis of its base.

3.1 Motor

The mechanism is actuated by a permanent magnet DC motor, with a printed-circuit rotor for small inertia. The axle carries a tachometric dynamo and a position transducer (resolver) on one side and a crankshaft on the other. This crankshaft moves a connecting rod, with needle bearings on both ends, which transforms the circular motion into a linear one. The motor shaft rotates through 180° for the total travel of the wire.

3.2 Push-pull device

The small end of the connecting rod acts on one side of a rocker, hinged at its middle. Both ends of the rocker act on arms which thus make a push-pull movement. These two arms traverse the wall of the vacuum vessel of the wire scanner, by two bellows with a stroke of 7 mm. Inside the vacuum the push-pull arms act on 4 rolling ribbons, fixed around the cylindrical base of the fork such that the linear movement of the arms is translated into the circular movement of the fork.

3.3 Fork

The prongs of the fork are stainless steel tubes, outer diameter 2 mm with 0.25 mm wall thickness. The parts closest to the wires have holes drilled for greater lightness. The wire is in fact a twisted strand of about 20 carbon fibres, each 7 μm thick. Their ends are copper plated to allow them to be soldered. The last cross drillings of the prongs bear a ceramic cartridge for electrical insulation (Fig. 9). Inside the cartridge is a copper connecting piece into which the end of the carbon wire is soldered. Electrical control wires inside the prongs of the fork, are soldered to the outside of the connecting piece.

The ends of the prongs are flat to act as a leaf spring. The wire is under a tension of about 20 grams. This is the breaking strength of a single fibre, hence there is a great margin.

The length of the wire is 107 mm. It moves over an angle of 130°: accelerating, coasting across the beam of, at 20, 15 or 10 m/s and then decelerating to a stop.

The base of the fork is a tube supported at both ends by bearings made of Vespel charged with MoS_2. This is a poly-imide, resistant against ionising radiation and able to stand baking up to 300°C.

3.4 Testing

The original wire scanner of 1984 was equipped with a 30 µm diameter Beryllium wire which usually broke after a few hundred measurements, presumably by fatigue, as the broken ends never showed signs of sputtering or melting. This was the reason to find another material, of low atomic weight, but with a greater mechanical resistance and about the same effective cross section.

The choice fell on a wire consisting of multiple carbon fibres, as there does not seem to be commercially available carbon fibres thicker than about 7 µm. Life time testing was performed on one mechanism only and was stopped after 5000 to-and-fro movements, the wire being still intact. In the PS, where 4 units are installed, no wire breakage has occurred after a year of operation.

4. Electronics

4.1 General

The electronics is housed in two racks placed close to the PS ring (Fig. 10). One rack contains the VME system, motor power supply and control modules. The high voltage supplies and stepping motor controllers are in the other rack. The VME system is connected to the PS control network via Ethernet and is used as a DSC (Device Stub Controller, front end intelligence part of the CERN standard for accelerator control).

4.2 Motor control

The motor controller module consists of a velocity servo loop, current limiter, fault detector and standby switches. The velocity servo compares the input command voltage with the tacho-generator voltage. The amplified difference feeds the motor. The output amplifier is a switched-mode bipolar supply working at about 18 kHz. It is capable of 30 A output current, but we limit it to 15 A in order to reduce the stress on the mechanism. The amplifier delivers a 95 V peak to peak square wave with very fast rise times. Possible interference on the tachometric feedback signal is avoided by a low pass filter connected to the output of the amplifier.

An 8-channel 12-bit DAC VME module (Pentland MPV954) delivers the input command voltage to the motor controller. The ±5 V full-scale output corresponds to ±1500 rpm. Motor speed is 1207 rpm for a wire speed of 20 m/s at the centre of the vacuum chamber. The acceleration time for this velocity is about 17 ms over an angle of 60°, then the speed is constant for the next 60° which takes about 8 ms. After that, it decelerates over about 50° to slow speed. It then continues until the 180° are completed and stops. The whole sequence takes about 50 ms.

The power supply for the motor controller consists of a 380V to 61V 3-phase transformer and full-wave rectifier delivering 95 VDC to the module. Because of the rapid magnetic circuit breakers and the size of the transformer (1 kVA), it is necessary to switch on the transformer in two steps. First, 46 ohms resistors are connected in series with each phase to limit the inrush current. Then, when the voltage on all 3 phases have increased to more than half of the mains voltage, the resistors are shorted out.

4.3 Position measurement

The angular position of the motor shaft is measured by a resolver, connected to the shaft of the drive motor via a nickel bellow coupling. The input to the resolver is a 7.8 kHz sine wave of 20V peak to peak. The resolver delivers two signals with amplitudes proportional to the sine and cosine of the resolver shaft angle. The position of the wire in the PS vacuum chamber is derived from the motor angle.

The resolver input signal is generated by a simple function generator. It consists of a counter, an EPROM and a DAC. The counter is clocked at 500 kHz and the 6 lowest bits are used as an address to the EPROM. The EPROM is programmed with the sine values for 64 points on a period.

The resolver signals are directly sampled. This avoids errors caused by the dynamic behaviour of the converter and is cheaper. The resolver is connected to two VME modules. One is a 32 channel ADC with a conversion time of 10 µs (Pentland MPV908A) for real time control of the motor. The other is a 16 channel 12 bit transient digitiser capable of 1 Megasamples/s (Hytec VTD1612). It has a memory of 128 kilosamples and is used for data taking.

The resolver signals are sampled twice per period at 90° and 270°. Taking the difference between the two samples, we get the sign of the signal and any DC offset is eliminated. Therefore we get 13 bit resolution from a 12 bit converter. This corresponds to an angular resolution of 0.014°. The precision of the resolver is better than ±3 arc-minutes = ± 0.050°. The calculated error of the wire position is then < ± 0.14 mm.

4.4 Electronics for Photomultipliers and optical filters

The PM is used in proportional mode. To send the signal over 300 m of coaxial cable, a buffer amplifier is installed in the PS ring about 2 m below the concrete floor level, shielded from radiation. It is connected to the PM by a 3 m long 50 Ω coaxial cable (RG 58C/U). The 300 pF capacity of the cable acts as integrating capacitor. The output impedance of the PM is 50 kΩ and the input one of the buffer amplifier is 5.1 kΩ, which gives a time constant of 1.4 µs. The bandwidth of the system extends from DC to 200 kHz.

A variable high voltage supply is used to set the gain of the PM. It is controlled by a VME module via a serial link.

The optical filters described in § 2.4.1 are mounted on a disk. A stepping motor rotates the disk to select the filter. The stepping motor controller receives pulses from a VME digital I/O module (ICV196). These pulses are generated by software before and after the profile measurement. A microswitch actuated by a cam on the disk signals the home position, allowing a precise reset after each measurement.

4.5 Data acquisition

Two VME modules are used for data taking, one for the PM signals, the other for position data from the resolvers. The PM signals are sampled once per revolution (about every 2.1 µs at high energy), synchronised with the revolution frequency delivered by the RF acceleration beam control of the machine to avoid ripple on the signal due to the bunched structure of the beam. The samples are stored in the VME module memory and read out when the measurement is finished.

The sine and cosine signals from the resolver are connected via a screened twisted-pair cable to the differential inputs of a transient digitiser and sampled every eighth PM sample. The period of the resolver signal is 128 µs so there are slightly less than 8 samples per period. These samples are also stored in the memory of the module and read out afterwards, for data treatment as explained in § 5.5.

5. Software

5.1 General

The specific software for the fast wire scanner is installed in the DSC. It was developed in C under the LynxOS operating system. It can run either in stand-alone mode, controlled from a terminal connected to the DSC, or in integrated mode, controlled from a workstation on the PS control network via the new PS/SL control protocol.

5.2 Setting-up of the Measurement

The system accepts a wide variety of measurement settings, in order to allow measurements under the different conditions in the PS machine.

A measurement can be made with one wire scanner or with two simultaneously. Any combination of two out of the four devices is accepted. The measurement can be carried out at a velocity of 10, 15 or 20 m/s of the carbon wire when it traverses the beam.

The measurement can be selected for any of the existing so-called PS "users" (which are labels describing the various cycles within the supercycle). The operator may choose whether to measure on the next occurrence of that "user" or on a specific occurrence (1-6) of the "user" in the supercycle. Moreover, there is a so-called "pbar" option, which allows the operator to let the instrument wait for the next occurrence of antiprotons in the machine.

One or two profiles per device, so-called single or double-sweep measurement, can be obtained on the same cycle. The sweeps of the measurement can be carried out at any C timing (PS general distribution 1 ms clock train) after injection (~215 ms), but a short dead time is necessary for the mechanism to settle between two sweeps.

For each device, the operator can either select the optical filter and the PM voltage manually or request an automatic setting, in which case he must supply an expected value of the beam intensity. A combination of filter transmission and PM voltage is calculated from this intensity and the momentum of the particles, which is deduced from the magnetic field corresponding to the preset C trigger (see below).

5.3 Measurement Procedure

Before a measurement can take place, a number of checks are performed in order to ensure that the system is operational and to obtain information needed for the measurement.

The vacuum in the sector of each of the devices selected for the measurement is verified, because the carbon wire may break when swept in atmospheric pressure. The measurement is cancelled if good vacuum is not confirmed.

Each device must begin the movement from the home position. Therefore, the position of each device is checked. If a device is not in its home position, it is first moved there at very low speed.

The resistance of the wire is measured. It is compared to the resistance and the number of fibres in the wire at the time of installation and yields an estimate of the present number of fibres in the wire. If any fibres seem to be broken, a warning is issued, but it is not considered a fatal error and does not inhibit the measurement.

If an automatic calculation of optical filter number and PM voltage has been requested, an approximate value of the magnetic field, B, is needed. This is obtained from a B pulse readout at the "user", occurrence, and C timing selected in the measurement settings. Since this must be done before the measurement can start, an automatic filter and PM voltage calculation costs a further supercycle or a further occurrence of the requested "user".

Information from the "user" matrix (the data base giving the basic properties of the PS "user", as defined in § 5.2) is used to find the particle type for the "user" requested for measurement. The charge of the particle, hence its direction of movement in the accelerator, decides which of the two photo multipliers associated with each device to use for the measurement.

If an automatic calculation of optical filter and PM high voltage has been requested, these values are calculated according to the sensitivity formula in § 2.4.2 in such a way that a filter with the highest possible transmission is chosen. If two devices have been selected for the measurement, they are treated individually with respect to the automatic calculation setting, i.e. it is possible to have an automatic setting for one and a manual setting for the other.

When all of the above steps have been completed, the selected optical filter is turned into position, the PM voltage is set, and the ABB power supply for the wire scanner motor is switched on. When the cycle corresponding to the requested "user" and occurrence arrives, the measurement is carried out at the preset C timing.

Immediately after the movement of the device has finished, the power supply and the PM voltage are switched off and the optical filter device turned back to its home position. Then the data from the sampling of the PM and the resolver sinus and cosine channels are read out.

5.4 Movement of the Wire

Each time a measurement is carried out, the device is moved first through the beam to its outer end position and then back to its home position again. In the case of a double-sweep measurement, the sweep back to the home position yields the second profile. In the case of a single-sweep measurement, the device is moved to the home position after the measurement cycle has finished and before the next cycle starts, i.e. when there is no beam in the machine.

When the measurement cycle begins, the motor is taken from standby to ready-mode. The DAC is loaded with a value corresponding to the speed set by the operator and started at a time such that the device

will pass the centre of the machine aperture at the C timing set for the measurement. As soon as the movement has started, the beam intensity signal is sampled.

When the resolver signals, which are read out every 64 μs, indicate that the motor axle has reached 60 degrees, data taking is started. This point corresponds approximately to where the wire enters the machine aperture, and by this time the motor has finished accelerating and reached its nominal speed. The B pulse is read out immediately after the start of data taking. This train, generated from the PS main magnet field, delivers a pulse for every increase by one gauss.

The data taking will continue autonomously until a preset number of samples have been taken, by which time the wire will have exited from the machine aperture on the other side. When the data taking has finished, the B value is read out again. The movement continues at full speed until the motor axle reaches 120 degrees, which is approximately where the wire leaves the machine aperture. At this point, the DAC is loaded with a small value that will make the motor brake and continue at very low speed. Just before the end position, 180 degrees, is reached, the DAC is set to 0 volt and then stopped, so that the motor stops at 180 degrees.

The movement in the other direction, back to the home position, is carried out in exactly the same fashion. In the single-sweep case, the movement is started at a time that allows the device to pass the centre of the vacuum chamber at the C timing requested for the second measurement, and in the double-sweep case, it is started when the cycle ends. When the second sweep has finished, the motor is put into standby.

5.5 Data Treatment

The principle for the data treatment is to convert the resolver sine and cosine data for each profile obtained from the measurement to corresponding positions of the wire and then to find the rms (root mean square) of the distribution of the PM signal with respect to the position.

The beam width, the emittance, and the normalised emittance are calculated from the rms. This procedure is done in several steps. First the offset of the PM signal is calculated. This value will be subtracted from the distribution later. Then the amount of PM and resolver data is reduced by selection of a smaller range centred around the peak of the PM signal. A parabola is fitted to the maximum of the PM profile in order to obtain a better value for the maximum of the distribution.

The value of the magnetic field at the time of traversal of the centre of the beam is calculated by interpolation of the two B values sampled before and after the data taking. They are interpolated linearly at the location of the fitted maximum of the PM signal. The momentum p is calculated from the interpolated B as $p = 2.2279 \times B\rho$, where B is the field and ρ the bending radius of the PS magnets.

The fitted PM maximum is also used to calculate a level at which the tails of the profile will be cut off. The tails of the distribution, which is approximately gaussian, will thus be replaced by true gaussian tails, in order to avoid the tails strongly influencing the calculation for the bulk of the beam [6]. The cut-off level is chosen as 7.5% of the value of the fitted PM maximum corrected for the offset.

The resolver cosine and sine values are converted to wire positions via a conversion to angles of the axle of the wire scanner motor. First, a set of angles is calculated by simply taking arctan of each sine value divided by its corresponding cosine value. Theoretically, these angle points should lie around a very short section of a sine wave period, if the motor is assumed to be moving with constant speed during the traversal of the beam. A parabola is used as an approximation of this sine wave, and a least-square fit of a parabola is made to these angles. Then the coefficients obtained from the least-square fit are used to calculate eight times as many angle points as there were sine and cosine samples from the beginning, since the PM signal was sampled with a frequency eight times that of the resolver signal sampling.

The angles of the motor axle are converted to corresponding positions of the wire projected on a plane perpendicular to the beam. The conversion is made with a formula based on the static geometry of the mechanics holding the wire (see Appendix). Therefore, a correction for the dynamic case is necessary. This correction is based on interpolation in tables established from calibration measurements in the lab.

These calibrations are made with a laser beam hitting a photo diode indicating a position in the vacuum chamber. The signal from the photo diode is sampled as the wire moves during a sweep. The interruption of this signal as the wire traverses the laser beam is used to calculate the angle of the motor axle and then the corresponding theoretical position at that particular real position. The laser beam and the photo diode are

moved to different positions in order to obtain a series of pairs of real and theoretical positions to make up a calibration table. A separate table is kept for each combination of device, velocity, and sweep direction.

The rms value of the new distribution obtained from the position samples and the PM samples subtracted by the offset and the 7.5% tails is calculated. The rms value is multiplied by 1.1764 to compensate for the cut-off tails. The emittance ε is then calculated from $\varepsilon = (2\sigma)^2/\beta_t$, where σ = 1.1764 × rms and β_t is the Twiss parameter for the location in the machine where the wire scanner is installed. β_t has been taken from the MAD simulation program [7]. The normalised emittance ε^* is calculated from $\varepsilon^* = \beta\gamma\varepsilon$. β and γ are the classical relativistic parameters and $\beta\gamma = p/m_o$, where p is the momentum calculated earlier and m_o is the rest mass of the particle type read out from the "user" matrix during the preparations of the measurement. The beam width is calculated from $w = 4\sigma$.

5.6 Integration with the PS Control System

The integrated version of the wire scanner system consists of three major components, namely the wire scanner program itself running on a DSC and constituting the hardware interface; the "user" interface which runs on a PS control workstation; and a server program, a so called equipment module, which runs on the DSC and which relays the communication between the application program and the hardware interface.

The communication between the wire scanner program and the equipment module is maintained via two message queues. One message queue holds control messages that the server sends to the wire scanner program when it receives requests from the application program. The other queue holds acquisition messages that the wire scanner program sends in reply to some of those control messages.

The wire scanner program is built on the skeleton program 'body', which facilitates the integration of DSC instrumentation software with the control system protocol [8], [9]. It consists of four POSIX threads (threads are parallel execution paths within a process sharing the same process context, and LynxOS provides a library conforming to the calling sequences proposed by POSIX, the so called "POSIX threads"). One of these is dedicated to reading incoming control messages and deciding upon the action to be taken. One thread executes the measurement itself, and another one processes the acquired measurement data and assembles an acquisition message to be returned to the server. The fourth thread deals only with exceptional cases, such as program abort, reset, and recover signals. The communication between the threads in the program takes place via LynxOS signals.

5.7 Application program

The application program is available from the standard Toolbar in the PS Operation environment on the workstations [10]. It allows to launch a measurement after specification of the conditions:

- the choice of device(s) and plane(s) (among the two horizontal and two vertical mechanisms) and the number of measurements to be executed on the same cycle (1 to 4 for forwards, backwards, horizontal and vertical),
- the "user" and its occurrence in the supercycle, or "pbar" option,
- the timing in C-train and the timing of the second measurement if requested,
- the expected beam current at the time of the measurement,
- the required velocity with a limited choice of a few values (10, 15 or 20 m/s).
- the PM voltage specified by the operator and the choice of optical filter, or the request for the EM to calculate the best voltage (from the expected I_p, the type of particle and the measured B train).

The results can be obtained from the last measurement performed or from any archived data. The display contains (Fig. 11):

- the measurements conditions: "user", occurrence, plane and monitor, timing, requested wire velocity, PM voltage,
- the measured beam intensity, particle type, B acquired, calculated p,
- the emittance and beam width measured and the normalised emittance $\varepsilon^*=\beta\gamma\varepsilon$
- the profile display: PM signals and positions 4σ before and 4σ after the beam maximum for the maximum of four profiles taken at each measurement.

6. Conclusion

The main feature of the first generation wire scanner, installed in 1985, was its high velocity, obtained with a high-torque motor and low inertia mechanism. The upgrading, completed in 1994, allows to reap the

full benefit from this performance after improvement in many respects. New photomultipliers provide better linearity and wider dynamic range. The beryllium wire was replaced by a strand of carbon fibres with a new method of fastening to the prongs of the fork. The position measurement and acquisition have been completely changed to attain a better precision. Electronics and controls software are totally new, which improves the measurement quality as well as the ease of operation, while bringing the system up to modern standards. Though then not completely operational, the new system was extensively used in December 1993, during a test run in which the PS produced a LHC-type beam of high luminosity [2]. During, this run, it performed more than 1300 measurements without failure and was essential in the success of these tests. It is estimated that the emittance, proportional to the square of the beam dimension, was determined with a precision of about 5% [2] [11]. During 1994, refinements were made to the software and the system as a whole was rendered fully operational. It is now one of the basic instruments for the evaluation of the PS beam quality.

6. Ackowledgements

The authors wish to thank all those who contributed to this development, and especially G. Benincasa, J.P. Bovigny, R. Cappi, S. Hancock, M. Hansen, H. Koziol, G. Martini, M. Martini, L. Merard, D. Pearson, T. Pettersson, K. Priestnall, U. Raich and M. van Rooij.

7. References

[1] - Ch. Steinbach and M. van Rooij, A scanning wire beam profile monitor, 1985 IEEE Particle Accelerator Conference, Vancouver, B.C., Canada.

[2] - E. Falk, F. Hoekemeijer, J. Olsfors, Ch. Steinbach, Use of the PS Fast Wire Scanner during the LHC Test Beam Machine Development of December 1993, PS/OP/Note 94-11(MD).

[3] - M. Martini, M. van Rooij, Ch. Steinbach, Experience with a fast wire scanner for beam profile measurements at the CERN PS, S. Hancock, Proceeding of the Workshop on Advanced Beam Instrumentation, KEK, Tsukuba, Japan (1991).

[4] - A. Burns, J. Camas, E. d'Amico, G. Ferioli, Q. King, K.H. Kissler, J. Mann, R. Schmidt, Wire scanner news from the CERN-SPS, 1989 IEEE Particle Accelerator Conference, Chicago, Il, USA.

[5] - R.W. Cahn, P. Haasen, E.J. Kramer, Materials Science and Technology, VCH editor.

[6] - H. Koziol, Evaluation of near Gaussian distributions with ill-defined tails, LAMPF Note MP-3-74-1.

[7] - H. Grote, F.Ch. Iselin, The MAD program Version 8.1, CERN/SL/90-13(AP)

[8] - M. Le Gras and J. Tedesco, Application typique du protocole pour l'instrumentation, PS/BD/93-02.

[9] - S. Johnston, Real-Time Program for the PS FFT Q-Measurement, PS/BD/94-2.

[10]- K. Priestnall, Private communication.

[11]- Ch. Steinbach, Emittance Measurements with the CERN PS Wire Scanner, Workshop on Emittance in Circular Accelerators, November 1994, Tsukuba, Japan.

APPENDIX

Calculation of the wire position

The wire fork angle at the home position is calculated first, then it is expressed for the current crankshaft angle. After that, the wire position is calculated from the difference between the two fork angles plus the initial fork angle (Fig. 12).

The crankshaft angle at the home position is:

$$\alpha_0 = \arccos\left(\frac{(C+B)^2 + V^2 + H^2 - A^2}{2\cdot(C+B)\cdot\sqrt{V^2+H^2}}\right)$$

where:

C = crank radius
B = length of connecting rod
V = vertical distance between motor shaft and rocker centre
H = horizontal distance between motor shaft and rocker centre
A = radius of rocker arm

The distance from motor shaft to rocker centre is:

$$d = \sqrt{(H - C\cdot\cos\alpha)^2 + (V - C\cdot\sin\alpha)^2}$$

where:

α = angle between crank shaft and a line from crank shaft centre to rocker centre

The angle of d is:

$$\beta = \arcsin\frac{H - C\cdot\cos\alpha}{d}$$

The angle between d and A is:

$$\gamma = \arccos\left(\frac{d^2 + A^2 - B^2}{2\cdot d\cdot A}\right)$$

The connecting rod lever angle is:

$$\delta = 270° - \beta - \gamma - \varphi$$

where:

φ = angle between rocker arm and connecting rod lever

Distance from rocker centre to fork shaft centre:

$$K = \sqrt{X^2 + Y^2}$$

Distance from top lever to fork shaft centre:

$$l = \sqrt{L^2 + X^2 + Y^2 - 2\cdot L\cdot(X+Y)\cdot\cos\left(\delta - \arctan\left(\frac{Y}{X}\right)\right)}$$

where:

Y = vertical distance from rocker centre to fork shaft centre
X = horizontal distance from rocker centre to fork shaft centre
L = radius of lever arm on rocker assembly

Angle between K and l:

$$\phi = \arccos\left(\frac{X^2 + Y^2 + l^2 - L^2}{2 \cdot (X + Y) \cdot l}\right)$$

Distance from bottom lever to fork shaft centre:

$$m = \sqrt{L^2 + X^2 + Y^2 - 2 \cdot L \cdot (X + Y) \cdot \cos\left(180° - \left(\delta - \arctan\left(\frac{Y}{X}\right)\right)\right)}$$

Angle between K and m:

$$\chi = \arccos\left(\frac{X^2 + Y^2 + m^2 - L^2}{2 \cdot (X + Y) \cdot m}\right)$$

Length of top push rod:

$$p = \sqrt{l^2 - (R + O)^2}$$

Length of bottom push rod:

$$q = \sqrt{m^2 - (R + O)^2}$$

Average length of the two push rods:

$$s = \frac{p - q}{2}$$

Fork angle is:

$$\eta = \frac{s}{R} + (\chi - \phi)$$

The vertical position of the wire is:

$$w = F \cdot \sin(\eta - \eta_0 + \psi)$$

where:
F = distance from fork shaft centre to wire centre
ψ = home angle of the fork
η_0 = fork angle at the home position ($\alpha = \alpha_0$).

FIGURES

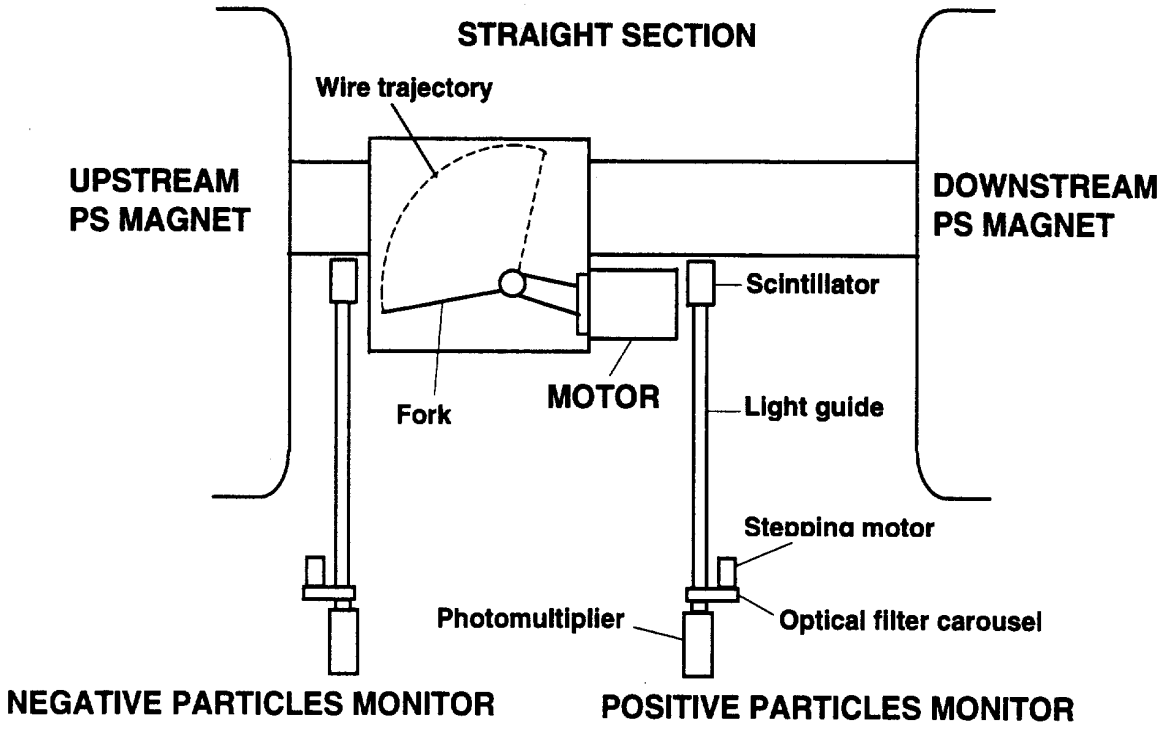

Fig. 1 - Schematic view of a vertical plane measurement device in the PS ring

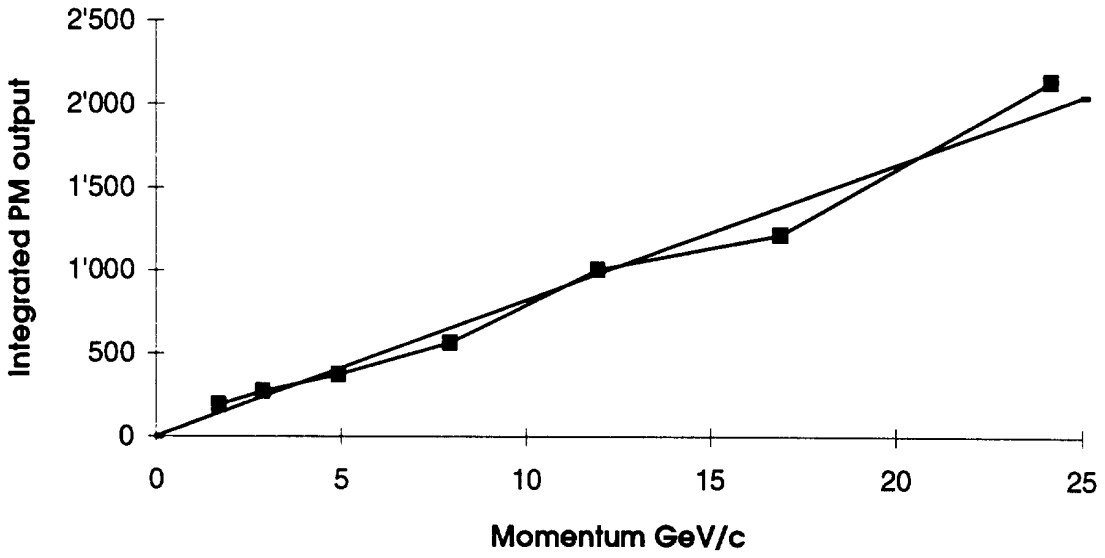

Fig. 2 - Momentum dependence of the integrated PM signal in arbitrary units for a beam intensity of 3×10^{11} ppp, a PM voltage of 800 V and an optical transmission of 100 %

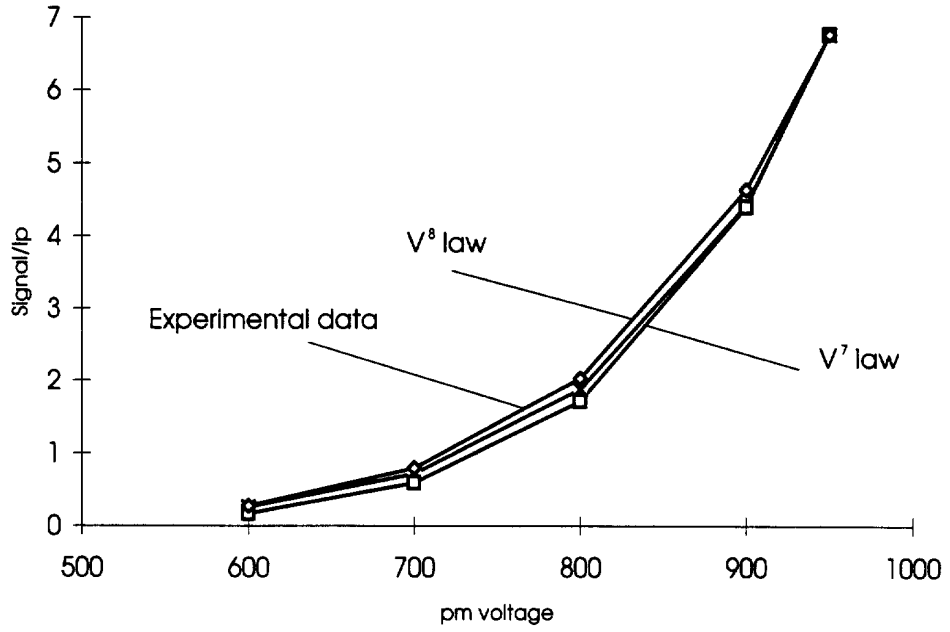

Fig. 3 - Experimental signal/beam intensity (in arbitrary units) versus PM voltage, compared with equation in 2.4.2

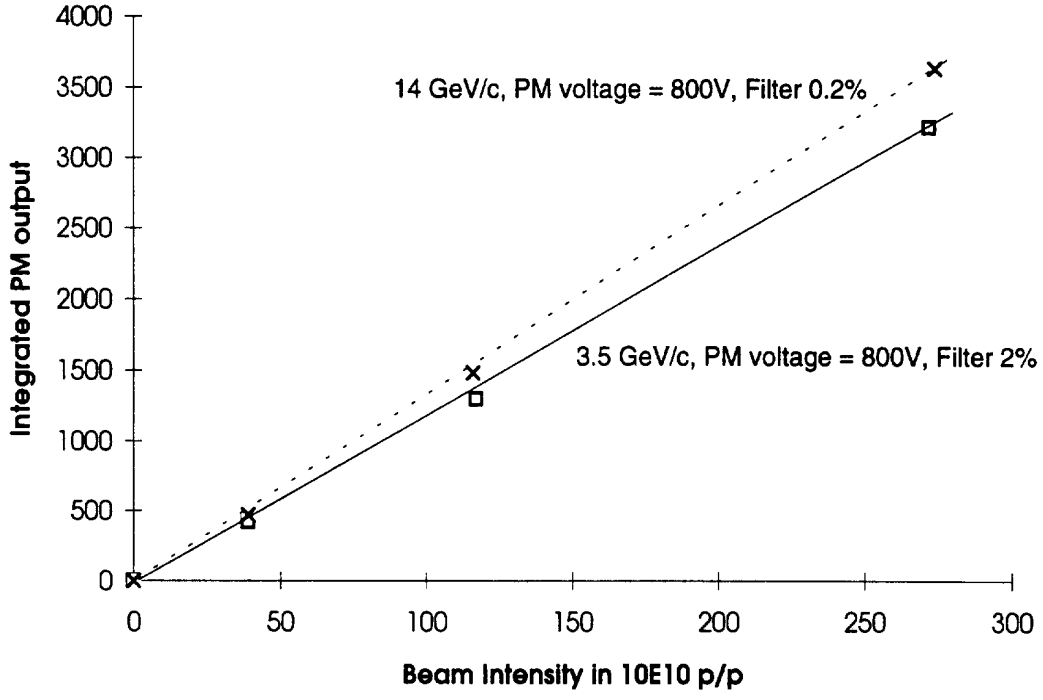

Fig. 4 - PM linearity check showing the integrated signal (in arbitrary units) versus intensity, at 3.5 GeV/c and 14 GeV/c

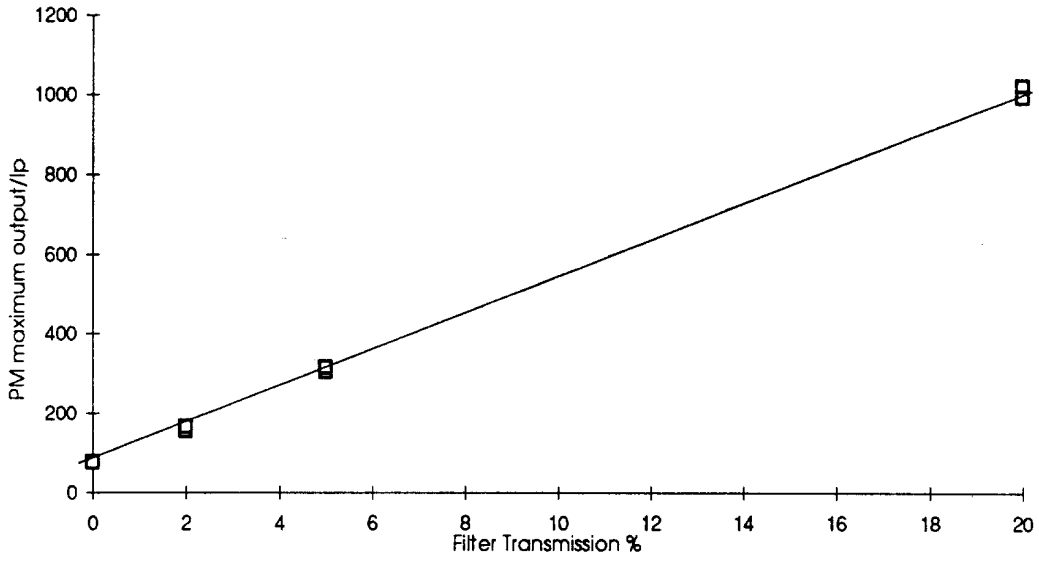

Fig. 5 - PM linearity check showing the signal maximum (in arbitrary units) normalised to the beam intensity versus the optical filter transmission factor at 1 GeV energy and an intensity of about 3×10^{12} ppp

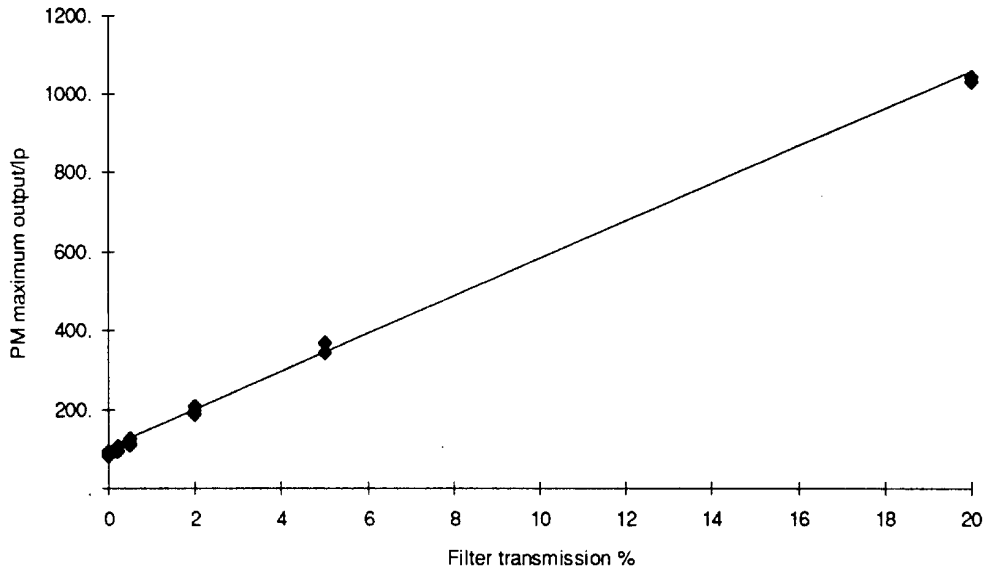

Fig. 6 - PM linearity check showing the signal maximum (in arbitrary units) normalised to the beam intensity versus the optical filter transmission factor at 14 GeV/c momentum and an intensity of about 9×10^{12} ppp

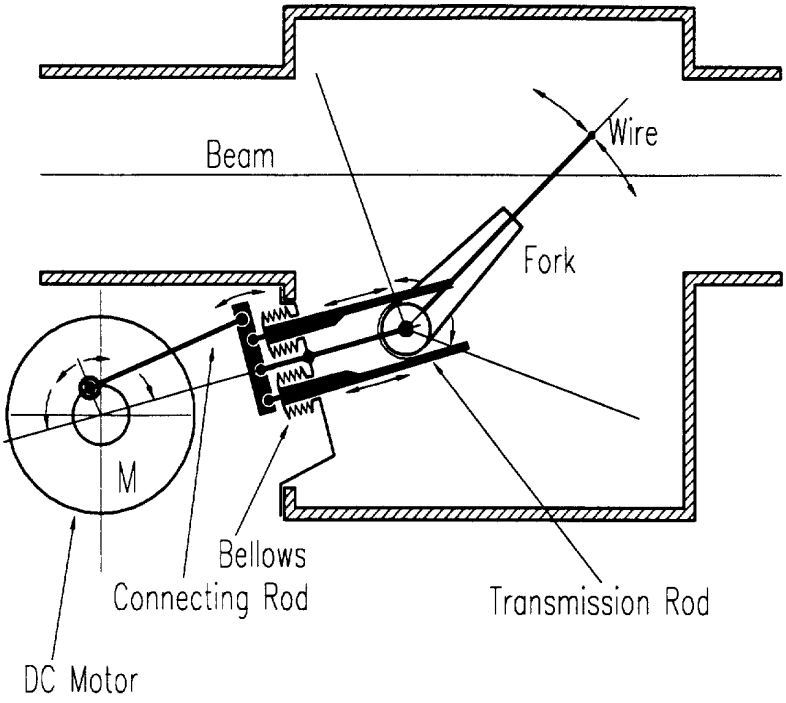

Fig. 7 -Schematic view of the wire scanner mechanism

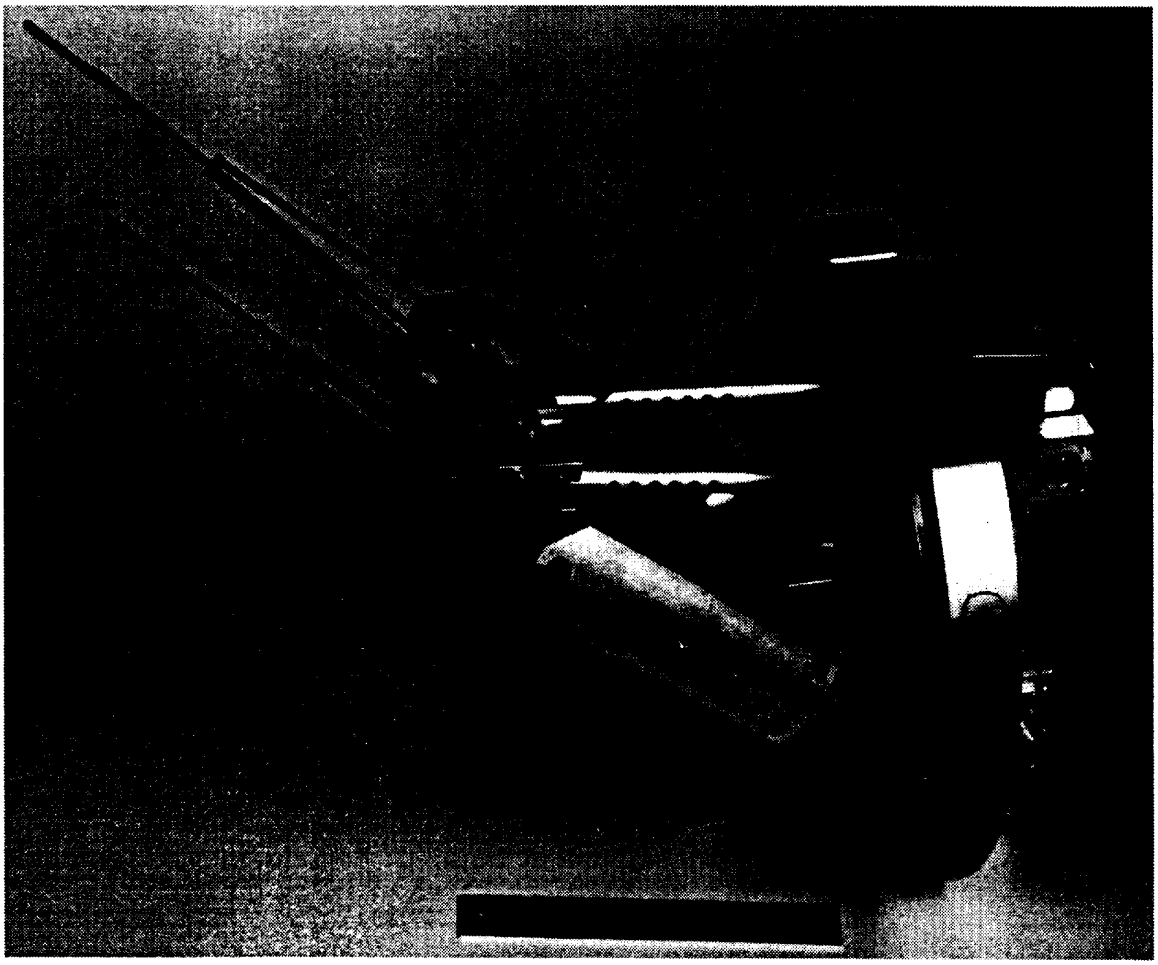

Fig. 8 - View of the mechanical assembly

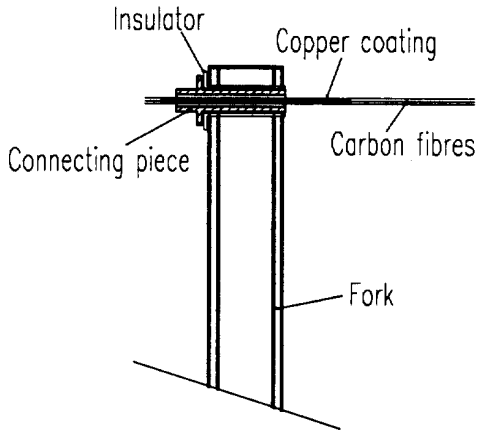

Fig. 9 - The extremity of one of the prongs, showing the wire fastening

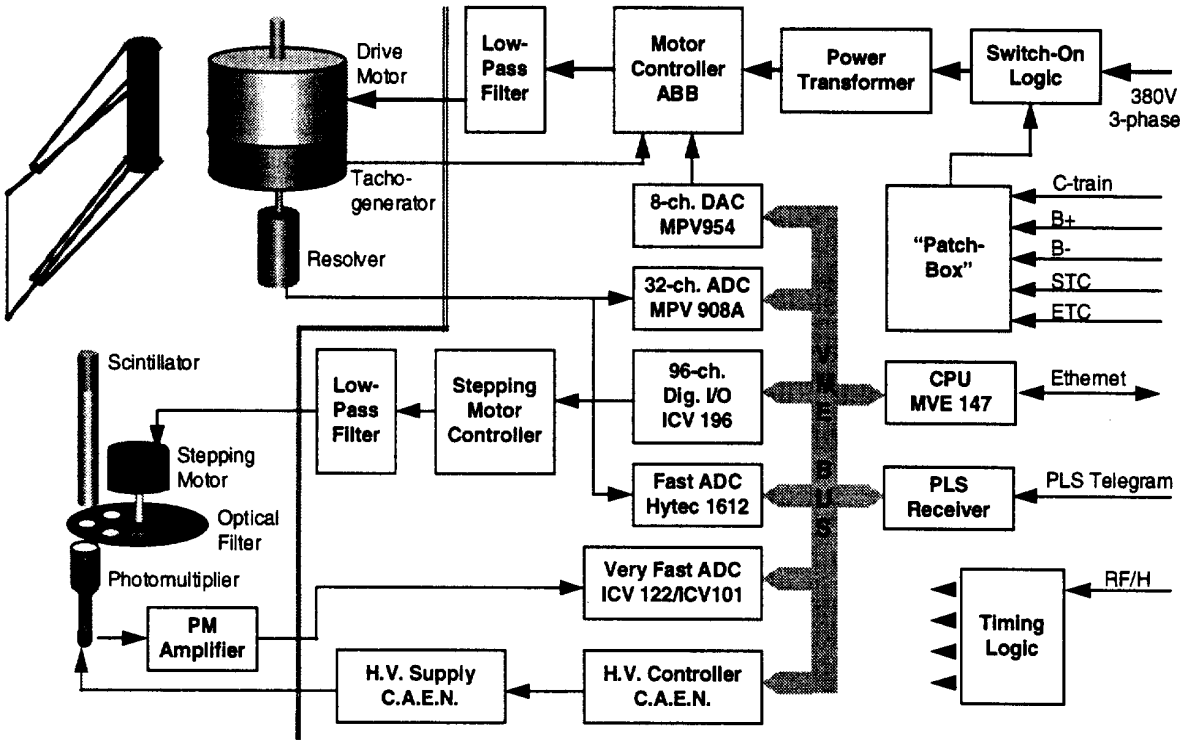

Fig. 10 - Block diagram of the electronics

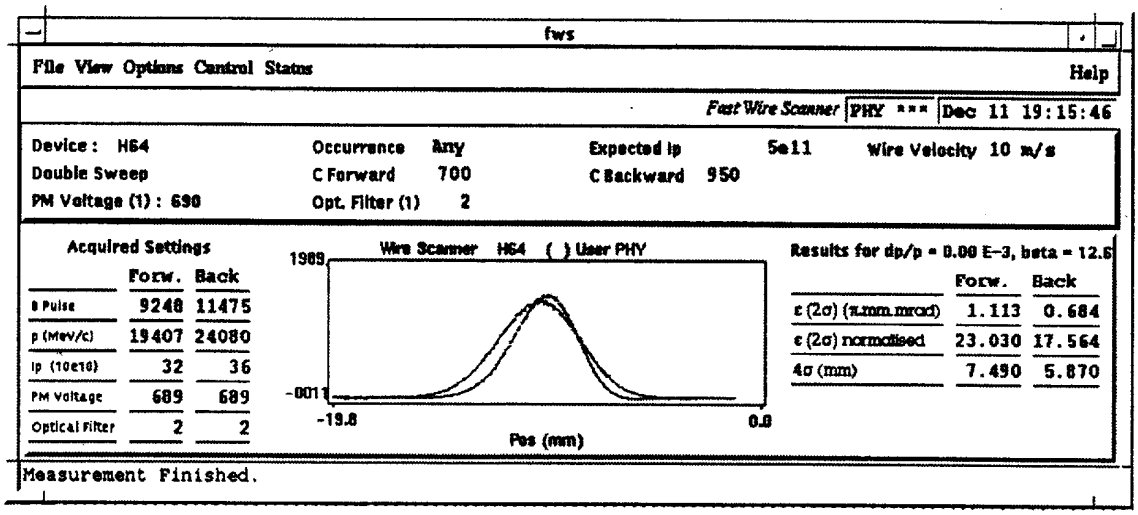

Fig. 11- Results from application program showing a forth and back scan

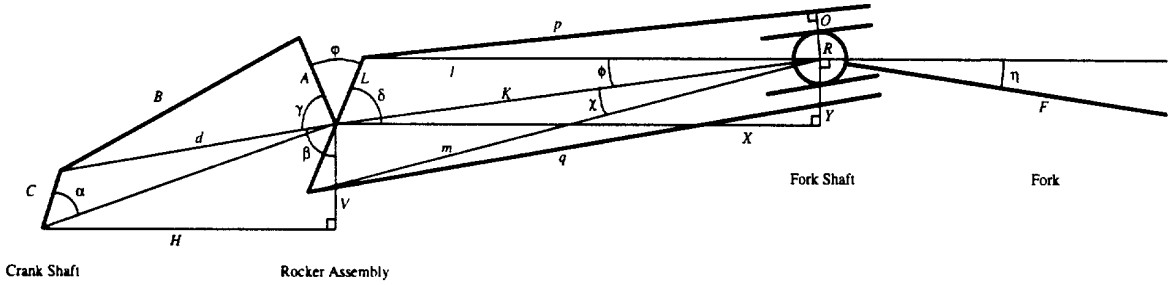

Fig. 12 - Geometry of movements

Appendix A

Precision Electroweak Tests at LEP

Precision Electroweak Tests at LEP

E. Falk
Lund University, Box 118, S-221 00 Lund
Sweden

Abstract

A presentation is given of a selection of the electroweak precision tests that have been carried out at LEP. Measurements of the Z^0 lineshape and asymmetries from the LEP1 era as well as measurements of the W mass from LEP2 are described, and up-to-date results presented. A brief overview is given of some experimental aspects that are crucial to the precision tests. Radiative corrections and some of the constraints that they impose on the Standard Model are discussed.

OPEN-98-024
15/12/98

1 Introduction

LEP has operated successfully since 1989, with steady improvements in its performance and increased integrated luminosity for each year. When the data taking at and in the vicinity of the Z^0 pole, $\sqrt{s} = 91$ GeV, finished in 1995, each of the four LEP experiments had collected an integrated luminosity of about 160 pb^{-1}, and together they had recorded approximately 20 million Z^0 bosons. This wealth of statistics has allowed unprecedented testing of the electroweak theory of the Standard Model, and the results obtained have been in excellent agreement with the model, leaving only small openings for any new physics beyond the Standard Model.

The LEP2 era started in the summer of 1996 with collisions at the threshold for W^+W^- production, $\sqrt{s} = 161$ GeV. The experiments each recorded about 10 pb^{-1} during this period. Later in the year, the energy was increased to $\sqrt{s} = 172$ GeV, and another 10 pb^{-1} were recorded by each experiment. In 1997 the energy was increased further to $\sqrt{s} = 183$ GeV, and the integrated luminosity at this energy reached about 55 pb^{-1} per experiment. The higher energies of LEP2 allow a range of precision tests of the Standard Model with W pairs, including a good determination of the mass of the W boson.

Section 2 presents a selection of the tests of the electroweak theory carried out at the Z^0 pole. A summary of the measurements of beam energy and luminosity, crucial to the precision of the electroweak tests, is given in Section 3. Section 4 contains a short introduction to the measurements of the W mass. Section 5 briefly discusses radiative corrections and presents some examples of how they are used to put constraints on the Standard Model.

2 Z^0 Lineshape Measurements and Asymmetries

2.1 Z^0 Lineshape

The Z^0 lineshape measurements consist of a series of measurements of cross sections of the production of different fermions at different energy points around the Z^0 resonance. The parameters that one has chosen to extract from these measurements are the mass of the Z^0 boson, m_Z, the total width, Γ_Z, the peak hadronic cross section, σ_h^0 and the ratios of partial widths for leptons, R_e, R_μ and R_τ, defined as $R_e \equiv \Gamma_h/\Gamma_{ee}$, where Γ_h is the partial width for decay into hadrons and Γ_{ee} the partial width for decay into an electron-positron pair, and analogously for the μ and τ leptons. When lepton universality is assumed, one quotes instead $R_l \equiv \Gamma_h/\Gamma_{ll}$, where l denotes charged leptons. This particular parameter choice has the advantages that the parameters are nearly statistically independent; they are easily related to basic electroweak parameters, such as coupling strengths; and they are also easily related to specific experimental errors. m_Z, Γ_Z and σ_h^0 also have a close correspondence to the position, the width and the height of the Z^0 resonance curve as a function of energy.

The parameters are extracted through a fit to a function describing the total cross section for decay into a pair of fermions, $e^+e^- \to f\bar{f}$, as a function of s, the square of the centre-of-mass energy:

$$\sigma_f(s) = \sigma_f^0 \frac{s\Gamma_Z^2}{(s-m_Z^2) + \frac{s^2\Gamma_Z^2}{m_Z^2}} + \gamma + \gamma Z^0, \tag{1}$$

where σ_f^0 is the peak cross section for decay into a fermion pair. The terms γ and γZ^0 represent contributions from photon exchange and $\gamma - Z^0$ interference. These contributions are small relative to that of Z^0 exchange at the Z^0 pole, $\mathcal{O}(1\%)$ [1], and are fixed to their Standard-Model values in the fit. Before the function is compared with the experimental results, it is convoluted with a function describing QED corrections (mainly initial-state radiation). The peak cross section for decay into fermions is defined as

$$\sigma_f^0 \equiv \frac{12\pi\Gamma_e\Gamma_f}{m_Z^2\Gamma_Z^2}. \tag{2}$$

Using this and

$$\Gamma_Z = \sum \Gamma_f,$$

one can extract the partial widths Γ and the ratios R from the fitted parameters. The current values of the lineshape parameters, where the results of the four LEP experiments have been averaged, are presented in Table 1.

Parameter	Average Value
m_Z (GeV)	91.1867 ± 0.0020
Γ_Z (GeV)	2.4948 ± 0.0025
σ_h^0 (nb)	41.486 ± 0.053
R_e	20.757 ± 0.056
R_μ	20.783 ± 0.037
R_τ	20.823 ± 0.050
R_l	20.775 ± 0.027

Table 1: Average lineshape parameters from the preliminary results of the four LEP experiments [2], [3], [4].

An important aspect of the Standard Model that is tested in the lineshape measurements is that of lepton universality. The partial widths Γ_l are proportional to the vector and axial-vector couplings g_{Vf} and g_{Af} of the Z^0 to fermions according to

$$\Gamma_f = \frac{G_F m_Z^3}{6\pi\sqrt{2}} \left(g_{Vf}^2 + g_{Af}^2\right), \tag{3}$$

where G_F is the Fermi constant. As a consequence thereof, the ratios R_e, R_μ and R_τ should be the same if the couplings to the different lepton flavours are the same. Lepton universality is excellently confirmed by the LEP experiments, with good agreement between the different ratios R, as shown in Table 1.

Another test of the Standard Model is to count the number of light neutrino species. This is done at LEP by measuring the invisible decay width $\Gamma_{inv} = N_\nu\Gamma_\nu$, where N_ν is the number of neutrino species and Γ_ν the partial width for decay into a neutrino-antineutrino pair. N_ν is determined from

$$N_\nu = \frac{\Gamma_l}{\Gamma_\nu}\frac{\Gamma_{inv}}{\Gamma_l} = \frac{\Gamma_l}{\Gamma_\nu}\left(\sqrt{\frac{12\pi R_l}{m_Z^2\sigma_h^0}} - R_l - 3\right), \tag{4}$$

where one uses the fact that

$$\Gamma_Z = \sum \Gamma_f = \Gamma_h + 3\Gamma_l + \Gamma_{inv} \tag{5}$$

and the definition of the peak cross section (eq. 2). The ratio Γ_{inv}/Γ_l is the measured quantity, and Γ_l/Γ_ν is taken from the Standard Model. The number of neutrinos measured in this way is

$$\boxed{N_\nu = 2.993 \pm 0.011.}$$

A different approach to this measurement is instead to assume that the number of neutrinos is 3 and extract an upper limit for additional invisible decays of the Z^0 by adding a term $\Delta\Gamma_{inv}$ to the fit. Limiting the result to include only positive values of $\Delta\Gamma_{inv}$ yields the upper limit

$$\boxed{\Delta\Gamma_{inv} < 2.8 \text{ MeV at } 95\% \text{ C.L.}}$$

2.2 Asymmetries

The asymmetries that are measured at LEP have their origin in the fact that neutral-current couplings are different for left-handed and for right-handed fermions:

$$\begin{aligned} g_{Lf} &= I^3_{Lf} - Q_f \sin^2\theta_W \\ g_{Rf} &= -Q_f \sin^2\theta_W, \end{aligned} \tag{6}$$

where g_{Lf} and g_{Rf} are the couplings to left-handed and right-handed fermions respectively, I^3_{Lf} and Q_f the weak isospin and the charge of the fermion and θ_W the electroweak mixing angle. This difference leads to polarisation effects and to forward-backward asymmetries that can be measured at LEP.

Using the relations

$$\begin{aligned} g_{Vf} &= g_{Lf} + g_{Rf} \\ g_{Af} &= g_{Lf} - g_{Rf}, \end{aligned} \tag{7}$$

one can express the difference in the neutral-current coupling in terms of the chiral-coupling asymmetry $\mathcal{A}_f$ defined as

$$\mathcal{A}_f \equiv \frac{g^2_{Lf} - g^2_{Rf}}{g^2_{Lf} + g^2_{Rf}} = \frac{2 g_{Vf} g_{Af}}{g^2_{Vf} + g^2_{Af}}. \tag{8}$$

The chiral-coupling asymmetry manifests itself in different ways that can be measured experimentally: There are the so-called left-right asymmetries, which require longitudinally polarised e^+e^- beams and which are measured at SLD; there are the forward-backward asymmetries, which are measured at LEP for the three lepton flavours and for b and c quarks; there are the polarisation asymmetries, which the LEP experiments measure for the τ lepton; and there are hadronic jet charge asymmetries. The charge asymmetries and the forward-backward asymmetries for quarks will not be discussed further here.

2.3 Forward-Backward Asymmetries

The forward-backward asymmetry A_{FB} for the process $e^+e^- \to Z^0 \to f\bar{f}$ is defined as

$$A_{FB}(s) = \frac{\sigma_F(s) - \sigma_B(s)}{\sigma_F(s) + \sigma_B(s)}, \tag{9}$$

where $\sigma_{F(B)}$ denotes the cross section for the antifermion emerging in the forward (backward) direction from the interaction point, the forward direction being that of the incoming positron (see Figure 1). The forward-backward asymmetry enters the polar-angular dependence of the cross section:

$$\frac{d\sigma}{d(\cos\theta)} = 1 + \cos^2\theta + \frac{8}{3} A_{FB} \cos\theta. \tag{10}$$

At LEP, where the beams are longitudinally unpolarised, one measures the forward-backward asymmetry at the Z^0 pole:

$$A_{FB}(s = m_Z^2) \simeq A^{0,f}_{FB} \equiv \frac{3}{4} \mathcal{A}_e \mathcal{A}_f, \tag{11}$$

where $A_{FB}^{0,f}$ is called the pole asymmetry. With polarised beams one can measure the left-right asymmetry A_{LR}, which is defined as

$$A_{LR} \equiv \frac{\sigma_L - \sigma_R}{\sigma_L + \sigma_R} \simeq \mathcal{A}_e, \tag{12}$$

where σ_L and σ_R refer to the cross sections for Z^0 decays for left- and right-polarised beams respectively. As mentioned previously, this measurement is carried out at SLD.

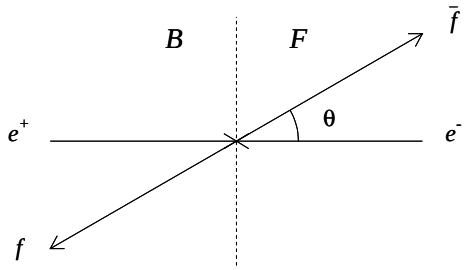

Fi gr e D eitfio m ol fraapg celin e^+cole lōisns. i

Th e faro dra-wbak d s ye mesmra e ea tc et dm fi sttoo tanlg ur l idasibutio n ve fs eta ea hc e gn pe im .tTh e e^+a eltāts ficeines a nsifici ng to nibutio n nf rchan nlee$^+$ (e lFab ah) s ct aing ma dh tt sbcoe rctr ee d f o r t h

Th e a s ye ny mea s me s pt v doan o ti hpeoarr ttstt eleo p tunio ensr aty lt; i h de ap so-y m me lesf o r it effr e dedp tt aoours fm t ubs e s t adhiffe t irhg ea eucoupl nig sr a ts ha e:m

$$A_{F^{\theta}B}, A_{\overline{F}^{\theta}B}, A_{\overline{F}^{\theta}B}, \quad . \tag{13}$$

Al osin ti ha sp ct L EatP hsl o stw r goevdi ecen f leo pr tunio ensr aty l(se eTable 2 .)

Parameter	Average Value
$A_{FB}^{0,e}$	0.0160 ± 0.0024
$A_{FB}^{0,\mu}$	0.0163 ± 0.0014
$A_{FB}^{0,\tau}$	0.0192 ± 0.0018
$A_{FB}^{0,l}$	0.0171 ± 0.0010

Table 2: Forward-backward asymmetries without and with lepton universality; average results from the four LEP experiments.

2.4 τ Polarisation

The τ polarisation $\mathcal{P}_\tau$ is defined as

$$\mathcal{P}_\tau \equiv \frac{\sigma_R - \sigma_L}{\sigma_R + \sigma_L}, \tag{14}$$

where $\sigma_{R(L)}$ is the cross section for a τ pair with the τ^- being right-(left-)handed. The chiral-coupling asymmetries $\mathcal{A}_e$ and $\mathcal{A}_\tau$ are extracted from the polar-angular dependence of the polarisation:

$$\mathcal{P}_\tau\,(\cos\theta) \simeq -\frac{\mathcal{A}_\tau + \frac{2\cos\theta}{1+\cos^2\theta}\mathcal{A}_e}{1 + \frac{2\cos\theta}{1+\cos^2\theta}\mathcal{A}_e\mathcal{A}_\tau}. \tag{15}$$

The polarisation of the τ lepton is measured through reconstruction of the kinematic parameters of its decay products. Five different decay modes are used: $\tau \to e\nu\bar{\nu}$; $\tau \to \mu\nu\bar{\nu}$; $\tau \to \pi\nu$; $\tau \to \rho\nu$; and $\tau \to a_1\nu$. The decay channels involving a π or a ρ yield the best sensitivity; the channel involving an a_1 has a relatively small branching fraction, and the purely leptonic channels have their polarisation signal diluted due to the fact that the two neutrinos involved in the decay prevent reconstruction of the decay angles. The experimental challenge lies in distinguishing between the different decay modes; the decay products of the τ are very well collimated due to the high momentum of the τ. The coupling asymmetries extracted from the τ polarisation measurements at LEP also show strong support for lepton universality (see Table 3).

Parameter	Average Value
$\mathcal{A}_e$	0.1399 ± 0.0073
$\mathcal{A}_\tau$	0.1411 ± 0.0064

Table 3: Chiral-coupling asymmetries from τ polarisation measurements; average results from the four LEP experiments.

2.5 Effective Couplings of the Z^0 Boson to Leptons

The data from the partial widths, the lepton forward-backward asymmetries and the τ polarisation can be combined to determine the effective couplings g_{Vl} and g_{Al} of the Z^0 to charged leptons. The couplings to the neutrinos can be measured from the invisible width of the Z^0, Γ_{inv}, under the assumptions that there are three identical neutrino generations ($\Gamma_{inv} = 3\Gamma_\nu$) and $g_{V\nu} \equiv g_{A\nu} \equiv g_\nu$. The averaged results, assuming lepton universality, for the effective couplings are given in Table 4. Figure 2 shows the 68% probability contours in the $g_{Al} - g_{Vl}$ plane.

Parameter	Average Value
g_{Vl}	-0.03681 ± 0.00085
g_{Al}	-0.50112 ± 0.00032
g_ν	$+0.50125 \pm 0.00092$

Table 4: Effective couplings of the Z^0 boson to leptons from LEP measurements of partial widths, lepton forward-backward asymmetries and τ polarisation. Lepton universality is assumed.

The asymmetry measurements determine the ratio g_{Vl}/g_{Al}, and the results are often expressed in terms of the effective electroweak mixing angle $\sin^2\theta_W^{eff}$ defined as

$$\sin^2\theta_W^{eff} \equiv \frac{1}{4}\left(1 - \frac{g_{Vl}}{g_{Al}}\right). \tag{16}$$

This definition of the electroweak mixing angle is convenient because it absorbs vertex corrections for leptons. The results of these determinations are shown in Table 5.

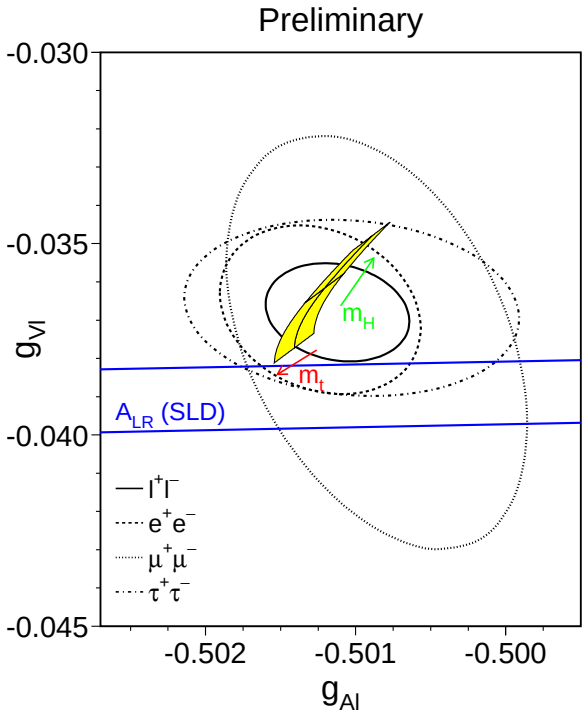

Figure 2: Contours of 68% probability in the $g_V - g_A$ plane from measurements of asymmetries and partial widths at LEP. The solid contour shows the result from a fit assuming lepton universality. Also included is the one-standard-deviation band from left-right asymmetry measurements at SLD. The shaded region shows the Standard-Model prediction for a top mass of $m_t = 175.6 \pm 5.5$ GeV and a Higgs mass of $m_H = 300^{+700}_{-240}$ GeV. The arrows point in the direction of increasing values of m_t and m_H.

3 Experimental Aspects

The high precision of the LEP experiments require very accurate measurements of the beam energy and of the luminosity. The main contribution to the error on the Z^0 mass comes from the uncertainty of the absolute beam energy, while the error on the Z^0 width is related to the uncertainty of the difference in centre-of-mass energies around the Z^0 pole. Accurate knowledge of the luminosity is crucial to the precision of the cross-section measurements.

3.1 Measurements of Beam Energy

Beam energy is measured at LEP through a method called resonant depolarisation [5], [7], which is the cornerstone in the determination of the beam energy. However, several corrections to the value measured by resonant depolarisation must be made before a final value of the energy is obtained. Resonant depolarisation makes use of the fact that transverse spin polarisation builds up naturally in e^+e^- storage rings through interaction of the electrons or positrons with the magnetic guide field, the so-called Sokolov-Ternov effect. The beam is depolarised by an applied oscillating magnetic field, which is made to resonate with the spin precession of the polarised beam electrons. The number of spin precessions per turn is proportional to the average beam energy. Such calibrations are typically performed at the end of physics fills, although they were less frequent in the early days of LEP. The intrinsic accuracy of the method is of the order of 200 keV [8].

	$\sin^2\theta_W^{eff}$
$A_{FB}^{0,l}$	0.23102 ± 0.00056
$\mathcal{A}_\tau$	0.23228 ± 0.00081
$\mathcal{A}_e$	0.23243 ± 0.00093
$A_{FB}^{0,b}$	0.23237 ± 0.00043
$A_{FB}^{0,c}$	0.2315 ± 0.0011
$< Q_{fb} >$	0.2322 ± 0.0010
Average(LEP)	0.23199 ± 0.00028
A_{LR} (SLD)	0.23055 ± 0.000412
Average(LEP+SLD)	0.23152 ± 0.00023

Table 5: Effective electroweak mixing angle determined from different asymmentry measurements. For comparison, values obtained from forward-backward asymmetries with b and c quarks and from charge asymmetries are also included, as well as the result from left-right asymmetry measurements at SLD.

Ground motion, due to terrestrial tides, heavy rainfalls, etc., causes the energy of LEP to vary with time, because the circumference is altered so that the ideal orbit no longer passes through the centre of the quadrupoles. The variation of the energy due to ground motion is about 10 MeV [9]. Therefore, the beam orbit is continually monitored during the physics periods.

The beam energy is extracted from a model that is based on the resonant-depolarisation measurement and which takes into account the beam-orbit measurements as well as other terms correcting for variations in, for example, RF cavity voltages, magnetic dipole fields and temperatures. The determination of the beam energy at LEP1 according to this method results in an uncertainty of 1.5 MeV in the Z^0 mass; the uncertainty in the Z^0 width is also 1.5 MeV [3].

The method of resonant depolarisation is not directly applicable at LEP2 energies; it becomes very difficult to achieve sufficient polarisation at beam energies above 45 GeV. Energy calibrations based on resonant polarisation are performed at lower energies, and the results are extrapolated to LEP2 energies. The extrapolation is based on magnetic-field measurements. The resulting uncertainty of the LEP energy is 30 MeV; however, the knowledge of the beam energy is less crucial at LEP2 than at LEP1 [4], [10].

3.2 Luminosity

The determination of luminosity at LEP is based on counting Bhabha events at low angles. Bhabha scattering is t-channel e^+e^- scattering, a well-known QED process with a large event rate and little dependence on the parameters to be measured in the precision tests. The differential cross section of the process has a steep angular dependence, $1/\theta^3$, which places high requirements on the electromagnetic calorimeters that are used as luminosity monitors. They must have good energy resolution; their geometrical acceptance must be known very precisely; and they must be very accurately positioned around the beam pipe on either side of the experiments. The inner edge of the monitors must be known with a precision better than 100 μm in order to match the statistical accuracy. Shifts in the location of the interaction point and in the beam alignment must also be carefully followed. The experimental uncertainty is now below 0.1% [9], which is smaller than the theoretical uncertainty of about 0.11% [3] in the calculation of the Bhabha cross section. The precision of the Bhabha cross section is currently limited by the lack of calculations of higher-order corrections.

4 Measurements of W Mass

The measurements of the W mass are treated elsewhere in these proceedings; therefore, only a brief indication of the principles and the results is given here.

Three channels are involved in the production of W pairs through $e^+e^- \to W^+W^-$ at LEP: s-channel exchange of a photon or a Z^0 and t-channel exchange of a neutrino ν_e. The decay modes are $W^+W^- \to q\bar{q}q\bar{q}$ with a branching ratio of 45.6%; $W^+W^- \to q\bar{q}l\nu$ with a branching ratio of 43.8% and $W^+W^- \to l\nu l\nu$ with a branching ratio of 10.6% [1].

At energies just above the threshold for W-pair production, the W mass is measured through the cross section for W production, which has its maximum sensitivity to the W mass in this region. The measured cross section is compared with the predicted cross section as a function of the W mass. Consequently, this method was used for the data collected at $\sqrt{s} = 161$ GeV. During this period of data taking, each of the four LEP experiments recorded about 30 W pairs. The W mass determined by this measurement, combining the results of the four experiments, is $80.40^{+0.22}_{-0.20}$ GeV (see Figure 3).

At higher energies, the W mass is determined through kinematic reconstruction of the decay products. This is the method used for data taken at $\sqrt{s} = 172$ GeV, as well as for data taken at $\sqrt{s} = 183$ GeV. Each experiment recorded approximately 100 W pairs at 172 GeV and close to 800 W pairs at 183 GeV. The W mass determined from the data collected at 172 GeV is 80.53 ± 0.18 GeV; combining it with the result from the measurement at 161 GeV yields a LEP average of the W mass of

$$\boxed{m_W = 80.48 \pm 0.14 \text{ GeV}.}$$

No result from the data taking at 183 GeV was available at the time of writing.

In addition, the LEP experiments determine the W-pair cross section also at energies above the threshold. These measurements are in excellent agreement with the Standard Model and show strong support for the existence of all of the three production channels mentioned above (see Figure 4).

5 Radiative Corrections and Constraints on the Standard Model

The high precision with which the LEP experiments measure the directly observable parameters of the Standard Model makes them sensitive also to parameters that appear virtually in some of the radiative corrections at LEP energies. If one assumes the validity of the Standard Model, the radiative effects can be measured and used to put constraints on these parameters. The sensitivity of the LEP experiments to radiative effects is illustrated in Figure 5. It was demonstrated by the highly successful prediction of the mass of the top quark before the top quark was discovered and its mass measured directly at the Tevatron: The last prediction from precision measurements before the top quark was observed at the Tevatron in 1994 was $m_t = 174 \pm 11^{+17}_{-19}$ GeV [11]; averaged results from the CDF and DØ collaborations give a current top mass of 175.6 ± 5.5 GeV [12], [13], [14].

5.1 Important Radiative Effects

The radiative effects that are important to the LEP experiments can be classified in different categories (see, e.g., [15], [16], [17], [18]):

- One large group of corrections are those that arise from pure QED effects, i.e., emission of real or virtual photons. They depend on energies, experimental cuts, etc., but can be calculated within the framework of QED. As mentioned in Section 2.1, the method to take these corrections into account is to convolute Eq. 1 by a radiator function before the lineshape parameters are extracted.

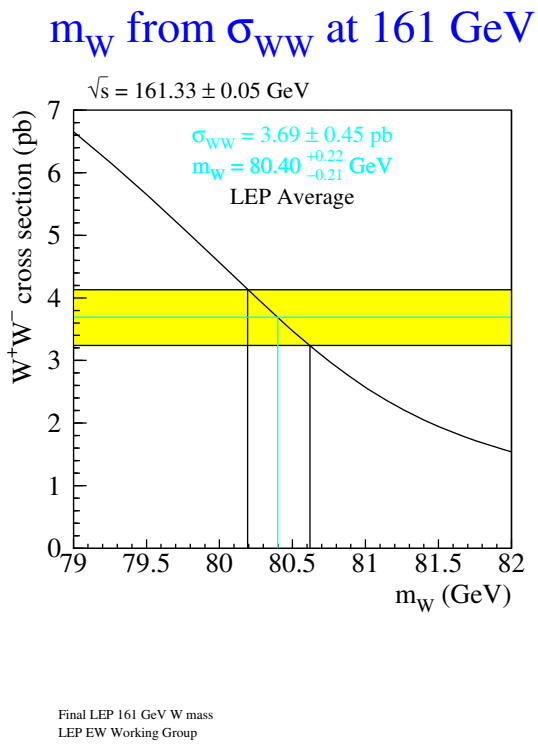

Figure 3: The determination of the mass of the W boson, m_W, from the cross section for W-pair production, σ_{WW}, at a centre-of-mass energy of 161 GeV. The curve shows the Standard-Model prediction for the cross section as a function of the W mass. The shaded band shows the measured cross section with its uncertainty.

- A second group pertains to the running of the QED coupling constant, α, due to the photon self energy:

$$\alpha \to \alpha(m_Z^2) = \frac{\alpha(0)}{1 - \Delta\alpha(m_Z^2)}. \tag{17}$$

The value of α at the Z^0 pole is an important input parameter to the precision electroweak measurements. Unfortunately, however, it is not known with great precision. The contribution from leptons to the photon self energy can be calculated analytically and is well known. The contribution from quarks is not entirely calculable due to uncertainty of the light quark masses; instead it is measured experimentally through integration of

$$R_h \equiv \frac{\sigma\left(e^+e^- \to \text{hadrons}\right)}{\sigma\left(e^+e^- \to \mu^+\mu^-\right)} \tag{18}$$

over $\sqrt{s}$. The largest uncertainty comes in the contribution from the low-energy range: More than 75% of the error comes from the range $1 \leq \sqrt{s} \leq 5$ GeV [19].

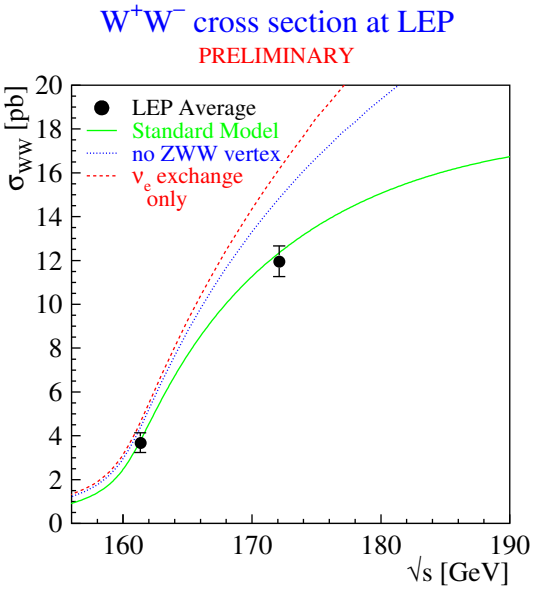

Figure 4: The cross section for W-pair production, σ_{WW}, as a function of the centre-of-mass energy. The dots show the LEP averages at 161 and 172 GeV. The solid curve shows the Standard-Model prediction when all three production channels are included (s-channel exchange of a γ or a Z^0 and t-channel exchange of a neutrino ν_e); the dotted curve shows the prediction if the ZWW coupling did not exist, and the dashed curve shows the prediction if only t-channel neutrino exchange existed.

- Loop corrections to Z^0 and W propagators give rise to corrections to the ρ parameter,

$$\rho = \frac{m_W^2}{\cos^2\theta_W m_Z^2}, \tag{19}$$

  which is equal to 1 at tree level. This group contains corrections that are sensitive to the top mass with a quadratic dependence:

$$\Delta\rho_t \sim \frac{m_t^2}{m_Z^2}.$$

  There is also sensitivity to the Higgs mass, although this dependence is much weaker; it is only logarithmic:

$$\Delta\rho_H \sim \log\frac{m_H^2}{m_Z^2}.$$

  However, the LEP experiments have now reached a level of sensitivity high enough for the constraints on the Higgs mass to be interesting, despite the weak dependence.

- Corrections to the $Z \to b\bar{b}$ vertex are sensitive to the top mass, with a quadratic dependence:

$$\delta_{vb} \sim \frac{m_t^2}{m_Z^2},$$

  where δ_{vb} is given by $\Gamma_{bb} = \Gamma_{dd}\,(1 + \delta_{vb})$.

5.2 Measurements

The Standard-Model parameters that are determined through radiative corrections at LEP are the mass of the top quark, the strong coupling constant $\alpha_s(m_Z^2)$ and either the mass of the Higgs boson or that

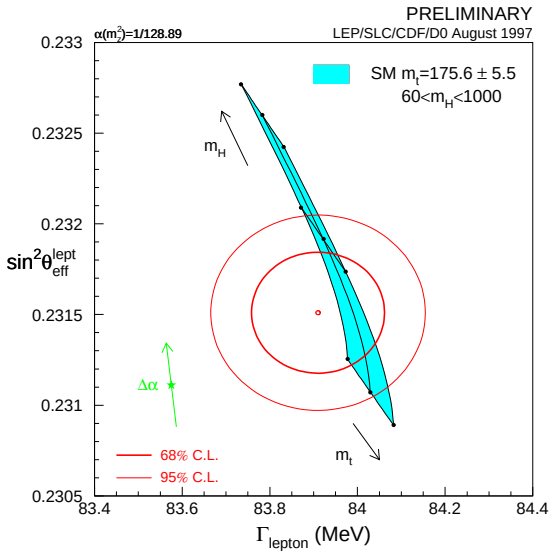

Figure 5: Contours of 68% and 95% probability of the effective electroweak mixing angle (LEP+SLD) *vs.* the leptonic partial width. The shaded area shows the Standard-Model prediction for a top mass of $m_t = 175 \pm 5.5$ GeV and a Higgs mass $m_H = 300^{+700}_{-240}$ GeV; the arrows indicate the directions of increasing top and Higgs masses. The star shows the Standard-Model prediction if all the electroweak radiative corrections except the running of α are left out. The arrow on the star indicates the influence of an uncertainty of one standard deviation on $\alpha(M_Z^2)$.

of the W boson. Different fit strategies are used to determine the different parameters. Three examples showing how m_H, m_t and m_W are determined are given here:

- An indirect measurement of m_t and m_W is compared to direct measurements at LEP2 and the Tevatron. The indirect measurement uses data from LEP, SLD and neutrino-scattering experiments, excluding data on m_W; m_W and m_t are left as free parameters in the fit. The indirect and the direct measurements are compatible, which implies stringent limits on physics beyond the Standard Model (see Figure 6).
- The Higgs mass is constrained in a fit that uses all LEP data, including m_W from LEP2; only m_t and m_H are left free in the fit.
- The best constraint on the Higgs mass is obtained from a fit using all available electroweak data from not only LEP but also SLD, $p\bar{p}$ colliders and neutrino-scattering experiments, notably the top mass from the Tevatron.

The results of the two different fits of the Higgs mass are shown in Figure 7. The fit to LEP data only shows a preference for a light Higgs boson and a light top quark. The fit to all data yields a Higgs mass of

$$\boxed{m_H = 115^{+116}_{-66}\ \text{GeV}.}$$

Figure 8 shows $\Delta\chi^2 = \chi^2 - \chi^2_{min}$ as a function of the Higgs mass for the fit using all available data. With the error on the theoretical calculations taken into account, this fit yields a one-sided confidence level for the Higgs mass of

$$\boxed{m_H < 420\ \text{GeV at 95\% C.L.}}$$

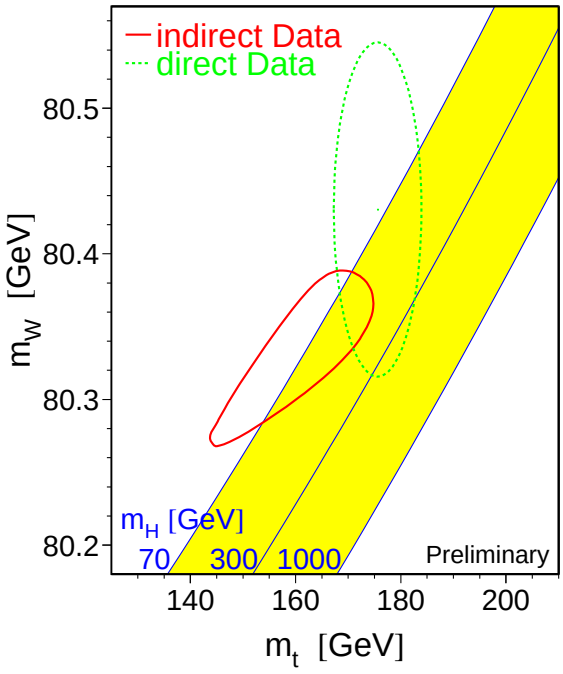

Figure 6: Contours of 68% probability for the W mass, m_W, *vs.* the top mass, m_t. The solid curve shows the result of the indirect measurement where data from LEP, SLD and neutrino-scattering experiments have been used. The dashed curve shows the results of direct measurements of m_W and m_t at LEP2 and at the Tevatron. The shaded region shows the Standard-Model relationship for the masses as a function of the Higgs mass. The LEP data indicate a preference for a light top quark and a light Higgs boson.

6 Conclusions and Outlook

The successful operation of LEP over several years has allowed precise tests of the Standard Model to be performed. The $SU(2)_L \times U(1)$ structure has been extremely well verified, with no deviation at the 10^{-3} level [9]. The radiative corrections have also been very well confirmed. The prediction of the top mass before it was discovered at the Tevatron in 1994 was indeed very successful. The predictions of the Higgs mass, together with the limits set by direct searches, are now becoming highly interesting and indicate the importance of the remaining years of data taking at high energies with LEP.

The LEP1 era ended in 1995. Some analyses are still unfinished, notably those of the τ polarisation and the quark forward-backward asymmetries. The results of what was probably the final LEP1 energy calibration were presented recently, and these results are now being taken into account by the experiments. At LEP2, improvements of the measurement of the W mass down to uncertainties of $\Delta m_W = 25 - 50$ MeV should be possible [1], [9]. When the LEP2 results are combined with those of the Tevatron, an uncertainty of $\Delta m_W \simeq 20$ MeV should be within reach [16].

The Higgs mass remains the only free parameter of the Standard Model still to be measured. Improvements in the prediction of the Higgs mass by precision electroweak tests will require improvements in all of the following [9], [16]:

- The determination of the top mass. This should come with increased statistics when the Tevatron restarts in 1999 after its upgrade.

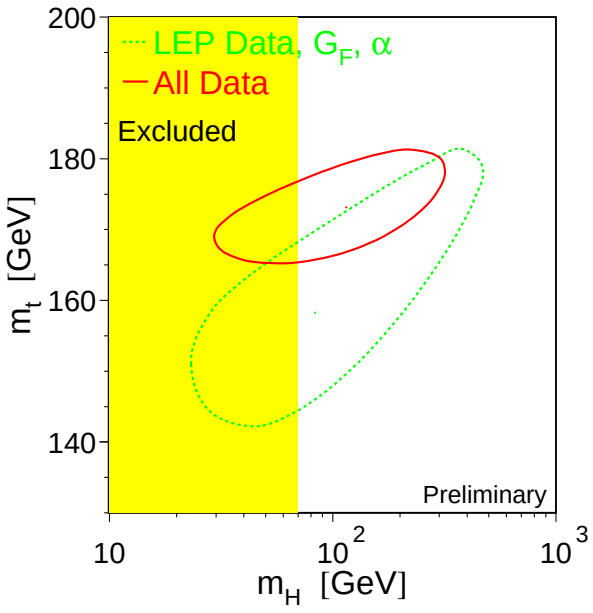

Figure 7: Contours of 68% probability for the top mass, m_t, *vs.* the Higgs mass, m_H. The dashed curve shows the result of the fit to LEP data only, with m_t and m_H left as free parameters. The solid curve shows the result of the fit using data from LEP, SLD, $p\bar{p}$ colliders and neutrino-scattering experiments, including the data on the top mass from the Tevatron. The shaded area shows the mass region excluded by direct searches. The LEP data again show a slight preference for a light top quark and a light Higgs boson.

- The measurements of $\sin^2\theta_W^{eff}$. The improvements will come from some unfinished analyses at LEP1 and from better statistics at SLD; the uncertainty can be expected to be reduced by a factor of 1.5 at most.
- The determination of $\alpha(m_Z^2)$. This is the most uncertain ingredient in an improved constraint on the Higgs mass. The improved value of $\alpha(m_Z^2)$ would come through measurements of low-energy hadronic cross sections, possibly from BES or Novosibirsk.

7 Acknowledgements

The author is greatly indebted to A. Blondel and A. Olchevski for their invaluable suggestions and help in selecting material. The underlying work of the LEP Electroweak Working Group in averaging the results of the four LEP experiments provided the platform for this presentation; most of the numbers and all of the graphs presented here were produced by them.

References

[1] D. Schaile in N. Ellis, M. Neubert, eds., CERN Yellow Report 97-03, p. 199.
[2] D. Ward, Talk given at the International Europhysics Conference on High Energy Physics, Jerusalem 1997.
[3] G. Quast, Talk given at the International Europhysics Conference on High Energy Physics, Jerusalem 1997.
[4] LEP Electroweak Working Group, Preprint CERN-PPE/96-183.
[5] LEP Polarization Collaboration, Preprint CERN-PPE/92-49.

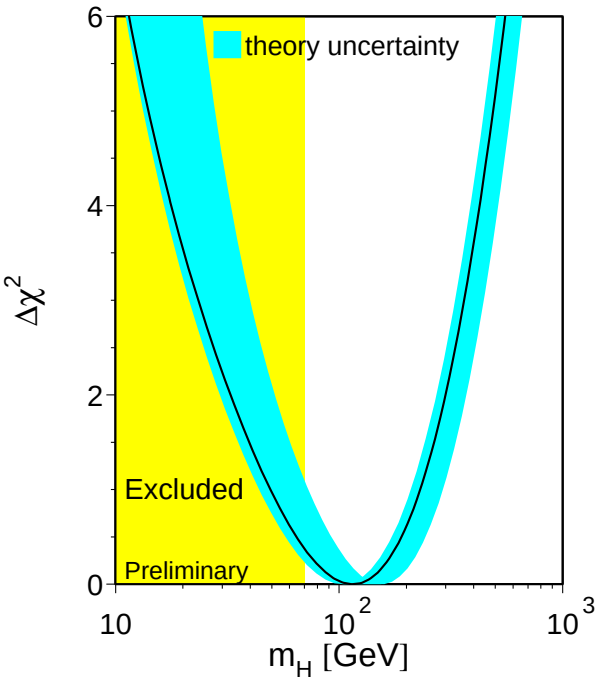

Figure 8: $\Delta\chi^2 = \chi^2 - \chi^2_{min}$ as a function of the Higgs mass, m_H. The curve shows the result of the fit using all available electroweak data, including the top mass from the Tevatron. The dark shaded region represents an estimate of the theoretical uncertainty due to missing higher-order corrections. The light shaded area shows the mass region excluded by direct searches.

[6] P. Langacker, ed., *Advanced Series on Directions in High Energy Physics,* vol. 14: *Precision Tests of the Standard Electroweak Model*, World Scientific Publishing Co., Singapore 1995.

[7] A. Blondel in [6], p. 277.

[8] A. Blondel in T. Riemann, J. Blümlein, eds., *Proceedings of the Zeuthen Workshop on Elementary-Particle Theory: Physics at LEP200 and Beyond*, Nucl. Phys. B, Proc. Suppl. 37B (1994) 3.

[9] A. Blondel in T. Ferbel, ed., *Techniques and Concepts of High Energy Physics IX*, p. 381, Plenum Press, New York 1997.

[10] A. Blondel *et al.* in *Proceedings of the 1997 Particle Accelerator Conference PAC '97,* Vancouver 1997.

[11] B. Pietrzyk, Talk given at the XXIX Rencontres de Moriond, Méribel 1994.

[12] CDF Collaboration, J. Lys, Talk given at the 28th International Conference on High Energy Physics ICHEP '96, Warsaw 1996; to appear in the proceedings.

[13] DØ Collaboration, S. Protopopescu, Talk given at the 28th International Conference on High Energy Physics ICHEP '96, Warsaw 1996; to appear in the proceedings.

[14] The results from CDF and DØ have been averaged together assuming a 3 GeV common systematic error.

[15] D. Schaile in [6], p. 215.

[16] A. Blondel, To appear in *Perspectives in Higgs Physics II,* ed. G.L. Kane, World Scientific Publishing Co.

[17] R.M. Barnett *et al.*, Physical Review D54, 1(1996).

[18] W. Hollik in [6], p. 37; p. 117.

[19] P. Renton in C.P. Zheng, H.S. Chen, eds., *Proceedings of the 17th International Symposium on Lepton-Photon Interactions LP '95*, p. 35, World Scientific Publishing Co., Singapore 1996.

[20] A. Blondel in CERN Yellow Report 92-06, p. 23.
[21] R. Miquel in CERN Yellow Report 92-06, p. 267.
[22] A. Olchevski in J. Lemmone, C. Vander Velde, F. Verbeure, eds., *Proceedings of the International Europhysics Conference on High-Energy Physics EPS-HEP '95*, World Scientific Publishing Co., Singapore 1996.
[23] A. Blondel, Private communication.
[24] A. Olchevski, Private communication.
[25] D. Treille in [6], p. 325.
[26] P. Langacker in [6], p. 15; p. 883.